UNIVERSITY
OF OSLO

Sajjad Ahmadigoltapeh

Exploring Fluid Properties in Confined Mineral Interfaces: A Molecular Investigation

– Implications for EOR

Thesis submitted for the degree of Philosophiae Doctor

Department of Geosciences
Faculty of Mathematics and Natural Sciences

2024

Series of dissertations submitted to the
Faculty of Mathematics and Natural Sciences, University of Oslo
No. 2781

ISSN 1501-7710

Cover: UiO.
Print production: Graphic center, University of Oslo.

To my beloved ones

Preface

As I began my doctoral research journey, I couldn't have imagined the unprecedented challenges that awaited. The onset of the COVID-19 pandemic in early 2020 shattered normalcy, deeply affecting not just daily life but also the trajectory of academic pursuits. Despite this turbulence, my dedication to advancing knowledge stayed unwavering, propelling me to navigate through uncertainties and persist in the pursuit of academic excellence. In the face of adversity, scientists worldwide mobilized their expertise and resources, ultimately delivering life-saving vaccines to combat the devastating effects of the coronavirus. While the loss of some million lives is a tragic reminder of the pandemic's severity, it underscores humanity's remarkable ability to overcome seemingly insurmountable challenges. This sobering lesson drives home the urgency of addressing global warming. Just as the pandemic exposed our vulnerabilities, the looming specter of climate change poses a grave risk to life on Earth. However, inspired by the resilience and collaboration witnessed in the fight against COVID-19, we embark on a new mission to confront the existential threat of climate change. In this endeavor, I hope that the findings of this Ph.D. project will make a meaningful contribution, fostering a brighter and more sustainable future for generations to come.

This dissertation is submitted to the Department of Geosciences of the Faculty of Mathematics and Natural Sciences, University of Oslo (UiO) in accordance with the requirements for the degree of *Philosophiae Doctor* (PhD). The candidate has been employed as a Ph.D. research fellow at this institution, with funding provided by the University of Oslo. Professor Helge Hellevang served as the main supervisor, with Associate Professor Rohaldin Miri providing co-supervision. Additionally, Professor Francois Renard contributed to scientific discussions, reviewed results, and provided feedback on the research.

This Ph.D. dissertation collects and summarizes the candidate's research findings, presented in accordance with the University's Manuscript Document Format. This thesis has focused on understanding fluid thermodynamics at confined mineral interfaces by simulating the rock-fluid interface at the nanoscale using first principle molecular dynamics technique. The present manuscript is organized into five main chapters:

- **Chapter 1** (Introduction) provides a framework for the coherence and scientific motivation of the dissertation, as well as identifying scientific questions.

- **Chapter 2** (Theoretical background) presents an overview of the theoretical foundation of the research.
- **Chapter 3** (Summary of papers and outlook for future works) summarizes the key findings and provides future directions for further investigations.
- **Chapter 4** (Journal papers) introduces three peer-reviewed published papers in which the candidate is the first author.
- **Chapter 5** (Appendices) provides summaries of conference proceedings and extended abstracts in which the candidate is the first author.

Sajjad Ahmadigoltapeh
Oslo, May 2024

Summary

Contact between rocks and fluids is ubiquitous in nature, observed in oceans, coastal boundaries, river banks, subsurface geological repositories, etc. Rocks are mostly made up of crystalline materials, known as minerals, which possess a periodic structure. The structural geometry of the constituent minerals determines the physical and chemical properties of the rocks. Among the organic and inorganic fluids that are in contact with rocks in nature, water is the dominant fluid playing the role of solvent in most cases. The rock-water interface is important because it does not only impacts processes like dissolution and precipitation but also serves as the location of interactions between the solid surface and the liquid phase. In addition to water molecules, the presence of other dissolved components, e.g., organic compounds, inorganic molecules, ions, and gases such as CO_2 affect the interface properties. On the one hand, these components interact with each other. On the other hand, they interact with the rock surface. The fluid-rock interaction influences the characteristics of the fluid entrapped at the boundary layer, causing the physical properties and phase behavior of the fluid to differ considerably from the equivalent bulk phase. The boundary layer, in this context, refers to a layer that is directly in contact with the rock surface. Regardless of whether the bulk fluid is in turbulent motion or not, the attraction forces between the rock surface and the fluid molecules restrict the fluid velocity to zero, resulting in the so-called noslip condition.

Although it has long been acknowledged that the solid mineral affects the fluid thermodynamic properties at the fluid-solid interface, the underlying mechanism of fluid-solid interactions still is inaccessible because of (i) limitations of the experimental technique and (ii) integration of experimental observations across relevant time scales. From a microscopic perspective, when the confinement size decreases and approaches the molecular dimension, which is comparable to the mean free path, the free thermal motion of fluid molecules is interrupted, resulting in diverse and unique thermodynamic properties. Therefore, it is critical to enhance our understanding of molecular aspects of fluid-solid interactions by employing a reliable approach. The first-principal molecular dynamics (MD) simulation is a trustworthy technique that can be utilized to study molecular aspects of fluid-rock interactions. Due to the developments in hardware (CPU and GPU) technology, the execution of MD computational algorithms has been shortened in terms of time. However, choosing large dimensions for the simulation box extends run-time, which means that the computational cost impact remains a challenge.

In this Ph.D. dissertation, the first-principal molecular dynamics simulation technique was utilized to capture the interaction between fluid molecules and the solid mineral surface. Furthermore, statistical associating fluid theory (SAFT) is

employed to model the complex thermodynamics of interfaces and incorporate the mineral effect into the fluid physicochemical properties confined in the nanopore. To be specific, the effort of this dissertation was to find answers for these key questions: (1) How to capture the above-mentioned deviations in fluid properties on the nanoscale? (2) How do we survey these deviations on the bulk scale? (3) How does the change in fluid chemistry affect the behavior of the mineral surface?
The above inquiries have been addressed through three distinct studies:

1. An investigation into the interface of pure water and calcite utilizing molecular dynamics simulation, alongside modelling the governing thermodynamics of the water-calcite interface with Perturbed Chain-Statistical Association Fluid Theory (PC-SAFT) equation of state.

2. An exploration of the properties of confined water sandwiched within a calcite nanopore, as well as modeling the dominant thermodynamics with the equation of state inspired by Statistical Association Fluid Theory (SAFT) .

3. The molecular dynamics simulation was used to examine the interface of low-saline water and calcite mineral with the aim of probing oil replacement dynamics and the behavior of various ions.

The methodology described and the subsequent outcomes of these basic studies can be applied in various fields of study. These applications include catalysis, contaminant transport, the effect of mineral grain size on chemical weathering, the effect of solid surfaces on limiting mineralization in oceans, the mechanisms by which microbes facilitate exchange between solid particles and solution, estimating solubility limits in multicomponent fluid processing, the mechanism of CO_2 exchange with sea water, enhanced oil recovery (EOR), subsurface CO_2 storage and more.

Sammendrag

Kontakt mellom bergarter og fluider i naturen foregår i sjøer, kystgrenser, elvebredder, underjordiske geologiske depoter, osv. Bergarter består for det meste av krystallinske materialer med periodiske strukturer, kjent som mineraler. Den strukturelle sammensetningen av mineraler i bergarter bestemmer deres fysiske og kjemiske egenskaper. Blandt de organiske og ikke-organiske fluider som er i kontakt med bergarter i naturen er vann et dominerende medium, og som oftest fungerer vannet som et løsemiddel. Grenseflaten mellom bergarter og fluider er viktig siden den ikke bare påvirker reaksjoner som oppløsning og utfelling, men også fungerer som stedet hvor alle interaksjoner mellom faste overflater og væsker foregår. I tillegg til vannmolekyler påvirker også tilstedeværelsen av andre oppløste komponenter, for eksempel organiske forbindelser, uorganiske molekyler, ioner, gasser som CO_2, grenseflateegenskapene. Dette skjer fordi disse komponentene på den ene siden påvirker hverandre samtidig som de på den andre siden interagerer med overflaten. Fluid-bergart interaksjoner påvirker egenskapene til fluider som er fanget i grensesjiktet. Dette gjør at de fysiske egenskapene og faseoppførselen til fluiden skiller seg fra den tilsvarende bulkfasen. Grensesjiktet i denne konteksten refererer til et lag som er i direkte kontakt med overflaten. Uavhengig av om fluiden er i turbulent bevegelse eller ei vil de tiltrekkende kreftene mellom overflaten og fluidmolekylene begrense fluidens hastighet til null, hvilket resulterer i den såkalte "noslip" tilstanden.

Selv om det lenge har vært kjent at mineraler påvirker en fluids termodynamiske egenskaper ved grenseflaten, er de underliggende mekanismene til fluid-fast-stoff-interaksjoner fortsatt ikke godt forstått på grunn av (i) begrensninger i eksperimentelle teknikker og (ii) integrasjon av eksperimentelle observasjoner over relevante tidsskalaer. Fra et mikroskopisk perspektiv, når størrelsen på et porerom reduseres og nærmer seg molekylære størrelser som er sammenlignbare med midlere fri veilengde (*mean free path*), blir de frie termodynamiske bevegelsene til fluidmolekylene begrenset, noe som resulterer i unike termodynamiske egenskaper. Det er derfor kritisk å fremme vår forståelse av molekulære aspekter ved fluid-fast-stoff-interaskjoner ved å ta i bruk en robust vitenskapelig tilnærming. Molekylærdynamiske (MD) simuleringer er en slik teknikk som kan brukes for å studerer molekylære aspekter ved fluid-stein interaksjoner. Takket være utviklingen i data-teknologi (CPU og GPU) tar kjøringen av MD beregnings-algoritmer mindre tid. Likevel er det fortsatt utfordringer relatert til begrensninger i tilgjengeling beregningstid og for store simuleringer på grunn av de tunge beregningene.

I denne doktorgradsavhandlingen ble molekylærdynamikksimulering benyttet for å forstå interaksjonen mellom fluid-molekyler og en mineraloverflate. Videre ble statistical associating fluid theory (SAFT) brukt til å modellere den komplekse

termodynamikkene ved grensesnitt og inkorporere effektev av mineraloverflaten på de fysikokjemiske egenskapene til vann som var innesluttet i en nanopore. Det spesifikke formålet med avhandlingen var å finne svar på følgende nøkkelspørsmål: (1) Hvordan beregne de nevnte avvikene i fluidegenskaper på nanoskala? (2) Hvordan undersøker vi disse avvikene på bulk-skala? (3) Hvordan påvirker endringen i fluidkjemi tilstanden til mineraloverflaten?
De nevnte spørsmålene har i neste steg blitt besvart i tre studier:

1. Undersøke grensesjiktet til rent vann og kalsitt med MD simulasjoner og modllere termodynamikken til vann-kalsitt-grenseflaten med PC-SAFT tilstandsligninger.

2. Undersøke egenskapene til vann innestengt i en nanopore med kalsitt på begge sider ved å bruke MD-simuleringer, og simmulere den termodynamikken med SAFT2 tilstandsligninger.

3. Bruke MD for å simulere grenseflaten til urent vann og kalsittmineraler, og undersøke dynamikken til de ulike komponentente.

Metoden og de påfølgende resultatene av disse grunnleggende studiene kan anvendes innen ulike fagfelt. Disse inkluderer katalyse, transport av forurensninger, effekten av mineralstørrelse på kjemisk forvitring, effekten av faste overflater på begrensning av mineralisering i havet, mekanismer der mikrober katalyserer utveksling mellom faste partikler og løsning, estimering av løselighetsgrenser i flerkomponent fluidbehandling, mekanismen for CO_2-utveksling med sjøvann, økt oljeutvinning (EOR), lagring av CO_2 under bakken, osv.

Acknowledgements

First, I extend my heartfelt gratitude to my supervisors, Professor Helge Hellevang and Associate Professor Rohaldin Miri, for their invaluable motivation, support, and expertise. Dear Helge, your enthusiasm and dedication to scientific research have been truly inspiring, helping me to develop confidence and independence as a researcher. Dear Rohaldin, I am immensely grateful for your availability whenever I needed help, your unwavering support, and your prompt responses even on weekends.

Special thanks to Professor Francois Renard for his invaluable advice, comments, and insightful ideas, which have significantly enhanced the quality of the research work. Dear Francois, your constructive feedback and valuable advice have greatly deepened my appreciation and interest in your field of expertise.

Throughout my time at the University of Oslo, it has been a privilege to be a member of the esteemed Department of Geosciences, where I have had the opportunity to apply my computational skills to the study of geological systems. I would like to thank all members of the department for fostering a positive atmosphere, offering generous support, and maintaining ongoing camaraderie. Special thanks to Professor Bernd Etzelmuller, Professor Valerie Maupin, Professor Emeritus Per Aagaard, Professor Jens Jahren, and Professor Nazmul Haque Mondol for their guidance and advice.

Endless gratitude for the companionship of my skilled and cheerful colleagues and office mates: Payman, Irfan, Clara, and Beyene. During my Ph.D. journey, I had the pleasure of collaborating with two brilliant friends Saeed and Jamluir, whose contributions greatly enriched my research. In particular, Jamilur, your unwavering support and determination have turned the seemingly impossible into reality.

I extend special thanks to my entire family, especially my parents, for their unwavering encouragement over the years. My wife deserves particular recognition for her patience and companionship. Her steadfast belief in me and enduring support have been crucial in helping me navigate the challenges and complexities of my academic journey. Last but certainly not least, I am deeply thankful for my little daughter. Though it has been a short time since you came into our lives, your love has been a constant source of strength and motivation, propelling me forward.

Sajjad Ahmadigoltapeh
Oslo, May 2024

List of papers

Paper I

Sajjad Ahmadi Goltapeh, Saeed Abdolahi, Rohaldin Miri and Helge Hellevang. "Extension of PC-SAFT equation of state to include mineral surface effect in fluid properties using molecular dynamics simulation". In: *Sustainable Energy Technologies and Assessments*. Vol. 48, (2021), pp. 101624.
DOI: https://doi.org/10.1016/j.seta.2021.101624.

Paper II

Sajjad Ahmadi Goltapeh, Rohaldin Miri, Per Aagaard and Helge Hellevang. "Extension of SAFT Equation of State for Fluids Confined in Nano-pores of Sedimentary Rocks Using Molecular Dynamics Simulation". In: *Journal of Molecular Liquids*. Vol. 348, (2022), pp. 118045.
DOI: https://doi.org/10.1016/j.molliq.2021.118045.

Paper III

Sajjad Ahmadi Goltapeh, Saeed Abdolahi, Jens Sigurd Jahren, Rohaldin Miri and Helge Hellevang. "Drivers of Low Salinity Effect in Carbonate Reservoirs Using Molecular Dynamics Simulation". In: *Journal of Molecular Liquids*. Vol. 360, (2022), pp. 119490.
DOI: https://doi.org/10.1016/j.molliq.2022.119490.

Conference proceedings

A: Sajjad Ahmadi Goltapeh, Saeed Abdolahi, Rohaldin Miri and Helge Hellevang. "Extension of SAFT equation of state to include calcite wall effect in water properties within water-calcite interface using molecular dynamic simulations." In: *InterPore* 13^{th} *Annual Meeting, 31May - 4June 2021.*

B: Sajjad Ahmadigoltapeh, Rohaldin Miri, Per Aagaard, Helge Hellevang. "Extension of the SAFT equation of state to capture the effect of the solid wall into the confined fluid properties: using molecular dynamic simulation." In: *InterPore* 14^{th} *Annual Meeting, 30May - 2June 2022.*

C: Sajjad Ahmadi Goltapeh, Saeed Abdolahi, Rohaldin Miri and Helge Hellevang. "Mineral-Fluid Interface Properties: A Molecular Dynamic Study." In: 83^{th} *EAGE Annual Conference & Exhibition, 6-9 June 2022, Madrid, Spain.* DOI: https://doi.org/10.3997/2214-4609.202210013.

D: Sajjad Ahmadi Goltapeh, Saeed Abdolahi, Rohaldin Miri and Helge Hellevang. "Low Salinity Water Impact on the Calcite-Water Interface: A Molecular Dynamic Study." In: *Geoconvension Conference, 20-22 June 2022, Calgary, Canada.* https://geoconvention.com

Contents

Preface iii

Summary v

Sammendrag vii

Acknowledgements ix

List of papers xi

Conference proceedings xiii

Contents xv

List of Figures xix

List of Tables xxiii

1 Introduction 1
1.1 Carbonate minerals . . . 1
1.1.1 Calcium carbonate in marine organisms . . . 1
1.1.2 Calcium carbonate in medicine . . . 2
1.1.3 Calcium carbonate in industrial applications . . . 2
1.2 Carbonate reservoirs . . . 3
1.3 Carbonate rock and aqueous phase interactions . . . 4
1.4 Water properties confined in mineral domains . . . 5
1.4.1 Aqueous phases confined at mineral interface . . . 5
1.4.2 Experimental methods and relevant limitations . . . 6
1.4.3 Computational techniques and relevant challenges . . . 7
1.4.4 Exploring mineral-water interfaces with molecular dynamics . . . 7
1.5 Motivation of the thesis . . . 9
1.6 Objectives . . . 9
1.7 Thesis structure . . . 11
1.8 Outline . . . 15

2 Theoretical background 17
2.1 Equation of state . . . 17
2.1.1 Cubic equation of state . . . 17
2.1.2 Limitations of cubic-type equations of state . . . 19
2.2 Statistical association fluid theory . . . 20

2.2.1 Hard-sphere (reference term) . . . 22
2.2.2 Chain term . . . 23
2.2.3 Dispersion term . . . 23
2.2.4 Association term . . . 23
2.2.5 Mixing rules . . . 24
2.2.6 Helmholtz term for water-calcite interaction . . . 24
2.3 Perturbed-Chain SAFT . . . 28
2.3.1 Hard-chain (reference term) . . . 29
2.3.2 Dispersion term . . . 30
2.3.3 Association term . . . 31
2.3.4 Ionic term . . . 31
2.3.5 Helmholtz contribution for water-calcite interaction . . . 31
2.4 Molecular dynamics . . . 34
2.4.1 Potentials in molecular dynamics simulations . . . 35
2.4.2 Newton's equations of motion . . . 37
2.4.3 Velocity Verlet algorithm . . . 38
2.4.4 Periodic boundary conditions . . . 40
2.4.5 Ergodicity hypothesis . . . 41
2.4.6 Nosé-Hoover thermostat . . . 42
2.4.7 Radial distribution function . . . 44
2.4.8 Energy minimization . . . 44
2.5 Material and geometry . . . 45
2.5.1 Hexagonal indices . . . 45
2.5.2 Calcite neutral plane . . . 46
2.5.3 Potential models for water . . . 48
2.5.4 Potentials for mono/divalent ions . . . 49

3 Summary of papers and outlook for future works 51
3.1 Development of PC-SAFT for one-dimensional confinement . . . 52
3.1.1 Paper I: . . . 52
3.1.2 My contribution . . . 52
3.1.3 Method . . . 53
3.1.4 Key findings . . . 53
3.2 Development of SAFT for two-dimensional confinement . . . 54
3.2.1 Paper II: . . . 54
3.2.2 My contribution: . . . 55
3.2.3 Method: . . . 55
3.2.4 Key findings: . . . 55
3.3 Underlying mechanisms driving smart water flooding . . . 58
3.3.1 Paper III: . . . 58
3.3.2 My contribution . . . 58
3.3.3 Method . . . 58
3.3.4 Key findings . . . 58
3.4 Conclusions . . . 60
3.5 Outlook . . . 63
3.5.1 Thermodynamic Modeling . . . 63

3.5.2 Machine Learning: An Alternative to Molecular Dynamics 63
3.5.3 Oil Displacement by Low-Salinity Water Injection 64
References 65

Papers **90**

I Extension of PC-SAFT equation of state to include mineral surface effect in fluid properties using molecular dynamics simulation **91**

II Extension of SAFT Equation of State for Fluids Confined in Nano-pores of Sedimentary Rocks Using Molecular Dynamics Simulation **103**

III Drivers of Low Salinity Effect in Carbonate Reservoirs Using Molecular Dynamics Simulation **129**

Appendices **155**

A InterPore 13th Annual Meeting, 31May - 4June 2021 **157**

B 83rd EAGE Annual Conference & Exhibition **159**

C InterPore 14th Annual Meeting, 30May - 2June 2022 **165**

D Geoconvension 2022 **167**

List of Figures

1.1 Some typical forms of calcite in nature, from left to right, top row: seashell, human spine bone, calcite crystal, crap shell. Bottom row: coral, mollucs, marble, and aragonite crystals. (images:freepik.com) 3

1.2 Sketch of the confinement geometry within water-calcite interface studied in Paper I. Lz is the distance from the uppermost layer of water bulk to the calcite surface. δ is the thickness of the surface-adsorbed layers. 12

1.3 Illustration of the confinement geometry within a calcite nanopore used for the simulations in Paper II. Lz denotes the width of the calcite pore. δ shows the thickness of the surface-adsorbed layers. 14

1.4 Sketch of the calcite-oil-brine system used in Paper III. Formation water (H_2O, Na^+, Cl^-,Ca^{2+}) and oil (toluene, decane, benzoic acid) and interact with the calcite ($10\bar{1}4$) surface. 14

2.1 A typical three-dimensional phase diagram and its projection onto pressure-temperature (P-T) and pressure-volume (P-V) planes [156]. 18

2.2 A brief overview of available thermodynamic EoS in literature [170]. 19

2.3 Visualizing the continuous spectrum of bond strengths . The energy spectrum highlighted in blue depicts the range from elementary van der Waals attractions to the formation of chemical bonds [172]. 20

2.4 Illustration of a typical SAFT molecular model, consisting of m spherical segments with diameter σ and three association sites. . 21

2.5 Different Helmholtz free energy contributions in SAFT. (a) Hard-spheres with repulsion-attraction interactions. (b) Formation of chains through covalent bonds between hard-spheres. (c) Dispersion interactions between the chains. (d) Association complex formation via association sites, such as hydrogen bonding, linking molecular structures. 22

2.6 Configuration of a calcite pore that contains water. The mineral walls interact with water molecules through a square-well potential [193]. As depicted, L_z is the distance between the outermost layers of the calcite surfaces. δ_{fw} and ε_{fw} are the width and depth of the square-well energy. $\sigma_i/2$ is the thickness of space above the calcite surface which contains no water molecule. 25

2.7 Illustration of different molecular contributions in PC-SAFT EoS including hard-chain (hc), dispersion (disp), association (ass) and ionic (ion). 28

2.8 Illustration of a water-calcite interface. The calcite nanoslab interacts with water molecules through square-well potential [201]. L_z is the distance between outermost layer of water and calcite surface. δ_{fw} and ε_{fw} are width and depth of the square-well energy. $\sigma_i/2$ is the thickness of vacant space above the calcite surface. 32

2.9 For molecular dynamics simulations, two main contributions of potential energy should be defined. The bonded term includes bond, angle, dihedral and improper species, while non-bonded one comprise van der Waals and electrostatic potentials [213] 35

2.10 Illustration of the Lennard-Jones (12−6 potential) function, where parameter r_m represents the equilibrium distance corresponding to the minimum bonding potential. The figure is adopted from [216]. 37

2.11 Overall approach of time integration in molecular dynamics simulations. The initial state (position and velocity) and interaction potential are input data to the simulations. 39

2.12 Sketch of a binary system, showing periodic boundary conditions. The black arrows show the velocity vector of the relevant particle. The central box represents the main simulation system. The particles that leave the central box are replaced by their image from the opposite box. Each particle interacts with the nearest image of other particles to adhere to minimum image convention. 40

2.13 Illustration of rhombohedral structure of calcite unit cell [240] . 46

2.14 Side views of different calcite cleaved planes: (a) (0001), (b) (1000), (c) (1120), (d) (1011), and (e) (1014). The planes (0001) and (1011) are depicted with a doubled unit cell along a direction, as the dipole perpendicular to the slab has been removed. Figure adapted from [246] 47

2.15 Assessment of different water models capability to account dipole (μ) and quadrupole (Q_T) moments. Adjusting the charge distribution in three- and four-point classical models (OPC) yields promising results [260] 48

3.1 Illustration of the density profile within region I and II at different Lz and T=300 K. The density is normalized between 0 and 1, which allows comparing the average density trends. The greatest and lowest average densities occur at Lz = 70 Å and Lz = 25 Å, respectively [201]. 54

3.2 Cross-sectional view of the calcite-water-calcite system. Water atoms are colored by red (oxygen) and white (hydrogen). Within the calcite structure, carbon, oxygen and calcium atoms are gray, green and purple, respectively. The colors of oxygen atoms in the three layers seen from the calcite surface are orange, pink, and turquoise, respectively. To the bottom, the water density is plotted along z-axis, with line segments colored after the layer number. Ovito was used for visualization. 57

3.3 The sketch depicts settlement of Na^+ and Cl^- in close proximity to the surface, resulting in the formation of a double electrical layer. In (a) black balls represent benzoic acid in the oil layer adhere to the calcite surface via formation water. In (b) the oil layer separates from surface after Na^+ and Cl^- have settled. . . 60

List of Tables

2.1 Comparative analysis of surface energies across various calcite crystallographic planes 47

Chapter 1

Introduction

To efficiently utilize our planet's resources located in the subsurface and effectively tackle environmental challenges, a deep understanding of the interactions between minerals and fluids is required. Imagine a future where one could efficiently remove contamination from water resources and soils [1, 2], precisely estimate water capacities in groundwater aquifers [3, 4], cost-effectively develop geological hydrogen storage [5–7], rapidly advance geological CO_2 storage [8, 9], accurately predict the behavior of petroleum fluids [10, 11] and thoroughly understand the geological factors influencing the enhancement of oil recovery [12, 13]. These challenges may appear complex and all involve processes at the mineral-fluid interface. Understanding these processes is critical to paving the way for a more eco-friendly and greener future.

1.1 Carbonate minerals

Carbonates are the most abundant minerals found in Earth's sedimentary layers [14]. They have a long history of construction, dating back to their use during the Roman Empire [15]. Often, children interact with calcium carbonate for the first time at school, where it is used to write on chalkboards, as chalk is composed of fine microcrystalline calcite particles [16]. Prehistoric paintings found in limestone caves reveal that humans from ancient times carved information onto limestone slabs[17]. The discovery of inscriptions (cuneiform texts) on limestone such as the Kish tablet [18] highlights the long-standing use of limestone as a writing tool for ancient civilizations [19, 20].

1.1.1 Calcium carbonate in marine organisms

Calcium carbonate is not limited to the Earth's crust, it is a key component in marine animals, including mollusks, invertebrates (corals, seashells), and even vertebrates, such as fish, which utilize biogenic calcium carbonate [21–23]. Combining organic molecules with biogenic calcium carbonate gives unique advantages to marine organisms, including precise control over the morphology of biogenic crystals of calcite or aragonite [24–26]. Coccolithophores, for example, demonstrate the ability to control the growth of calcite shells in seawater through biomineralization [27]. Marine organisms utilize calcite to grow skeletons and exoskeletons, which exhibit stronger mechanical strength compared to non-biogenic ones [28, 29]. The improved strength is attributed to the incorporation of amino acids into their structure [30]. Furthermore, the hierarchical structure of these biominerals plays a significant role in their overall hardness, enhancing their ability to tolerate external pressure [31]. This mechanical strength makes

biogenic calcium carbonate an excellent choice for the development of composites with improved stiffness [32, 33].

1.1.2 Calcium carbonate in medicine

Another example of the versatility of calcite can be seen in its numerous applications in the field of medicine. Calcite is used for applications such as the development of synthetic bones and the treatment of bone defects [34, 35]. Its suitability is attributed to a range of valuable properties, including its antibacterial activity [36], biocompatibility [37, 38], bioinductivity [39] and non-toxicity [40]. Furthermore, due to slow degradation and sensitivity to pH, calcite can function as a controlled release agent, ensuring that drugs remain at targeted sites in the body for longer periods after administration [41]. It is worth noting that its history in dentistry dates back more than a century, when calcium carbonate was used as filling materials to seal root perforation [42].

1.1.3 Calcium carbonate in industrial applications

Calcite has attracted interest in various industrial applications due to its natural abundance and low production cost. Some notable applications of calcite include, but are not limited to, environmental utilization, surfactants, paint manufacturing, paper production, fire extinguisher formulation, adhesives, household cleaning products, food coloring, and cosmetics [43–45]. Ordinary concrete, for example, is highly valued in the construction industry due to its compressive strength [46]. In cement limestone production, mainly composed of calcite, limestone is used as a permitted and essential additive [47]. When water is added to cement, it initiates a chemical reaction (cement hydration), resulting in the formation of a C-S-H paste. This paste hardens and reinforces the strength of hydrated cement [48]. Recent progress in nanotechnology has opened up new possibilities for the modification of cement-based materials on the nanoscale [49]. To be specific, the mechanical [50] and chemical adjustments [51] of cement on a nanoscale enable the generation of cement composites with improved properties and functionalities [52].

In addition, in alignment with global efforts to reduce greenhouse gas emissions, interest in environmentally friendly green cement has increased. One novel approach for green cement production involves the use of the microbiologically induced calcium carbonate precipitation (MICP) technique [53], employing the biomineralization reaction of $CaCO_3$. This process begins with the hydrolysis of urea catalyzed by urease, leading to an increase in pH through the following reaction [54]:

$$CO(NH_2) + 3H_2O \rightarrow 2NH_4^+ + HCO_3^- + OH^-$$

then, produced bicarbonate ions together with calcium ions Ca^{2+} will induce calcium carbonate precipitation:

$$HCO_3^- + Ca^{2+} + OH^- \rightarrow CaCO_3 \downarrow + H_2O$$

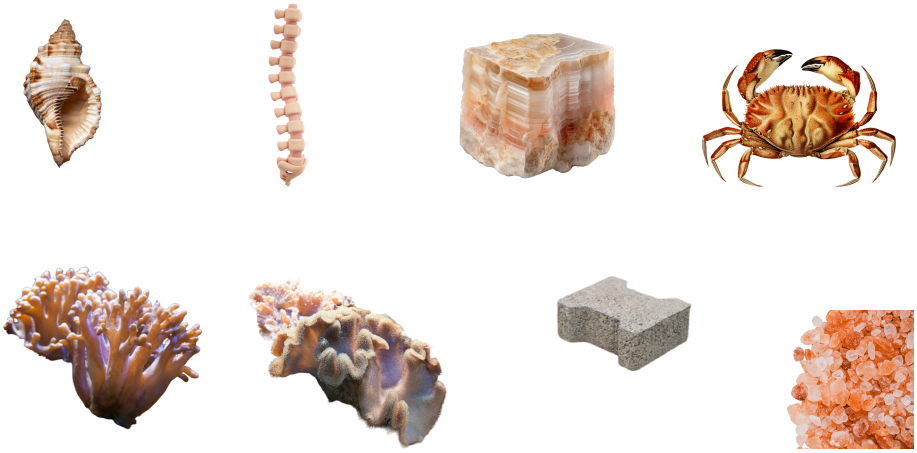

Figure 1.1: Some typical forms of calcite in nature, from left to right, top row: seashell, human spine bone, calcite crystal, crap shell. Bottom row: coral, mollucs, marble, and aragonite crystals. (images:freepik.com)

The urease enzyme, which is present in bacteria, plants and some invertebrates, plays an essential role in this process [55]. It is important to note that alternative materials, such as coal ash and slag from the blast furnace [56], as well as food wastes [57] can serve as the main components in the production of green cement. Green cement has a significant advantage due to its lower CO_2 emission rate compared to the conventional method, because it eliminates the need for a high-temperature calcination step in cement production [58]. In addition to its environmental benefits, green cement technology provides an opportunity to utilize waste streams [59, 60].

1.2 Carbonate reservoirs

In sedimentary basins, two main types of reservoir rocks can be defined: sandstone sequences [61] and carbonate sequences [62]. The former are mainly composed of quartz and other detritic minerals, and the latter are mainly composed of carbonate minerals, such as calcite and dolomite [63]. Carbonate rocks are formed through the accumulation and cementation of organic remains on the seabed [64]. These rocks have a porous structure that allows them to store a significant amount of fluid. They may host important groundwater aquifers and promising sites for CO_2 storage because of available storage capacity and geological integrity when covered by low-permeability caprocks [65, 66]. In addition, carbonate rocks are recognized as reservoirs for significant petroleum deposits. In fact, calcite is the major component of more than 50% of the world's oil reservoirs [67, 68]. In particular, the Middle East region is characterized

by its huge carbonate fields, housing around 70% oil and 90% gas reservoirs [69, 70]. In the North Sea, the Ekofisk field is another example of a reservoir characterized by high porosity and low permeability that has been in continuous production since 1987 [71].

1.3 Carbonate rock and aqueous phase interactions

In subsurface carbonate reservoirs, the interactions between calcite grains and aqueous phases are crucial. These interactions occur at the calcite-fluid interface, where water serves as the primary solvent [72]. To initiate a chemical reaction, it is essential for ions to attach to the calcite surface, necessitating the displacement of adsorbed water molecules. In other words, to make room for ions to interact with the calcite surface, water molecules that were previously attached to the calcite surface must be pushed away [73–75]. Therefore, water interactions with the surface of the calcite are an important part of any chemical reaction [76–78].

In general, interpreting the interactions between calcite rock and water is a complex task due to the diverse phenomena observed at mineral-fluid interfaces [79]. Each of the observed phenomena is potentially governed by distinct mechanisms, making it challenging. For instance, water weakening, a frequently reported phenomenon in carbonate reservoirs, occurs as a result of interactions between the calcite and aqueous phase. Basically, water injection into the oil reservoir is performed to compensate for the pore pressure (ensuring that the crude oil remains above the bubble point) and improves the sweeping efficiency [80, 81]. However, interactions between calcite and water for long periods can affect the mechanical strength of the reservoir and lead to compaction and subsidence [82, 83]. Studies have shown that various factors such as surface energy [84] and the physicochemical properties of water [85] contribute to water weakening, finally leading to the deformation of carbonate rocks [86–89].

Another well-documented phenomenon in subsurface carbonate reservoirs is wettability alteration of carbonate rocks. The surface of calcite is naturally hydrophilic, namely it has an inherent tendency to adsorb water [90]. This is due to the positive electrostatic charges present on the calcite surface that attract water molecules, resulting in a water-wet surface [91]. However, in subsurface reservoirs, calcite exhibits moderate to strongly oil-wet behavior [92]. Wettability alteration in calcite occurs because of its interaction with hydrocarbon fluid at the calcite-fluid aqueous interface. This interaction results in the adsorption of polar compounds such as carboxylic acids and asphaltenes contained in crude oil [93] leading to the oil-wet surface property of calcite.

The examples mentioned above represent only a few instances among many, providing insights into colloidal interactions at the calcite-water interface in subsurface reservoirs. This complexity makes it a challenging but interesting field of study. One significant challenge that will be the central focus of this Ph.D. dissertation arises at the interface where calcite and water come into contact. At this nanoscale proximity, the behavior of water differs from its behavior in bulk scale. Indeed, when two opposing surfaces of calcite and water become very

close on a nanoscale level, the characteristics of water are affected and deviate from what is typically observed in bulk water.

1.4 Water properties confined in mineral domains

Mineral-induced changes in the physicochemical properties of fluid occur at confined mineral interfaces where a nanometer thick water layer interacts with the mineral surface. Understanding the underlying mechanisms of mineral-fluid interactions plays a crucial role in various fundamental and practical areas, ranging from surface science to materials science [94, 95]. In recent years, scientists have utilized diverse methodologies to accurately predict and determine the phase behavior and thermodynamic properties of fluids confined within restrictive nanoscale cavities [96, 97]. These cavities typically have dimensions ranging from 1 to 10 nm, imposing significant limitations on the fluid's behavior. For example, in a comprehensive investigation, Knight et al.[98] sought to understand the effects of nanoscale confinement on water properties. By combining experimental analyses and observations, they successfully demonstrated that mineral confinement at the nanoscale induces significant alterations in the physical properties of water. They observed a decrease in the melting and freezing point temperature of confined water as the spatial confinement level increased. Furthermore, they observed notable changes in the hydrogen-bonding network within the confined water.

Studying the unique physical and chemical properties exhibited by confined water under mineral confinement requires advanced empirical techniques for molecular scale investigations. An interesting area of study is the behavior of pure water at confined mineral interfaces. In pioneering studies, Salmeron and co-workers [99, 100] applied polarized force between the tip of atomic force microscopy and the solid mineral to investigate the condensation and evaporation processes of water. They found a relation between environmental humidity and formation of water monolayers on the mica surface. Their observations showed that when humidity remains below 25% a thin water film over mica surface grew to a thickness of several angstroms. However, for humidity over 25%, they reported the formation of a second layer of water, leading to the creation of large islands with distinct geometrical shapes [101]. In another study Wu et al.[102] used a nuclear magnetic resonance instrument to investigate how water behaves in calcite and silica pores. Their findings showed that the water molecules trapped within the calcite pores exhibited higher activity compared to those in the silica pores. This discrepancy can be attributed to the different kinds of hydroxyl groups at calcite and silica surfaces, leading to variations in the distribution of water molecules within the pores, resulting in higher activity for water in contact with calcite pore.

1.4.1 Aqueous phases confined at mineral interface

Expanding our understanding of mineral-fluid interactions, some studies have explored the behavior of aqueous phases confined at mineral interfaces. For

example, Ruiz and Putnis [103, 104] revealed that the rate of calcite dissolution in a water environment is influenced by the type and concentration of the electrolyte solution. This influence is explained by changes in the dynamics of water structure, particularly the alteration of the activation energy barrier for breaking water-water interactions. In a related study, Li et al. [105] investigated the growth of calcite crystals under conditions involving confinement near an aqueous phase. They identified two common types of confined growth: smooth and rough, which are not unique to calcite, but a general consequence of confinement.

Guren et al. [106] investigated the remediation potential of the calcite mineral for contaminated water resources. They utilized atomic force microscopy to investigate dissolution-precipitation processes in nanoslab calcite exposed to an aqueous phase enriched with chromium ions. They observed that chromium ions were trapped within the nanopores of the calcite surface, formed as a result of dissolution-precipitation mechanisms. The precipitated chromium carbonate established a passive layer on the calcite surface, effectively preventing further dissolution of the calcite. To this end, Julia et al. [107] investigated the efficiency of the carbonate rock surface in sequestering cadmium from contaminated water. Their findings revealed that the presence of a calcite surface facilitated cadmium precipitation from aqueous phase by a coupled dissolution-precipitation process.

Dziadkowiec et al.[108] highlighted how the composition of the aqueous phase and the hydration characteristics govern the thickness of the surface-adsorbed water layers on calcite. They studied the adhesive forces between two cleaved $(10\bar{1}4)$ calcite surfaces submerged in aqueous solutions with atomic force microscopy. They found altering the Ca^{2+} content in aqueous phase had a limited impact on the adhesive forces between calcite pore-walls. However, Ca^{2+} ions have stronger effect on adhesion, compared with Na^{+} ions. Furthermore, strongly hydrated ions like Ca^{2+} supported thicker water film on the calcite surface compared to Na^{+}.

1.4.2 Experimental methods and relevant limitations

Despite numerous efforts, directly visualizing the mineral-water interface and measuring its physicochemical properties remains a challenge. This challenge stems primarily from limitations in experimental techniques. For example, the dynamic nature of the water film adhered to the mineral surface often requires experiments to be conducted under ultra-high vacuum conditions and cryogenic temperatures [109, 110]. Additionally, experiments with atomic force microscopy may lead to the formation of an ice structure due to the application of local pressure [111]. There are challenges in completely isolating water films when using the electron spectroscopy technique [112], and the water film on the mineral surface may be perturbed by scanning tunneling microscopy tip, causing the water molecules to move and form a cluster [113]. Alternatively, semi-empirical models such as Langmuir [114], Freundlich [115], and Brunauer-Emmett-Teller (BET) [116] adsorption methods may be used to determine the local properties of the fluid confined within a nanopore. These approaches are nevertheless incapable of capturing phase transitions. The time costs, non-repeatability, and

operational constraints (i.e., temperature and pressure) make it difficult for the mentioned empirical and semi-empirical methods to accurately forecast the confined fluid properties.

1.4.3 Computational techniques and relevant challenges

In the exploration of atomic-scale complexities related to mineral-fluid interfaces, computational techniques such as Density Functional Theory (DFT) and Molecular Dynamics (MD) have gained popularity as viable alternatives to direct empirical measurements and observations [117, 118]. These methods offer a comprehensive understanding of the underlying phenomena at the molecular level, offering valuable insights into the behavior of fluids confined within mineral nano-structures. DFT is a computational technique rooted in the principles of quantum mechanics that explicitly incorporates electron interactions, allowing the modeling of reaction mechanisms between calcite, oil, and brine water. Nevertheless, the complexity of composition and structure in most minerals, along with the numerous interactions involved in the mineral-fluid interface, often makes the use of DFT methods impractical due to their limited time- and length-scales. However, molecular dynamics (MD) simulations offer a reliable alternative to investigate the fluid properties at the solid-fluid interface. In molecular dynamics simulations, atoms are treated as spheres bonded to one another through a set of springs. This simplified approach, compared to DFT, enables simulations with significantly larger time- and length-scales [119].

The primary limitation of classical molecular dynamics (MD) simulations lies in their inability to capture bond breaking and formation, thereby hindering the modeling of chemical reactions without specialized parameter sets. Despite this drawback, classical MD simulations are gaining prominence as a crucial technique for investigating mineral-fluid interfaces, thanks to their capability to elucidate physical processes at the molecular level [120–122].

1.4.4 Exploring mineral-water interfaces with molecular dynamics

Using molecular dynamic simulations, de Leeuv and co-workers [123] reported that the physisorption of water molecules on the $10\bar{1}4$ cleavage plane of calcite is favorable in terms of energy. Then, in a separate study, Kerisit and Parker [124] calculated the adsorption free energy of water on the $10\bar{1}4$ calcite surface and demonstrated a reduction in water diffusion near the calcite surface. Rahaman et al. [125] simulated the calcite-water interface using molecular dynamics. They studied different humidity conditions in simulation domains to study the formation of interfacial liquid water on the $10\bar{1}4$ surface of calcite. The results demonstrated that the mobility of water molecules increases when humidity remains high. In simpler terms, under low humidity conditions, water molecules strongly stick to the calcite surface, indicating that the water molecules occupied well-defined sites at the calcite surface. Furthermore, they reported that the water molecules exhibited higher mobility along the calcite surface compared to

the perpendicular motion, which required substantial initial forces to overcome the steep barrier.

To better understand the interaction of water molecules with different sites on the calcite surface, Wolthers et al.[126] used molecular dynamic simulations. They chose $10\bar{1}4$ surface of calcite, including the etch pit and growth island as the mineral surface. Simulations revealed that calcium ions on the mineral surface may adsorb up to three water molecules, depending on their surface position (face, edge, or corner). Additionally, carbonate groups on the mineral surface can interact with water molecules through all oxygen atoms, depending on whether they were located on a face, an edge, or a corner of the calcite lattice. This study concluded that the topography of the calcite surface determines its reactivity. In their computational experiment, Brekke-Svaland and Bresme[127] simulated the $10\bar{1}4$ surface of calcite and the 001 surface of aragonite at a nanometer distance submerged in water using Large Atomic/Molecular Massively Parallel Simulator (LAMMPS) [128]. They quantified how the mineral-mineral interactions depend on the topography of the mineral surface structure of the adsorbed water on the mineral surface.

Regarding the behavior of organic and inorganic fluids dissolved in aqueous phases, Zhang [129] et al. studied the characteristics of oil and water within a calcite nanopore by analyzing the volumetric flow flux, the velocity profiles of water and oil, and the molecular configurations in the layers of oil and water. They observed that water tends to accumulate on the calcite surface as a result of the hydrophilic nature of this mineral, leading to specific flow phenomena. They reported that at low oil percentages, a slug flow regime is observed, characterized by the formation of a water bridge in the middle of the pore. As the oil content increases, a layered structure of water-oil-water forms, leading to a laminar flow regime. Ultimately, the transition from slug flow to laminar flow results in a significant decrease in the total volumetric flux.

Sedghi [130] et al. conducted a series of MD simulations to investigate the effect of pore-fluid interactions on threshold capillary pressures during crude oil-water brine displacements in angular calcite nanopores. To create realistic models of typical black crude oils, mixtures of various polar and nonpolar oil molecules were considered. Simulations examined the interfacial tension and contact angle under different oil compositions, brine compositions, as well as temperature and pressure conditions. The trends observed in the simulations revealed that the addition of polar components in crude oil led to a decrease in interfacial tension while increasing the contact angle, while the calcite surface remained strongly water-wet. Conversely, the salinity of the water had a negligible effect on contact angle but increased the interfacial tension. They introduced a novel effective theory that incorporates a slip boundary into the Navier-Stokes equation, providing a robust framework for describing the flow behavior of mixtures in nanoscale channels. Through rigorous validation, the authors demonstrated the efficiency of their theory in accurately capturing and describing the complex mixture flow phenomena that occur in nanoscale channels.

1.5 Motivation of the thesis

Contact between rocks and fluids is ubiquitous in nature, observed in oceans, coastal boundaries, river banks, subsurface geological repositories, and many other geological settings. Among the organic and inorganic fluids that are in contact with rocks in nature, water is the dominant fluid playing the role of solvent.

While conventional prospective in geochemistry defines thermodynamic properties of fluids at bulk scale, real interactions often occur at the confined interfaces between minerals and aqueous phases. For example, functionalized mineral-fluid interfaces offer effective solutions for waste water treatment [131, 132] and soil contamination remediation [133]. Although bulk water at atmospheric pressure solidifies within a phase at 273K, it has been shown that water confined between graphene sheets experiences difference ice phases [134]. Moreover, empirical investigations showed that the adjustment of nanoscale features at the mineral-liquid interface controls the storage capacity of shale type reservoirs [135].

The phase behavior and thermodynamic properties of fluids confined within nanopore minerals deviate significantly from that observed in bulk scale. From a microscopic perspective, at the rock-fluid interface, rock and fluid molecular structures are related but not identical to the bulk structure. This implies that neither the mineral nor the fluid is similar to the bulk counterparts. For minerals, surface characteristics such as dangling bonds[136, 137], defects [138, 139], surface topology [140], among others, play a significant role. In fluids, the free thermal motion of fluid molecules is interrupted as the size of mineral confinement decreases and approaches the molecular dimensions, resulting in diverse and unique thermodynamic properties. Therefore, it is imperative to develop a deeper understanding of how mineral confinement influences the properties of confined fluids, including water and crude oil. This Ph.D. thesis aims to develop a method to investigate how the properties of confined water within calcite nanopores deviate from bulk water, as understanding of these deviations is crucial for developing accurate reservoir models that impact hydrocarbon recovery from subsurface carbonate rocks.

1.6 Objectives

In this Ph.D. dissertation, I employed statistical associating fluid theory (SAFT) to model the complex thermodynamics of the calcite-water interface at nanoscale level. Within this framework, I developed an equation of state (EoS) that calculates the properties of water confined near a calcite surface. To account for the impact of the calcite surface on confined fluid properties, a new formulation was derived for Helmholtz free energy and incorporated into the Helmholtz summation of SAFT. This newly defined Helmholtz equation describes the properties of confined fluid as a function of the calcite nanopore characteristics. In order to determine the newly defined Helmholtz free energy species, one needs

to calculate the confinement parameters and local properties in advance. To achieve this, I utilized first-principal molecular dynamics simulations to capture the interactions between water molecules and the calcite surface. I used the open source code Large-scale Atomic/Molecular Massively Parallel Simulator [128] (LAMMPS). To build the calcite-water interface, I chose the neutral surface of calcite, specifically the plane $10\bar{1}4$, to mimic the solid mineral surface at the nanoscale. To start, I used pure water as the interacting fluid and then introduced mono- or divalent ions to establish a more realistic system.
Numerous studies have examined the interactions between calcite and water, yet, to my knowledge, none have introduced a robust theoretical method to assess macroscopic changes resulting from microscopic interactions. To that end, the development of an equation of state is essential to accurately quantify the macroscopic properties of water influenced by the presence of the calcite surface on the pore scale (nanoscale). This EoS will also serve as a tool to predict the thermodynamical behaviour of confined water under different temperature and pressure conditions. The following chapter will introduce key thermodynamic concepts and quantities to build such an EoS. To approach this problem, a few key questions need to be addressed:

(i)-How can we link the complex interactions at microscopic level to the observable properties of the system at macroscopic scale?

The first step is to identify a theoretical method that can effectively translate the microscopic interactions of fluid molecules at the nanoscale into macroscopic properties. This involves modeling two fundamental types of molecular interactions near the calcite surface, namely, water-water and calcite-water interactions. To do this, I adopted a molecular-based equation of state inspired by SAFT. SAFT was chosen because of its proven ability to model strong intermolecular interactions within fluid molecules, such as hydrogen bonding between water molecules. This is in contrast to cubic EoS, which are mainly designed to model weak intermolecular interactions such as van der Waals forces. SAFT also has the potential to accommodate non-homogeneous interactions between calcite and water, a challenge that conventional cubic EoS often struggle with.

(ii)-How does the Statistical Associating Fluid Theory (SAFT) contribute to model complex interactions?

SAFT encapsulates all types of molecular interactions by incorporating relevant Helmholtz free energies. It models the strong interactions between water molecules by including an association term for Helmholtz free energy. Additionally, using fundamental principles in statistical mechanics, a Helmholtz term can be derived that represents calcite-water interactions. By incorporation of the square well formed between the adsorbed water and calcite surface, the latter Helmholtz term is defined as a function of the square-well characteristics. Hence, the newly derived Helmholtz term will be a function of confinement characteristics. More detailed explanation can be found in the forthcoming theoretical background.

(iii)-Which technique can be used to explore nanoscale interactions and calculate the necessary parameters for Helmholtz terms?

The molecular dynamics technique was employed to gain insight into how calcite influences the water molecules at the calcite-water interfaces. The previously discussed Helmholtz term that captures calcite-water interactions relies on various confinement parameters, including the potential of calcite-water interactions, the degree of confinement, the fraction of adsorbed water molecules and temperature. Molecular dynamics simulations emerge as a reliable method to calculate these parameters. Moreover, in the process of deriving the molecular-based equation of state, the density of confined water is counted as a key parameter. Molecular dynamics simulations are well suited to meet these demands, offering a proven capability to address these essential aspects.

The described methodology and consequent outcomes of these basic studies may find applications in several study fields such as catalysis, contaminant transfer, the effect of mineral grain size on chemical weathering, the effect of the calcite surface in limiting mineralization in oceans, the estimate of solubility limits in multicomponent fluid processing, and enhanced oil recovery (EOR), among other topics.

1.7 Thesis structure

The main focus of this study is behavior of water molecules at the calcite-water interface, and how the thermodynamic properties of water evolve from discrete near the interface, to bulk properties far from the interface.

In the absence of confinement in the bulk phase, water-water interactions govern and determine bulk water properties. However, introducing the calcite mineral into the bulk water system adds a group of extra molecular interactions, called calcite-water interactions. Thus, accurate estimations of bulk properties require a deep understanding of the underlying mechanisms, including the formation of the first adsorbed layer, the identification of multilayer structures bonding to the adsorbed layer, and the influence of environmental parameters like temperature, pressure, and confinement size. In the confined interface, water molecules are held close to the calcite surface through a combination of electrostatic attraction, repulsion, and induction energies. These energies collectively account for the physisorption of water onto the calcite surface. Therefore, an exploration of the energy and density profiles of confined water can provide valuable insights into the underlying interaction mechanisms between water and calcite. This leads to our first research question:

Research Question-1 (RQ-1): How does the combination of water-water and calcite-water interactions affect the macroscopic properties of water, under one-dimensional confinement?

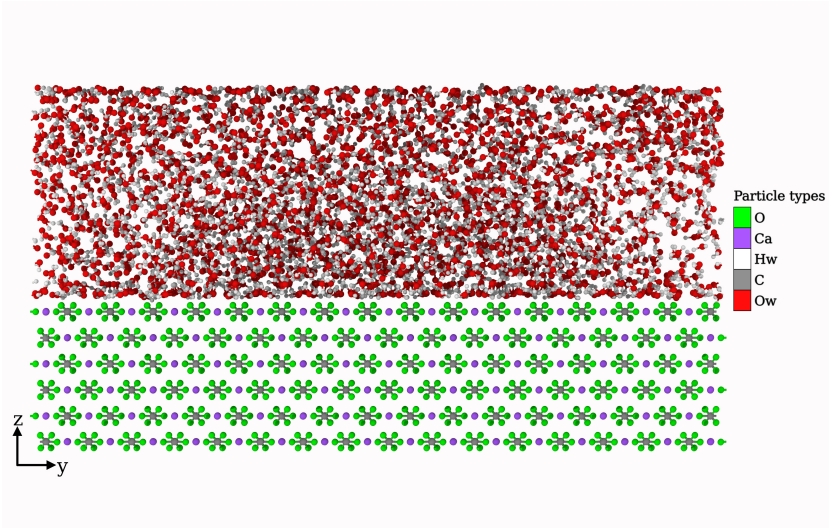

Figure 1.2: Sketch of the confinement geometry within water-calcite interface studied in Paper I. Lz is the distance from the uppermost layer of water bulk to the calcite surface. δ is the thickness of the surface-adsorbed layers.

Paper(I) replies to this question by presenting simulation results of a model system with one-dimensional confinement for water molecules. In fact, adding this confinement will divide the simulated domain into several discrete regions with distinct behaviors: i) a region with adsorbed water molecules over the hydrophilic surface of calcite and ii) a region wherein water molecules tend to behave like bulk water far from any confinement.

In order to predict the water properties at near a calcite surface, a new contribution for the Helmholtz energy extended from Perturbed-Chain SAFT (PC-SAFT) EoS was defined. The new Helmholtz energy contribution depends on the confinement parameters, i.e. the potential of water-calcite interaction (ϵ), confinement degree (θ), bulk-like density (ρ), and fraction of confined molecules (F_{pr}), which were estimated by molecular dynamics simulations. The simulation results also show the adsorption of the fully structured layers of water on the calcite surface. In addition, the simulations confirm the energy deviation within the layering zone. Finally, it has been demonstrated that with increasing temperature and the level of confinement, the properties of confined water tend to align with those of the bulk liquid. Figure 1.2 shows the schematic geometry of the simulated system.

When a one-dimensional confinement is introduced to the system, multiple layers of water are adsorbed over the calcite surface. Beyond these adsorbed layers, water molecules form a network through hydrogen bonding, and water-water interactions are developed. As mentioned above, within one-dimensional confinement, molecular interactions shift from predominantly calcite-water

interactions to water-water interactions. As one moves away from the calcite surface, the attractive forces diminish, and water-water interactions approach bulk-like interactions where no confinement is present. What if one imposes two-dimensional confinement and prevents the establishment of pure water-water interactions from either end? This scenario sets the stage for the second research question:

Research Question-2 (RQ-2): when water is constrained within a two-dimensional confinement, how does the interplay between water-water interactions and calcite-water interactions on both sides influence the bulk properties?

Paper(II) replies to this question by simulating a system that comprises two calcite nanoslabs with water in between. In the context of a two-dimensional confinement, the hydrophilic nature of calcite slabs on both sides provides dual fronts of calcite-water interactions, encapsulating a cluster of water molecules that fall within the categories of calcite-water and water-water interactions in terms of energy. The two-dimensional confinement will separate the confined space into several regions. Reducing the confinement size may lead to the overlap of different regions, resulting in a new behavior. Analysis of the energy and density profile of confined water within different regions contributes to a better understanding of the phenomenon.
In order to incorporate the impact two-dimensional confinement on the properties of confined water, I developed an EoS based on SAFT principles. In this work, the newly introduced Helmholtz energy depends not only on the potential of water-calcite interactions (ε) and bulk-like density (ρ), but also on a novel parameter called CF, representing the density fraction within the adsorbed layer and bulk-like zone. Unlike cubic EoSs, which often use empirical parameters without physical meaning, CF is defined by the physics of the simulated system. Investigating various pore sizes at different temperatures reveals that temperature causes the density in the layering zone to rise, which differs from earlier findings. Furthermore, coupling CF with proposed EoS decreased the absolute relative error by nearly 50% at low temperatures, demonstrating that other parameters, such as geometry and layering pattern, influenced the properties of the confined fluid. Figure 1.2 shows the schematic geometry of the simulated system.

Up to this point, we have examined the interactions of pure water with calcite. The neutral surface $(10\bar{1}4)$ of the calcite is chosen to avoid the intervention of additional partial charges from the mineral side. By altering temperature and confinement size, we have investigated how water-water and water-calcite interactions combine under one- and two-dimensional confinements, resulting in distinct properties for confined water. The inherent hydrophilic properties of calcite result in the adsorption of water molecules onto its surface. This occurs as the surface Ca^{2+} cations coordinate with oxygen atoms in water and surface CO_3^{2-} anions make hydrogen bonds with hydrogen atoms in water. In fact, the surface chemistry of calcite imparts hydrophilic characteristics to its surface. Previous studies have investigated how physical parameters like temperature

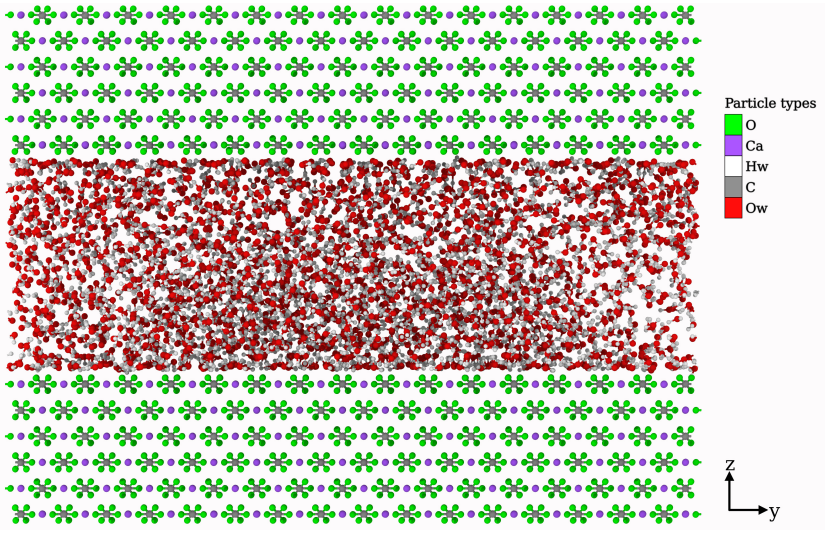

Figure 1.3: Illustration of the confinement geometry within a calcite nanopore used for the simulations in Paper II. Lz denotes the width of the calcite pore. δ shows the thickness of the surface-adsorbed layers.

and confinement size affect the surface chemistry of calcite. It is now time to investigate the influence of chemical modifications on the surface chemistry of calcite. These modifications involve the introduction of anions and cations into the water, and the goal is to analyze how these changes affect the adsorption behavior of calcite. This question forms the basis for the third scientific question:

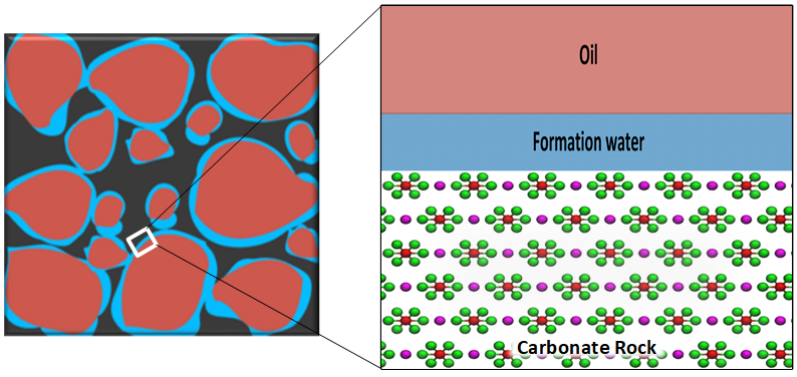

Figure 1.4: Sketch of the calcite-oil-brine system used in Paper III. Formation water (H_2O, Na^+, Cl^-,Ca^{2+}) and oil (toluene, decane, benzoic acid) and interact with the calcite ($10\bar{1}4$) surface.

Research Question-3 (RQ-3): How do mono/divalent ions at the brine water-oil-calcite interface affect the adsorption behavior of the calcite surface?

Paper(III) replies to this question by simulating a calcite-oil-brine system so that high salinity brine, oil, and low salinity brine lay across a calcite nanoslab, respectively. The oil phase contains toluene, decane, and benzoic acid to simulate aromatic, hydrocarbon, and polar constituents dissolved in oil. The high- and low-salinity solutions contained water molecules in combination with mono/divalent ions, i.e., Na^+, Cl^-, Ca^{2+}, Mg^{2+} and SO_4^{2-}. The results of molecular dynamics simulation show that mono- and divalent ions initially undergo hydration, with monovalent ions forming an electrical double layer above the calcite surface. Characterizing the dynamics of different ions denotes that the monovalent ions (Na^+ and Cl^-) settle within the compact hydration layers on the calcite surface. However, divalent ions show different behaviors. Initially, Ca^{2+} ions, which are observed in close proximity to the calcite surface, migrate away over time. On the other hand, Mg^{2+} and SO_4^{2-}, which were initially distant from the calcite surface, move closer to the calcite surface following oil displacement. In essence, prior to oil displacement, the positions of (Na^+, Cl^-) and Ca^{2+} becomes fixed and the trend of double electric layer expands. This signifies that the detachment of oil from the calcite-brine interface occurs simultaneously with extension in charge density. Figure 1.4 shows the schematic geometry of the simulated system.

This Ph.D. dissertation collects and summarizes the findings from above mentioned questions, each of which will be answered in its own research paper.

1.8 Outline

This Ph.D. dissertation follows the Manuscript Document Format of Oslo University and is organized into three main chapters. Chapter 1 is referred to as the Introduction serves as a framework for better understanding the dissertation's coherence and motivation. Chapter 2 puts the research theory into a broader context by providing the theoretical background for statistical association fluid theory (SAFT) and molecular dynamics (MD) toolboxes, which were used as the main computational tools in the papers. Chapter 3 contains the key findings of the research and provides future directions for further investigation. Chapter 4 includes three published papers in which I am the first author. A summary of the appendices is given in Chapter 5, including several conference proceedings and extended abstracts.

Chapter 2

Theoretical background

Modern tools for calculating the properties of pure substances and mixtures are highly based on the cubic-type equation of states [141–143]. However, these equations struggle to accurately model complex molecular interactions found in polar systems, chain-like molecules, associating fluids, and electrolyte systems [144–147]. Moreover, this challenge extends to the precise calculation of liquid densities due to the inadequacy of the repulsive reference term in van der Waals equations [148, 149]. The challenges originate from the fact that cubic-type equations were initially formulated to characterize fluids composing of relatively simple molecules governed by van der Waals interactions and weak-dipole-induced electrostatic forces. However, in real-world scenarios, many fluids exhibit strong attractive forces between their molecules, presenting a challenge to the cubic-type equation of states. Here, statistical associating fluid theory (SAFT) becomes invaluable, providing an effective approach for modeling none-ideal and intense intermolecular interactions [150–153]. This chapter briefly reviews the main modeling tools used in this Ph.D. dissertation:

- Statistical Association Fluid Theory (SAFT)
- Molecular Dynamics Simulations

2.1 Equation of state

In thermodynamics, equations of states (EoS) establish relationships among state variables, including pressure (P), volume (V), and temperature (T), under specific physical conditions. These equations serve as fundamental tools, providing a mathematical framework that connects P-V-T. In addition to the physical properties of pure substances, EoSs are able to predict the properties of mixtures, phase equilibrium conditions, boundary between states, and elucidate phase behavior [154, 155]. In the oil and gas industries, EoSs are widely used to calculate the properties of petroleum fluids. Figure 2.1 shows a typical 3-dimensional phase diagram [156].

2.1.1 Cubic equation of state

The simplest equation of state is the ideal gas law, which is presented in equation (2.1).

$$PV = nRT \tag{2.1}$$

This equation relates pressure, volume and absolute temperature with an universal gas constant (R) and n which is the number of moles of the gas. In the

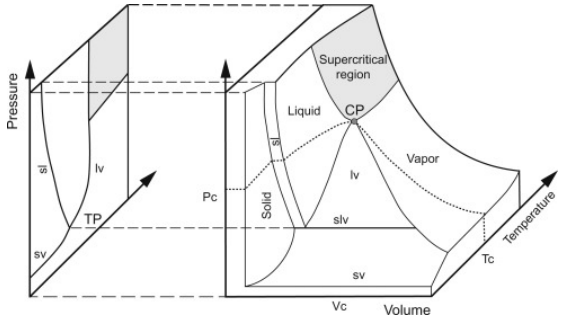

Figure 2.1: A typical three-dimensional phase diagram and its projection onto pressure-temperature (P-T) and pressure-volume (P-V) planes [156].

ideal gas context, gas molecules are assumed as point masses possessing perfectly elastic collisions. While this hypothesis is correct for dilute gases, Johannes D. van der Waals [157] improved the ideal gas law in 1873 by introducing two extra parameters: molecular size and molecular interaction forces. Equation (2.2) represents the van der Waals EoS for n moles of gas:

$$\left(P + a\left(\frac{n}{V}\right)^2\right)\left(\frac{V}{n} - b\right) = RT, \tag{2.2}$$

where a accounts for the intermolecular interactions and b represents the volume occupied by the molecules. Rearranging the equation (2.2) to solve for V gives a third order polynomial as:

$$V^3 - \left(\frac{RT}{P} + b\right)V^2 + \left(\frac{a}{P}\right)V - \frac{ab}{P} = 0. \tag{2.3}$$

The equation (2.3) represents a cubic function with respect to volume. In thermodynamics, the critical point denotes a state at which the liquid-vapor phase boundary vanishes, marking the endpoint of the equilibrium diagram. Thus, at the critical point, the volume equals the volume under critical [1] conditions, expressed as $V - V_c = 0$. Substituting V from equation (2.3), one can express the van der Waals equation in terms of Z, known as compressibility factor [2]:

$$Z^3 - (1 + B)Z^2 + AZ - AB = 0, \tag{2.4}$$

which introduces another cubic equation in terms of Z, where the dimensionless parameters A and B are defined as:

$$A = \frac{aP}{RT^2} \tag{2.5}$$

[1] The subscript c denotes the critical point
[2] Compressibility factor indicates how far a real gas deviates from an ideal gas

$$B = \frac{bP}{RT} \tag{2.6}$$

and a and b are defined as:

$$a = \frac{27R^2T_c^2}{64P_c} \tag{2.7}$$

$$b = \frac{RT_c}{8P_c} \tag{2.8}$$

where T_c and P_c represent the temperature and pressure at critical point.

Notably, the van der Waals equation of state marked a significant milestone, as it effectively represented the coexistence of vapor and liquid for the first time. This equation models fluid particles as hard spheres interacting through repulsive and attractive forces. Originally developed for simple fluids with weak intermolecular interactions, it offers a qualitative description of vapor-liquid phase transitions [158]. However, its accuracy is limited for critical properties and phase equilibrium calculations. Consequently, many research efforts since 1873 have concentrated on adopting the van der Waals equation of states to the fluids possessing more complex intermolecular interactions. Some studies have focused on modifying the attractive term [159–161] , while others have addressed the repulsive term [162–164]. Additionally, certain studies have considered modifications to attractive and repulsive terms simultaneously [165–169].

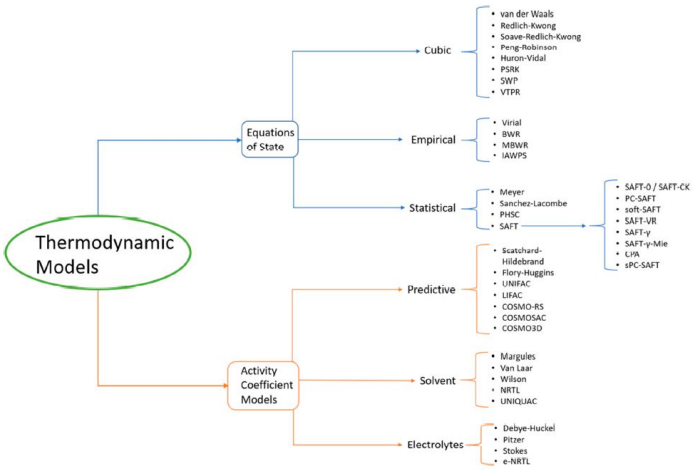

Figure 2.2: A brief overview of available thermodynamic EoS in literature [170].

2.1.2 Limitations of cubic-type equations of state

Van der Waals-based equations of state rely on a concept of hard-sphere interactions, wherein weak long-range dispersion forces are approximated at the mean-field level [171]. This approach works well for fluids with spherical or

nearly spherical molecules interacting with weak intermolecular forces. Examples include low molecular mass hydrocarbons (e.g. methane) and simple organic (e.g., Toluene) and inorganic molecules (e.g. N_2 and O_2) [172].

However, more complex fluids, such as electrolytes, polar solvents and polymers present a different challenge. Unlike the simple fluids mentioned earlier, these fluids possess molecules exhibiting non-spherical (aspherical) shape interacting with highly directional forces [173]. In these complex fluids, the natural tendency is formation of associated species like dimers, trimers and longer chain-like structures. This category consists of fluids characterized by hydrogen bonding, charge transfer, non-homogeneous (non-ideal) interactions (e.g. mineral-fluid interaction) and various type of complexities [174].

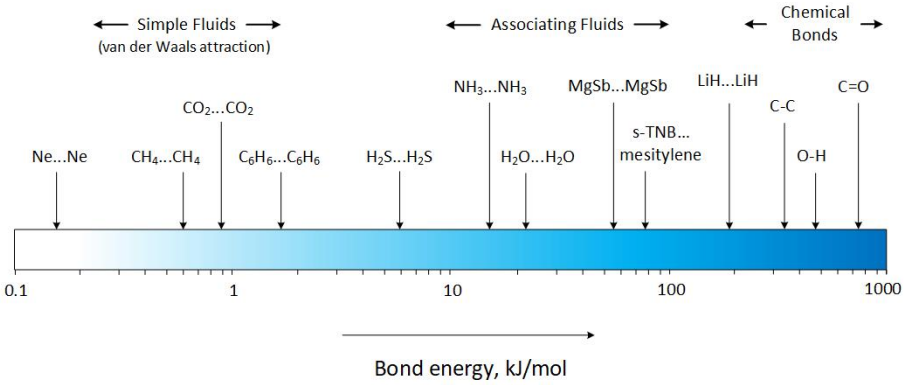

Figure 2.3: Visualizing the continuous spectrum of bond strengths . The energy spectrum highlighted in blue depicts the range from elementary van der Waals attractions to the formation of chemical bonds [172].

For instance, the association species in water are formed by the hydrogen bonding, which is a strong electrostatic interaction between hydrogen and oxygen atoms. The associated species continuously form and break apart due to thermal motion. The concentration and lifetime of these aggregates depend strongly on temperature and density [175].

In practice, well-established cubic equations of states are a common choice for modeling complex fluids [176, 177]. However, their limitations become apparent with the introduction of complex and unrealistic mixing rules [178] alongside temperature-dependent binary parameters [179], leading to a decrease in precision [180]. Therefore, the framework of cubic-type EoSs are poor to generate reliable predictions for fluids with complex intermolecular interactions [145, 181].

2.2 Statistical association fluid theory

The progress in statistical mechanics coupled with improved computational capabilities has paved the way for the utilization of equations of state based

on molecular principles. The statistical associating fluid theory (SAFT) is a molecular-based equation of states developed by Chapman and coworkers [182–185] based on the thermodynamic perturbation theory (TPT) of Wertheim [186–189]. Perturbation theories offer straightforward approximate solutions for a given molecular model by partitioning the total intermolecular forces into reference and perturbation terms. In this framework, the reference term corresponds to repulsive forces, while the perturbation term represents attractive forces [190]. The general framework of SAFT-type equations of state are written in the terms of Helmholtz free energy $A(N, V, T)$ with the functional parameters representing the number of particles, volume and temperature of the system. In SAFT, molecules are seen as flexible chains, each consisting of m tangential segments (hard-spheres) with a diameter of σ. These chains may also have sites attracting other chains to associate with. Figure 2.4 presents a typical molecular chain with three association sites.

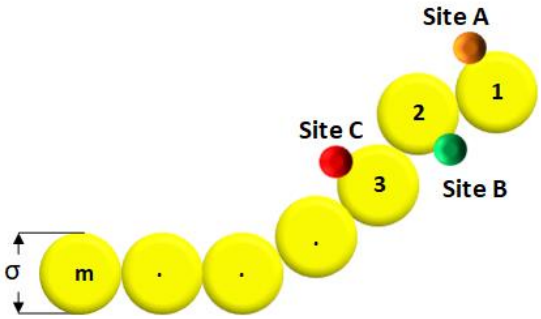

Figure 2.4: Illustration of a typical SAFT molecular model, consisting of m spherical segments with diameter σ and three association sites.

The definition of different intermolecular contributions in SAFT begins by introducing the dimensionless form of the total Helmholtz free energy:

$$\tilde{a} = \frac{A}{Nk_BT}. \tag{2.9}$$

In equation (2.9), the symbols N, k_B, T denote number of particles, Boltzmann constant and absolute temperature, respectively. Then, by considering the residual Helmholtz energy as $\tilde{a}^{res} = \tilde{a} - \tilde{a}^{id}$, the fundamental formulation of the SAFT-type equations of state can be expressed in terms of the residual Helmholtz energy [191]:

$$\tilde{a}^{res} = \underbrace{\tilde{a}^{hs}}_{\text{reference term}} + \underbrace{\tilde{a}^{chain} + \tilde{a}^{disp} + \tilde{a}^{assoc}}_{\text{perturbation term}}. \tag{2.10}$$

Different contributions in equation (2.10) are interpreted as:

- $\tilde{a}^{hs}$ serves as the reference term, corresponding to the contribution of the hard-sphere and accounting for the repulsion interactions between the hard-spheres.
- $\tilde{a}^{chain}$ illustrates the chain contribution, corresponding to the formation of chains between hard-spheres through bonding (e.g. covalent bonding).
- $\tilde{a}^{disp}$ represents the dispersion contribution, corresponding to the attractive interactions between the chains.
- $\tilde{a}^{assoc}$ denotes the association contribution, corresponding to the formation of association complexes between the chains (e.g. hydrogen bonding)

Figure 2.5, provides graphical insights into the various elements incorporated in equation (2.9).

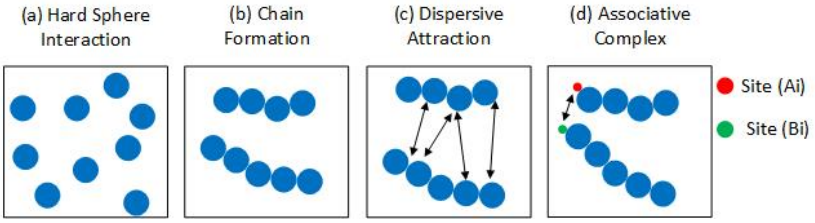

Figure 2.5: Different Helmholtz free energy contributions in SAFT. (a) Hard-spheres with repulsion-attraction interactions. (b) Formation of chains through covalent bonds between hard-spheres. (c) Dispersion interactions between the chains. (d) Association complex formation via association sites, such as hydrogen bonding, linking molecular structures.

2.2.1 Hard-sphere (reference term)

The hard-sphere term is defined as [174]:

$$\tilde{a}^{hs} = m\frac{4\eta - 3\eta^2}{(1-\eta)^2}, \tag{2.11}$$

where m is the number of spherical segments per molecule and η is the reduced density defined as:

$$\eta = 0.74048\rho m v^0, \tag{2.12}$$

where v^0 is the close-packed hard-core volume of the fluid. Based on the Chapman et al., [185] definition, v^0 is calculated from :

$$v^0 = v^{00}\left(\frac{1+\frac{0.2977}{C}}{1+\frac{0.33163}{C}+\frac{0.0010477+0.025337\left(\frac{m-1}{m}\right)}{C^2}}\right), \tag{2.13}$$

where, $C = u^0/kT$ is the dispersion energy per segment. Generally, m, v^{00} and u^0/k are available for different fluids.

2.2.2 Chain term

The chain term is calculated as follows:

$$\tilde{a}^{chain} = (1-m)\ln\frac{1-0.5\eta}{(1-\eta)^3}. \tag{2.14}$$

2.2.3 Dispersion term

Chapman et al., [185] definition for dispersion term is:

$$\tilde{a}^{disp} = m\frac{u^0}{kT}\left(a_1^{disp} + \left(\frac{u^0}{kT}\right)a_2^{disp}\right), \tag{2.15}$$

where,

$$a_1^{disp} = -11.604\eta - 6.132\eta^2 - 2.871\eta^3 + 13.885\eta^4, \tag{2.16}$$

and

$$a_2^{disp} = -2.575\eta + 13.463\eta^2 - 29.992\eta^3 + 21.470\eta^4. \tag{2.17}$$

2.2.4 Association term

The association term for the residual Helmholtz free energy is calculated as [185]:

$$\tilde{a}^{ass} = \sum_{i=1}^{N_c} x_i \left(\sum_{A_i=1}^{n_i}\left(\ln X^{A_i} - \frac{X^{A_i}}{2}\right) + \frac{M_i}{2}\right), \tag{2.18}$$

where,

N_c: number of components in the mixture,

n_i: number of association sites of each molecule of component i,

A_i: association site A in molecule i,

M_i: number of association sites (A, B, C, ...) in molecule i.

$\sum_i$ and $\sum_{A_i}$ in equation (2.18) are described as the summation over all components and summation over association sites, respectively. Furthermore, X^{A_i} is the fraction of molecules i which is not bonded at the site A and is defined as:

$$X^{A_i} = \left(1 + \dot{\rho}\sum_{j=1}^{N_c}\sum_{B_j=1}^{n_i} x_j X^{A_i}\Delta^{A_iB_j}\right)^{-1}, \tag{2.19}$$

where,

$\Delta^{A_iB_j}$ is a parameter that describes the association strength between site A on molecule i and site B on molecule i, which is expressed as:

$$\Delta^{A_iB_j} = g_{ij}^{hs}\left(\exp\left(\frac{\varepsilon^{A_iB_j}}{k_BT}\right)-1\right)\sigma_{ij}^3\kappa^{A_iB_j}. \tag{2.20}$$

To describe an associating fluid with SAFT, it is necessary to specify two pure-component parameters: association energy ε^{AB} and effective association volume of κ^{AB}. These parameters are in addition to the three pure-component parameters for simple fluids (m, v^{00} and u^0/k), all of which can be adjusted to match the data of pure component.

2.2.5 Mixing rules

Using straight-forward mixing rules are important to calculate the mixture parameters. In this regard, the mixing rule of Berthelot-Lorentz is used for pair of unlike segments:

$$\sigma_{ij} = \frac{1}{2}(\sigma_i+\sigma_j), \tag{2.21}$$

$$\varepsilon_{ij} = (1-k_{ij})\left(\varepsilon_i\varepsilon_j\right)^{0.5}. \tag{2.22}$$

The cross-associating interactions between associating components are evaluated by mixing rules of Wolbach and Sandler [192]:

$$\varepsilon^{A_iB_j} = \frac{1}{2}\left(\varepsilon^{A_iB_i}+\varepsilon^{A_jB_j}\right), \tag{2.23}$$

$$\kappa^{A_iB_j} = \left(\kappa^{A_iB_i}\kappa^{A_jB_j}\right)^{0.5}\left(\frac{(\sigma_i\sigma_j)^{0.5}}{0.5(\sigma_i+\sigma_j)}\right)^3. \tag{2.24}$$

2.2.6 Helmholtz term for water-calcite interaction

The essence of SAFT is that the residual Helmholtz energy ($\tilde{a}^{res}$) is given by a sum of Helmholtz species ($\tilde{a}^i$) to account for the effects of hard sphere, chain, dispersion, association. As seen in equation (2.10), it is possible to describe a particular intermolecular interaction using relevant Helmholtz species. Hence, to include the interaction between water and calcite, the key step is to define a residual Helmholtz term associated with the water-calcite interaction. This defined species is then incorporated into the broader Helmholtz summation, highlighting its significance in modeling the complexities of water-mineral interactions. Figure 2.6 illustrates our assumptions and provides a better understanding of water-water and water-calcite interactions, wherein water is confined between two calcite nanoslabs. As seen, the confinement space is partitioned into three distinct regions based on their proximity to the calcite wall.

Region I (bulk-like) is the outermost section nearest to the pore center. The dominant interactions here are fluid-fluid interactions, which are characterized by a square-well potential. Region II (layering zone) with a thickness of δ_{fw} involves water-calcite interactions, which are characterized by a square-well potential. Finally, Region III displays an empty margin adjacent to the pore walls with no water molecules inside, characterized by a thickness of $\sigma_i/2$.

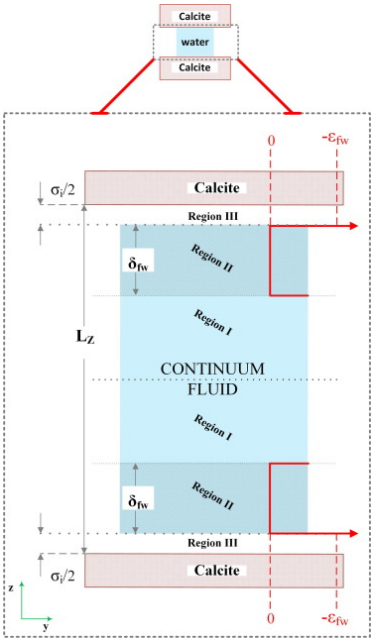

Figure 2.6: Configuration of a calcite pore that contains water. The mineral walls interact with water molecules through a square-well potential [193]. As depicted, L_z is the distance between the outermost layers of the calcite surfaces. δ_{fw} and ε_{fw} are the width and depth of the square-well energy. $\sigma_i/2$ is the thickness of space above the calcite surface which contains no water molecule.

In order to derive a definition for Helmholtz free energy in the context of water-calcite interaction, one can start the process by formulating the partition function equation. This equation serves as a bridge to relate the microscopic states of a system with its macroscopic properties observed at thermal equilibrium. Defining a partition function Q for a system of N particles gives [194, 195]:

$$Q_{N,V,T} = \left(\frac{q_{\text{int}}^N}{\lambda^{3N} N!} V_f^N \exp\left(\int_\infty^T \frac{E_{\text{conf}}}{kT^2} dT \right) \right), \tag{2.25}$$

where, q_{int} is the internal partition function, λ represents the de Broglie wavelength, T is the absolute temperature, E_{conf} is the configurational energy, and V_f denotes the free volume defined as:

$$V_f = V - \frac{N}{\rho_{max}}, \tag{2.26}$$

where, ρ_{max} is the molecular density of the closed-pack fluid. The configurational energy E_{conf} in equation (2.25) includes the attractive part of the average total energy for N molecules in a system with volume V. In other words, E_{conf} defines the attractive part of the molecule–molecule interactions that occur throughout the system volume. Therefore, for a confined fluid, the definition of E_{conf} should take into account the fluid-fluid and fluid-wall interactions, namely:

$$E_{conf} = E_{conf-ff} + E_{conf-fw}, \tag{2.27}$$

where, the subscripts *ff* and *fw* describe fluid-fluid and fluid-wall interactions, respectively. Assuming that these interactions occur pairwise through the square-well potential, for fluid-fluid interactions, we have:

$$u\left(r_{ij}\right) = \begin{cases} \infty, & r_{ij} < \sigma_{ij} \\ -\varepsilon_{ij} & \sigma_{ij} < r_{ij} < \sigma_{ij} + \delta_{ij} \\ 0 & r_{ij} > \sigma_{ij} + \delta_{ij}, \end{cases} \tag{2.28}$$

where r_{ij} represents the distance between two water molecules, ε_{ij} is the depth of the square-well, δ_{ij} is the relevant width of the square-well, and σ_{ij} is defined as the molecular diameter of the water. Here, the attractive part of interaction energy is defined based on the pairwise additive hypothesis, namely:

$$u(r_1, r_2, \ldots, r_N) = \sum_i \sum_j u\left(r_{ij}\right). \tag{2.29}$$

By extending this hypothesis to the attractive part of fluid-wall interactions, we have the following:

$$u(l_{fw}) = \begin{cases} \infty & l_{fw} > L_Z - 2\sigma_i \\ -\varepsilon_{fw} & L_Z - 2\sigma_i - 2\delta_{fw} < l_{fw} < L_Z - 2\sigma_i \\ 0 & l_{fw} < L_Z - 2\sigma_i - 2\delta_{fw}, \end{cases} \tag{2.30}$$

where, l_{fw} is the distance between water molecules and calcite slab, L_Z denotes the width of the calcite nanoslabs (pore size) and ε_{fw} indicates the depth of square-well. Now, based on the square-well potentials defined in equations (2.28) and (2.30), one can redefine the attractive part of the interaction energy using E_{conf} as follows:

$$E_{conf} = -(N/2)N_c\varepsilon_{ij} - NC_F\varepsilon_{fw}. \tag{2.31}$$

The right side of equation (2.31) comprises two terms: the first term represents the water-water interaction, while the second term describes the water-calcite interaction. N_c represents the coordination number and C_F is the fraction counting the confined fluid density compared to the bulk-like fluid density. In fact, C_F incorporates the effect of the number of confined molecules and their

associated confined volume into the total E_{conf}. C_F will be calculated with molecular dynamic simulations. Substituting equation (2.31) into equation (2.25) yields:

$$Q_{N,V,T} = \left(\frac{q_{\text{int}}^N}{\lambda^{3N} N!} V_f^N \exp\left(\int_\infty^T \frac{E_{\text{conf-ff}}}{kT^2} dT \right) \exp\left(\int_\infty^T \frac{E_{\text{conf-fw}}}{kT^2} dT \right) \right). \tag{2.32}$$

Based on the definition of the Helmholtz free energy, expressed as $A = -kT\ln(Q)$, incorporating the V_f from equation (2.26), substituting the relevant square-well potential from equations (2.28) and (2.30) and applying the natural logarithm to equation (2.32) gives:

$$\tilde{a}^{fw} = \left(\ln\left(\lambda^3\right) - \ln\left(\frac{1}{\rho} - \frac{1}{\rho_{\max}} \right) - \left(\frac{\varepsilon_{\text{conf-ff}}}{kT} - 1 \right) - \left(\frac{\varepsilon_{\text{conf-fw}}}{kT} \right) \right), \tag{2.33}$$

where, $\varepsilon_{\text{conf-ff}}$ describes the water-water interaction energy that is available in the literature for pure water, while $\varepsilon_{\text{conf-fw}}$ and the fluid density under confinement will be calculated with molecular dynamics simulations. Adding the new developed term of $\tilde{a}^{fw}$ to the summation of Helmholtz terms gives:

$$\tilde{a}^{res} = \tilde{a}^{hs} + \tilde{a}^{chain} + \tilde{a}^{disp} + \tilde{a}^{assoc} + \tilde{a}^{fw}. \tag{2.34}$$

Once the total Helmholtz energy is calculated, the rest of the thermodynamic properties can be evaluated on the basis of the total Helmholtz energy. For example, based on the residual Helmholtz derivatives, the residual chemical potential μ_k^{res} as:

$$\frac{\mu_k^{res}(T,\nu)}{kT} = \tilde{a}^{res} + \left(\frac{\partial \tilde{a}^{res}}{\partial x_k} \right)_{T,\nu,x_{i\neq k}} - \sum_{j=1}^{N} \left[x_j \left(\frac{\partial \tilde{a}^{res}}{\partial x_j} \right)_{T,\nu,x_{i\neq j}} \right] + (Z-1), \tag{2.35}$$

where, x is the mole fraction of component i and Z is the compressibility factor written as:

$$Z = 1 + \eta \left(\frac{\partial \tilde{a}^{res}}{\partial \eta} \right)_{T,x_i}. \tag{2.36}$$

Here, η is the packing fraction. Then, the fugacity coefficient can be simply written with respect to μ_k^{res} and Z:

$$\ln \phi_k = \frac{\mu_k^{res}(T,\nu)}{kT} - \ln Z. \tag{2.37}$$

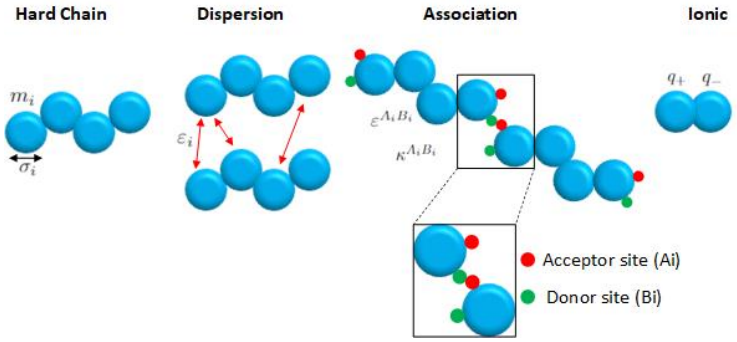

Figure 2.7: Illustration of different molecular contributions in PC-SAFT EoS including hard-chain (hc), dispersion (disp), association (ass) and ionic (ion).

2.3 Perturbed-Chain SAFT

Gross and Sadowski [196, 197] introduced a variant of SAFT known as Perturbed-Chain SAFT (PC-SAFT). They applied Barker and Henderson's [198, 199] perturbation theory to address the dispersion contribution (a^{disp}), which will be added to the reference term of hard-chain instead of hard-spheres. In essence, the formalism of PC-SAFT can be expressed as:

$$\tilde{a}^{res} = \underbrace{\tilde{a}^{hc}}_{\text{reference term}} + \underbrace{\tilde{a}^{disp} + \tilde{a}^{assoc} + \tilde{a}^{ion}}_{\text{perturbation term}}. \tag{2.38}$$

Here, $\tilde{a}^{hc}$, $\tilde{a}^{disp}$, $\tilde{a}^{assoc}$ and $\tilde{a}^{ion}$ indicate the contributions to the Helmholtz energy attributed to hard-sphere chain, dispersion, association and ionic interactions, respectively. Figure 2.7, provides graphical insights into the various species incorporated in equation (2.38). As seen in equation (2.38), the distinction between PC-SAFT and SAFT is addressed to the different reference system term that is considered. In other words, the reference system in PC-SAFT is composed of both hard-sphere and chain. Then, dispersion, association and ionic terms are introduced as the perturbation to the reference system.

Non-associating fluids are modeled with PC-SAFT using three parameters m, σ and ε, representing the number of hard spheres in a chain, segment diameter and dispersion energy, respectively. However, to model a fluid with association and ionic contributions, three additional pure-component parameters are required. These are the association volume ($\kappa^{A_iB_j}$), the association energy ($\varepsilon^{A_iB_j}$) and the ionic valance (ν_j). In this context, A_i and B_i indicate different associating sites. The mentioned parameters are available in the literature for different fluids. The description of different contributions represented in equation (2.38) can be pursued in the following.

2.3.1 Hard-chain (reference term)

The hard-chain term in PC-SAFT, showing with $\tilde{a}^{hc}$ accounts for the repulsion of the chain molecules and is written as:

$$\begin{aligned}\tilde{a}^{hc} &= \overline{m}\tilde{a}^{hs} + \tilde{a}^{ch} \\ &= \overline{m}\tilde{a}^{hs} - \sum_{i=1}^{N_c} x_i(m_i - 1)\ln g_{ii}^{hs},\end{aligned} \tag{2.39}$$

where,

x_i: mole fraction of the component i in chain,

m_i: segment number in a chain of component i,

N_c: number of particles,

in equation (2.39), $\overline{m}$ indicates mean segment number, which is calculated by:

$$\overline{m} = \sum_{i=1}^{N_c} x_i m_i. \tag{2.40}$$

Furthermore, hard-sphere contribution $\tilde{a}^{hs}$ and radial pair distribution of component i and g_{ii}^{hs} are respectively given by:

$$\tilde{a}^{hs} = \frac{1}{\xi_0}\left[\frac{3\xi_1\xi_2}{(1-\xi_3)} + \frac{\xi_2^3}{\xi_3(1-\xi_3)^2} + \left(\frac{\xi_2^3}{\xi_3^2} - \xi_0\right)\ln(1-\xi_3)\right], \tag{2.41}$$

$$g_{ij}^{hs} = \frac{1}{1-\xi_3} + \left(\frac{d_i d_j}{d_i + d_j}\right)\frac{3\xi_2}{(1-\xi_3)} + \left(\frac{d_i d_j}{d_i + d_j}\right)^2 \frac{2\xi_2^2}{(1-\xi_3)^3}, \tag{2.42}$$

where,

d_i is segment diameter of component i, which is calculated by:

$$d_i(T) = \sigma_i\left[1 - 0.12\exp\left(\frac{-3\varepsilon_i}{k_B T}\right)\right], \tag{2.43}$$

and ξ_i is defined as:

$$\xi_n = \frac{\pi}{6}\dot{\rho}\sum_{i=1}^{N_c} x_i m_i d_i^n \qquad n \in \{0,1,2,3\}. \tag{2.44}$$

In equation (2.44), $\dot{\rho}$ represents the total number density, indicating the quantity of particles within a given volume.

2.3.2 Dispersion term

The description of the Helmholtz contribution for dispersion interactions is provided in equation (2.45). This description reveals two distinct statements, the first relates to the 1^{st} order perturbation term and the second one addresses the 2^{nd} order perturbation term.

$$\tilde{a}^{disp} = \underbrace{-2\pi\dot{\rho}I_1(\eta,\overline{m})\overline{m^2\varepsilon\sigma^3}}_{\text{first order}} - \underbrace{\pi\dot{\rho}\overline{m}C_1I_2(\eta,\overline{m})\overline{m^2\varepsilon^2\sigma^3}}_{\text{second order}}, \tag{2.45}$$

where,

C_1, $I_1(\eta,\overline{m})$, $I_2(\eta,\overline{m})$, $\overline{m^2\varepsilon\sigma^3}$ and $\overline{m^2\varepsilon^2\sigma^3}$ are defined as:

$$\begin{aligned} C_1 &= \left(1 + Z^{hc} + \rho\frac{\partial Z^{hc}}{\partial\rho}\right)^{-1} \\ &= \left(1 + \overline{m}\frac{8\eta - 2\eta^2}{(1-\eta)^4} + (1-\overline{m})\frac{20\eta - 27\eta^2 + 12\eta^3 - 2\eta^4}{(1-\eta)^2(2-\eta)^2}\right)^{-1}, \end{aligned} \tag{2.46}$$

$$I_1(\eta,\overline{m}) = \sum_{i=0}^{6} a_i(\overline{m})\eta^i, \tag{2.47}$$

$$I_2(\eta,\overline{m}) = \sum_{i=0}^{6} b_i(\overline{m})\eta^i, \tag{2.48}$$

$$\overline{m^2\varepsilon\sigma^3} = \sum_{i=1}^{N_c}\sum_{j=1}^{N_c} x_i x_j m_i m_j \left(\frac{\varepsilon_{ij}}{k_B T}\right)\sigma_{ij}^3, \tag{2.49}$$

$$\overline{m^2\varepsilon^2\sigma^3} = \sum_{i=1}^{N_c}\sum_{j=1}^{N_c} x_i x_j m_i m_j \left(\frac{\varepsilon_{ij}}{k_B T}\right)^2\sigma_{ij}^3. \tag{2.50}$$

Here, i and j represent a pair of non-identical segments. In equations (2.47) and (2.48) two coefficients a_i and b_i are defined as functions of chain length:

$$a_i(\overline{m}) = a_{0i} + \left(\frac{\overline{m}-1}{\overline{m}}\right)a_{1i} + \left(\frac{\overline{m}-1}{\overline{m}}\right)\left(\frac{\overline{m}-2}{\overline{m}}\right)a_{2i}, \tag{2.51}$$

$$b_i(\overline{m}) = b_{0i} + \left(\frac{\overline{m}-1}{\overline{m}}\right)b_{1i} + \left(\frac{\overline{m}-1}{\overline{m}}\right)\left(\frac{\overline{m}-2}{\overline{m}}\right)b_{2i}, \tag{2.52}$$

The coefficient η in equation (2.46) is packing factor and its value varies between 0 and 0.745. Other parameters i.e., $a_{0i}, a_{1i}, a_{2i}, b_{0i}, b_{1i}$ and b_{2i} are constant numbers varying by changing the pure component to another. These parameters can be found in the literature.

2.3.3 Association term

The association term is considered for components characterized by hydrogen bonding between identical and nonidentical molecules such as water. PC-SAFT utilizes the same association term as the earlier SAFT equations, as discussed in Section 2.2.4.

2.3.4 Ionic term

The PC-SAFT model developed by Gross and Sadowski [196, 197] does not contain the ionic term. However, Cameretti et al. [200] modified PC-SAFT to include the electrostatic effect in the fluid properties. They defined the ions as charged hard-spheres in a dielectric continuum. The contribution of Helmholtz energy is written as:

$$\tilde{a}^{ion} = \frac{\kappa}{12\pi\varepsilon k_B T} \sum_i x_i q_i^2 \chi, \tag{2.53}$$

where,

$\sum_i$: summations over all ions in the mixture,

q_i: charge of the ion.

The parameters κ and χ in equation (2.53) are defined as:

$$\kappa = \left(\frac{\dot{\rho} e^2}{k_B T \varepsilon} \sum_i \nu_i^2 x_i \right)^{\frac{1}{2}}, \tag{2.54}$$

$$\chi_i = \frac{3}{(\kappa\alpha_i)^3} \left(\frac{3}{2} + \ln(1+\kappa\alpha_i) - 2(1+\kappa\alpha_i) + \frac{1}{2}(1+\kappa\alpha_i)^2 \right), \tag{2.55}$$

where,

ν_i: valance of ion i,

e: 1.6022×10^{-19},

ε: dielectric constant.

2.3.5 Helmholtz contribution for water-calcite interaction

To establish a definition for $\tilde{a}^{fw}$, we start by revisiting the concept of canonical partition function. As introduced previously, the canonical partition function is defined as:

$$Q_{N,V,T} = \left(\frac{q_{\text{int}}^N}{\lambda^{3N} N!} V_f^N \exp\left(\int_\infty^T \frac{E_{\text{conf}}}{kT^2} dT \right) \right). \tag{2.56}$$

For a detailed explanation of the parameters in equation (2.56), the reader can refer to Section (2.2.6). Now, let's delve into the schematic setup depicted in Figure 2.8, illustrating the interface between a calcite nanoslab and water. This figure visually depicts the underlying assumptions of the model.

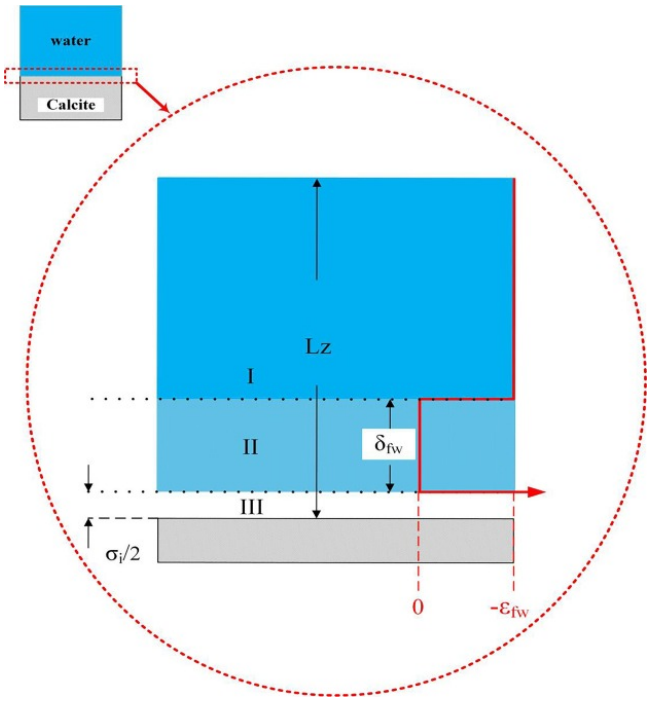

Figure 2.8: Illustration of a water-calcite interface. The calcite nanoslab interacts with water molecules through square-well potential [201]. L_z is the distance between outermost layer of water and calcite surface. δ_{fw} and ε_{fw} are width and depth of the square-well energy. $\sigma_i/2$ is the thickness of vacant space above the calcite surface.

In a scenario involving bulk water without a calcite slab, interactions purely occur between water molecules. However, introducing a calcite nanoslab results in three distinct zones near the calcite surface:

- Region I is located far from the calcite surface. It involves dominant water-water interactions with the thickness of $L_z - (\delta_{fw} - \sigma_i/2)$.

- Region II includes dominant water-calcite interactions with the thickness of δ_{fw}.
- Region III exhibits the vacant space above the calcite surface with the thickness of $\sigma_i/2$.

Assuming pairwise interactions between the molecules, the interaction between water molecules will be modeled through square-well potential as follows:

$$u\left(r_{ij}\right)=\begin{cases}\infty & r_{ij}<\sigma_{ij}\\ -\varepsilon_{ij} & \sigma_{ij}<r_{ij}<\sigma_{ij}+\delta_{ij}\\ 0 & r_{ij}>\sigma_{ij}+\delta_{ij}\end{cases} \tag{2.57}$$

based on the same hypothesis, the square-well potential for water-calcite interaction is expressed as:

$$u(l_{fw})=\begin{cases}\infty & l_{fw}<\frac{\sigma_i}{2}\\ -\varepsilon_{fw} & \frac{\sigma_i}{2}<l_{fw}<\frac{\sigma_i}{2}+\delta_{fw}\\ 0 & l_{fw}>\frac{\sigma_i}{2}+\delta_{fw}\end{cases} \tag{2.58}$$

To address the confined fluid condition at the water-calcite interface, it is necessary to modify the definition of configurational energy, by including the interactions between water molecules and calcite wall. Thus, E_{conf} will be split into fluid-fluid and fluid-wall interactions, allowing us to include the attractive part of the dominant molecular interactions within the system volume. In the subsequent analysis, we will utilize Travalloni's [202] approach and adopt his methodology to the geometry presented in Figure (2.8). By assuming the pairwise interaction energies, the modified configurational energy can be formulated as:

$$E_{conf}=\underbrace{-(N/2)N_c\varepsilon_{ij}}_{\text{water-water interaction}}-\underbrace{NF_p\varepsilon_{fw}}_{\text{water-calcite interaction}} \tag{2.59}$$

where,

N_c: is the water-water coordination number

ε_{ij}: is the depth of the square-well for water-water interaction

ε_{fw}: is the depth of the square-well for water-calcite interaction

F_p: is separately expressed with the following equation:

$$F_p=F_{pr}+(1-F_{pr})\left(1-\exp\left(\frac{-\varepsilon_{fw}}{kT}\right)\right)\left(1-\frac{\rho}{\rho_{max}}\right)^{\theta} \tag{2.60}$$

where,

θ is confinement degree and is given by:

$$\theta=\frac{l_z}{\delta_{fw}+\frac{\sigma}{2}} \tag{2.61}$$

and then,

F_{pr} is expressed as:

$$
\begin{aligned}
F_{pr} &= \frac{\text{volume of region II}}{\text{volume of region I + volume of region II}} \\
&= \frac{\left(l_z - \frac{\sigma}{2}\right) A_{xy} - \left(l_z - \frac{\sigma}{2} - \delta_{fw}\right) A_{xy}}{\left(l_z - \frac{\sigma}{2}\right) A_{xy}} \\
&= \frac{\left(l_z - \frac{\sigma}{2}\right) - \left(l_z - \frac{\sigma}{2} - \delta_{fw}\right)}{\left(l_z - \frac{\sigma}{2}\right)}
\end{aligned}
\tag{2.62}
$$

where,

A_{xy} is the area of the calcite surface extended along xy-axis.

As per Travalloni's [202] definition in equation (2.60), F_p denotes the fraction of water molecules confined within the attractive field of the calcite nanoslab. This parameter essentially characterizes the distribution of water molecules within the confinement, which depends on parameters like temperature, interaction energy, fluid density, and confinement geometry [203]. by plugging in the equations (2.59), (2.60) and (2.62) into the definition of partition function in equation (2.56), $\tilde{a}^{fw}$is estimated as:

$$
\tilde{a}^{fw} = -\frac{\varepsilon_{fw}}{k}\left[\frac{F_{pr}}{T} + (1 - F_{pr})\left(1 - \frac{\rho}{\rho_{max}}\right)^{\theta}\left(\frac{k\left(\exp\left(-\frac{\varepsilon_{fw}}{kT}\right) - 1\right)}{\varepsilon_{fw}} + \frac{1}{T}\right)\right] \tag{2.63}
$$

As seen, the expression for $\tilde{a}^{fw}$ relies on confinement parameters ε_{fw}, F_{pr}, θ and density of the confined fluid. These parameters can be determined through molecular dynamics simulation.

2.4 Molecular dynamics

Molecular dynamics simulations are computational tools that allow simulating a microscopic system, using simple principles in classical mechanics. This computational technique utilizes the Born-Oppenheimer [204] approximation, which separates the motion of the atomic nuclei and electrons. Within this framework, atomic nuclei are treated as points of mass, allowing the classical Newtonian equations of motion to describe the behavior of a many-body system. Various molecular dynamics simulation packages such as DLPOLY [205, 206], GROMACS [207–209] and LAMMPS [128] have been developed for different scientific aims. The remarkable advantages provided by molecular dynamics simulations have encouraged numerous researchers to extensively use this tool for various scientific purposes. These applications range from exploring space regions and time resolutions inaccessible through experimental methods [210] to predicting functional properties in biological systems [211] and even refining molecular structures obtained by experimental data [212].

2.4.1 Potentials in molecular dynamics simulations

To conduct molecular dynamics simulations for a system, it is necessary to establish the potential function. This function defines how the particles interact with each other, contributing to the overall potential energy. Different potential energy contributions are schematically illustrated in Figure 2.9.

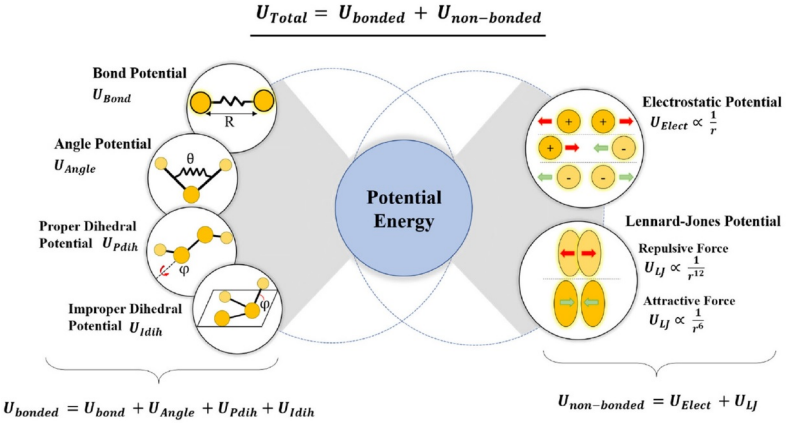

Figure 2.9: For molecular dynamics simulations, two main contributions of potential energy should be defined. The bonded term includes bond, angle, dihedral and improper species, while non-bonded one comprise van der Waals and electrostatic potentials [213]

.

Typically, the total potential energy contains contributions from bonded and non-bonded interactions [214]

$$U(r) = U_{bonded} + U_{non-bonded}. \tag{2.64}$$

Here, covalent and non-covalent type interactions are represented with bonded and non-bonded subscripts, respectively. Bonded potentials account for the stretching, bending and angle of chemical bonds, as well as the rotations around these bonds. These interactions are relatively strong and directly connected by chemical bonds [215]. U_{bonded} can be expanded as:

$$U_{bonded} = \sum_i U_i^{bond} + \sum_i U_i^{angle} + \sum_i U_i^{dihedral} + \sum_i U_i^{improper}, \tag{2.65}$$

where:

$$U_i^{bond} = K_i^b(r_i - r_0)^2,$$
$$U_i^{angle} = K_i^\theta(\theta - \theta_0)^2,$$

$$U_i^{dihedral} = K_i^{\phi}\left[1 - \cos\left(n\phi\right)\right],$$

$$U_i^{improper} = K_i^{\omega}(\omega - \omega_0)^2.$$

In equation (2.65), all bonded contributions were presented with harmonic potential formalism. The first term represents the energy as a result of variation in bond length. The second term represents the energy caused by the alteration in the bond angle. The third and fourth terms represent the contributions from dihedral and improper angles, respectively. These terms quantify the energy associated with deviations from a planar configuration and flipping over the mirror image. In other words, improper dihedrals are responsible for maintaining the planarity of planar groups and preventing molecules from flipping over to their mirror images. Furthermore, $K_i^b, K_i^\theta, K_i^\phi, K_i^\omega$ are harmonic coefficients and $r_0, \theta_0, n, \omega_0$ are initial geometric constants. On the other hand, non-bonded potentials refer to interactions between particles that are not directly connected by chemical bonds. They consist of van der Waals forces and electrostatic interactions as represented below:

$$U_{non-bonded} = \sum_i U_i^{vdW} + \sum_i U_i^{elec}. \tag{2.66}$$

Non-bonded potentials are typically weaker compared to bonded interactions and act over longer ranges. The van der Waals term includes forces originating from temporary dipoles that can either attract or repel particles based on the distance between them. The van der Waals potential is typically modeled by Lennard Jones as follows:

$$U^{vdw} = 4\varepsilon\left[\left(\frac{\sigma}{r}\right)^{12} + \left(\frac{\sigma}{r}\right)^{6},\right] \tag{2.67}$$

where ε is the depth of the potential well, σ is the distance at which the interaction potential reaches zero, and r is the distance between two particles. Figure 2.10 shows the profile of potential energy versus particle-particle distance according to the classical $12-6$ Lennard-Jones.

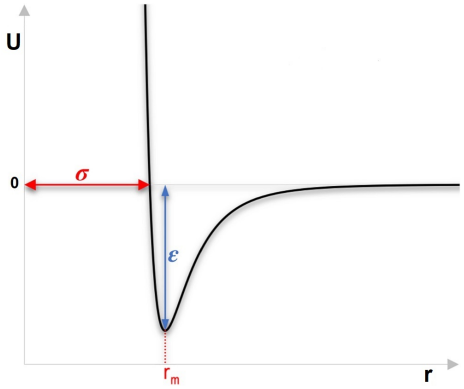

Figure 2.10: Illustration of the Lennard-Jones ($12-6$ potential) function, where parameter r_m represents the equilibrium distance corresponding to the minimum bonding potential. The figure is adopted from [216].

Electrostatic interactions involve the attraction or repulsion between charged particles and follow the Coulomb interaction formalism:

$$U^{elec} = \frac{1}{4\pi\varepsilon}\frac{q_i q_j}{r} \tag{2.68}$$

where ε is the dielectric constant, r is the distance between point charges q_i and q_j. The potential function formulation and parameters chosen for each species are given in equations (2.65) and (2.66). These parameters typically rely on fitting available experimental data. To be specific, coefficients for each term are adjusted to better match the experimental data.

2.4.2 Newton's equations of motion

In molecular dynamics, the motion of the particles is computed by Newton's equations of motion. According to classical mechanics, the total force acting on each particle is derived from the gradient of the potential energy $U(r)$, mathematically represented by:

$$\begin{aligned} F &= -\nabla U\,(r) \\ &= -\left(\frac{\partial U}{\partial x} + \frac{\partial U}{\partial y} + \frac{\partial U}{\partial z}\right), \end{aligned} \tag{2.69}$$

where, F represents the total force, U denotes the potential energy and position vector r consists of the components along the x, y and z axes. Once the force is known, the acceleration can be obtained using Newton's second law. Re-writing the definition of acceleration $\left(a = \frac{dv}{dt}\right)$ and velocity $\left(v = \frac{dr}{dt}\right)$ with Hamiltonian

formalism leads to a system of differential equations:

$$\frac{dp}{dt} = F \tag{2.70a}$$

$$\frac{dr}{dt} = \frac{p}{m}, \tag{2.70b}$$

where p is the momentum and t is time. The numerical solution of the differential equation system introduced in equations (2.70a,2.70b) provides information on the dynamic evolution of the system, by calculating the trajectories of interacting particles over time. In essence, equation (2.70a,2.70b) is the basis for time integration in molecular dynamics simulations and propagation of the system forward in time.

2.4.3 Velocity Verlet algorithm

Velocity Verlet [217] algorithm is widely used for integrating Newton's equations of motion due to its time reversibility and energy conservation [218]. This algorithm has been consistently applied in all molecular dynamics simulations conducted within this thesis. It computes the positions and velocities of particles as follows:

- Calculate velocity at half time-step: $\mathbf{v}(t + \frac{1}{2}dt) = \mathbf{v}(t) + \frac{1}{2}\left(\frac{\mathbf{F}(t)}{m}\right) \cdot dt$,

- Correct position: $\mathbf{r}(t + dt) = \mathbf{r}(t) + \mathbf{v}(t + \frac{1}{2}dt) \cdot dt$.

Using the above algorithm, one can represent the time integration sequences in molecular dynamics simulation as [219]:

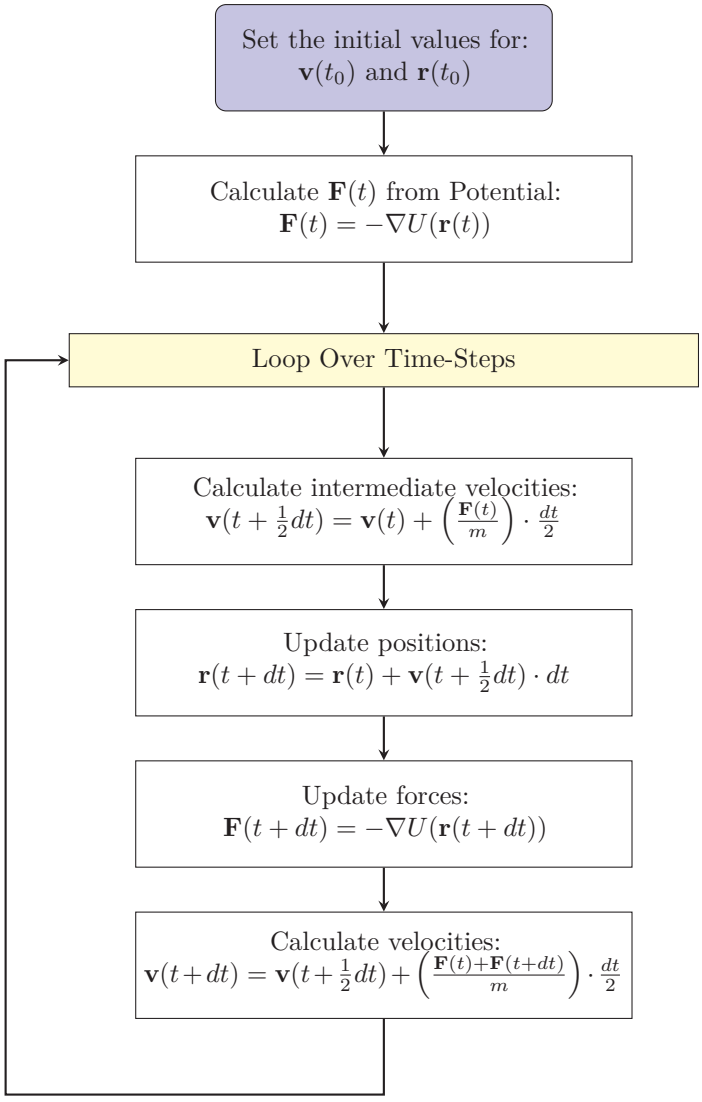

Figure 2.11: Overall approach of time integration in molecular dynamics simulations. The initial state (position and velocity) and interaction potential are input data to the simulations.

As seen, the intermediate velocity at half time-step $\frac{dt}{2}$ is calculated based on the force at the previous time-step t. Then, this intermediate velocity is used to calculate the position at the time-step dt. Now, forces can be updated based on the position at a new time-step. Finally, the velocity at time-step dt is calculated based on the intermediate velocity and total force acting on a particle. In molecular dynamics simulations, choosing an appropriate time-step

is crucial to prevent error accumulation. Large time-steps lead to significant error accumulation, while excessively small ones are computationally inefficient. As molecular vibrations occur approximately at frequencies of the order of 10^{14} Hz, a period of about 10 fs ($10^{-15}s$) is required. In this Ph.D. thesis, time-step of 1 fs and 0.5 fs were chosen.

2.4.4 Periodic boundary conditions

With today's high-performance computing facilities, molecular dynamics simulation can model thousands of particles [220]. Yet, directly simulating systems on a macroscopic scale, close to Avogadro's number (6.02×10^{23}) remains unfeasible due to high computational costs. Instead, utilizing periodic boundary conditions along with the minimum image convention facilitates the exploration of macroscopic properties within nanoscale simulations. Under the minimum image convention, only the nearest image of each particle within the periodic boundary conditions is taken into account for pair interactions [221].

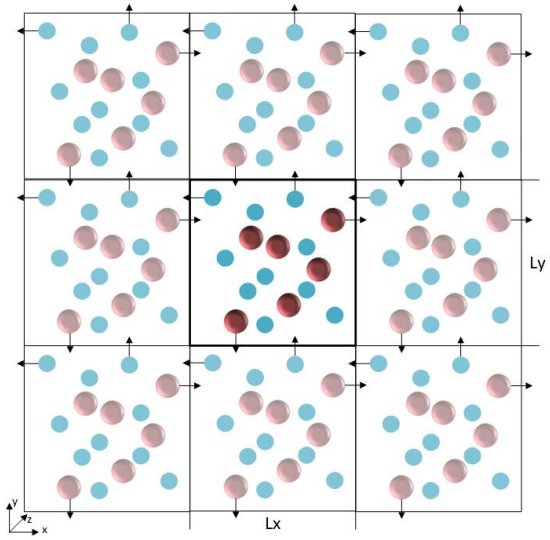

Figure 2.12: Sketch of a binary system, showing periodic boundary conditions. The black arrows show the velocity vector of the relevant particle. The central box represents the main simulation system. The particles that leave the central box are replaced by their image from the opposite box. Each particle interacts with the nearest image of other particles to adhere to minimum image convention.

With periodic boundary conditions, one can replicate an infinite system by ensuring that a particle exiting the simulation box through one side re-enters from the opposite side. The visual representation of a binary system with periodic boundary conditions is shown in Figure 2.12. In this illustration, the central box depicts the main simulated system, while the periodic images of this

system are mapped around it. For a system of dimensions $L_x \times L_y \times L_z$, the mathematical representation of the periodic boundary condition for particle i is given as:

$$x_i^{new} = x_i - L_x \left(\frac{x_i}{L_x} \right) \tag{2.71a}$$

$$y_i^{new} = y_i - L_y \left(\frac{y_i}{L_y} \right) \tag{2.71b}$$

$$z_i^{new} = z_i - L_z \left(\frac{z_i}{L_z} \right) \tag{2.71c}$$

The minimum image convention, on the other hand, calculates the shortest distance between particles in a periodic system. In other words, the convention algorithm considers the periodic nature of the system to determine the shortest possible distance.

2.4.5 Ergodicity hypothesis

In experimental methods, computing a property involves conducting measurements over time and averaging them. Similarly, in molecular dynamics simulations, the properties of interest are averaged by numerically evolving the system. In these simulations, a sufficient run-time is required to set the time-averaged property equal to the ensemble-averaged property over the phase space, which includes all possible states in the simulated system [222]. Consider a system containing N particles, each identified with position r_i and momentum p_i. In this system a specific microstate in phase space is represented as $\Gamma(r^N, p^N)$ where $r^N \in \{r_1, r_2, \ldots, r_N\}$ and $p^N \in \{p_1, p_2, \ldots, p_N\}$. If the property of interest is denoted as $A(\Gamma)$, it changes as the system evolves over time. Thus, ensemble-averaged property can be expressed as:

$$\langle A\left(r^N, p^N\right)\rangle = \lim_{t\to\infty} \frac{1}{t} \int_0^t A\left(\Gamma(r^N, p^N, t)\right) dt. \tag{2.72}$$

In molecular dynamics simulations, it is clear that we cannot extend the integral in equation (2.72) to infinite time, but it can potentially be approximated (fulfilled) by averaging over a sufficiently long finite time τ such that $\tau < t$, namely:

$$\langle A\left(r^N, p^N\right)\rangle = \frac{1}{\tau} \sum_{\tau=0}^{\tau<t} A\left(\Gamma(r^N, p^N, \tau)\right). \tag{2.73}$$

According to the ergodicity hypothesis, in an adequately long molecular dynamics simulation, the system will explore all possible configurations consistent with the given energy, resulting in time-averaged properties that match the ensemble-averaged properties [223]. To meet the requirements of the ergodicity hypothesis in this Ph.D. thesis, the run-time of all simulation is partitioned

into equilibration and production phases. During equilibration, the system's properties such as temperature and energy stabilize gradually, ensuring the system reaches a state representative of the desired conditions. Following the equilibration, production begins, during which the system remains stable and data are collected for analysis.

2.4.6 Nosé-Hoover thermostat

In molecular dynamics simulations, the behavior of a system is studied within a specific thermodynamic ensemble, allowing for a comprehensive exploration of the dynamics, interactions, and properties exhibited by the simulated system. The thermodynamic ensemble of a system comprising a fixed number of atoms (N) confined within a fixed volume (V) at a constant temperature (T), commonly denoted as NVT, is known as the canonical ensemble in thermodynamics. Characterization of a system at constant temperature in molecular dynamics can be achieved through various methods. For instance, there exists an early proposal suggesting the control of the system's temperature by limiting kinetic energy. In this method, the velocity of the particle alters at every simulation time-step to comply with the Maxwell-Boltzmann distribution [224, 225]. However, the drawback of this method is that the effects on the dynamical properties of the system are ignored [226]. In this Ph.D. thesis, a thermostat proposed by Nosé-Hoover [227, 228] controls the establishment of NVT ensemble. In this method, the simulation box is exposed to an external heat bath to achieve equilibrium, presuming that the simulation box boundaries permit only the exchange of energy, not mass. Thus, as the simulation box reaches equilibrium with the external heat bath, the components of both systems reach a uniform temperature T [229]. The following outline the essential steps to derive Nosé-Hoover thermostat, adopted from Frenkel and Smith's [119] work:
The Lagrangian $\mathcal{L}$ in a classical system is defined as:

$$\mathcal{L} = K - U, \tag{2.74}$$

where K is a kinetic energy and U is a potential energy. Nosé initially derived Lagrangian of a classical system by assuming an additional coordinate s as:

$$\mathcal{L}_{Nosé} = \sum_{i=1}^{N} \frac{1}{2} m_i \left(s \frac{dr_i}{dt} \right)^2 - U(r^N) + \frac{1}{2} Q \left(\frac{ds^2}{dt} \right)^2 - \frac{3N}{\beta} \ln s \tag{2.75}$$

where $\beta = \frac{1}{kT}$, m is the mass of particle i and Q is an effective mass related to the additional variable s. Considering the momentum conjugate of r_i and s which is defined respectively as :

$$p_i = \frac{\partial \mathcal{L}}{\partial r_i} = m_i s^2 \frac{dr_i}{dt} \tag{2.76}$$

$$p_s = \frac{\partial \mathcal{L}}{\partial \frac{ds}{dt}} = Q\frac{ds}{dt}, \tag{2.77}$$

the Hamiltonian of the system plus one extended variable can be expressed as:

$$\mathcal{H}_{Nosé} = \sum_{i=1}^{N} \frac{p_i^2}{2m_i s^2} + U(r^N) + \frac{p_s^2}{2Q} + \frac{3N \ln s}{\beta}. \tag{2.78}$$

Hereafter, the real variables are marked with prime (r', p', s', t') to distinguish them from virtual heat bath variables (r, p, s, t). The relationships between the real and virtual variables are then defined as:

$$\begin{aligned} r' &= r, \\ p' &= \frac{p}{s}, \\ s' &= s, \\ dt' &= \frac{dt}{s}, \end{aligned} \tag{2.79}$$

then, equation of motions with respect to the real variables are written as:

$$\frac{dr_i'}{dt'} = s\frac{dr_i}{dt} = \frac{p_i}{m_i s} = \frac{p_i'}{m_i}, \tag{2.80}$$

$$\frac{dp_i'}{dt'} = s\frac{d(\frac{p_i}{ds})}{dt} = \frac{dp_i}{dt} - \frac{p_i}{s}\frac{ds}{dt} = -\frac{\partial U(r'^N)}{\partial r_i'} - \frac{s'p_s'}{Q}p_i', \tag{2.81}$$

$$\frac{1}{s}\frac{ds'}{dt'} = \frac{s}{s}\frac{ds}{dt} = \frac{s'p_s'}{Q}, \tag{2.82}$$

$$\frac{d(s'\frac{p_s'}{Q})}{dt'} = \frac{s}{Q}\frac{dp_s}{dt} = \frac{1}{Q}\left(\sum_{i=1}^{N}\frac{(p_i')^2}{m_i} - \frac{3N}{\beta}\right), \tag{2.83}$$

The above equations of motion become simpler by the definition of thermodynamic friction coefficient ($\xi = \frac{s'p_s'}{Q}$) which was introduced by Hoover:

$$\frac{dr_i}{dt} = \frac{p_i}{m_i}, \tag{2.84}$$

$$\frac{dp_i}{dt} = -\frac{\partial U(r^N)}{\partial r_i} - \xi p_i, \tag{2.85}$$

$$\frac{d\xi}{dt} = \frac{1}{Q}\left(\sum_{i=1}^{N}\frac{(p_i)^2}{m_i} - \frac{3N}{\beta}\right), \tag{2.86}$$

$$\frac{1}{s}\frac{ds}{dt} = \frac{d\ln s}{dt} = \xi. \tag{2.87}$$

Finally, the Nosé-Hoover Hamiltonian for an extended system can be written as:

$$\mathcal{H}_{\text{Nosé-Hoover}} = \sum_{i=1}^{N} \frac{p_i}{2m_i} + U(r^N) + \frac{\xi^2 Q}{2} + \frac{3N}{\beta} \ln s, \tag{2.88}$$

where, the total energy $\mathcal{H}_{\text{Nosé-Hoover}}$ is conserved.

2.4.7 Radial distribution function

The radial distribution function (*rdf* or *g(r)*) is a valuable tool to evaluate the spatial distribution of particles around a reference particle. Essentially, *rdf* reveals the probability of finding a particle at a certain distance from another particle [230]. Depending on the simulated system in molecular dynamics, *rdf* applied to an atom, molecule, or molecular clusters. Widely used in molecular dynamics simulations, the radial distribution function provides valuable information such as insight into particle interaction potentials [231], structure analysis [232], molecular orientation [233] and more. To compute *g(r)* for a given reference particle i within a fluid system, the distribution of other particles (such as j) is determined relative to i. However, this distribution requires statistical averaging due to varying positions experienced by fluid atoms, defined by:

$$g(r) = \frac{\langle \rho(r) \rangle}{\rho_v}, \tag{2.89}$$

where $r = |r_i - r_j|$ and ρ_v is number density of particle i within volume $4\pi r^2 dr$. In this dissertation, *rdf* is used to calculate the solvation shell around mono/divalent ions.

2.4.8 Energy minimization

In mathematics for a multivariate function like f that depends on multiple independent variables $x_i \in \{x_1, x_2, \ldots, x_n\}$, minimization refers to determining a set of these independent variables at which f reaches its minimum value, that is:

$$\frac{\partial f}{\partial x_i} = 0 \tag{2.90a}$$

$$\frac{\partial^2 f}{\partial x_i^2} > 0. \tag{2.90b}$$

In molecular dynamics, the initial configuration of a simulated system might not necessarily correspond to an optimized conformation in terms of energy. Thus, energy minimization is carried out to discover a configuration for the simulated system that matches an optimized conformation. The objective of energy minimization is to identify a local minimum within the energy landscape.

This algorithm iteratively adjusts the position of each particle r to minimize the potential energy function *U(r)*. Mathematically, the set of the positions r^* minimizing *U(r)* is shown as [234, 235]:

$$r^* = \underset{r}{\operatorname{argmin}}\, U(r). \tag{2.91}$$

This optimization technique utilizes various algorithms such as gradient descent and conjugate gradient methods to modify particle positions until arriving at a local minimum in the potential energy landscape. The resulting configuration ideally represents a stable conformation or a minimum energy state for the simulated system. [236, 237]. In this Ph.D. thesis, energy minimization is carried out initially in each simulation to ensure that the system is free from steric clashes or improper geometry. This step helps relaxing the structure while gradually ramping up the temperature.

2.5 Material and geometry

The main materials utilized in this study involve calcite, representing the surface of the mineral, and water, which mimics the fluid phase. Water interacts directly with calcite and also serves as a solvent, including mono- and divalent ions. The objective of this section is to provide an elaborate description of the calcite and water used in molecular dynamics simulations.

2.5.1 Hexagonal indices

In crystallography, the structure of a crystal is expressed based on the spatial arrangement of its atoms, each occupying a specific point in a three-dimensional Cartesian coordinate system. Thus, each point of a crystal lattice can be represented by a linear combination of primitive lattice vectors such as:

$$\mathbf{R} = n_1\mathbf{a} + n_2\mathbf{b} + n_3\mathbf{c}, \tag{2.92}$$

where, n_1, n_2 and n_3 are integer numbers which are multiplied by linearly independent lattice vectors $\mathbf{a}, \mathbf{b}$ and $\mathbf{c}$. Miller indices, shown by (hkl), represent the planes where the crystal axes intersect at points $\frac{\mathbf{a}}{h}$, $\frac{\mathbf{b}}{k}$ and $\frac{\mathbf{c}}{l}$. Essentially, Miller indices (hkl) are integer numbers that indicate planes orthogonal to reciprocal lattice vectors, defined as:

$$\mathbf{r}_{hkl} = h\mathbf{a}^* + k\mathbf{a}^* + l\mathbf{c}^*, \tag{2.93}$$

where, $\mathbf{a} \cdot \mathbf{a}^* = 0$, $\mathbf{b} \cdot \mathbf{b}^* = 0$ and $\mathbf{c} \cdot \mathbf{c}^*$ represent orthogonality between lattice vectors and their Miller counterparts. However, for the hexagonal and rhombohedral lattice structure, an additional index, denoted as i, is introduced to aid in distinguishing between crystal planes more effectively. The relation between the index i and other Miller indices is defined as:

$$i = -(h + k). \tag{2.94}$$

Calcite has a rhombohedral structure [238] and its crystal structure can be defined by hexagonal indices ($hkil$). The unit cell of calcite is identified by $a = b = 4.990$Å and $c = 17.061$Å, $\alpha = \beta = 90°$ and $\gamma = 120°$ [239]. Figure2.13 depicts the rhombohedral structure of the calcite unit cell.

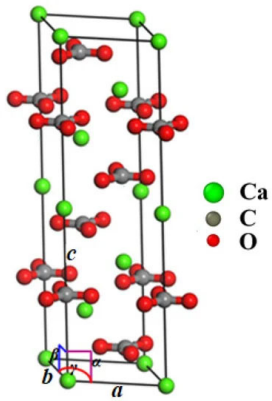

Figure 2.13: Illustration of rhombohedral structure of calcite unit cell [240]

.

2.5.2 Calcite neutral plane

Calcite can be analyzed across various crystallographic planes, each characterized by specific molecular structures. For example, cleaving calcite along planes like (1000) and (10$\bar{1}$1) results in surfaces terminated by either calcium (Ca-terminated plane) or carbonate (CO_3^{2-}-terminated plane). This cleavage generates dipoles, highlighting the diverse termination points within the crystal structure. Conversely, cleaving along (10$\bar{1}$4) plane provides a smooth and neutral surface. Moreover, various cleaved planes exhibit varying surface energies, depending on the molecular configuration formed on the cleaved surface. This variability in surface energies among different planes underscores the diverse stability associated with each crystallographic surface in calcite. Among various calcite planes, the (10$\bar{1}$4) emerges as the most stable, exhibiting consistently low surface energy in both hydrated and unhydrated conditions. The remarkable stability of the (10$\bar{1}$4) plane has been confirmed experimentally with Atomic Force Microscopy [241] and scanning electron microscopy (SEM) [242]. Simultaneously, theoretical studies confirm stability of (10$\bar{1}$4) plane [243–245] in terms of surface energy. Table 2.1 illustrates a comparative analysis of surface energy across various calcite crystallographic planes. Figure 2.14 depicts side views of various calcite crystallographic planes: (a) (0001), (b) (1000), (c) (1120), (d) (1011), and (e) (1014) [246].

In this Ph.D. thesis, the cleavage plane chosen for calcite is the (10$\bar{1}$4) plane, identified as the most stable surface under ambient conditions [241, 244]. The (10$\bar{1}$4) plane includes Ca^{2+} and CO_3^{2-} atoms that form a charge-neutral surface.

Table 2.1: Comparative analysis of surface energies across various calcite crystallographic planes

Calcite plane	$\left(\frac{J}{m^2}\right)$ [79]	$\left(\frac{J}{m^2}\right)$ [83]	$\left(\frac{J}{m^2}\right)$ [84]	$\left(\frac{J}{m^2}\right)$[85]
$(10\bar{1}4)$	0.86	0.23	0.60	0.59
(0001)Ca	1.44	1.6	0.97	0.97
$(0001)CO_3$	1.44	1.6	0.99	0.99
$(10\bar{1}0)$	1.37	0.52	1.59	0.97
$(10\bar{1}1)$Ca	1.49	-	1.03	1.23
$(10\bar{1}1)CO_3$	1.49	-	1.08	1.14
$(11\bar{2}0)$	1.66	0.5	1.43	1.39

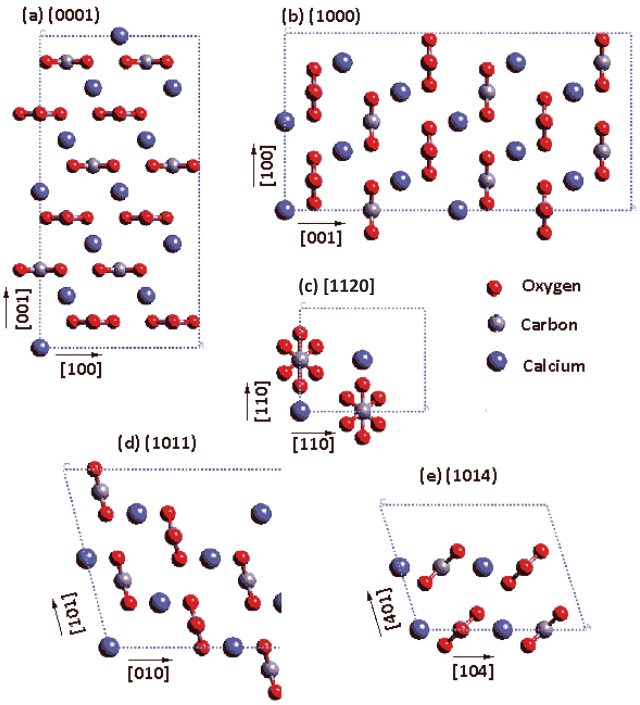

Figure 2.14: Side views of different calcite cleaved planes: (a) (0001), (b) (1000), (c) (1120), (d) (1011), and (e) (1014). The planes (0001) and (1011) are depicted with a doubled unit cell along a direction, as the dipole perpendicular to the slab has been removed. Figure adapted from [246]

.

However, cleaving along alternate planes results in surfaces terminated either by a layer of calcium ions or by carbonate ions, consequently yielding surfaces with positive or negative charges. These polar surfaces tend to adsorb ions or undergo reconstruction to eliminate dipole moments, rendering them unstable.

2.5.3 Potential models for water

Water has been extensively studied and remains a focal point in scientific literature due to its importance and complexity. The primary focus in theoretical investigations since the advent of molecular simulations has been to define the force field of water, describing the natural characteristics of water. Numerous potential models have emerged based on experimental data and quantum mechanical calculations [247, 248], exhibiting different performances [249, 250]. The most widely used water models are classical potentials, known for being rigid and non-polarized, including SPC [251], SPC/E [252] and transferable interatomic potential series like TIP3P [253],TIP4P [254] and TIP5P [255]. There exist flexible models (i.e., flexible bond lengths, bond angles, and dihedral angles) and polarizable models, capable of altering the electron-cloud distribution. Some of these models include AIMD1 [256], AIMD2 [257], QM-4MM [258], QM-4TIP5P [258] and QM-230TIP5P [259]. These models are specifically designed to account for the dynamic nature of water molecules.

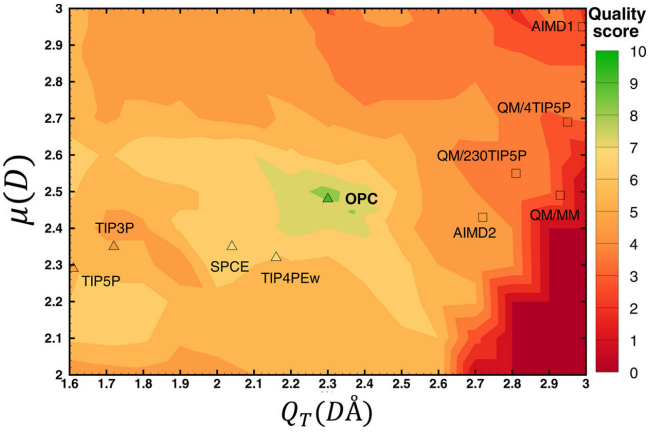

Figure 2.15: Assessment of different water models capability to account dipole (μ) and quadrupole (Q_T) moments. Adjusting the charge distribution in three- and four-point classical models (OPC) yields promising results [260]

.

In a comprehensive study conducted by Izadi et al. [260], various water models, ranging from classical to flexible polarized, were investigated. The evaluation focused on the ability of different models to capture dipole (μ) and quadrupole (Q_T) moments, as these two electrostatic moments have a strong effect on the liquid phase structure of water and its diagram behavior [258,

261–263]. The results indicate that the models that incorporate flexibility and polarization based on quantum mechanics scored relatively low, as illustrated in Figure 2.15. Nonetheless, improving the charge distribution in the three- and four-point models (Optimal Point Charge or OPC) led to improved outcomes. This implies that despite extensive efforts to assess classical rigid water models, there is still considerable room for improvement. Moreover, while polarizable models are considerably more computationally expensive [264], they do not consistently offer higher accuracy compared to classical models. Thus, the selection of water models should prioritize accuracy in reproducing specific properties. The water models utilized in this Ph.D. thesis are SPC/E [252], SPCE/FW [252] and TIP3P [253]. These three-point models were chosen due to their high accuracy in predicting the density and low computational cost.

2.5.4 Potentials for mono/divalent ions

In an earlier section (1.3), it was explained that within subsurface reservoirs, the adsorption of polar components found in oil on the surface of carbonate rock leads to the development of an oil-wet behavior in carbonate rock. [265], while calcite naturally exhibits hydrophilic characteristics. On the other hand, when aqueous phases containing mono/divalent ions, commonly referred to as brine water, are introduced to oil-wet rock, it leads to the detachment of oil. Namely, introducing brine water into an oil-wet system allows the carbonate rock surface to revert to a hydrophilic state. This phenomenon was initially introduced a long time ago [266, 267], evolving and gaining further understanding over time [268–270]. This approach serves as the foundation for a technology known as smart water flooding, which has the potential to significantly increase the total oil recovery up to 50-70% [72]. However, conventional methods generally allow the extraction of only 30-35% [271] of the hydrocarbons available in the reservoir.

Despite the extensive effort made to understand the physical and chemical processes involved in smart water flooding within carbonate reservoirs [272–274] and numerous mechanisms interpreting this phenomena from different angles [275–278], there is still a gap in exploring the molecular interactions among carbonate rock, crude oil and brine water. This Ph.D. thesis also aims to shed light on some molecular aspects of the interactions among calcite, crude oil and brine water within subsurface carbonate reservoirs. To achieve this goal, I utilized molecular dynamics simulation, providing high-resolution insights into the phenomenon across both time and space. Within this framework, two distinct compositions of brine water, along with crude oil, were introduced to interact with a calcite slab. Formation water (FW) comprising Na^+, Cl^- and Ca^{2+} and low saline water (LSW) containing Na^+, Cl^-, Mg^{2+} and SO_4^{2-} were used as brine water in molecular dynamics simulations. However, crude oil composed of Toluene, Decane, and Benzoic acid served as a representative of crude oil. Different potentials are utilized to model interatomic interactions in the aqueous phases and crude oil. The interatomic potentials for Na^+, Cl^-, Mg^{2+} and Ca^{2+} are defined using Optimized Potentials for Liquid Simulations-All-Atom (OPLS-AA) [279], while the potential proposed by Williams et al. [280] controls

the interatomic potentials for SO_4^{2-}. Additionally, the interactions between the oil components are modeled by OPLS-AA [279].

Chapter 3

Summary of papers and outlook for future works

This chapter summarizes the articles that contribute to the main research topic outlined in Chapter 1. This Ph.D. thesis includes three articles where I am the first author. The papers and proceedings are attached at the end of the thesis in chronological order. I wrote the papers and performed simulations using SAFT and molecular dynamics, which involved coding, simulations, data collection, and visualizations. My supervisors and co-authors provided input to the articles through discussions and added their comments before submission of the article and during the journal review process.

In-house models and equations of state based on Statistical Association Fluid Theory (SAFT) and Perturbed-Chain Statistical Association Fluid Theory (PC-SAFT) have been developed for some years at the Department of Geosciences, University of Oslo [281–284]. The former model was developed with the FORTRAN programming language, and the latter model was developed in the MATLAB environment. These two in-house models are currently under continuous development and advancement. Before starting this Ph.D. project, the SAFT equation of state had been applied to various studies such as (a) using the SAFT1 equation of state to predict the phase behavior and estimate the density of the aqueous phase in a ternary mixture consisting of CO_2-SO_2-H_2O across a wide range of temperatures and pressures [281], and (b) using SAFT1-RPM to predict the properties of a quaternary mixture consisting of CH_4-CO_2-H_2O-NaCl, incorporating Coulombic and polar forces [282]. The PC-SAFT model had also been utilized for two different projects prior to this Ph.D. A project predicting the phase behavior of asphaltene in crude oil [283] and one predicting the phase behavior of CO_2 interacting with brine water (H_2O, Na^+,Cl^-) [284]. Furthermore, some extensions of PC-SAFT had been integrated into the Matlab Reservoir Simulation Toolbox (MRST) [285, 286].

This Ph.D. work systematically explores the molecular aspects of the rock-fluid interface. The first part involves developing a tool to predict the macroscopic behavior of confined fluids influenced by solid minerals by examining molecular interactions at the nanoscale. This is achieved through the development of a thermodynamic model based on the SAFT framework, with relevant parameters computed through molecular dynamics simulations. Papers I and II tackle the topic of one- and two-dimensional confinements, respectively. In particular, both papers employ pure water to mimic the confined fluid, with the calcite $10\bar{1}4$ plane serving as the nanoscale slab. Paper I adopts PC-SAFT for one-dimensional confinement, while Paper II employs SAFT2 for two-dimensional confinement. To the best of our knowledge, this is the first time that equations of state inspired

by the SAFT framework have been developed to systematically consider the impact of solid confinement on the properties of a confined fluid. In a subsequent part of the Ph.D., molecular dynamics simulations were used to investigate the rock-oil-brine interface. In line with the rock-fluid interface, in Paper III, I investigated the rock-oil-brine interface to gain a comprehensive understanding of molecular interactions through molecular dynamics simulations. Although there are numerous mechanisms to interpret the consequences of smart water flooding (i.e., injection of low-salinity water during oil recovery), many lack microscopic examinations. Understanding the oil displacement process during smart water injection requires consideration of both macroscopic observations and microscopic mechanisms. In this study, the molecular dynamics simulation setup includes aqueous water (water + mono/divalent ions), oil (Toluene + Decane + Benzoic acid) and the calcite neutral plane ($10\bar{1}4$) to study the rock-oil-brine interface at the molecular scale. The molecular insights gained from this work may pave the way for future improvements in smart water flooding, a widely used technique in enhanced oil recovery (EOR). The summary of the articles and key findings are described in the following sections.

3.1 Development of PC-SAFT for one-dimensional confinement

3.1.1 Paper I:

Extension of PC-SAFT Equation of State to Include Mineral Surface Effect in Fluid Properties Using Molecular Dynamics Simulation

This paper uses the capability of PC-SAFT equation of state (EoS) to quantify the effect of carbonate rock on the physicochemical properties of a fluid confined at the mineral-fluid interface. Molecular dynamics simulations were employed to compute confinement parameters (section 2.3.5) necessary for the execution of PC-SAFT. Although PC-SAFT displays promise in modeling associating and polar fluids at a bulk scale, it has not yet addressed the impact of mineral confinement on fluid properties. This study develops PC-SAFT to determine the properties of water confined at the $10\bar{1}4$ calcite interface.

3.1.2 My contribution

Previous versions of PC-SAFT models before this Ph.D. project overlooked the effect of mineral confinement on fluid properties, treating both bulk and confined fluids similarly with identical parameters for the Helmholtz free energy. However, under confinement, the molecular arrangement of fluids differs on the basis of the governing thermodynamic conditions, chemistry, and the size of the mineral confinement. These variations determine the deviation of fluid properties from those observed in bulk. In this study, I used the MATLAB environment to incorporate the effect of solid calcite into the water properties using the PC-SAFT equation of state. The required confinement parameters were then

computed with the molecular dynamics simulations. For conducting molecular dynamics simulations, I used LAMMPS which is the classical molecular dynamic program from Sandia National Laboratories.

3.1.3 Method

To study the effect of confinement on fluid properties, a simulation domain was established including a calcite nanoslab and water. Calcite is dominant in carbonate reservoirs, and water is a known associating fluid found in the crude oil composition. Within the established setup, a calcite nanoslab was introduced into water along the z-axis from one side, serving as a suitable starting point to evaluate our novel approach.

After adjusting the setup, the next step involved defining new parameters for PC-SAFT to enable its distinction between confined water and bulk water. To derive the geometrical parameters necessary for this distinction, the approach outlined by Travalloni et al. [202] was utilized. Then, along with the previous developments for PC-SAFT, a code was developed within the MATLAB environment to define confinement parameters and Helmholtz free energy, specifically addressing the interactions between calcite and water. The new Helmholtz free energy is derived as a function of the confinement parameters, which need to be calculated for the successful execution of PC-SAFT. Calculating these confinement parameters was achieved through molecular dynamics simulation conducted for different water thicknesses at different temperatures.

3.1.4 Key findings

After collecting data from molecular dynamics simulations, the density and energy profiles of water were plotted along the z-axis at different temperatures and thicknesses of water. In the subsequent stage, the outcomes of the newly developed PC-SAFT model were compared with the results of molecular dynamics for Region II (layering zone). The following are the key findings of the work:

- The general perspective of the water density and energy profiles shows that both profiles start from zero at the calcite surface (Region III) and experience some large peaks within layering zone (Region II) and then stabilize in bulk-like zone (Region I). Different regions are marked in the density profiles depicted in Figure 3.1. Details of each region are also described in Figure 2.8.

- On closer examination, it becomes apparent that maintaining a fixed water thickness while increasing the temperature leads to a lower average density within both the layering zone and the bulk-like zone. Furthermore, maintaining a constant temperature while increasing the water thickness results in a higher average density within both Regions I and II.

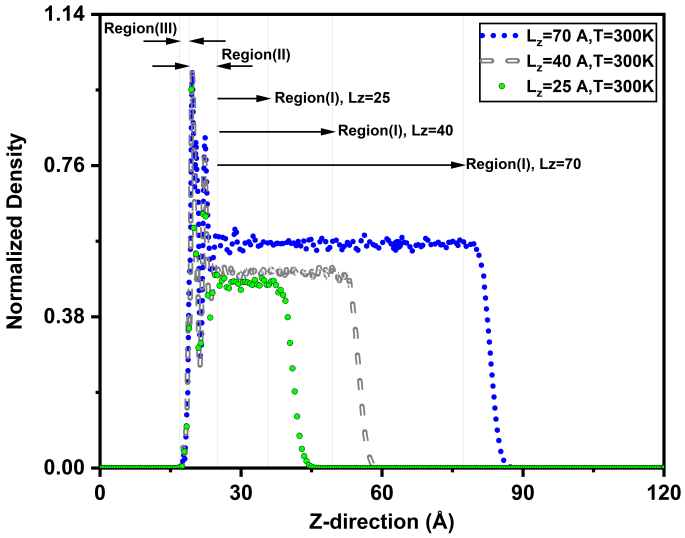

Figure 3.1: Illustration of the density profile within region I and II at different Lz and T=300 K. The density is normalized between 0 and 1, which allows comparing the average density trends. The greatest and lowest average densities occur at Lz = 70 Å and Lz = 25 Å, respectively [201].

- It is a promising alignment between the PC-SAFT modeling and the molecular dynamics findings. Namely, maintaining a constant water thickness while increasing the temperature leads to a decrease in the average density within Region II. Conversely, maintaining a constant temperature while increasing the thickness of the water results in an elevated average density within Region II.
- Comparison between PC-SAFT and molecular dynamics simulations indicates that the relative error increases with the growth of water thickness at a constant temperature. Similarly, the relative error increases with increasing temperature at a constant water thickness.

3.2 Development of SAFT for two-dimensional confinement

3.2.1 Paper II:

Extension of SAFT Equation of State for Fluids Confined in Nano-Pores of Sedimentary Rocks Using Molecular Dynamics Simulation

This paper demonstrates how SAFT2 EoS effectively captures the long-range interactions of calcite nanoslabs from opposing sides, affecting the macroscopic behavior of confined water. Calculating the confinement parameters required for SAFT2 execution is performed through molecular dynamics simulations. As two hydrophilic calcite nanoslabs begin competing to attract water molecules, this interaction results in unique deviations in water properties owing to the interplay of non-homogeneous attractions from both sides.

3.2.2 My contribution:

Previous studies before this Ph.D. project had utilized SAFT1 and SAFT1-RPM to investigate the phase behavior of aqueous solutions and electrolytes under reservoir pressure and temperature conditions, overlooking the possible influence of mineral confinement on the properties of the confined fluid. The previous approach in Paper I introduced a calcite wall on one side, emphasizing the calcite-water interaction on that side, while assuming water-water interactions approach bulk interactions on the opposite end. However, Paper II focuses on water confined within a two-dimensional confinement. To address this, a new framework of SAFT is required to consider the amplified attraction arising from opposing walls across a longer range, compared with that of Paper I. Put it differently, this novel model should capture the long-range interactions between hydrophilic calcite slabs and water. Therefore, SAFT2 [287, 288] was chosen as the suitable framework for development, due to its improved square-well width (λ), enabling it to effectively model long-range interactions. Furthermore, given that SAFT2 was specifically designed to model multivalent ions, it could serve as a suitable platform for future developments, potentially adapting it to simulate the interaction between rock, oil and brine water. Finally, the new SAFT2 formalism was coded in the FORTRAN language and integrated into the existing SAFT model. The required confinement parameters were calculated by molecular dynamics simulations, conducted with the package LAMMPS.

3.2.3 Method:

I established a setup in which water is encapsulated within two calcite nanoslabs cleaved along the $(10\bar{1}4)$ plane. Adding the effect of two-dimensional confinement to the SAFT2 equation of states involves a two-step process i) to calculate the confinement parameters; and ii) to develop the Helmholtz free energy. Both may vary depending on the thermodynamic conditions and confinement size. In fact, the Helmholtz free energy is a function of confinement parameters, which will be determined through molecular dynamics simulations for various pore sizes and under different thermodynamic conditions.

3.2.4 Key findings:

After the molecular dynamics results were collected, the density and energy profiles of encapsulated water were plotted with respect to the width of the

calcite nanopore at different temperatures. The following are the key findings:

- In each density and energy plot, three distinct regions become apparent. Closest to the calcite surface on both sides lies Region III (forbidden zone), where both plots register zero values. Moving outward, Region II (layering zone) shows prominent peaks, indicating the structured water layers adsorbed onto the surface of calcite nanoslabs. The density and energy trends from both sides converge in the middle, forming the boundaries of Region I (bulk-like zone). Figure 3.2 represents the molecular visualization of water molecule arrangements along with relevant density profiles within different regions. More descriptions are provided in Figure 2.6.

- Density profiles, plotted for Region II (layering zone) and Region I (bulk-like zone), respectively, showing distinct behaviors. In the bulk-like zone, where the pore size is kept constant, the density decreases with rising temperature, resembling the behavior of bulk water. This trend implies that the density within Region I is predominantly governed by water-water interactions, as higher temperatures lead to an increased distance between water molecules, resulting in lower density.

- On the contrary, within the layering zone, an increase in temperature results in a larger density. This observation can be interpreted as water molecules inside Region I form a more dense network compared to those in Region II. As the temperature rises the distance between water molecules in the bulk-like zone increases, expanding the water network. Thus, some water molecules move into the empty cavities formed in Region II. To be specific, the existing gaps between adsorbed water molecules are filled with newly introduced ones, leading to higher density values at high temperature.

- At a constant temperature, as the pore size grows, the average density within the layering zone and central zone rises. The density within the bulk-like zone rises as the widening pore approaches conditions similar to bulk water. Additionally, the increase within the layering zone is attributed to the strengthening of water-water interactions, which compete with the calcite-water interactions. Therefore, the increase in pore size results in a higher average density both within the layering zone and within the bulk-like zone.

- At a constant temperature, a unique characteristic is evident in the density profile as the pore size decreases and reaches Lz = 1.5 nm. This deviation is attributed to the overlapping attraction potentials from both walls, specifically in terms of the calcite-water interaction. For Lz = 1.5 nm, water molecules experience a significantly confined space in the central zone, intensifying calcite-water interactions in comparison to water-water interactions. Thus, the water molecules inside the central zone are predominantly influenced by the porewall attractions on both sides.

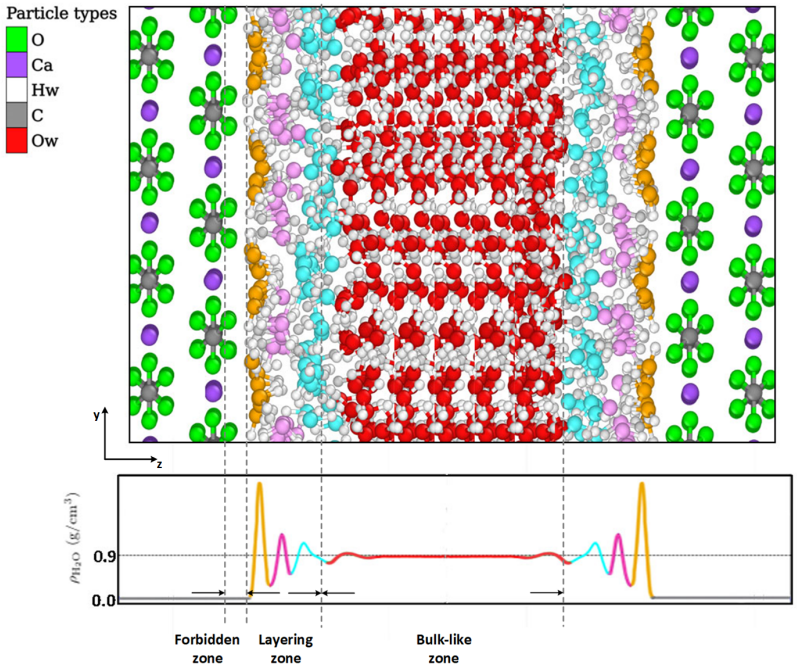

Figure 3.2: Cross-sectional view of the calcite-water-calcite system. Water atoms are colored by red (oxygen) and white (hydrogen). Within the calcite structure, carbon, oxygen and calcium atoms are gray, green and purple, respectively. The colors of oxygen atoms in the three layers seen from the calcite surface are orange, pink, and turquoise, respectively. To the bottom, the water density is plotted along z-axis, with line segments colored after the layer number. Ovito was used for visualization.

- The SAFT2 results were compared with molecular dynamics, revealing a good agreement at high temperature (T = 400 and 450 K). However, there is a noticeable increase in the absolute relative error at low temperatures. To address this issue, a new CF parameter was introduced. CF is defined as the fraction representing the density ratio within Region II and I, denoted as $\frac{\rho_{RegionII}}{\rho_{RegionI}}$. The introduced CF is aimed to enhance the alignment between molecular dynamics and SAFT2 simulations for low temperatures.

3.3 Underlying mechanisms driving smart water flooding

3.3.1 Paper III:

Drivers of Low-Salinity Effect in Carbonate Reservoirs Using Molecular Dynamics Simulations

This paper investigates the molecular aspects of low-salinity water (LSW) injection, an effective technique in enhanced oil recovery (EOR). The findings of this study contribute to better understand the effective mechanisms governing oil displacement after injection of low-salinity water into the rock-brine-oil system.

3.3.2 My contribution

Despite the proven success of low-salinity water injection, the fundamental mechanism driving oil displacement within the rock-brine-oil system remains uncertain. The challenge lies in connecting macroscopic observations with molecular scale mechanisms. To address this challenge, a suitable tool is required to examine the rock-oil-brine interface at the molecular scale. In this regard, molecular dynamics simulation is chosen as a computational tool to generate high resolution data in terms of time and space. In this study, in addition to $10\bar{1}4$ plane of calcite as a solid phase, three different fluid layers are modeled to mimic the rock-oil-brine interface. To be specific, I modeled two layers of brine water, one with higher salinity referred to as formation water (FW) and the other with lower salinity, named low salinity water (LSW). Additionally, an oil layer was modeled, consisting of hydrocarbon, aromatic and resin components. These simulated fluid layers were mounted above the $10\bar{1}4$ surface of nanoslab calcite. The molecular dynamics simulations in this study were conducted with LAMMPS.

3.3.3 Method

In the simulation box, I configured a setup, including calcite nanoslab with a thickness of 16.7 Å positioned at the bottom. Directly above the calcite, there is a 5 Å thick layer of formation water consisting of H_2O, Na^+, Cl^-, and Ca^{2+}. Above this, a 10 Å wide layer of oil is placed. Lastly, the uppermost fluid in the simulation box is a 20 Å thick layer of low saline water, composed of H_2O, Na^+, Cl^-, Mg^{2+}, and SO_4^{2-}, situated above the oil layer. It is essential to note that the brine water data was selected from experimental results reported by Zhang and Sarma [289], while the oil composition was derived from the SARA test, including toluene (37%), decane (44.7 %) and benzoic acid (18.3%). All molecular dynamics simulations were conducted using LAMMPS.

3.3.4 Key findings

In order to explore the preference of various species for settling on a thin calcite-brine film, the density profiles of different ions and water along the z-axis were

plotted. Following the data collection from molecular dynamics simulations:

- The profile of water density explicitly illustrates the adsorption of two water monolayers onto the calcite surface.
- Following the water monolayers, density profiles of monovalent ions are observed. The peak of Na^+ ions was found within the adsorbed water layers, whereas the peak of Cl^- ions appeared after the adsorbed water layers.
- The density profiles of the divalent ions including Ca^{2+}, Mg^{2+}, and SO_4^{2-} exhibit a peak farther from the calcite surface, immediately following the monovalent ions.
- The radial distribution functions plotted for different ions show that all mono- and divalent ions are hydrated with respective diameters of 2.45 Å, 2.35 Å, 1.95 Å, 2.35 Å and 1.75 Å for Na^+, Cl^-, Mg^{2+}, Ca^{2+}, SO_4^{2-}.
- Analysis of the brine water density profile in different time steps and temperatures indicates that at T=300 K, the oil displacement occurs gradually in two distinct steps. On the contrary, at T = 360 K, the transition occurs immediately, complete with the detachment in a single step. More precisely, the initiation of the transition at T = 300 K is delayed, while at T = 360 K, it has a shorter duration.
- The dynamics of different ions shows distinct behaviors. Monovalent ions (Na^+,Cl^-) settle within compact water layers on the calcite surface, while divalent ions exhibit varied movements. Initially, Ca^{2+} ions are close to the surface and migrate away over time, whereas Mg^{2+} and SO_4^{2-}, initially distant, move closer to the calcite surface, following oil displacement. Figure 3.3 illustrates the arrangement of Na^+ and Cl^- above the calcite surface, leading to the displacement of the oil layer.
- Examining the charge density profile at different time steps and temperatures reveals large oscillation trends near the calcite surface, indicating the formation of an electrical double layer (EDL) immediately after the calcite surface.
- As long as the oil layer adheres to the calcite-brine interface, the electrical double layer profile remains zero across the oil phase. The observed discontinuity between the head and tail of the charge density profile, where the charge density trend reaches zero, underscores that neither mono- nor divalent ions diffuse into the organic components of the oil layer.
- Over time, the discontinuity in the charge density profile is compensated by detachment of the oil layer from the calcite-brine interface. More precisely, the detachment of the oil occurs concurrently with the bridging of the gap in the charge density profile.

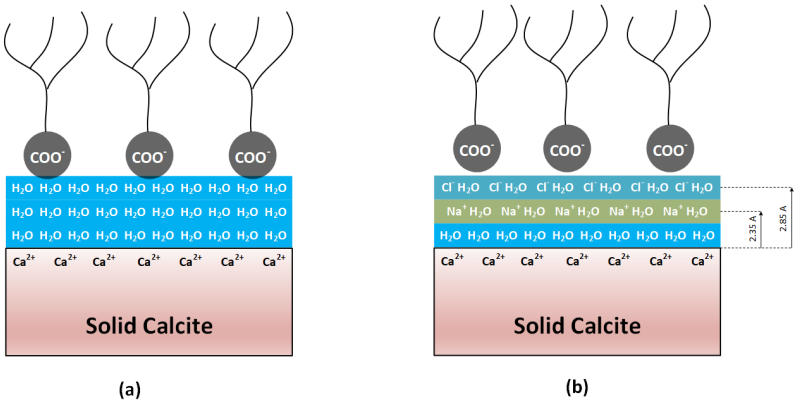

Figure 3.3: The sketch depicts settlement of Na^+ and Cl^- in close proximity to the surface, resulting in the formation of a double electrical layer. In (a) black balls represent benzoic acid in the oil layer adhere to the calcite surface via formation water. In (b) the oil layer separates from surface after Na^+ and Cl^- have settled.

- Similar to the trends observed in the density profile, at T=360 K, the gap in the charge density profile is filled more rapidly than at T=300 K. This gap compensation explicitly indicates oil detachment from the calcite-brine interface, which experiences a delay at T=300 K compared to T=360 K.

- Upon analysis of the results, it is apparent that there is minimal change in the positions of Na^+,Cl^- and H_2O with temperature variations. On the contrary, the positions of Mg^{2+}, Ca^{2+}, and SO_4^{2-} exhibit variations with temperature, indicating a dynamic response to changes in temperature.

3.4 Conclusions

The interfaces between rocks and fluids are pivotal in determining the reactivity and fate of fluids confined within subsurface reservoirs and aquifers. Understanding the complex nature of these interfaces requires a comprehensive study of the relationship between macroscopic observations and molecular interactions, as explored partly in this Ph.D. thesis. This complexity is due to the dynamic behavior of the rock-fluid interface across time and space, which closely links chemical reactions, species transport, and the physicochemical properties of both rocks and fluids.

One example that illustrates the aforementioned complexity is the varying behavior of water when solid calcite is introduced from opposite sides compared to just one side. The distinct nature of the governing interactions at the molecular level prompted the use of the PC-SAFT and SAFT2 models, each employed

to respectively capture diverse attractions induced by the calcite slabs. This methodology proves relevant for quantifying the impact of other minerals on different fluids, although to varying extent.

Furthermore, in the comparison between SAFT-based models and molecular dynamics, a divergence emerges when confined water approaches bulk water properties. This discrepancy exists between the predictions of SAFT-based models and outcomes of molecular dynamics. This analysis suggests that SAFT-based models, tuned to predict the properties of confined water, effectively distinguish between confined and bulk fluids. However, the increased discrepancy at higher temperatures, specifically for the PC-SAFT, may be attributed to the limitations inherent in the PC-SAFT model. To elaborate, molecular dynamics simulations utilize the SPC/E model for water molecules. The decreasing accuracy of this chosen water model with increasing temperature may introduce errors in the PC-SAFT predictions during the computation of confinement parameters. While this limitation may be valid for SAFT2, its impact is likely less pronounced due to a lower threshold of maximum temperature, compared to PC-SAFT.

At the second research topic, the introduction of a correction factor, CF, to improve the alignment between SAFT2 and molecular dynamics results, particularly at low temperatures, highlights that beyond the calcite-water interactions, other factors may control the properties of confined fluid. In other words, at lower temperatures and smaller confinement dimensions, the impact of the confinement constraints is more pronounced. This finding provides a foundation for further exploration into how additional constraints (e.g. geometry of confinement, layering patterns, and the mutual interaction of different regions) impact the characteristics of confined fluids.

Upon comparing the findings of the first and second research, it is evident that the density of confined water remains consistently lower than that of the bulk, regardless of whether it is subject to one- or two-dimensional confinement. However, confinement on one side offers more room for water molecules from a front not exposed to calcite, mitigating the influence of calcite-water interactions. To put it differently, the dual front of calcite-water interactions induced by hydrophilic calcite surfaces, reinforces the calcite-water interactions. This principle remains valid for both layering and bulk-like zones.

Variations in the density of water under confinement underscore the impact of the confinement on accurately predicting the physiochemical properties of the confined fluid. This aspect is often overlooked by commonly used equations of state, employed for the calculation of physiological properties. Consequently, these oversights contribute to inaccuracies in predicting the phase behavior of confined fluid.

In the third research topic, we employed the LAMMPS software to conduct molecular dynamics simulations, aligning with the rock-fluid interface. Our aim was to investigate the mechanisms that influence the detachment of oil from the rock-brine interface during low-salinity water injection. Molecular dynamics simulations, known for their capability to offer high-resolution data, effectively

capture the early stage interactions occurring at the rock-oil-brine system. We examined how both mono- and divalent ions contribute to the detachment of oil. This was achieved by analyzing the profile of mass density and charge density along with the radial distribution function at different temperatures.

The findings reveal the formation of a hydrate shell around mono- and divalent ions. The first molecules observed above the calcite surface are water molecules, forming structured layers approximately 2 Å away from the calcite surface. Thus, neither mono- nor divalent ions adsorb on the calcite surface directly. In essence, the first water monolayer acts as a bridge between the calcite surface and other ions.

Moreover, divalent ions such as Ca^{2+}, Mg^{2+}, and SO_4^{2-} are located at a greater distance from the calcite surface compared to monovalent ions. This distinctive ordering of mono- and divalent ions above the calcite mineral results from the energy penalty associated with the solvation shell of each ion. This ordering provides compelling evidence of the ions' preference to bind to the calcite surface. Simply put, monovalent ions exhibit a stronger affinity for the calcite surface compared to that of the divalent counterparts, as monovalent ions diffuse into the structured water layers, while divalent ions remain positioned farther from the calcite surface.

It is reasonable to attribute the formation of an electrical double layer to the distribution of monovalent ions above the calcite surface. This association becomes apparent as the development of the electrical double layer coincides with the settling of Na^+ and Cl^- near the calcite surface, at around 2.5 Å. On the contrary, the divalent ions remain at a greater distance, approximately 7-10 Å, and shift their position with temperature. However, the positions of monovalent ions exhibit minimal variation with temperature.

The oil detachment process occurs gradually in a few steps at 5 ns and 10 ns when T=300 K, while it takes place within a single step at 10 ns for T=360 K. This observation can be interpreted as the impact of temperature and kinetic energy on the efficiency of low-salinity water in the separation of the oil layer from the rock-brine interface.

The presence of an oil layer adhering to the rock-brine interface was identified by discontinuity between the head and tail of the charge density profile, as discussed earlier. As time progresses, this gap is simultaneously filled with the displacement of oil. At both T = 300 K and T = 360 K, the bridging of the gap temporally overlaps with the detachment of the oil layer from the rock-brine interface. Thus, the expansion of the electrical double layer coincides temporally with the displacement of the oil layer. The temporal overlap mentioned was also confirmed by the mass density profile. This molecular-scale observation supports the hypothesis suggesting the expansion of the electrical double layer as the main cause of oil detachment from the rock-brine interface.

3.5 Outlook

Throughout this Ph.D. work, numerous compelling ideas emerged during meetings and scientific discussions with supervisors and colleagues. These concepts sparked research questions and prompted the need for further research. Despite my interest, time constraints prevented me from delving deeper into many of these interesting concepts. These unexplored ideas stand as a testament to the wide range of research possibilities. Although we are actively working on some ideas, their inclusion in this dissertation awaits completion. As my Ph.D. journey concludes, several promising research avenues will remain unexplored, inviting future exploration and inquiry. Here, I present a list of scientific research topics related to this Ph.D. work that deserve further consideration.

3.5.1 Thermodynamic Modeling

In this Ph.D., my focus was on the calcite cleavage surface $(10\bar{1}4)$, which is chemically hydrophilic. However, the effect of other minerals (e.g. silicate and clay) and hydrophobic surfaces on confined fluid remains unexplored. Furthermore, it is worth studying other available planes of calcite, each of which has specific characteristics and charge distribution.

We modeled water molecules in liquid state in all case studies mentioned here. It is possible to build a model for the gas phase confined within a nanopore, by adjusting the thermodynamic conditions [290–292]. This model could pave the way for certain environmental challenges, such as storage of CO_2 and H_2 in geological formations. Investigating the molecular aspects of rock-CO_2 and rock-H_2 interactions is an essential study that can be conducted using similar techniques presented in this thesis.

A brief review indicates that the literature lacks sufficient attention to a molecular-based equation of state capable of quantifying and predicting the amount of required ions dissolved in low saline water injection [274, 293]. Given the ability of SAFT-based equations of state in modeling ionic solutions and the advances made to incorporate rock effects into confined fluid properties, it would be worth developing an SAFT-based equation of state for predicting the optimized quantity of ions required in low saline water[294–296].

3.5.2 Machine Learning: An Alternative to Molecular Dynamics

Molecular simulations like molecular dynamics provide high resolution data that allow the study of different processes at the nanoscale. However, their computational cost remains a challenge [297]. To address this challenge, neural network models can be executed along with MD simulations to learn the trend of molecular dynamics outcomes [298, 299]. Then, the trained network can be used to intra- and extrapolate for margins in which molecular dynamics data is not available. This approach has the potential to save time and cost.

3.5.3 Oil Displacement by Low-Salinity Water Injection

The thickness of the water film placed between the rock surface and the crude oil can determine the oil-wet or water-wet behavior of the rock [300]. A thick water film maintains water-wet conditions, whereas a thin film, prone to instability, may break, leading to the adsorption of polar oil components onto the rock surface. Additionally, the stability of the water film is influenced not only by its thickness but also by the disjoining pressure [301, 302]. Therefore, employing molecular dynamics to investigate the rock-oil-brine system with varying water film thicknesses while simultaneously monitoring the disjoining pressure would be a useful approach.

In our study, temperature displayed dual characteristics. On the one hand, temperature variations influenced the regime of oil detachment and the positioning of divalent ions. On the other hand, changes in temperature had minimal impact on the locations of Na^+ and Cl^- ions in the confined water layer. Further investigations across a broader temperature range are recommended to fully understand the influence of temperature on the efficiency of smart water injection.

Wettability alteration of the carbonate rocks in subsurface reservoirs is dictated by chemistry of mineral surface and interacting fluid both. Regardless of computational cost, it would be worth examining a rock-oil-brine system with different brines interacting with different mineral surfaces.

References

[1] Alvarez, P. J. et al. “Emerging opportunities for nanotechnology to enhance water security”. In: *Nature nanotechnology* vol. 13, no. 8 (2018), pp. 634–641.

[2] Ossai, I. C. et al. “Remediation of soil and water contaminated with petroleum hydrocarbon: A review”. In: *Environmental Technology & Innovation* vol. 17 (2020), p. 100526.

[3] Alley, W. M. et al. “Flow and storage in groundwater systems”. In: *science* vol. 296, no. 5575 (2002), pp. 1985–1990.

[4] Famiglietti, J. S. “The global groundwater crisis”. In: *Nature Climate Change* vol. 4, no. 11 (2014), pp. 945–948.

[5] Ozarslan, A. “Large-scale hydrogen energy storage in salt caverns”. In: *International journal of hydrogen energy* vol. 37, no. 19 (2012), pp. 14265–14277.

[6] Amid, A., Mignard, D., and Wilkinson, M. “Seasonal storage of hydrogen in a depleted natural gas reservoir”. In: *International journal of hydrogen energy* vol. 41, no. 12 (2016), pp. 5549–5558.

[7] Sáinz-García, A. et al. “Assessment of feasible strategies for seasonal underground hydrogen storage in a saline aquifer”. In: *International journal of hydrogen energy* vol. 42, no. 26 (2017), pp. 16657–16666.

[8] Matter, J. M. and Kelemen, P. B. “Permanent storage of carbon dioxide in geological reservoirs by mineral carbonation”. In: *Nature Geoscience* vol. 2, no. 12 (2009), pp. 837–841.

[9] Alcalde, J. et al. “Estimating geological CO2 storage security to deliver on climate mitigation”. In: *Nature communications* vol. 9, no. 1 (2018), p. 2201.

[10] Bocquet, L. and Barrat, J.-L. “Hydrodynamic boundary conditions and correlation functions of confined fluids”. In: *Physical review letters* vol. 70, no. 18 (1993), p. 2726.

[11] Agrawal, K. V. et al. “Observation of extreme phase transition temperatures of water confined inside isolated carbon nanotubes”. In: *Nature nanotechnology* vol. 12, no. 3 (2017), pp. 267–273.

[12] Prabhakar, S. and Melnik, R. “Wettability alteration of calcite oil wells: Influence of smart water ions”. In: *Scientific reports* vol. 7, no. 1 (2017), p. 17365.

[13] Ding, F. and Gao, M. “Pore wettability for enhanced oil recovery, contaminant adsorption and oil/water separation: A review”. In: *Advances in Colloid and Interface Science* vol. 289 (2021), p. 102377.

[14] Morse, J. W., Arvidson, R. S., and Lüttge, A. “Calcium carbonate formation and dissolution”. In: *Chemical reviews* vol. 107, no. 2 (2007), pp. 342–381.

[15] Amato, I. “Concrete solutions: Cement manufacturing is a major source of greenhouse gases. But cutting emissions means mastering one of the most complex materials known”. In: *Nature* vol. 494, no. 7437 (2013), pp. 300–302.

[16] Deer, W., Howie, R., and Zussman, J. “An introduction to the rock-forming minerals 2nd edn”. In: *Harlow: Longman Group Limited, London, UK* vol. 696 (1992).

[17] Aubert, M. et al. “Pleistocene cave art from Sulawesi, Indonesia”. In: *Nature* vol. 514, no. 7521 (2014), pp. 223–227.

[18] Hooke, S. “The early history of writing”. In: *Antiquity* vol. 11, no. 43 (1937), pp. 261–277.

[19] Diringer, D. *The book before printing: ancient, medieval and oriental*. Courier Corporation, 2013.

[20] Layard, A. H. *Nineveh and Babylon: A narrative of a second expedition to Assyria during the years 1849, 1850, & 1851*. J. Murray, 1874.

[21] Meldrum, F. “Calcium carbonate in biomineralisation and biomimetic chemistry”. In: *International Materials Reviews* vol. 48, no. 3 (2003), pp. 187–224.

[22] Seto, J. et al. “Structure-property relationships of a biological mesocrystal in the adult sea urchin spine”. In: *Proceedings of the National Academy of Sciences* vol. 109, no. 10 (2012), pp. 3699–3704.

[23] Checa, A. G. et al. “Origin of the biphase nature and surface roughness of biogenic calcite secreted by the giant barnacle Austromegabalanus psittacus”. In: *Scientific RepoRtS* vol. 10, no. 1 (2020), p. 16784.

[24] Mann, S. et al. “Crystallization at inorganic-organic interfaces: biominerals and biomimetic synthesis”. In: *Science* vol. 261, no. 5126 (1993), pp. 1286–1292.

[25] Stupp, S. I. and Braun, P. V. “Molecular manipulation of microstructures: biomaterials, ceramics, and semiconductors”. In: *Science* vol. 277, no. 5330 (1997), pp. 1242–1248.

[26] Li, L. and Ortiz, C. “Pervasive nanoscale deformation twinning as a catalyst for efficient energy dissipation in a bioceramic armour”. In: *Nature materials* vol. 13, no. 5 (2014), pp. 501–507.

[27] Claxton, L. et al. “Eocene emergence of highly calcifying coccolithophores despite declining atmospheric CO2”. In: *Nature Geoscience* vol. 15, no. 10 (2022), pp. 826–831.

[28] Ashby, M. F. et al. “The mechanical properties of natural materials. I. Material property charts”. In: *Proceedings of the Royal Society of London. Series A: Mathematical and Physical Sciences* vol. 450, no. 1938 (1995), pp. 123–140.

[29] Jackson, A., Vincent, J. F., and Turner, R. “The mechanical design of nacre”. In: *Proceedings of the Royal society of London. Series B. Biological sciences* vol. 234, no. 1277 (1988), pp. 415–440.

[30] Kim, Y.-Y. et al. “Tuning hardness in calcite by incorporation of amino acids”. In: *Nature materials* vol. 15, no. 8 (2016), pp. 903–910.

[31] Yang, W. et al. “Natural flexible dermal armor”. In: *Advanced Materials* vol. 25, no. 1 (2013), pp. 31–48.

[32] Owuamanam, S. and Cree, D. “Progress of bio-calcium carbonate waste eggshell and seashell fillers in polymer composites: a review”. In: *Journal of Composites Science* vol. 4, no. 2 (2020), p. 70.

[33] Long, X., Ma, Y., and Qi, L. “Biogenic and synthetic high magnesium calcite–A review”. In: *Journal of Structural Biology* vol. 185, no. 1 (2014), pp. 1–14.

[34] Maleki, S. et al. “Calcium carbonate nanoparticles; potential applications in bone and tooth disorders”. In: *Pharmaceutical Sciences* vol. 20, no. 4 (2015), pp. 175–182.

[35] Rodríguez-Sánchez, J. et al. “Setting behavior and bioactivity assessment of calcium carbonate cements”. In: *Journal of the American Ceramic Society* vol. 102, no. 11 (2019), pp. 6980–6990.

[36] Tanomaru-Filho, M. et al. “In vitro antimicrobial activity of endodontic sealers, MTA-based cements and Portland cement”. In: *Journal of Oral Science* vol. 49, no. 1 (2007), pp. 41–45.

[37] Braz, M. G. et al. “Evaluation of genetic damage in human peripheral lymphocytes exposed to mineral trioxide aggregate and Portland cements”. In: *Journal of oral rehabilitation* vol. 33, no. 3 (2006), pp. 234–239.

[38] Biradar, S. et al. “Calcium carbonate nanoparticles: synthesis, characterization and biocompatibility”. In: *Journal of Nanoscience and nanotechnology* vol. 11, no. 8 (2011), pp. 6868–6874.

[39] Juárez Broon, N. et al. “Healing of root perforations treated with Mineral Trioxide Aggregate (MTA) and Portland cement”. In: *Journal of Applied Oral Science* vol. 14 (2006), pp. 305–311.

[40] Ribeiro, D. A. et al. “Genotoxicity and cytotoxicity of mineral trioxide aggregate and regular and white Portland cements on Chinese hamster ovary (CHO) cells in vitro”. In: *Oral Surgery, Oral Medicine, Oral Pathology, Oral Radiology, and Endodontology* vol. 101, no. 2 (2006), pp. 258–261.

[41] Qian, K. et al. “Preparation and characterization of nano-sized calcium carbonate as controlled release pesticide carrier for validamycin against Rhizoctonia solani”. In: *Microchimica Acta* vol. 173 (2011), pp. 51–57.

[42] Shahi, S. et al. “Portland cement: an overview as a root repair material”. In: *BioMed Research International* vol. 2022 (2022).

[43] Zamanian, K., Pustovoytov, K., and Kuzyakov, Y. “Pedogenic carbonates: Forms and formation processes”. In: *Earth-Science Reviews* vol. 157 (2016), pp. 1–17.

[44] Groenendijk, D. J. and Wunnik, J. N. van. “The impact of micelle formation on surfactant adsorption–desorption”. In: *ACS omega* vol. 6, no. 3 (2021), pp. 2248–2254.

[45] Al Omari, M. et al. “Calcium carbonate”. In: *Profiles of drug substances, excipients and related methodology* vol. 41 (2016), pp. 31–132.

[46] Brunel, F. et al. “Elastic response of cementitious gels to polycation addition”. In: *ACS omega* vol. 2, no. 5 (2017), pp. 2148–2158.

[47] Matschei, T., Lothenbach, B., and Glasser, F. P. “The role of calcium carbonate in cement hydration”. In: *Cement and concrete research* vol. 37, no. 4 (2007), pp. 551–558.

[48] Zhou, F. et al. “Influence of CSH grown in situ on steel slag powder on the performance of fresh and hardened cement pastes”. In: *Construction and Building Materials* vol. 344 (2022), p. 128269.

[49] Kawashima, S. et al. “Modification of cement-based materials with nanoparticles”. In: *Cement and concrete composites* vol. 36 (2013), pp. 8–15.

[50] Zhou, Y. and Zhang, Z. “Effect of fineness on the pozzolanic reaction kinetics of slag in composite binders: Experiment and modelling”. In: *Construction and Building Materials* vol. 273 (2021), p. 121695.

[51] Joseph, S. and Cizer, Ö. “Hydration of hybrid cements at low temperatures: A study on portland cement-blast furnace slag—Na2SO4”. In: *Materials* vol. 15, no. 5 (2022), p. 1914.

[52] Li, X., Bizzozero, J., and Hesse, C. “Impact of CSH seeding on hydration and strength of slag blended cement”. In: *Cement and Concrete Research* vol. 161 (2022), p. 106935.

[53] Stocks-Fischer, S., Galinat, J. K., and Bang, S. S. “Microbiological precipitation of CaCO3”. In: *Soil Biology and Biochemistry* vol. 31, no. 11 (1999), pp. 1563–1571.

[54] Zehner, J., Røyne, A., and Sikorski, P. “A sample cell for the study of enzyme-induced carbonate precipitation at the grain-scale and its implications for biocementation”. In: *Scientific Reports* vol. 11, no. 1 (2021), p. 13675.

[55] Blakeley, R. L. and Zerner, B. “Jack bean urease: the first nickel enzyme”. In: *Journal of molecular catalysis* vol. 23, no. 2-3 (1984), pp. 263–292.

[56] Duxson, P. et al. “The role of inorganic polymer technology in the development of ‘green concrete’”. In: *cement and concrete research* vol. 37, no. 12 (2007), pp. 1590–1597.

[57] Machida, K. and Sakai, Y. “Development of novel construction material from Food Waste”. In: (2021).

[58] Gartner, E. “Industrially interesting approaches to “low-CO2” cements”. In: *Cement and Concrete research* vol. 34, no. 9 (2004), pp. 1489–1498.

[59] Komnitsas, K., Zaharaki, D., and Perdikatsis, V. “Geopolymerisation of low calcium ferronickel slags”. In: *Journal of Materials Science* vol. 42 (2007), pp. 3073–3082.

[60] Pacheco-Torgal, F., Castro-Gomes, J., and Jalali, S. “Investigations about the effect of aggregates on strength and microstructure of geopolymeric mine waste mud binders”. In: *Cement and Concrete Research* vol. 37, no. 6 (2007), pp. 933–941.

[61] Talal, A.-B. “The impact of water content and ionic diffusion on the uniaxial compressive strength of shale”. In: *Egyptian Journal of Petroleum* vol. 22, no. 2 (2013), pp. 249–260.

[62] Al-Saedi, H. N., Flori, R. E., and Brady, P. V. “Effect of divalent cations in formation water on wettability alteration during low salinity water flooding in sandstone reservoirs: Oil recovery analyses, surface reactivity tests, contact angle, and spontaneous imbibition experiments”. In: *Journal of Molecular Liquids* vol. 275 (2019), pp. 163–172.

[63] Dimri, V., Srivastava, R., and Vedanti, N. “Reservoir geophysics: Some basic concepts”. In: *Handbook of geophysical exploration: Seismic exploration*. Vol. 41. Elsevier, 2012, pp. 89–118.

[64] De Waele, J. and Gutiérrez, F. *Karst hydrogeology, geomorphology and caves*. John Wiley & Sons, 2022.

[65] Raza, A. et al. “Preliminary assessment of CO2 injectivity in carbonate storage sites”. In: *Petroleum* vol. 3, no. 1 (2017), pp. 144–154.

[66] Jitmahantakul, S. et al. “Dynamic estimates of pressure and CO2-storage capacity in carbonate reservoirs in a depleted gas field, northeastern Thailand”. In: *Case Studies in Chemical and Environmental Engineering* vol. 8 (2023), p. 100422.

[67] Akbar, M. et al. “A snapshot of carbonate reservoir evaluation”. In: *Oilfield review* vol. 12, no. 4 (2000), pp. 20–21.

[68] Marathe, R., Turner, M. L., and Fogden, A. “Pore-scale distribution of crude oil wettability in carbonate rocks”. In: *Energy & fuels* vol. 26, no. 10 (2012), pp. 6268–6281.

[69] Sadeq, Q. M. and Yusoff, W. I. B. W. “Porosity and permeability analysis from well logs and core in fracture, vugy and intercrystalline carbonate reservoirs”. In: *Journal of Aquaculture Research & Development* vol. 6, no. 10 (2015), p. 1.

[70] Lee, H., Lee, S. G., and Doyle, P. S. “Photopatterned oil-reservoir micromodels with tailored wetting properties”. In: *Lab on a Chip* vol. 15, no. 14 (2015), pp. 3047–3055.

[71] Gennaro, M. et al. “Characterization of dense zones within the Danian chalks of the Ekofisk Field, Norwegian North Sea”. In: *Petroleum Geoscience* vol. 19, no. 1 (2013), pp. 39–64.

[72] Derkani, M. H. et al. “Low salinity waterflooding in carbonate reservoirs: Review of interfacial mechanisms”. In: *Colloids and Interfaces* vol. 2, no. 2 (2018), p. 20.

[73] Xie, Y., Khishvand, M., and Piri, M. “Wettability of calcite surfaces: impacts of brine ionic composition and oil phase polarity at elevated temperature and pressure conditions”. In: *Langmuir* vol. 36, no. 22 (2020), pp. 6079–6088.

[74] Badizad, M. H. et al. “Atomistic insight into the behavior of ions at an oil-bearing hydrated calcite surface: implication to ion-engineered waterflooding”. In: *Energy & Fuels* vol. 35, no. 16 (2021), pp. 13039–13054.

[75] Sagbana, P. I., Sarkodie, K., and Nkrumah, W. A. “A critical review of carbonate reservoir wettability modification during low salinity waterflooding”. In: *Petroleum* (2022).

[76] Van Cappellen, P. et al. “A surface complexation model of the carbonate mineral-aqueous solution interface”. In: *Geochimica et Cosmochimica Acta* vol. 57, no. 15 (1993), pp. 3505–3518.

[77] Shi, X., Rosa, R., and Lazzeri, A. “On the coating of precipitated calcium carbonate with stearic acid in aqueous medium”. In: *Langmuir* vol. 26, no. 11 (2010), pp. 8474–8482.

[78] Hakim, S. et al. “Interactions of the calcite {10.4} surface with organic compounds: structure and behaviour at mineral–organic interfaces”. In: *Scientific reports* vol. 7, no. 1 (2017), p. 7592.

[79] Ruiz-Lopez, M. F. et al. “Molecular reactions at aqueous interfaces”. In: *Nature Reviews Chemistry* vol. 4, no. 9 (2020), pp. 459–475.

[80] Ji, Y. et al. “Transition From Slow to Fast Injection-Induced Slip of an Experimental Fault in Granite Promoted by Elevated Temperature”. In: *Geophysical Research Letters* vol. 49, no. 23 (2022), e2022GL101212.

[81] Ji, Y., Wanniarachchi, W. A. M., and Wu, W. “Effect of fluid pressure heterogeneity on injection-induced fracture activation”. In: *Computers and Geotechnics* vol. 123 (2020), p. 103589.

[82] Minde, M. W. and Hiorth, A. “Compaction and fluid—Rock interaction in chalk insight from modelling and data at pore-, core-, and field-scale”. In: *Geosciences* vol. 10, no. 1 (2019), p. 6.

[83] Cai, X. et al. “Water-weakening effects on the mechanical behavior of different rock types: phenomena and mechanisms”. In: *Applied Sciences* vol. 9, no. 20 (2019), p. 4450.

[84] Geremia, D. et al. “An integrated study of water weakening and fluid rock interaction processes in porous rocks: linking mechanical behavior to surface properties”. In: *Applied Sciences* vol. 11, no. 23 (2021), p. 11437.

[85] Hosseinzadehsadati, S. et al. “Thermo-hydro-mechanical-chemical coupling in chalk reservoirs: Impact on fluid flow and deformation during water injection”. In: *International Journal of Rock Mechanics and Mining Sciences* vol. 170 (2023), p. 105514.

[86] Croize, D., Renard, F., and Gratier, J.-P. “Compaction and porosity reduction in carbonates: A review of observations, theory, and experiments”. In: *Advances in geophysics* vol. 54 (2013), pp. 181–238.

[87] Javadi, S. “Interaction between two calcite surfaces in aqueous solutions: Study of nano-scale interfacial forces using AFM and SFA”. In: (2019).

[88] Eyinla, D. S. et al. “A comprehensive review of the potential of rock properties alteration during CO2 injection for EOR and storage”. In: *Fuel* vol. 353 (2023), p. 129219.

[89] Kibikas, W. M. et al. “Water-Weakening and Time-Dependent Deformation of Organic-Rich Chalks”. In: *Rock Mechanics and Rock Engineering* (2023), pp. 1–19.

[90] Wojas, N. A. et al. “Nanoscale Wear and mechanical properties of calcite: effects of stearic acid modification and water vapor”. In: *Langmuir* vol. 37, no. 32 (2021), pp. 9826–9837.

[91] Gomari, K. R. and Hamouda, A. “Effect of fatty acids, water composition and pH on the wettability alteration of calcite surface”. In: *Journal of petroleum science and engineering* vol. 50, no. 2 (2006), pp. 140–150.

[92] Karimi, M. et al. “Mechanistic study of wettability alteration of oil-wet calcite: The effect of magnesium ions in the presence and absence of cationic surfactant”. In: *Colloids and Surfaces A: Physicochemical and Engineering Aspects* vol. 482 (2015), pp. 403–415.

[93] Sauerer, B. et al. “Quantifying mineral surface energy by scanning force microscopy”. In: *Journal of colloid and interface science* vol. 472 (2016), pp. 237–246.

[94] Henderson, M. A. “The interaction of water with solid surfaces: fundamental aspects revisited”. In: *Surface Science Reports* vol. 46, no. 1-8 (2002), pp. 1–308.

[95] Carrasco, J., Hodgson, A., and Michaelides, A. “A molecular perspective of water at metal interfaces”. In: *Nature materials* vol. 11, no. 8 (2012), pp. 667–674.

[96] Pitakbunkate, T. et al. “Effect of confinement on pressure/volume/temperature properties of hydrocarbons in shale reservoirs”. In: *Spe Journal* vol. 21, no. 02 (2016), pp. 621–634.

[97] Pathak, M., Cho, H., and Deo, M. “Experimental and molecular modeling study of bubble points of hydrocarbon mixtures in nanoporous media”. In: *Energy & Fuels* vol. 31, no. 4 (2017), pp. 3427–3435.

[98] Knight, A. W. et al. “Water properties under nano-scale confinement”. In: *Scientific reports* vol. 9, no. 1 (2019), p. 8246.

[99] Xu, L. et al. “Wetting and capillary phenomena of water on mica”. In: *The Journal of Physical Chemistry B* vol. 102, no. 3 (1998), pp. 540–548.

[100] Miranda, P. et al. “Icelike water monolayer adsorbed on mica at room temperature”. In: *Physical review letters* vol. 81, no. 26 (1998), p. 5876.

[101] Hu, J. et al. “Imaging the condensation and evaporation of molecularly thin films of water with nanometer resolution”. In: *Science* vol. 268, no. 5208 (1995), pp. 267–269.

[102] Wu, Q. et al. “Effect of Mineral Surface Properties on Water Behaviors in Pores Constructed by Calcite and Silica Particles”. In: *The Journal of Physical Chemistry C* vol. 123, no. 21 (2019), pp. 13288–13294.

[103] Ruiz-Agudo, E. et al. “The role of background electrolytes on the kinetics and mechanism of calcite dissolution”. In: *Geochimica et cosmochimica acta* vol. 74, no. 4 (2010), pp. 1256–1267.

[104] Putnis, C. V. and Ruiz-Agudo, E. “The mineral–water interface: where minerals react with the environment”. In: *Elements* vol. 9, no. 3 (2013), pp. 177–182.

[105] Li, L. et al. “Growth of calcite in confinement”. In: *Crystals* vol. 7, no. 12 (2017), p. 361.

[106] Guren, M. G. et al. “Direct imaging of coupled dissolution-precipitation and growth processes on calcite exposed to chromium-rich fluids”. In: *Chemical Geology* vol. 552 (2020), p. 119770.

[107] Julia, M. et al. “Coupled dissolution-precipitation and growth processes on calcite, aragonite, and Carrara marble exposed to cadmium-rich aqueous solutions”. In: *Chemical Geology* vol. 621 (2023), p. 121364.

[108] Dziadkowiec, J. et al. “Ca2+ Ions Decrease Adhesion between Two (104) Calcite Surfaces as Probed by Atomic Force Microscopy”. In: *ACS Earth and Space Chemistry* vol. 5, no. 10 (2021), pp. 2827–2838.

[109] Thiel, P. A. and Madey, T. E. “The interaction of water with solid surfaces: Fundamental aspects”. In: *Surface Science Reports* vol. 7, no. 6-8 (1987), pp. 211–385.

[110] Hodgson, A. and Haq, S. “Water adsorption and the wetting of metal surfaces”. In: *Surface science reports* vol. 64, no. 9 (2009), pp. 381–451.

[111] Jinesh, K. and Frenken, J. “Experimental evidence for ice formation at room temperature”. In: *Physical review letters* vol. 101, no. 3 (2008), p. 036101.

[112] Verdaguer, A. et al. “Molecular structure of water at interfaces: Wetting at the nanometer scale”. In: *Chemical reviews* vol. 106, no. 4 (2006), pp. 1478–1510.

[113] Bampoulis, P. et al. “Water confined in two-dimensions: Fundamentals and applications”. In: *Surface Science Reports* vol. 73, no. 6 (2018), pp. 233–264.

[114] Langmuir, I. “The constitution and fundamental properties of solids and liquids. Part I. Solids.” In: *Journal of the American chemical society* vol. 38, no. 11 (1916), pp. 2221–2295.

[115] Freundlich, H. “Über die adsorption in lösungen”. In: *Zeitschrift für physikalische Chemie* vol. 57, no. 1 (1907), pp. 385–470.

[116] Brunauer, S., Emmett, P. H., and Teller, E. “Adsorption of gases in multimolecular layers”. In: *Journal of the American chemical society* vol. 60, no. 2 (1938), pp. 309–319.

[117] Schoonen, C. and Lutsko, J. F. “Using classical density functional theory to determine crystal-fluid surface tensions”. In: *Physical Review E* vol. 106, no. 6 (2022), p. 064110.

[118] Pizio, O. and Sokołowski, S. “Effects of fluid–solid interaction strength on wetting of graphite-like substrates by water: density functional theory”. In: *Molecular Physics* vol. 120, no. 6 (2022), e2011454.

[119] Frenkel, D., Smit, B., and Ratner, M. A. *Understanding molecular simulation: from algorithms to applications*. Vol. 2. Academic press San Diego, 1996.

[120] Zeitler, T. et al. “Molecular dynamics simulation of resin adsorption at kaolinite edge sites: Effect of surface deprotonation on interfacial structure”. In: *The Journal of Physical Chemistry C* vol. 121, no. 41 (2017), pp. 22787–22796.

[121] Mehana, M. et al. “Molecular simulation of double layer expansion mechanism during low-salinity waterflooding”. In: *Journal of Molecular Liquids* vol. 318 (2020), p. 114079.

[122] Sui, H. et al. “Molecular simulations of oil adsorption and transport behavior in inorganic shale”. In: *Journal of Molecular Liquids* vol. 305 (2020), p. 112745.

[123] De Leeuw, N., Parker, S., and Rao, K. H. “Modeling the competitive adsorption of water and methanoic acid on calcite and fluorite surfaces”. In: *Langmuir* vol. 14, no. 20 (1998), pp. 5900–5906.

[124] Kerisit, S. and Parker, S. C. “Free energy of adsorption of water and metal ions on the {1014} calcite surface”. In: *Journal of the American Chemical Society* vol. 126, no. 32 (2004), pp. 10152–10161.

[125] Rahaman, A., Grassian, V. H., and Margulis, C. J. "Dynamics of water adsorption onto a calcite surface as a function of relative humidity". In: *The Journal of Physical Chemistry C* vol. 112, no. 6 (2008), pp. 2109–2115.

[126] Wolthers, M. et al. "Calcite surface structure and reactivity: molecular dynamics simulations and macroscopic surface modelling of the calcite–water interface". In: *Physical Chemistry Chemical Physics* vol. 14, no. 43 (2012), pp. 15145–15157.

[127] Brekke-Svaland, G. and Bresme, F. "Interactions between hydrated calcium carbonate surfaces at nanoconfinement conditions". In: *The Journal of Physical Chemistry C* vol. 122, no. 13 (2018), pp. 7321–7330.

[128] Plimpton, S. "Fast parallel algorithms for short-range molecular dynamics". In: *Journal of computational physics* vol. 117, no. 1 (1995), pp. 1–19.

[129] Zhang, W. et al. "Molecular simulation study of oil-water two-phase fluid transport in shale inorganic nanopores". In: *Chemical Engineering Science* vol. 245 (2021), p. 116948.

[130] Sedghi, M., Piri, M., and Goual, L. "Atomistic molecular dynamics simulations of crude oil/brine displacement in calcite mesopores". In: *Langmuir* vol. 32, no. 14 (2016), pp. 3375–3384.

[131] Parvulescu, V. I. et al. "Recent progress and prospects in catalytic water treatment". In: *Chemical Reviews* vol. 122, no. 3 (2021), pp. 2981–3121.

[132] Farias, M. B. de, Prediger, P., and Vieira, M. G. A. "Conventional and green-synthesized nanomaterials applied for the adsorption and/or degradation of phenol: A recent overview". In: *Journal of Cleaner Production* (2022), p. 132980.

[133] Elsaid, K. et al. "Membrane processes for environmental remediation of nanomaterials: Potentials and challenges". In: *Science of The Total Environment* vol. 879 (2023), p. 162569.

[134] Ruiz Pestana, L., Felberg, L. E., and Head-Gordon, T. "Coexistence of multilayered phases of confined water: the importance of flexible confining surfaces". In: *ACS nano* vol. 12, no. 1 (2018), pp. 448–454.

[135] Arif, M. et al. "X-ray tomography imaging of shale microstructures: A review in the context of multiscale correlative imaging". In: *International journal of coal geology* vol. 233 (2021), p. 103641.

[136] Putnis, C. V. et al. "Crystallization via Nonclassical Pathways: Nanoscale Imaging of Mineral Surfaces". In: *Crystallization via Nonclassical Pathways Volume 2: Aggregation, Biomineralization, Imaging & Application*. ACS Publications, 2021, pp. 1–35.

[137] Cui, W. and Chen, J. "Insight into mineral flotation fundamentals through the DFT method". In: *International Journal of Mining Science and Technology* vol. 31, no. 6 (2021), pp. 983–994.

[138] Kiselev, A. et al. “Active sites in heterogeneous ice nucleation—the example of K-rich feldspars”. In: *Science* vol. 355, no. 6323 (2017), pp. 367–371.

[139] Backus, E. H., Schaefer, J., and Bonn, M. “Probing the mineral–water interface with nonlinear optical spectroscopy”. In: *Angewandte Chemie International Edition* vol. 60, no. 19 (2021), pp. 10482–10501.

[140] Noiriel, C. and Soulaine, C. “Pore-scale imaging and modelling of reactive flow in evolving porous media: Tracking the dynamics of the fluid–rock interface”. In: *Transport in Porous Media* vol. 140, no. 1 (2021), pp. 181–213.

[141] Martin, J. J. “Cubic equations of state-which?” In: *Industrial & Engineering Chemistry Fundamentals* vol. 18, no. 2 (1979), pp. 81–97.

[142] Kiselev, S. “Cubic crossover equation of state”. In: *Fluid Phase Equilibria* vol. 147, no. 1-2 (1998), pp. 7–23.

[143] Kiselev, S. and Friend, D. G. “Cubic crossover equation of state for mixtures”. In: *Fluid Phase Equilibria* vol. 162, no. 1-2 (1999), pp. 51–82.

[144] Gibbons, R. M. and Laughton, A. P. “An equation of state for polar and non-polar substances and mixtures”. In: *Journal of the Chemical Society, Faraday Transactions 2: Molecular and Chemical Physics* vol. 80, no. 9 (1984), pp. 1019–1038.

[145] Trebble, M. and Bishnoi, P. “Accuracy and consistency comparisons of ten cubic equations of state for polar and non-polar compounds”. In: *Fluid Phase Equilibria* vol. 29 (1986), pp. 465–474.

[146] Valderrama, J. O. “The state of the cubic equations of state”. In: *Industrial & engineering chemistry research* vol. 42, no. 8 (2003), pp. 1603–1618.

[147] Kontogeorgis, G. M. and Folas, G. K. *Thermodynamic models for industrial applications: from classical and advanced mixing rules to association theories*. John Wiley & Sons, 2009.

[148] Kac, M., Uhlenbeck, G., and Hemmer, P. “On the van der Waals Theory of the Vapor-Liquid Equilibrium. I. Discussion of a One-Dimensional Model”. In: *Journal of Mathematical Physics* vol. 4, no. 2 (1963), pp. 216–228.

[149] Chandler, D., Weeks, J. D., and Andersen, H. C. “Van der Waals picture of liquids, solids, and phase transformations”. In: *Science* vol. 220, no. 4599 (1983), pp. 787–794.

[150] Jog, P. K. et al. “Application of dipolar chain theory to the phase behavior of polar fluids and mixtures”. In: *Industrial & engineering chemistry research* vol. 40, no. 21 (2001), pp. 4641–4648.

[151] Patel, B. H. et al. “Prediction of the salting-out effect of strong electrolytes on water+ alkane solutions”. In: *Industrial & engineering chemistry research* vol. 42, no. 16 (2003), pp. 3809–3823.

[152] Huynh, D. N. et al. “Application of GC-SAFT EOS to polycyclic aromatic hydrocarbons”. In: *Fluid phase equilibria* vol. 254, no. 1-2 (2007), pp. 60–66.

[153] Lymperiadis, A. et al. “A group contribution method for associating chain molecules based on the statistical associating fluid theory (SAFT-γ)”. In: *The Journal of chemical physics* vol. 127, no. 23 (2007).

[154] Patel, N. C. and Teja, A. S. “A new cubic equation of state for fluids and fluid mixtures”. In: *Chemical Engineering Science* vol. 37, no. 3 (1982), pp. 463–473.

[155] Wei, Y. S. and Sadus, R. J. “Equations of state for the calculation of fluid-phase equilibria”. In: *AIChE journal* vol. 46, no. 1 (2000), pp. 169–196.

[156] Brignole, E. and Pereda, S. “Phase Equilibrium Diagrams”. In: *Supercritical Fluid Science and Technology*. Vol. 3. Elsevier, 2013, pp. 33–56.

[157] Van der Waals, J. “On the continuity of the gases and liquid state”. In: *Doctoral Dissertation, Leiden University* (1873).

[158] Van Konynenburg, P. and Scott, R. “Critical lines and phase equilibria in binary van der Waals mixtures”. In: *Philosophical Transactions of the Royal Society of London. Series A, Mathematical and Physical Sciences* vol. 298, no. 1442 (1980), pp. 495–540.

[159] Redlich, O. and Kwong, J. N. “On the thermodynamics of solutions. V. An equation of state. Fugacities of gaseous solutions.” In: *Chemical reviews* vol. 44, no. 1 (1949), pp. 233–244.

[160] Soave, G. “Equilibrium constants from a modified Redlich-Kwong equation of state”. In: *Chemical engineering science* vol. 27, no. 6 (1972), pp. 1197–1203.

[161] Peng, D.-Y. and Robinson, D. B. “A new two-constant equation of state”. In: *Industrial & Engineering Chemistry Fundamentals* vol. 15, no. 1 (1976), pp. 59–64.

[162] Reiss, H., Frisch, H., and Lebowitz, J. “Statistical mechanics of rigid spheres”. In: *The Journal of Chemical Physics* vol. 31, no. 2 (1959), pp. 369–380.

[163] Thiele, E. “Equation of state for hard spheres”. In: *The Journal of Chemical Physics* vol. 39, no. 2 (1963), pp. 474–479.

[164] Carnahan, N. F. and Starling, K. E. “Equation of state for nonattracting rigid spheres”. In: *The Journal of chemical physics* vol. 51, no. 2 (1969), pp. 635–636.

[165] Carnahan, N. F. and Starling, K. E. “Intermolecular repulsions and the equation of state for fluids”. In: *AIChE Journal* vol. 18, no. 6 (1972), pp. 1184–1189.

[166] Chen, S. S. and Kreglewski, A. “Applications of the augmented van der Waals theory of fluids.: I. Pure fluids”. In: *Berichte der Bunsengesellschaft für physikalische Chemie* vol. 81, no. 10 (1977), pp. 1048–1052.

[167] Christoforakos, M. and Franck, E. “An equation of state for binary fluid mixtures to high temperatures and high pressures”. In: *Berichte der Bunsengesellschaft für physikalische Chemie* vol. 90, no. 9 (1986), pp. 780–789.

[168] Heilig, M. and Franck, E. “Calculation of thermodynamic properties of binary fluid mixtures to high temperatures and high pressures”. In: *Berichte der Bunsengesellschaft für physikalische Chemie* vol. 93, no. 8 (1989), pp. 898–905.

[169] Heilig, M. and Franck, E. “Phase equilibria of multicomponent fluid systems to high pressures and temperatures”. In: *Berichte der Bunsengesellschaft für physikalische Chemie* vol. 94, no. 1 (1990), pp. 27–35.

[170] Crespo, E. A. and Coutinho, J. A. “A statistical associating fluid theory perspective of the modeling of compounds containing ethylene oxide groups”. In: *Industrial & Engineering Chemistry Research* vol. 58, no. 9 (2019), pp. 3562–3582.

[171] Carnahan, N. F. and Starling, K. E. “Thermodynamic properties of a rigid-sphere fluid”. In: *The Journal of Chemical Physics* vol. 53, no. 2 (1970), pp. 600–603.

[172] Müller, E. A. and Gubbins, K. E. “Molecular-based equations of state for associating fluids: A review of SAFT and related approaches”. In: *Industrial & engineering chemistry research* vol. 40, no. 10 (2001), pp. 2193–2211.

[173] Kovalenko, A. and Hirata, F. “First-principles realization of a van der Waals–Maxwell theory for water”. In: *Chemical physics letters* vol. 349, no. 5-6 (2001), pp. 496–502.

[174] Economou, I. G. “Statistical associating fluid theory: A successful model for the calculation of thermodynamic and phase equilibrium properties of complex fluid mixtures”. In: *Industrial & engineering chemistry research* vol. 41, no. 5 (2002), pp. 953–962.

[175] Buckingham, A., Del Bene, J., and McDowell, S. “The hydrogen bond”. In: *Chemical Physics Letters* vol. 463, no. 1-3 (2008), pp. 1–10.

[176] Kontogeorgis, G. M. et al. “Ten years with the CPA (Cubic-Plus-Association) equation of state. Part 1. Pure compounds and self-associating systems”. In: *Industrial & engineering chemistry research* vol. 45, no. 14 (2006), pp. 4855–4868.

[177] Lopez-Echeverry, J. S., Reif-Acherman, S., and Araujo-Lopez, E. “Peng-Robinson equation of state: 40 years through cubics”. In: *Fluid Phase Equilibria* vol. 447 (2017), pp. 39–71.

[178] Wong, D. S. H. and Sandler, S. I. "A theoretically correct mixing rule for cubic equations of state". In: *AIChE Journal* vol. 38, no. 5 (1992), pp. 671–680.

[179] Twu, C. H. et al. "A cubic equation of state with a new alpha function and a new mixing rule". In: *Fluid Phase Equilibria* vol. 69 (1991), pp. 33–50.

[180] Knudsen, K., Stenby, E., and Fredenslund, A. "A comprehensive comparison of mixing rules for calculation of phase equilibria in complex systems". In: *Fluid Phase Equilibria* vol. 82 (1993), pp. 361–368.

[181] Yarrison, M. and Chapman, W. G. "A systematic study of methanol+ n-alkane vapor–liquid and liquid–liquid equilibria using the CK-SAFT and PC-SAFT equations of state". In: *Fluid phase equilibria* vol. 226 (2004), pp. 195–205.

[182] Jackson, G., Chapman, W. G., and Gubbins, K. E. "Phase equilibria of associating fluids: Spherical molecules with multiple bonding sites". In: *Molecular Physics* vol. 65, no. 1 (1988), pp. 1–31.

[183] Chapman, W. G., Jackson, G., and Gubbins, K. E. "Phase equilibria of associating fluids: chain molecules with multiple bonding sites". In: *Molecular Physics* vol. 65, no. 5 (1988), pp. 1057–1079.

[184] Chapman, W. G. et al. "SAFT: Equation-of-state solution model for associating fluids". In: *Fluid Phase Equilibria* vol. 52 (1989), pp. 31–38.

[185] Chapman, W. G. et al. "New reference equation of state for associating liquids". In: *Industrial & engineering chemistry research* vol. 29, no. 8 (1990), pp. 1709–1721.

[186] Wertheim, M. S. "Fluids with highly directional attractive forces. I. Statistical thermodynamics". In: *Journal of statistical physics* vol. 35, no. 1-2 (1984), pp. 19–34.

[187] Wertheim, M. S. "Fluids with highly directional attractive forces. II. Thermodynamic perturbation theory and integral equations". In: *Journal of statistical physics* vol. 35, no. 1-2 (1984), pp. 35–47.

[188] Wertheim, M. "Fluids with highly directional attractive forces. III. Multiple attraction sites". In: *Journal of statistical physics* vol. 42, no. 3-4 (1986), pp. 459–476.

[189] Wertheim, M. "Fluids with highly directional attractive forces. IV. Equilibrium polymerization". In: *Journal of statistical physics* vol. 42, no. 3-4 (1986), pp. 477–492.

[190] Tumakaka, F., Gross, J., and Sadowski, G. "Thermodynamic modeling of complex systems using PC-SAFT". In: *Fluid Phase Equilibria* vol. 228 (2005), pp. 89–98.

[191] Gross, J. and Sadowski, G. "Application of perturbation theory to a hard-chain reference fluid: an equation of state for square-well chains". In: *Fluid Phase Equilibria* vol. 168, no. 2 (2000), pp. 183–199.

[192] Wolbach, J. P. and Sandler, S. I. “Using molecular orbital calculations to describe the phase behavior of cross-associating mixtures”. In: *Industrial & engineering chemistry research* vol. 37, no. 8 (1998), pp. 2917–2928.

[193] Goltapeh, S. A. et al. “Extension of SAFT equation of state for fluids confined in nano-pores of sedimentary rocks using molecular dynamic simulation”. In: *Journal of Molecular Liquids* vol. 348 (2022), p. 118045.

[194] Sandler, S. I. “The generalized van der Waals partition function. I. Basic theory”. In: *Fluid Phase Equilibria* vol. 19, no. 3 (1985), pp. 238–257.

[195] Lee, K.-H., Lombardo, M., and Sandler, S. “The generalized van der Waals partition function. II. Application to the square-well fluid”. In: *Fluid Phase Equilibria* vol. 21, no. 3 (1985), pp. 177–196.

[196] Gross, J. and Sadowski, G. “Perturbed-chain SAFT: An equation of state based on a perturbation theory for chain molecules”. In: *Industrial & engineering chemistry research* vol. 40, no. 4 (2001), pp. 1244–1260.

[197] Gross, J. and Sadowski, G. “Modeling polymer systems using the perturbed-chain statistical associating fluid theory equation of state”. In: *Industrial & engineering chemistry research* vol. 41, no. 5 (2002), pp. 1084–1093.

[198] Barker, J. A. and Henderson, D. “Perturbation theory and equation of state for fluids: the square-well potential”. In: *The Journal of Chemical Physics* vol. 47, no. 8 (1967), pp. 2856–2861.

[199] Barker, J. A. and Henderson, D. “Perturbation theory and equation of state for fluids. II. A successful theory of liquids”. In: *The Journal of chemical physics* vol. 47, no. 11 (1967), pp. 4714–4721.

[200] Cameretti, L. F., Sadowski, G., and Mollerup, J. M. “Modeling of aqueous electrolyte solutions with perturbed-chain statistical associated fluid theory”. In: *Industrial & engineering chemistry research* vol. 44, no. 9 (2005), pp. 3355–3362.

[201] Goltapeh, S. A. et al. “Extension of PC-SAFT equation of state to include mineral surface effect in fluid properties using molecular dynamic simulation”. In: *Sustainable Energy Technologies and Assessments* vol. 48 (2021), p. 101624.

[202] Travalloni, L. et al. “Thermodynamic modeling of confined fluids using an extension of the generalized van der Waals theory”. In: *Chemical Engineering Science* vol. 65, no. 10 (2010), pp. 3088–3099.

[203] Travalloni, L., Castier, M., and Tavares, F. W. “Phase equilibrium of fluids confined in porous media from an extended Peng–Robinson equation of state”. In: *Fluid Phase Equilibria* vol. 362 (2014), pp. 335–341.

[204] Born, M. and Oppenheimer, R. “Zur quantentheorie der molekeln”. In: *Annalen der physik* vol. 389, no. 20 (1927), pp. 457–484.

[205] Smith, W. and Forester, T. “DL_POLY_2. 0: A general-purpose parallel molecular dynamics simulation package”. In: *Journal of molecular graphics* vol. 14, no. 3 (1996), pp. 136–141.

[206] Todorov, I. T. et al. “DL_POLY_3: new dimensions in molecular dynamics simulations via massive parallelism”. In: *Journal of Materials Chemistry* vol. 16, no. 20 (2006), pp. 1911–1918.

[207] Van Der Spoel, D. et al. “GROMACS: fast, flexible, and free”. In: *Journal of computational chemistry* vol. 26, no. 16 (2005), pp. 1701–1718.

[208] Hess, B. et al. “GROMACS 4: algorithms for highly efficient, load-balanced, and scalable molecular simulation”. In: *Journal of chemical theory and computation* vol. 4, no. 3 (2008), pp. 435–447.

[209] Pronk, S. et al. “GROMACS 4.5: a high-throughput and highly parallel open source molecular simulation toolkit”. In: *Bioinformatics* vol. 29, no. 7 (2013), pp. 845–854.

[210] Matsumoto, M., Saito, S., and Ohmine, I. “Molecular dynamics simulation of the ice nucleation and growth process leading to water freezing”. In: *Nature* vol. 416, no. 6879 (2002), pp. 409–413.

[211] Karplus, M. and McCammon, J. A. “Molecular dynamics simulations of biomolecules”. In: *Nature structural biology* vol. 9, no. 9 (2002), pp. 646–652.

[212] Karplus, M. and Petsko, G. A. “Molecular dynamics simulations in biology”. In: *Nature* vol. 347, no. 6294 (1990), pp. 631–639.

[213] Ghasemi, M., Shafiei, A., and Foroozesh, J. “A systematic and critical review of application of molecular dynamics simulation in low salinity water injection”. In: *Advances in Colloid and Interface Science* vol. 300 (2022), p. 102594.

[214] Rapaport, D. C. *The art of molecular dynamics simulation*. Cambridge university press, 2004.

[215] Brooks, B. R. et al. “CHARMM: a program for macromolecular energy, minimization, and dynamics calculations”. In: *Journal of computational chemistry* vol. 4, no. 2 (1983), pp. 187–217.

[216] Sikorska, C. and Gaston, N. “Modified Lennard-Jones potentials for nanoscale atoms”. In: *Journal of Computational Chemistry* vol. 41, no. 22 (2020), pp. 1985–2000.

[217] Verlet, L. “Computer" experiments" on classical fluids. I. Thermodynamical properties of Lennard-Jones molecules”. In: *Physical review* vol. 159, no. 1 (1967), p. 98.

[218] Frenkel, D. and Smit, B. *Understanding molecular simulation: from algorithms to applications*. Elsevier, 2023.

[219] Allen, M. P. and Tildesley, D. J. *Computer simulation of liquids*. Oxford university press, 2017.

[220] Kadau, K., Germann, T. C., and Lomdahl, P. S. “Large-scale molecular-dynamics simulation of 19 billion particles”. In: *International Journal of Modern Physics C* vol. 15, no. 01 (2004), pp. 193–201.

[221] McGaughey, A. J. and Kaviany, M. “Phonon transport in molecular dynamics simulations: formulation and thermal conductivity prediction”. In: *Advances in heat transfer* vol. 39 (2006), pp. 169–255.

[222] Dittmer, R. et al. “Ergodicity reflected in macroscopic and microscopic field-dependent behavior of BNT-based relaxors”. In: *Journal of Applied Physics* vol. 115, no. 8 (2014).

[223] Coveney, P. V. and Wan, S. “On the calculation of equilibrium thermodynamic properties from molecular dynamics”. In: *Physical Chemistry Chemical Physics* vol. 18, no. 44 (2016), pp. 30236–30240.

[224] Woodcock, L.-V. “Isothermal molecular dynamics calculations for liquid salts”. In: *Chemical Physics Letters* vol. 10, no. 3 (1971), pp. 257–261.

[225] Abraham, F. F., Koch, S., and Desai, R. C. “Computer-simulation dynamics of an unstable two-dimensional fluid: time-dependent morphology and scaling”. In: *Physical Review Letters* vol. 49, no. 13 (1982), p. 923.

[226] Schneider, T. and Stoll, E. “Molecular-dynamics study of structural-phase transitions. I. One-component displacement models”. In: *Physical Review B* vol. 13, no. 3 (1976), p. 1216.

[227] Nosé, S. “A unified formulation of the constant temperature molecular dynamics methods”. In: *The Journal of chemical physics* vol. 81, no. 1 (1984), pp. 511–519.

[228] Hoover, W. G. “Canonical dynamics: Equilibrium phase-space distributions”. In: *Physical review A* vol. 31, no. 3 (1985), p. 1695.

[229] Rafii-Tabar, H. “Modelling the nano-scale phenomena in condensed matter physics via computer-based numerical simulations”. In: *Physics reports* vol. 325, no. 6 (2000), pp. 239–310.

[230] Levine, B. G., Stone, J. E., and Kohlmeyer, A. “Fast analysis of molecular dynamics trajectories with graphics processing units—Radial distribution function histogramming”. In: *Journal of computational physics* vol. 230, no. 9 (2011), pp. 3556–3569.

[231] Lyubartsev, A. P. and Laaksonen, A. “Calculation of effective interaction potentials from radial distribution functions: A reverse Monte Carlo approach”. In: *Physical Review E* vol. 52, no. 4 (1995), p. 3730.

[232] Li, F. and Lannin, J. S. “Radial distribution function of amorphous carbon”. In: *Physical review letters* vol. 65, no. 15 (1990), p. 1905.

[233] Zhang, L. and Greenfield, M. L. “Molecular orientation in model asphalts using molecular simulation”. In: *Energy & fuels* vol. 21, no. 2 (2007), pp. 1102–1111.

[234] Levitt, M. “Protein folding by restrained energy minimization and molecular dynamics”. In: *Journal of molecular biology* vol. 170, no. 3 (1983), pp. 723–764.

[235] Kresse, G. and Hafner, J. “Ab initio molecular dynamics for liquid metals”. In: *Physical review B* vol. 47, no. 1 (1993), p. 558.

[236] Payne, M. C. et al. “Iterative minimization techniques for ab initio total-energy calculations: molecular dynamics and conjugate gradients”. In: *Reviews of modern physics* vol. 64, no. 4 (1992), p. 1045.

[237] Kresse, G. and Hafner, J. “Ab initio molecular-dynamics simulation of the liquid-metal–amorphous-semiconductor transition in germanium”. In: *Physical Review B* vol. 49, no. 20 (1994), p. 14251.

[238] Bragg, W. L. “The analysis of crystals by the X-ray spectrometer”. In: *Proceedings of the Royal Society of London. Series A, Containing Papers of a Mathematical and Physical Character* vol. 89, no. 613 (1914), pp. 468–489.

[239] Markgraf, S. A. and Reeder, R. J. “High-temperature structure refinements of calcite and magnesite”. In: *American Mineralogist* vol. 70, no. 5-6 (1985), pp. 590–600.

[240] Luo, C., Yang, X., and Li, J. “Mechanical Properties of Single-Crystal Calcite and Their Temperature and Strain-Rate Effects”. In: *Materials* vol. 15, no. 13 (2022), p. 4613.

[241] Ohnesorge, F. and Binnig, G. “True atomic resolution by atomic force microscopy through repulsive and attractive forces”. In: *Science* vol. 260, no. 5113 (1993), pp. 1451–1456.

[242] Didymus, J. M. et al. “Influence of low-molecular-weight and macromolecular organic additives on the morphology of calcium carbonate”. In: *Journal of the Chemical Society, Faraday Transactions* vol. 89, no. 15 (1993), pp. 2891–2900.

[243] TobyáKelsey, E. et al. “Computer modelling of inorganic solids and surfaces”. In: *Faraday Discussions* vol. 95 (1993), pp. 75–84.

[244] Leeuw, N. de and Parker, S. “Atomistic simulation of the effect of molecular adsorption of water on the surface structure and energies of calcite surfaces”. In: *Journal of the Chemical Society, Faraday Transactions* vol. 93, no. 3 (1997), pp. 467–475.

[245] Leeuw, N. H. de and Parker, S. C. “Surface structure and morphology of calcium carbonate polymorphs calcite, aragonite, and vaterite: an atomistic approach”. In: *The Journal of Physical Chemistry B* vol. 102, no. 16 (1998), pp. 2914–2922.

[246] Hwang, S., Blanco, M., and Goddard, W. A. “Atomistic simulations of corrosion inhibitors adsorbed on calcite surfaces I. Force field parameters for calcite”. In: *The Journal of Physical Chemistry B* vol. 105, no. 44 (2001), pp. 10746–10752.

[247] Guillot, B. “A reappraisal of what we have learnt during three decades of computer simulations on water”. In: *Journal of molecular liquids* vol. 101, no. 1-3 (2002), pp. 219–260.

[248] Paschek, D. “Temperature dependence of the hydrophobic hydration and interaction of simple solutes: An examination of five popular water models”. In: *The Journal of chemical physics* vol. 120, no. 14 (2004), pp. 6674–6690.

[249] Sanz, E. et al. “Phase diagram of water from computer simulation”. In: *Physical review letters* vol. 92, no. 25 (2004), p. 255701.

[250] Abascal, J. et al. “A potential model for the study of ices and amorphous water: TIP4P/Ice”. In: *The Journal of chemical physics* vol. 122, no. 23 (2005).

[251] Berendsen, H. J. et al. “Interaction models for water in relation to protein hydration”. In: *Intermolecular forces: proceedings of the fourteenth Jerusalem symposium on quantum chemistry and biochemistry held in jerusalem, israel, april 13–16, 1981*. Springer. 1981, pp. 331–342.

[252] Berendsen, H. J., Grigera, J. R., and Straatsma, T. P. “The missing term in effective pair potentials”. In: *Journal of Physical Chemistry* vol. 91, no. 24 (1987), pp. 6269–6271.

[253] Jorgensen, W. L. et al. “Comparison of simple potential functions for simulating liquid water”. In: *The Journal of chemical physics* vol. 79, no. 2 (1983), pp. 926–935.

[254] Jorgensen, W. L. and Madura, J. D. “Temperature and size dependence for Monte Carlo simulations of TIP4P water”. In: *Molecular Physics* vol. 56, no. 6 (1985), pp. 1381–1392.

[255] Mahoney, M. W. and Jorgensen, W. L. “A five-site model for liquid water and the reproduction of the density anomaly by rigid, nonpolarizable potential functions”. In: *The Journal of chemical physics* vol. 112, no. 20 (2000), pp. 8910–8922.

[256] Silvestrelli, P. L. and Parrinello, M. “Structural, electronic, and bonding properties of liquid water from first principles”. In: *The Journal of chemical physics* vol. 111, no. 8 (1999), pp. 3572–3580.

[257] Site, L. D., Alavi, A., and Lynden-Bell, R. “The electrostatic properties of water molecules in condensed phases: an ab initio study”. In: *Molecular Physics* vol. 96, no. 11 (1999), pp. 1683–1693.

[258] Niu, S., Tan, M.-L., and Ichiye, T. “The large quadrupole of water molecules”. In: *The Journal of Chemical Physics* vol. 134, no. 13 (2011).

[259] Coutinho, K. et al. “Electronic polarization of liquid water: converged Monte Carlo-quantum mechanics results for the multipole moments”. In: *Chemical physics letters* vol. 369, no. 3-4 (2003), pp. 345–353.

[260] Izadi, S., Anandakrishnan, R., and Onufriev, A. V. "Building water models: a different approach". In: *The journal of physical chemistry letters* vol. 5, no. 21 (2014), pp. 3863–3871.

[261] Barnes, P. et al. "Cooperative effects in simulated water". In: *Nature* vol. 282, no. 5738 (1979), pp. 459–464.

[262] Watanabe, K. and Klein, M. L. "Effective pair potentials and the properties of water". In: *Chemical Physics* vol. 131, no. 2-3 (1989), pp. 157–167.

[263] Abascal, J. L. and Vega, C. "The water forcefield: Importance of dipolar and quadrupolar interactions". In: *The Journal of Physical Chemistry C* vol. 111, no. 43 (2007), pp. 15811–15822.

[264] Wang, L.-P. et al. "Systematic improvement of a classical molecular model of water". In: *The Journal of Physical Chemistry B* vol. 117, no. 34 (2013), pp. 9956–9972.

[265] Strand, S. et al. ""Smart water" for oil recovery from fractured limestone: a preliminary study". In: *Energy & fuels* vol. 22, no. 5 (2008), pp. 3126–3133.

[266] Goolsby, J. and Anderson, R. "Pilot water flooding in a dolomite reservoir, the McElroy field". In: *Journal of Petroleum Technology* vol. 16, no. 12 (1964), pp. 1345–1350.

[267] Bernard, G. G. "Effect of floodwater salinity on recovery of oil from cores containing clays". In: *SPE Western Regional Meeting*. Spe. 1967, SPE–1725.

[268] Puntervold, T., Strand, S., and Austad, T. "New method to prepare outcrop chalk cores for wettability and oil recovery studies at low initial water saturation". In: *Energy & Fuels* vol. 21, no. 6 (2007), pp. 3425–3430.

[269] RezaeiDoust, A. et al. "Smart water as wettability modifier in carbonate and sandstone: A discussion of similarities/differences in the chemical mechanisms". In: *Energy & fuels* vol. 23, no. 9 (2009), pp. 4479–4485.

[270] Mahani, H. et al. "Insights into the mechanism of wettability alteration by low-salinity flooding (LSF) in carbonates". In: *Energy & Fuels* vol. 29, no. 3 (2015), pp. 1352–1367.

[271] Sheng, J. J. *Enhanced oil recovery field case studies*. Gulf Professional Publishing, 2013.

[272] Sheng, J. J. "Critical review of low-salinity waterflooding". In: *Journal of Petroleum Science and Engineering* vol. 120 (2014), pp. 216–224.

[273] Afekare, D. A. and Radonjic, M. "From mineral surfaces and coreflood experiments to reservoir implementations: Comprehensive review of low-salinity water flooding (LSWF)". In: *Energy & fuels* vol. 31, no. 12 (2017), pp. 13043–13062.

[274] Bartels, W.-B. et al. "Literature review of low salinity waterflooding from a length and time scale perspective". In: *Fuel* vol. 236 (2019), pp. 338–353.

[275] Seccombe, J. C. et al. “Improving Wateflood Recovery: LoSal™ EOR Field Evaluation”. In: *SPE Improved Oil Recovery Conference?* SPE. 2008, SPE–113480.

[276] Nasralla, R. A. and Nasr-El-Din, H. A. “Double-layer expansion: is it a primary mechanism of improved oil recovery by low-salinity waterflooding?” In: *SPE Reservoir Evaluation & Engineering* vol. 17, no. 01 (2014), pp. 49–59.

[277] Karimi, M. et al. “Wettability alteration and oil recovery by spontaneous imbibition of low salinity brine into carbonates: Impact of Mg2+, SO42- and cationic surfactant”. In: *Journal of Petroleum Science and Engineering* vol. 147 (2016), pp. 560–569.

[278] Ding, H. and Rahman, S. “Experimental and theoretical study of wettability alteration during low salinity water flooding-an state of the art review”. In: *Colloids and Surfaces A: Physicochemical and Engineering Aspects* vol. 520 (2017), pp. 622–639.

[279] Jorgensen, W. L., Maxwell, D. S., and Tirado-Rives, J. “Development and testing of the OPLS all-atom force field on conformational energetics and properties of organic liquids”. In: *Journal of the American Chemical Society* vol. 118, no. 45 (1996), pp. 11225–11236.

[280] Williams, C. D. et al. “The Development of a Classical Force Field to Determine the Selectivity of an Aqueous Fe3+–Eda Complex for Tco4– and So42–”. In: *Journal of chemical theory and computation* vol. 10, no. 8 (2014), pp. 3345–3353.

[281] Miri, R., Aagaard, P., and Hellevang, H. “Examination of CO2–SO2 solubility in water by SAFT1. Implications for CO2 transport and storage”. In: *The Journal of Physical Chemistry B* vol. 118, no. 34 (2014), pp. 10214–10223.

[282] Miri, R. et al. “Phase relations in the Longyearbyen CO2 Lab reservoir–forecasts for CO2 injection and migration”. In: *Norwegian Journal of Geology* vol. 94 (2014), pp. 217–232.

[283] Masoudi, M. et al. “Modified PC-SAFT characterization technique for modeling asphaltenic crude oil phase behavior”. In: *Fluid Phase Equilibria* vol. 513 (2020), p. 112545.

[284] Parvin, S. et al. “Continuum scale modelling of salt precipitation in the context of CO2 storage in saline aquifers with MRST compositional”. In: *International Journal of Greenhouse Gas Control* vol. 99 (2020), p. 103075.

[285] Aarnes, J. E., Gimse, T., and Lie, K.-A. “An introduction to the numerics of flow in porous media using Matlab”. In: *Geometric modelling, numerical simulation, and optimization: applied mathematics at SINTEF*. Springer, 2007, pp. 265–306.

[286] Bao, K. et al. “Fully implicit simulation of polymer flooding with MRST”. In: *Computational Geosciences* vol. 21, no. 5-6 (2017), pp. 1219–1244.

[287] Tan, S. P. et al. “Statistical associating fluid theory coupled with restrictive primitive model extended to bivalent ions. SAFT2: 1. single salt+ water solutions”. In: *The Journal of Physical Chemistry B* vol. 110, no. 33 (2006), pp. 16694–16699.

[288] Ji, X. et al. “Statistical associating fluid theory coupled with restrictive primitive model extended to bivalent ions. SAFT2: 2. Brine/seawater properties predicted”. In: *The Journal of Physical Chemistry B* vol. 110, no. 33 (2006), pp. 16700–16706.

[289] Zhang, Y. and Sarma, H. “Improving waterflood recovery efficiency in carbonate reservoirs through salinity variations and ionic exchanges: A promising low-cost" smart-waterflood" approach”. In: *Abu Dhabi International Petroleum Exhibition and Conference*. SPE. 2012, SPE–161631.

[290] Braga, S. et al. “Hydrogen storage in carbon nanoscrolls: An atomistic molecular dynamics study”. In: *Chemical physics letters* vol. 441, no. 1-3 (2007), pp. 78–82.

[291] Iglauer, S., Mathew, M., and Bresme, F. “Molecular dynamics computations of brine–CO2 interfacial tensions and brine–CO2–quartz contact angles and their effects on structural and residual trapping mechanisms in carbon geo-sequestration”. In: *Journal of colloid and interface science* vol. 386, no. 1 (2012), pp. 405–414.

[292] Ma, Z. and Ranjith, P. G. “Review of application of molecular dynamics simulations in geological sequestration of carbon dioxide”. In: *Fuel* vol. 255 (2019), p. 115644.

[293] Katende, A. and Sagala, F. “A critical review of low salinity water flooding: Mechanism, laboratory and field application”. In: *Journal of Molecular Liquids* vol. 278 (2019), pp. 627–649.

[294] Galindo, A. et al. “SAFT-VRE: phase behavior of electrolyte solutions with the statistical associating fluid theory for potentials of variable range”. In: *The Journal of Physical Chemistry B* vol. 103, no. 46 (1999), pp. 10272–10281.

[295] Gil-Villegas, A., Galindo, A., and Jackson, G. “A statistical associating fluid theory for electrolyte solutions (SAFT-VRE)”. In: *Molecular Physics* vol. 99, no. 6 (2001), pp. 531–546.

[296] Tan, S. P., Adidharma, H., and Radosz, M. “Statistical associating fluid theory coupled with restricted primitive model to represent aqueous strong electrolytes”. In: *Industrial & engineering chemistry research* vol. 44, no. 12 (2005), pp. 4442–4452.

[297] Jones, D. et al. “Accelerators for classical molecular dynamics simulations of biomolecules”. In: *Journal of chemical theory and computation* vol. 18, no. 7 (2022), pp. 4047–4069.

[298] Song, X. and Zhang, Z. “Determination of clay-water contact angle via molecular dynamics and deep-learning enhanced methods”. In: *Acta Geotechnica* vol. 17, no. 2 (2022), pp. 511–525.

[299] Leverant, C. J. et al. “Machine Learning Predictions of Simulated Self-Diffusion Coefficients for Bulk and Confined Pure Liquids”. In: *Journal of Chemical Theory and Computation* (2023).

[300] Fathi, S. J., Austad, T., and Strand, S. “Water-based enhanced oil recovery (EOR) by “smart water”: Optimal ionic composition for EOR in carbonates”. In: *Energy & fuels* vol. 25, no. 11 (2011), pp. 5173–5179.

[301] Basu, S. and Sharma, M. M. “Measurement of critical disjoining pressure for dewetting of solid surfaces”. In: *Journal of colloid and interface science* vol. 181, no. 2 (1996), pp. 443–455.

[302] Xie, Q. et al. “Extended DLVO-based estimates of surface force in low salinity water flooding”. In: *Journal of Molecular Liquids* vol. 221 (2016), pp. 658–665.

Papers

Paper I

Extension of PC-SAFT equation of state to include mineral surface effect in fluid properties using molecular dynamics simulation

Sajjad Ahmadi Goltapeh, Saeed Abdolahi, Rohaldin Miri, and Helge Hellevang

Published in *Sustainable Energy Technologies and Assessments*, 2021, volume 48, pp. 101624. DOI: https://doi.org/10.1016/j.seta.2021.101624.

Sustainable Energy Technologies and Assessments 48 (2021) 101624

Contents lists available at ScienceDirect

Sustainable Energy Technologies and Assessments

journal homepage: www.elsevier.com/locate/seta

Extension of PC-SAFT equation of state to include mineral surface effect in fluid properties using molecular dynamic simulation

Sajjad Ahmadi Goltapeh [a,*], Saeed Abdolahi [b], Rohaldin Miri [c], Helge Hellevang [a]

[a] Department of Geosciences, University of Oslo, P.O. Box 1047 Blindern, 0316 Oslo, Norway
[b] Department of Chemical Engineering, Amirkabir University of Technology, 424 Hafez Avenue, Tehran, Iran
[c] School of Chemical Engineering, Iran University of Science and Technology (IUST), P.O. Box 16765-163, Tehran, Iran

ARTICLE INFO

Keywords:
Molecular Dynamic
PC-SAFT
Calcite-Water Interface
Thermodynamic Properties
Fluid-Mineral Interfacial Properties

ABSTRACT

In the vicinity of fluid-mineral interfaces a transition zone exist in which the order and packing of the molecules differ from that of the bulk phase where the distribution of intermolecular forces exhibit a more homogenous form. To develop an understanding of the thermodynamic properties in the fluid-mineral interface molecular dynamic (MD) simulation was conducted for the water-calcite system. To predict the water properties near the calcite wall, we have defined a contribution for Helmholtz energy extended from PC-SAFT equation of state (EOS). The new energy contribution depends on the confinement parameters i.e. potential of fluid-wall interaction, confinement degree, bulk density, and fraction of confined molecules estimated by MD simulation. The outcomes of MD simulation exhibit the layering transition of water on the water-calcite interface. In addition, MD simulation confirm the energy deviation within the layering transition zone, where the calcite adsorbs the water molecules. In this approach, the modified PC-SAFT showed a good agreement with MD observations. The results of this study can contribute to a better understanding of fluid behavior at the fluid-mineral interface. In addition, this technique is a valuable tool that can be used to estimate solubility limits in multicomponent fluid processing and pipeline transport.

Introduction

Energy has a significant role in social and economic developments. As the population grows, the demand for energy consumption increases. To mitigate the environmental impacts of the greenhouse gases, development of renewable energy resources is the prevalent solution. However, achieving the sustainable solutions with low impact on environment is a long-term plan. On the other hand, current renewable supplies are not enough to keep up with the energy demand and the need to traditional energy resources would remain. In order to achieve low carbon intensive systems, optimized methods in thermodynamic assessment of hydrocarbons play a significant role. Improved recovery from oil and gas reservoirs and cost-effective design of downstream facilities requires accurate knowledge of phase behavior and thermodynamic properties [1,2]. Equation of states (EOS) are suitable tools performing the thermodynamic properties calculation and phase behavior analysis. The EOSs define a mathematical relationship between the pressure (P), volume (V) and temperature (T). Then, all thermodynamic properties are computable with known relation between P, V and T. Most of the EOSs can be classified in three main categories i.e. virial, cubic and molecular-based. The virial EOS of high order are precise enough to cover a wide range of fluid types but they are not efficient because they need a large empirical database for convergence [3]. The most widely used EOSs in engineering applications are cubic EOSs which originally introduced by Van der Waals [4]. The conventional cubic EOSs although predict the behavior of simple components precisely but they suffer from lack of accuracy in describing the complex molecules and mixtures having strong intermolecular forces.

The molecular based EOSs so-called SAFT-type EOSs are constructed based on the statistical associating fluid theory and they formulate dispersive and associative interactions upon Barker-Henderson and Wertheim theories [5,6]. Furthermore, SAFT has shown great success in the simulation of polar fluids with non-ideal intermolecular interactions [7–10].

The interfacial effect between minerals and fluids is a non-ideal interaction and its significant role in thermodynamic modeling has been recognized [11]. On one hand, it is imperative to develop our understanding about fluid-mineral governing interactions for precise assessment of fluid recovery from geological media. On the other hand,

* Corresponding author at: Department of Geosciences, University of Oslo, P.O. Box 1047 Blindern, 0316 Oslo, Norway.
E-mail address: sajjadah@uio.no (S. Ahmadi Goltapeh).

https://doi.org/10.1016/j.seta.2021.101624
Received 25 May 2021; Received in revised form 3 August 2021; Accepted 14 September 2021
Available online 2 October 2021

Nomenclature

A	Helmholtz free energy [kcal]
a	Intensive Helmholtz free energy [kcal/mol]
E_{conf}	Configurational energy [kcal]
E_u/k	Dispersion energy parameter [K]
F_p	Local distribution of the molecules inside the interface region
F_{pr}	Fraction of the confined molecules in the square well of interface region
H	Hamiltonian [kcal/mol]
k	Boltzmann constant
K_E	Kinetic Energy [kcal/mol]
L	Length of the water bulk mounted above calcite [Å]
M_{int}	Internal partition function
m	Particle mass [kg]
m^{seg}	Segment number
N	Total number of particles
p	Momentum [kg.m/s]
P_E	Potential energy [kcal/mol]
Q	Partition function
r	Position [m]
T	Temperature[K]
V	Volume [$Å^3$]

Greek Letters

α	Number of adsorbed water molecules to the calcite surface
σ'	Segment diameter [Å]
σ	Average molecular diameter [Å]
λ	Broglie wavelength [Å]
ε	Attractive potential of molecule-wall interaction [kcal/mol]
$\varepsilon^{A_iB_i}$	Association energy parameter [K]
ρ	Density under confinement [kg/m^3]
$\kappa^{A_iB_i}$	Association volume
δ	Square well width [Å]
μ	Chemical potential [kcal/mol]

Subscripts and Superscripts

ass	Association
conf	Configurational
conf-ff	Configurational due to fluid–fluid interaction
conf-fw	Configurational due to fluid-wall interaction
diss	Dissociation
f	free
ff	Fluid-Fluid
fw	Fluid-Wall
hs	Hard sphere
i,j	counter
int	Internal
max	maximum
z	Z-axis

cubic EOSs are not suitable candidates to capture the molecular interactions of fluid-mineral. In this regard, SAFT-type EOSs with some modifications and tunings are probably able to capture the fluid-rock mutual interactions. However, an experimental data set illustrating fluid-rock interactions is required for such SAFT modifications.

Herein, Molecular Dynamic (MD) simulation is introduced to provide insights on confined fluid properties. This approach considers the simulation outcomes as pseudo experimental data to develop a new model [12]. The molecular simulation inspired by MD is able to simulate the fluid-mineral interface with known chemistry. MD simulations have emerged as a suitable technique to study the interfacial effects in systems containing complex fluids [13]. Recently, the study of fluid-rock interface with MD simulation has gained numerous contributions in the literature [14–16]. Kirch et al.[17] have studied the mutual effect of calcite interface and electrolyte ions (Na, Cl, and Ca) on water structure with MD modeling and Nuclear Magnetic Resonance (NMR). They illustrated that the strong ordering of surface water on calcite interface inhibits the adsorptions of chemical species. Ricci et al.[18] investigated the water-calcite interface with Atomic Force Microscopy (AFM) experiments and MD simulation. With MD simulation, they observed a shorter residence of Ca^{2+} ions than Na^{+} ions on the calcite surface, and they validated this finding with AFM experiment.

Few studies have looked at the impact of a mineral on the interface characteristics, and even fewer studied have utilized MD modeling to modify the EOS in which interface properties are computed. This research not only uses MD simulation to investigate the function of a particular mineral, such as calcite, on interface characteristics, but it also offers a method for calculating confinement parameters and incorporating them into Perturbation-Chain SAFT (PC-SAFT) [19] to measure interface properties.

In this study, we added calcite ($CaCO_3$) wall effect into the PC-SAFT, which led to the definition of confinement parameters. We modeled the water-calcite interface with MD technique to estimate the confinement parameters. Calcite (1014) surface was chosen to represent a carbonate rock (oil reservoir rock) because calcite is the most abundant and ubiquitous mineral in large carbonate reservoirs. Water, considered to be pure, is also one of the petroleum constituents with strong polar behavior. The estimated confinement parameters by MD were replaced in the modified PC-SAFT. Finally, PC-SAFT results were compared with the MD outcomes.

The remainder of this paper is organized as follows. In Section2, we describe the theoretical method for PC-SAFT modification and details of MD simulation. In Section 3, the modified PC-SAFT model is validated with MD results. In Section 4, we summarize the list of findings and conclusions.

Theoretical background

Modification on PC-SAFT equation of state

Figure 1 displays the scheme of the interfacial confinement between water and calcite. Three different regions are visible in this sketch. Region I displays the bulk region where water-water interactions govern the intermolecular interactions. Here, L_z is the distance from the water bulk top layer to the calcite surface. The thickness of L_z were 25 Å, 40 Å and 70 Å in MD simulations. Region II with thickness of δ is the surface-adsorbed zone where the water-calcite interactions are dominant interactions. Region III is free of any water molecule because its thickness ($\sigma_i/2$) is less than half of the water molecules diameter ($\sigma_i/2 \leq 0.5$ Å) [20]. In other words, the thickness of this region is very narrow such that no water molecule could reside there. Within the confined geometry presented in Fig. 1, homogeneous and heterogeneous phase interactions mainly control the fluid phase behavior. The interactions in homogeneous and heterogeneous phases apply to the water-water and water-calcite, respectively.

Equation (1) shows a square-well potential, which estimates the interaction between the water molecules, where r_{ij} is the distance between two molecules, ε_{ij} is the depth of the square well, δ_{ij} is the relevant width of square well, and σ_{ij} is defined as the mean molecular diameter for water.

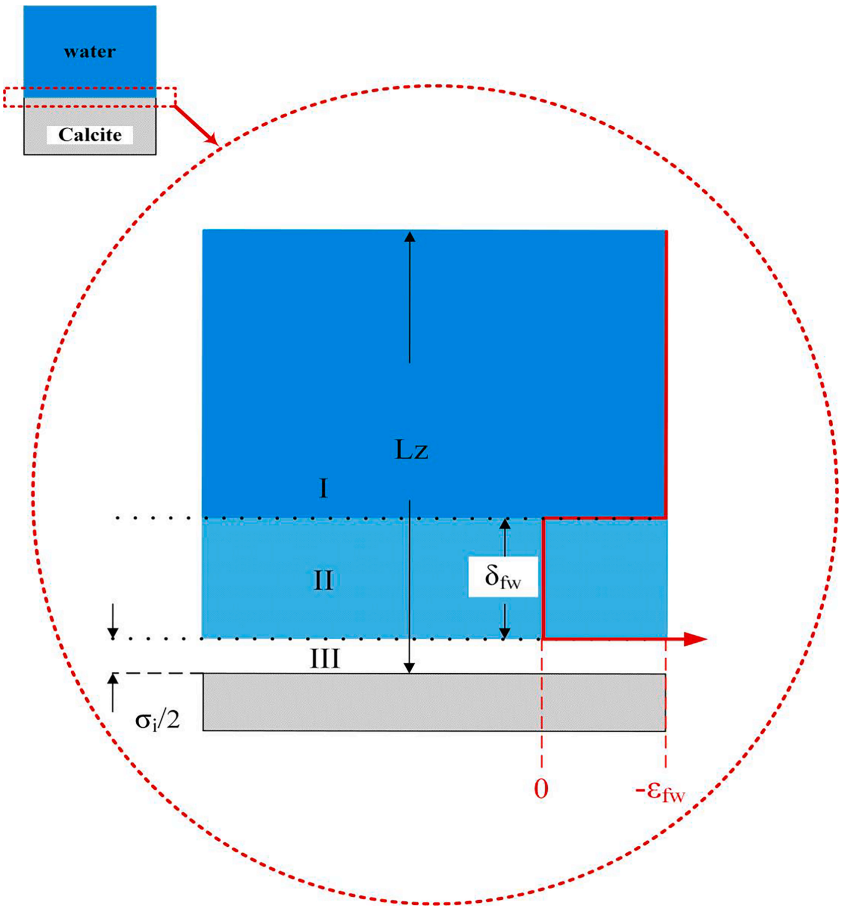

Fig. 1. Illustration of the confinement within water-calcite interface. Three different regions are visible here. Region I is the bulk region where molecular interactions are governed by water-water interactions. Lz is the distance from the water bulk top layer to the calcite surface, which is assumed to be 25 Å, 40 Å and 70 Å in MD simulations. Region II is the surface-adsorbed region where the molecular interactions are governed by water-calcite interactions and its thickness is shown by δ. Region III is forbidden zone, which is supposed to include no water molecule. This region, marking with σ, is very narrow such that the center of mass of water molecules cannot reside here.

$$u_{ij}(r_{ij}) = \begin{cases} \infty & r_{ij} < \sigma_{ij} \\ -\varepsilon_{ij} & \sigma_{ij} < r_{ij} < \sigma_{ij} + \delta_{ij} \\ 0 & r_{ij} > \sigma_{ij} + \delta_{ij} \end{cases} \quad (1)$$

Similarly, water and calcite molecules are supposed to interact through a square well, which is defined in equation (2):

$$u_i(l_i) = \begin{cases} \infty & l_i < \frac{\sigma_i}{2} \\ -\varepsilon_{fw,i} & \frac{\sigma_i}{2} < l_i < \frac{\sigma_i}{2} + \delta_{fw} \\ 0 & l_i > \frac{\sigma_i}{2} + \delta_{fw} \end{cases} \quad (2)$$

According to equation (2), $\varepsilon_{fw,i}$ moves toward infinite within region III. Therefore, the landing of the water molecules in this narrow region is not probable. Hereafter, $L_z/(0.5\sigma_i)$ is called length-ratio (L-R), showing the dimensionless water thickness in the water-calcite system.

In this context, we used Travalloni et. al.[21], approach to modify PC-SAFT EOS. To modify PC-SAFT equation of state, it is required to start from the original definition of partition function, because partition function provides a theoretical platform to derive the thermodynamic properties. General definition of partition function is given in equation (3) [22]:

$$Q(N,V,T) = \left(\frac{M_{int}^N}{\lambda^{3N}N!}\right) v_f^N exp\left(\int_\infty^T \frac{E_{conf}}{kT^2} dT\right) \quad (3)$$

On the left side of equation (3) are the total number of particles (N), the system volume (V), and the temperature (T). On the right side, M_{int} is the internal partition function, λ is the de Broglie thermal wavelength, E_{conf} is configurational energy and k is the Boltzmann constant. The general definitions of Helmholtz free energy and chemical potential are written as:

$$A(N,V,T) = -kT\ Q(N,V,T) \quad (4)$$

$$\mu = \left(\frac{\partial A}{\partial N}\right)_{T,V} \quad (5)$$

The term of Helmholtz energy for water-water interaction in the homogeneous phase (region I) can be defined with equations (1), (3), and (4). To complete the thermodynamics of the system, it is required to add the wall effect contribution into the partition function. Equation (6) includes the effect of the calcite wall on water-calcite interface. As can be observed, the configurational energy contribution has been split into fluid–fluid and fluid-wall:

$$Q(N,V,T) = \left(\frac{M_{int}^{N}}{\lambda^{3N}N!}\right) v_f^N \, exp\left(\int_{\infty}^{T} \frac{E_{conf-ff}}{kT^2}dT\right) exp\left(\int_{\infty}^{T} \frac{E_{conf-fw}}{kT^2}dT\right) \quad (6)$$

In equation (6), $E_{conf\text{-}ff}$ and $E_{conf\text{-}fw}$ denote contributions of fluid–fluid and fluid-wall interactions, respectively. The first three terms in the right hand side ofequation (6) correspond to the Helmholtz free energy in the bulk phase and the last term applies to the Helmholtz free energy within the interface confinement. In other words, equation (3) is modified to equation (6) by adding a fluid-wall contribution. Substitution of Helmholtz free energy in bulk phase gives:

$$\begin{aligned} Q(N,V,T) &= exp\left(-\frac{A^{ff}}{kT}\right) \times exp\left(\int_{\infty}^{T} \frac{E_{conf-fw}}{kT^2}dT\right) \\ &= exp\left(-\frac{A^{ff}}{kT}\right) \times exp\left(-\frac{A^{fw}}{kT}\right) \end{aligned} \quad (7)$$

A^{ff} in equation (7) shows the Helmholtz free energy in the bulk phase. Additionally, the integral product of the second component in the right hand side of equation (7) has been replaced with A^{fw}, which stands for Helmholtz free energy for water-calcite interaction.

The natural logarithm of equation (7) gives:

$$ln\ Q(N,V,T) = -\frac{1}{kT}\left(A^{ff} + A^{fw}\right) \quad (8)$$

In equation (9), the terms of Helmholtz free energy corresponds to the calcite wall effect has been presented separately:

$$\left(\frac{A^{fw}(N,V,T)}{kT}\right) = \left(-\int_{\infty}^{T} \frac{E_{conf-fw}}{kT^2}dT\right) \quad (9)$$

Now, the partition function for water-calcite interface can be defined as a list of different terms, which contribute to total Helmholtz energy.

$$ln\ Q(N,V,T) = -\frac{1}{kT}\left(A^{hs} + A^{disp} + A^{assoc} + A^{fw}\right) \quad (10)$$

According to PC-SAFT, the Helmholtz contribution for bulk (A^{ff}) can be broken down into hard-sphere (A^{hs}), dispersion (A^{disp}), and association (A^{assoc}). It is worth to note that, in this simulation, water is assumed completely pure, namely no cation and anion exit in water bulk. Table 1 shows the pure component parameters of water used in PC-SAFT EOS [23].

Where m^{seg} is the segment diameter, E_u/k is the dispersion energy parameter, $\varepsilon^{A_iB_i}$is the association energy parameter, $\kappa^{A_iB_i}$is the association volume and σ' is the segment diameter determined using the formula in Table 1.

To make an intensive term, N is added to the denominator, which gives:

$$ln\ Q(N,V,T) = \tilde{a}^{hs} + \tilde{a}^{dis} + \tilde{a}^{ass} + \tilde{a}^{fw} \quad (11)$$

Equation (11) expresses the partition function in terms of well-defined Helmholtz energy contributions. To estimate a^{fw}, we have applied equation (12) which uses F_p to relate the energy parameter of water-calcite to configurational energy [21]:

$$E_{conf-fw} = -NF_p\varepsilon_{fw} \quad (12)$$

In equation (12), ε_{fw} is the energy parameter associated with water-calcite interaction. F_p also is defined as:

$$F_p = F_{pr} + \left(1 - F_{pr}\right)\left(1 - exp\left(\frac{-\varepsilon_{fw}}{kT}\right)\right)\left(1 - \frac{\rho}{\rho_{max}}\right)^{\theta} \quad (13)$$

According to Travalloni et. al. [21], θ and F_{pr} are confinement degree and fraction of the water molecules in the square well. The equations (14) and (15) present θ and F_{pr} definitions, based on the depicted assumptions in Fig. 1:

$$F_{pr} = \frac{\left(L_Z - \frac{\sigma}{2}\right) - \left(L_Z - \frac{\sigma}{2} - \delta\right)}{\left(L_Z - \frac{\sigma}{2}\right)} \quad (14)$$

$$\theta = \frac{L_Z}{\delta + \frac{\sigma}{2}} \quad (15)$$

where, L_z is length of water bulk mounted over calcite wall, δ is width of the square well, and σ is average dimeter of the water molecules.

In order to compute the Helmholtz free energy incorporating calcite-wall effect, ε_{fw}, ρ_{max}, θ and F_{pr} must be calculated in advance using MD simulation. In the next step, F_p is computed using confinement parameters mentioned before. Calculated F_p is put into equation (12) and the results are plugged into equation (9). The integral product of $E_{conf\text{-}fw}$ is then used to calculate A_{fw} in equation (9). Equation (10), which sums up the Helmholtz species, yields the Helmholtz free energy corresponds to the interface confinement.

MD simulation

The MD simulation applies the Born-Oppenheimer approximation to model the dynamics of the multi-particle systems built upon a certain thermodynamic ensemble [24]. In this approximation, Newton's law of motion governs the dynamic of the nuclei corresponding to the atoms or molecules. Therefore, the non-relativistic Hamiltonian becomes an implicit function of nuclei positions and momentums [25]:

$$H(p,r) = K_E + U = \sum_{i=1}^{N} \frac{p_i^2}{2m_i} + U(r_1 + r_2 + \ldots + r_i + \ldots + r_N) \quad (16)$$

Where, p_i and r_i are set of particle momenta and positions, K_E is kinetic energy, U(r) is potential energy, m_i is particle mass, and N is the total number of particles.

We used the open source LAMMPS software as the classical molecular dynamic code for molecular dynamic simulation [26]. The Newtonian equation of motions developed by the velocity Verlet algorithm adopts the time step of 1 fs for all simulations. Each MD simulation was executed with a constant temperature. The temperature itself was updated through a loop in the LAMMPS code.

The developed force field by Zhao et al. [27] defined the internal forces between 480 calcite molecules. These molecules are sorted into 6 layers along (1014) a perfect calcite surface. The SPC/E [28,29] model described the internal interactions among the molecules of water bulk. Fig. 2 shows the calcite-water layout in the simulation box. As it is seen, we have built a molecular system including a water bulk mounted above the calcite slab along the z-direction. In the simulation box, water bulk was prepared with three different lengths along the z-axis: 25 Å, 40 Å, and 70 Å. For both the x and y directions, the boundary conditions were periodic. The boundary condition for the z-direction was set to be constant, and a reflecting wall was inserted above the water bulk to avoid atom loss.

To wrap the molecules of the calcite slab and water bulk, we applied

Table 1
PC-SAFT parameters for pure water.

m^{seg}	σ' [Å]	E_u/k [K]	$\varepsilon^{A_iB_i}$ [K]	$\kappa^{A_iB_i}$
1.2047	*	353.95	2425.7	0.0451

*$\sigma = 2.7927 + 10.11exp(-0.01775 \times T) - 1.417exp(0.01146 \times T)$, T is the temperature in [K]

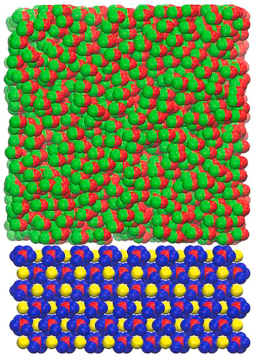

Fig. 2. Illustration of water-calcite system for MD simulation. The calcite slab includes 6 layers sorted along the (1014) plane and overlaps with water bulk on xy plane. The water bulk has extended along the z-axis with 25 Å, 40 Å and 70 Å thickness.

PACKMOL [30] that compacts the molecules with a certain distance such that the structure of molecules remains intact. Running the minimize function with conjugate gradient algorithm lets the molecules remain at a reasonable distance and the energy flood during the simulation run is avoided. The equilibration process in each simulation is fulfilled by initializing the particles velocity with a set temperature. Then, the equilibration followed by Nose-Hoover NVT thermostat until 3 ns in which temperature remains constant at T = 300 K, 400 K and 500 K. Finally, LAMMPS measured the thermodynamic properties by averaging over total run time.

Results and discussion

Density profile at constant length ratio

Figure 3 illustrates the profile of water density inside the layering zone and bulk phase. The length-ratio (L-R) and temperature, respectively in each row and column, are constant. From left to right the simulation temperature increases from 300 K to 400 K and 500 K while from top to bottom the L-R decreases from 140 to 80 and 50. The density plot has oscillatory behavior near the calcite-wall so-called layering zone. In fact, the layering zone and bulk imply regions II and I according to the zone classification in Fig. 1.

In the first row with L-R = 140, when T = 300 K, the density experience the longest peak in region II and flatten at bulk density inside region I. However, the shortest peak in region II and minimum density inside region I belongs to T = 500 K. Simultaneously, the density values at T = 400 K remain between T = 300 K and T = 500 K. Compared with the first row, the same regime is observed in the second and third row for L-R = 80 and L-R = 50, respectively. It means, with constant L-R, the highest density inside region I and II belongs to T = 300 K. Whilst the lowest density in region I and II corresponds to T = 500 K. Therefore, for a constant L-R, the density inside the region I and region II varies with respect to the mean distance between the water molecules. In other words, with constant length-ratio, T = 300 K, 400 K and 500 K provide the minimum, medium and maximum mean distance among the water molecules, which respectively leads to maximum, medium and minimum density in region I and II.

Density profile at a constant temperature

The first, second and third column in Fig. 3 display density profile at constant temperature and different L-R values. A deceptive point that one may notice at first glance is the ascending behavior of the density profile from top to bottom. Namely, the longest and shortest peak in region II occur at L-R = 50 and L-R = 140. Within region I from top to bottom, on the other hand, the density trend of L-R = 140, lays on higher values than L-R = 80 and L-R = 50. In Fig. 3, this regime is repeated in all columns.

For ease of comparison at constant temperature and variable L-R, the depicted density profiles in Fig. 3, have been normalized between 0 and 1. Fig. 4a–c display the variation of normalized density with respect to the L-R at constant temperature. In Fig. 4a–c, one can visually compare the size of the marked area showing average density. For example, at T = 300 K the smallest area belongs to L-R = 50 compared with L-R = 80 and L-R = 140. It means, L-R = 140 and L-R = 50 make the max and min average density at T = 300 K while the relevant density for L-R = 80 remains larger than L-R = 50 and smaller than L-R = 140. This regime is replicated in Fig. 4b and c. Therefore, with fixed temperature, the min and max length-ratio provide minimum and maximum average density within region II and I, respectively.

This fact is consistent with the definition of interface confinement within the water bulk and calcite-wall. To be specific, reduction in confinement size reduces the density, and raising the confinement size provides density growth. In our simulation, L-R = 140 is the maximum confinement and gives larger water density than L-R = 80 and L-R = 50. The maximum density is potentially achieved in a water-calcite system with an infinite length-ratio (L-R=∞) or a water bulk without the presence calcite-wall. Even though L-R = 140 and L-R = 50 give the greatest and lowest average density within regions II and I, how the local peaks inside region II are interpreted remains a mystery.

In fact, the adsorbed water molecules on the calcite-wall are apparent in the local peaks of region II. On the one hand, the number of water molecules adsorbed to the calcite surface is controlled by the calcite's attraction. On the other hand, the average attraction force inside region II, is the consequence of a trade-off between the calcite-wall attraction and the water bulk attraction. It means that thin layers of water are more attracted to the calcite-wall than thicker ones. Additionally, it may be said that $\alpha_{50} > \alpha_{80} > \alpha_{140}$ where α represents the number of water molecules within the first adsorbed layer, and the subscripts express the L-R values. Consequently, the extension of the water bulk along the z-axis increases the waterside's average attraction force and decreases water adsorption on the calcite-wall, and reducing the water length, on the other hand, results in a notable local peak of density inside region II. To sum up, the highest local density is achieved at the first adsorbed layer when the lowest confinement is used. However, as seen in Fig. 4a–c, the average density under minimum confinement remains minimal.

Energy behavior with respect to L-R and temperature variation

Figure 5 demonstrates the total energy profile inside region II and I for different length-ratios and temperatures. The vertical columns display the energy behavior at fixed temperature and L-R = 140, 80 and 50. The horizontal rows express the energy variation at constant L-R and T = 300 K, 400 K and 500 K. Moving from left to right where L-R = 140, one observe the decay in the absolute energy values such that $E_{300K} > E_{400K} > E_{500K}$. The same pattern is noticed in the second and third row, which means at constant length-ratio, higher temperature causes lower energy inside the layering zone and bulk.

From left to right, comparison of the energy profiles with the density trends in Fig. 3, reveals that max and min density within region II and I corresponds to the maximum and minimum energy respectively. For example, in the first row of Fig. 3 one notices $\rho_{300K} > \rho_{400K} > \rho_{500K}$. It means with T = 300 K the water molecules stand at shorter distance than T = 400 K and T = 500 K. Therefore, with constant L-R, the higher the temperature the lower the total energy.

Moving from top to bottom, one observes the length of local peaks within region II increases, whereas the widths of the curves narrow

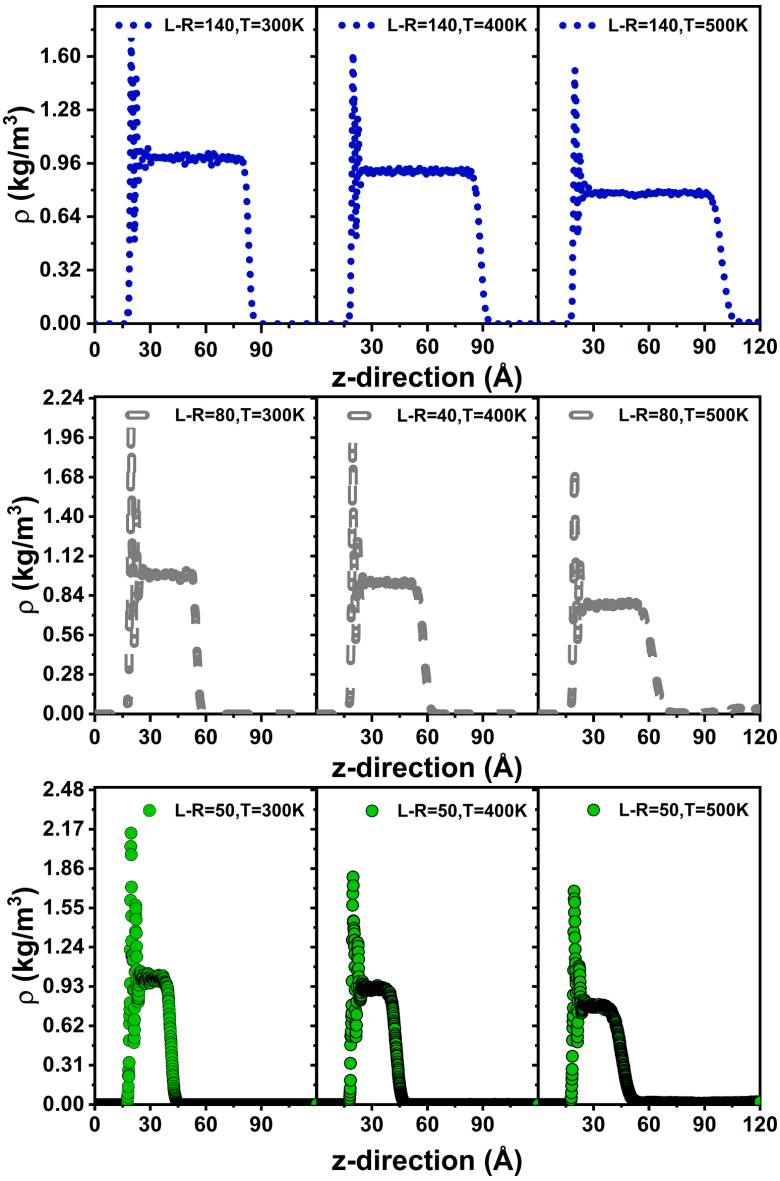

Fig. 3. Illustration of the density profile inside region I and II at several length-ratios and different temperatures. The plotted curves in each row represent the density profile at constant L-R, while each column presents the density profile at fixed temperature. From left to right the simulation temperature increases from 300 K to 400 K and 500 K. The L-R, from top to bottom, decreases from 140 to 80 and 40.

down. This energy pattern provides smaller average energy for smaller confinement and vice versa. For example, in the last column of Fig. 5 where T = 500 K, the absolute value of the integral over L-R = 50 trend corresponds to the minimum average energy. Whereas the absolute value of integral over L-R = 140 illustrates the maximum average energy. Therefore, with T = 500 K, the reduction in length-ratio reduces the absolute average total energy, i.e., $E_{140} > E_{80} > E_{50}$. This pattern is observed in the first and second columns.

To sum up, the stronger effect of the calcite attraction forces on thin bulk of water leads to the higher adsorption at the first adsorbed layer of water molecules over calcite-wall. High adsorption at the first adsorbed layer results short intermolecular distance. When the intermolecular distance at the first adsorbed layer diminishes, the length of the local peaks for density and energy increases. Whilst, thick bulk of water have

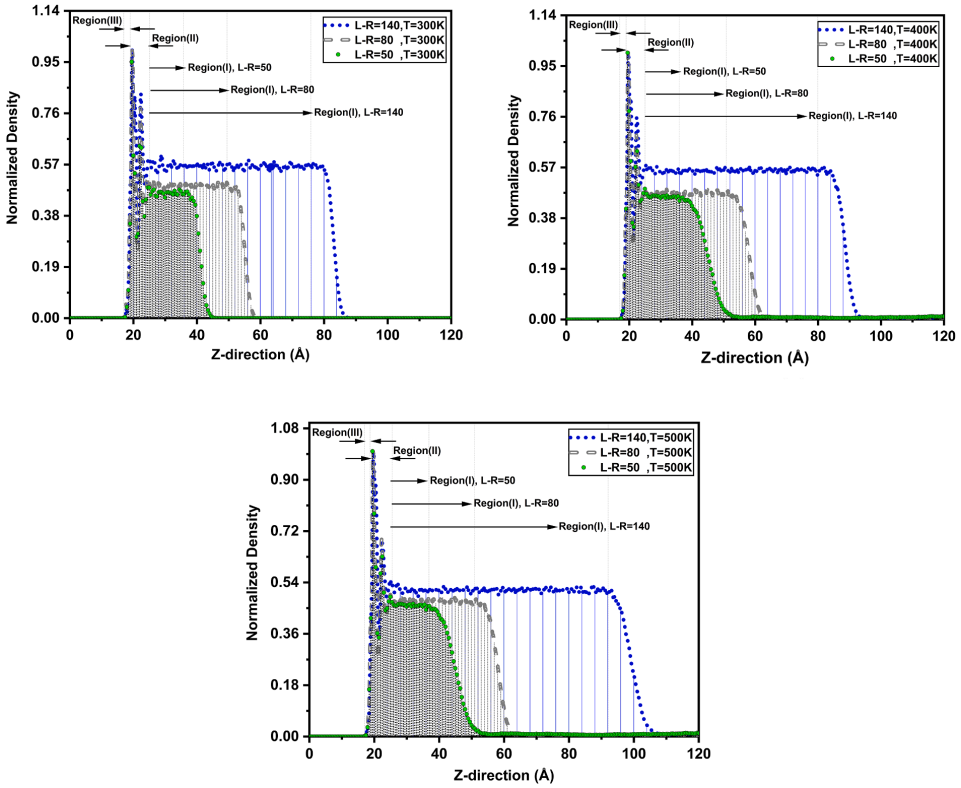

Fig. 4. Illustration of the density profile within region I and II at different L-R and constant temperature. The density is normalized between 0 and 1, which allows comparing the average density trend. The integral of the density inside region I and II is shown by the darkened regions beneath the trends (blue > gray > green). The greatest and lowest average densities at constant temperature, according to the shaded area under the curve, are L-R = 140 and L-R = 50, respectively. In addition, the marked up regions depict the skematic thickness of regions I, II, and III. (For interpretation of the references to colour in this figure legend, the reader is referred to the web version of this article.)

stronger intermolecular attractions and cancels out the effect of the calcite attraction. Hence, the density within the first adsorbed layer over the calcite-wall decreases. The reduction in density within the first adsorbed layer shortens the length of the local peaks for density and energy. Therefore, the shorter the water bulk the larger the local peak in density, but the smaller the average density. In addition, high and low values of average density correspond to the high and low values of average total energy, respectively. Therefore, with fixed L-R and variable temperature, the molecule–molecule distance controls the density and energy. Nevertheless, with variable L-R and fixed temperature, the balance between molecular attraction forces of calcite-wall and water bulk controls the density and energy.

Comparison of PC-SAFT and MD simulation

In section 2.1, the confinement parameters were introduced by equations (13), (14) and (15). We applied MD simulations to estimate the introduced confinement parameters. Table 2 presents calculated confinement parameters under different confinement sizes and temperatures. In this table, the potential of the water-calcite interaction (ε_{fw}) was calculated by the integral of the energy over the layering zone [31]. The fraction of confined molecules (F_{pr}) and confinement degree (θ) were determined according to the defined formula in equations (14) and (15).

To estimate the bulk density (ρ_{max}), we simulated water in MD without the presence of the calcite-wall. Because, at a known temperature, the density of water without the presence of the calcite-wall is maximum. Hence, water was simulated with MD at T = 300 K, 350 K, 400 K, 450 K, and 500 K which the results were tabulated in Table 3.

Table 3 displays simulation (MD and PC-SAFT) and laboratory results for water density without the presence of calcite-wall. To be specific, Table 3 reports the reliability of MD and PC-SAFT for predicting the water density without the presence of calcite-wall. The columns |RE-1| and |RE-2| show the absolute relative errors for MD and PC-SAFT, respectively. As shown, for a specific range of temperature, the obtained results from MD and PC-SAFT are reliable, although the absolute relative error increases with temperature rise.

Table 4 listed the predictions of MD and modified PC-SAFT for the interface layer within region II. One can compare Table 4 with Table 3 at relevant temperatures. As seen, because of the calcite-wall presence, the reported densities in Table 4 are smaller than the relevant ones in Table 3.

The plot in Fig. 6 compares the modified PC-SAFT with MD results at different temperatures. The diamond, circle and square exhibit the MD results at L-R = 50, 80 and 140, respectively. In addition, blue, red and green curves are representative of modified PC-SAFT predictions L-R =

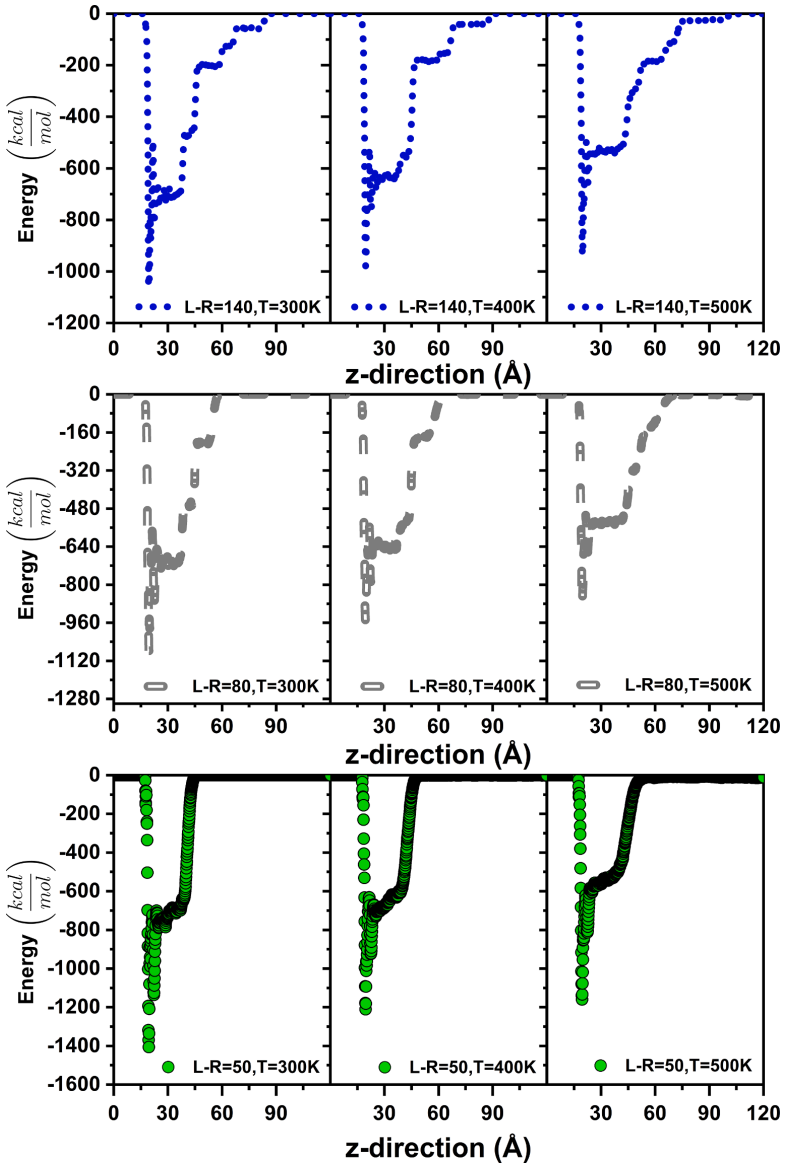

Fig. 5. Illustration of the energy profile inside region I and II at several length-ratios and different temperatures. The plotted figures in each row and column represent the energy trend at constant length-ratio (L-R) and temperature respectively. From left to right the simulation temperature increases from 300 K to 400 K and 500 K while from top to bottom the L-R decreases from 140 to 80 and 50.

50, 80, and 140. At the bottom of the plot box, the profile of absolute relative error shows the deviation of modified PC-SAFT from MD results. To be specific, dashed, dotted and doubled lines are the trajectory of relative error at L-R = 50, 80 and 140, respectively. The vertical axis at the left is the density ratio, including the bulk density in the denominator, which implies ρ_{max}.

As seen in Fig. 6, when L-R increases at a fixed temperature, both MD and PC-SAFT predict larger fractions of ρ/ρ_{max} [33]. This means with a fixed temperature, by growth in confinement size, the confined density (ρ) increases which leads to a reduction of the gap between ρ and ρ_{max}. This fact also satisfies the mathematical limit in equation (13), which says, by extending the water length above the calcite-wall ($L_z \rightarrow \infty$), the density within the layering zone approaches the bulk density ($\rho = \rho_{max}$). Substitution of $\rho = \rho_{max}$ in equation (13) gives homogeneous distribution within the region II ($F_p = F_{pr}$).

In addition, when the temperature rises for a fixed L-R, the MD

Table 2
Estimated confinement parameters with MD simulations. The ε_{fw}, ρ_{max}, F_{pr} and θ respectively present potential of fluid-wall interaction, bulk density, fraction of confined molecules and confinement degree.

T = 300 [K]					
L-R	ε_{fw} [kcal]	ρ_{max} [kg/m^3]	δ [Å]	F_{pr}	θ
50	−3248.525	957.650	5.6	0.229	3
80	−2686.685	973.203	5.9	0.149	6
140	−2695.768	982.393	6.1	0.087	10
T = 400 [K]					
50	−3023.907	888.010	5.6	0.229	3
80	−2511.321	898.869	5.9	0.149	6
140	−2497.062	905.682	6.1	0.087	10
T = 500 [K]					
50	−2722.839	770.170	5.6	0.229	3
80	−2246.411	774.076	5.9	0.149	6
140	−2271.883	780.998	6.1	0.087	10

Table 3
List of the water density at different temperatures without the presence of calcite-wall. This table compares the laboratory data with the outcomes of MD and PC-SAFT. The columns |RE-1| and |RE-2| display the absolute relative error for MD and PC-SAFT, respectively.

Liquid water density					
T [K]	Laboratory [32] [kg/m^3]	MD [kg/m^3]	PC-SAFT [kg/m^3]	|RE-1| %	|RE-2| %
300	996.499	1000.003	990.490	0.352	0.603
350	973.693	970.383	973.365	0.339	0.033
400	937.465	923.463	952.634	1.494	1.618
450	890.319	861.221	926.686	3.268	4.085
500	831.302	791.007	893.784	4.847	7.516

Table 4
Comparison between MD outcomes as a pseudo experiment and modified PC-SAFT for region II. As it is seen, when the temperature is fixed, PC-SAFT prediction grows with growth in L-R. While with constant L-R, PC-SAFT prediction decreases with temperature growth.

Region (II): Liquid water density						
T K	MD [kg/m^3]			Modified PC-SAFT [kg/m^3]		
	L-R = 50	L-R = 80	L-R = 140	L-R = 50	L-R = 80	L-R = 140
300	890.251	899.404	916.439	990.569	990.586	990.621
400	836.394	846.519	857.083	952.708	952.725	952.750
500	766.145	771.005	784.565	893.907	893.908	893.930

predicts a smaller ratio of ρ/ρ_{max}, and relevant |RE| has increased. In other words, under a fixed confinement size, going up in temperature increases the gap between confined density and ρ_{max}. The behavior of the absolute relative error in Table 3 is consistent with the profile of |RE| in Fig. 6. Regarding the |RE| profile at the bottom, two factors result in smaller errors, i.e., the larger confinement and lower temperature. The former moves the properties of the confined water toward the properties of the water bulk, as discussed already. The latter refers to the accuracy of chosen model for water in MD simulation because the accuracy of SPC/E model deteriorates at high temperatures [34]. According to the hypothesis of SPC/E model, the water molecule is fixed-charge, rigid, and non-polarized with an on-plane location. However, in reality, the "charge–distances–angle" parameters for the water molecules fluctuate routinely, affecting the molecule's electrostatic, and therefore the consequence bulk properties. Because of high temperature, the limitations of SPC/E model to predict the water properties increases because i) at increasing temperatures, the spatial fluctuation of

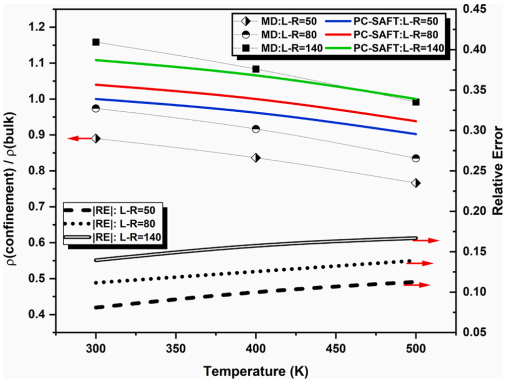

Fig. 6. Graph compares the predictions of MD and modified PC-SAFT at T = 300 K, 400 K and 500 K. The diamond, circle and square exhibit the MD results at L-R = 50, 80 and 140. The blue, red and green curves are representative of modified PC-SAFT predictions at L-R = 50, 80 and 140. In the bottom of plot box, the profile of absolute relative error shows the deviation of modified PC-SAFT from MD results. (For interpretation of the references to colour in this figure legend, the reader is referred to the web version of this article.)

"charge–distances–angle" rises. Therefore, the legitimacy of "simple 3-point charge" models diminishes ii) as temperature rises, the non-polarized assumption loses its validity due to increasing collision between the molecules. As a result, SPCE's ability to forecast water characteristics at high temperatures has deteriorated [35].

Summary and conclusions

To develop our understanding for confinement within fluid-rock interface we simulated water-calcite system with three different thickness of water bulk: L-R = 140, 80 and 50. In our numerical experiments, we observed that going down in water thickness at a fixed temperature, provides smaller density and energy within the water-calcite interface. Furthermore, with a constant L-R, low temperature give rise in density and energy within the layering zone. Then, we concluded that at constant L-R mean distance between water molecules controls the density and energy trend. Whereas at constant temperature the attraction forces of calcite control the density and energy profile. To develop a thermodynamic model for predicting the density change due to calcite-wall presence, we defined a new contribution for Helmholtz free energy in PC-SAFT. Then, the introduced confinement parameters: potential of fluid-wall interaction (ε_{fw}), bulk density (ρ_{max}), fraction of confined molecules (F_{pr}) and confinement degree (θ) were adjusted against MD calculations. The prediction of modified PC-SAFT were validated with MD and good agreement was observed. The uncertainty of the modified PC-SAFT increases with reduction in confinement or temperature.

In conclusion, MD simulation demonstrates that at the water-calcite interface, a smaller L-R provides a lower density at given temperature while low temperatures increase density and energy with a given L-R. Furthermore, the density, energy, and geometry of confinement at the layering zone influence the derived contribution for Helmholtz free energy. Finally, as a result of the addition of introduced Helmholtz energy to PC-SAFT, one may anticipate the interface properties in good agreement with MD results.

CRediT authorship contribution statement

S. Ahmadi G.: Conceptualization, Methodology, Software, Validation, Writing – original draft, Visualization, Formal analysis, Investigation, Writing - review & editing. **S. Abdolahi:** Software, Validation,

Investigation. **R. Miri:** Supervision, Writing - review & editing. **H. Hellevang:** Supervision, Writing - review & editing.

Declaration of Competing Interest

The authors declare that they have no known competing financial interests or personal relationships that could have appeared to influence the work reported in this paper.

References

[1] Qiu X, Yang H, Dejam M, Tan SP, Adidharma H. Experiments on the capillary condensation/evaporation hysteresis of pure fluids and binary mixtures in cylindrical nanopores. J Phys Chem C 2021;125:5802–15.
[2] Nikpoor MH, Dejam M, Chen Z, Clarke M. Chemical–gravity–thermal diffusion equilibrium in two-phase non-isothermal petroleum reservoirs. Energy Fuels 2016; 30:2021–34.
[3] Sengers JV, Kayser RF, Peters CJ, White HJ. Equations of state for fluids and fluid mixtures. Elsevier; 2000.
[4] Rowlinson JS. JD van der Waals: On the Continuity of the Gaseous and Liquid States. North-Holland; 1988.
[5] Barker JA, Henderson D. Perturbation theory and equation of state for fluids. II. A successful theory of liquids. J Chem Phys 1967;47:4714–21.
[6] Wertheim MS. Fluids with highly directional attractive forces. IV. Equilibrium polymerization. J Stat Phys 1986;42:477–92.
[7] Chapman WG, Jackson G, Gubbins KE. Phase equilibria of associating fluids: chain molecules with multiple bonding sites. Mol Phys 1988;65:1057–79.
[8] Chapman WG, Gubbins KE, Jackson G, Radosz M. New reference equation of state for associating liquids. Ind Eng Chem Res 1990;29:1709–21.
[9] Tan SP, Adidharma H, Radosz M. Recent advances and applications of statistical associating fluid theory. Ind Eng Chem Res 2008;47:8063–82.
[10] Michelsen ML, Mollerup J. Thermodynamic modelling: fundamentals and computational aspects. Tie-Line Publications 2004.
[11] Sedghi M, Piri M, Goual L. Atomistic molecular dynamics simulations of crude oil/brine displacement in calcite mesopores. Langmuir 2016;32:3375–84.
[12] Cárdenas H, Müller EA. Extension of the SAFT-VR-Mie equation of state for adsorption. J Mol Liq 2019;294:111639.
[13] Ghatee MH, Koleini MM, Ayatollahi S. Molecular dynamics simulation investigation of hexanoic acid adsorption onto calcite (101 4) surface. Fluid Phase Equilib 2015;387:24–31.
[14] Bourg IC, Lee SS, Fenter P, Tournassat C. Stern layer structure and energetics at mica–water interfaces. J Phys Chem C 2017;121:9402–12.
[15] Yousefi F, Khoeini F, Rajabpour A. Thermal rectification and interfacial thermal resistance in hybrid pillared-graphene and graphene: a molecular dynamics and continuum approach. Nanotechnology 2020;31:285707.
[16] Adapa S, Swamy DR, Kancharla S, Pradhan S, Malani A. Role of mono-and divalent surface cations on the structure and adsorption behavior of water on mica surface. Langmuir 2018;34:14472–88.
[17] Kirch A, Mutisya SM, Sánchez VM, de Almeida JM, Miranda CR. Fresh molecular look at calcite–brine nanoconfined interfaces. J Phys Chem C 2018;122:6117–27.
[18] Ricci M, Spijker P, Stellacci F, Molinari J-F, Voïtchovsky K. Direct visualization of single ions in the Stern layer of calcite. Langmuir 2013;29:2207–16.
[19] Gross J, Sadowski G. Perturbed-chain SAFT: an equation of state based on a perturbation theory for chain molecules. Ind Eng Chem Res 2001;40:1244–60.
[20] D'Arrigo JS. Screening of membrane surface charges by divalent cations: an atomic representation. Am J Physiol Physiol 1978;235:C109–17.
[21] Travalloni L, Castier M, Tavares FW, Sandler SI. Thermodynamic modeling of confined fluids using an extension of the generalized van der Waals theory. Chem Eng Sci 2010;65:3088–99.
[22] Hill TL. An introduction to statistical thermodynamics. Courier Corporation 1986.
[23] Fuchs D, Fischer J, Tumakaka F, Sadowski G. Solubility of amino acids: Influence of the pH value and the addition of alcoholic cosolvents on aqueous solubility. Ind Eng Chem Res 2006;45:6578–84.
[24] Born M, Oppenheimer R. Ann. Phys. 1927.
[25] Landau LD. EM Lifshitz Statistical Physics. Course Theor Phys 1980;5:396–400.
[26] Plimpton S. Fast parallel algorithms for short-range molecular dynamics. J Comput Phys 1995;117:1–19.
[27] Zhao J, Yao G, Ramisetti SB, Hammond RB, Wen D. Molecular dynamics investigation of substrate wettability alteration and oil transport in a calcite nanopore. Fuel 2019;239:1149–61.
[28] Berendsen HJC, Grigera JR, Straatsma TP. The missing term in effective pair potentials. J Phys Chem 1987;91:6269–71.
[29] Vega C, Abascal JLF. Simulating water with rigid non-polarizable models: a general perspective. Phys Chem Chem Phys 2011;13:19663–88.
[30] Martínez L, Andrade R, Birgin EG, Martínez JM. PACKMOL: a package for building initial configurations for molecular dynamics simulations. J Comput Chem 2009; 30:2157–64.
[31] Tarazona P, Evans R. A simple density functional theory for inhomogeneous liquids: Wetting by gas at a solid-liquid interface. Mol Phys 1984;52:847–57.
[32] Doble M. Perry's chemical engineers' handbook. New York, USA: McGraw-Hill; 2007.
[33] Knight AW, Kalugin NG, Coker E, Ilgen AG. Water properties under nano-scale confinement. Sci Rep 2019;9:1–12.
[34] Shi B, Sinha S, Dhir VK. Molecular dynamics simulation of the density and surface tension of water by particle-particle particle-mesh method. J Chem Phys 2006;124: 204715.
[35] Izadi S, Onufriev AV. Accuracy limit of rigid 3-point water models. J Chem Phys 2016;145:74501.

Paper II

Extension of SAFT Equation of State for Fluids Confined in Nano-pores of Sedimentary Rocks Using Molecular Dynamics Simulation

Sajjad Ahmadi Goltapeh, Rohaldin Miri, Per Aagaard and Helge Hellevang

Published in *Journal of Molecular Liquids*, 2022, volume 348, pp. 118045. DOI: https://doi.org/10.1016/j.molliq.2021.118045.

II

Journal of Molecular Liquids 348 (2022) 118045

Contents lists available at ScienceDirect

Journal of Molecular Liquids

journal homepage: www.elsevier.com/locate/molliq

Extension of SAFT equation of state for fluids confined in nano-pores of sedimentary rocks using molecular dynamic simulation

Sajjad Ahmadi Goltapeh [a,*], Rohaldin Miri [b], Per Aagaard [a], Helge Hellevang [a]

[a] Department of Geosciences, University of Oslo, PO Box 1047 Blindern, 0316 Oslo, Norway
[b] School of Chemical Engineering, Iran University of Science and Technology (IUST), PO Box 16765-163, Tehran, Iran

ARTICLE INFO

Article history:
Received 21 September 2021
Revised 30 October 2021
Accepted 5 November 2021
Available online 11 November 2021

Keywords:
Molecular Dynamic
Statistical Association Fluid Theory (SAFT)
Confinement Effect on Fluid Properties
Calcite Nanopore
Equation of State (EoS)
Helmholtz Free Energy of Confined Fluid
Fluid-Wall interaction Potential within a Nanopore

ABSTRACT

Confined fluids in nano-mineral pores show notably different thermodynamic behavior compared with those of the same fluid in bulk. We have extended an equation of state (EoS) inspired by statistical association fluid theory (SAFT) to incorporate the fluid-mineral effect into the pure fluid properties confined in the nanopore. The established EoS is coupled with a Helmholtz free energy contribution which is a function of confinement characteristics: the potential of fluid-mineral interaction, bulk-like density and CF. The novel fitting parameter CF relies on the local properties of confined fluid and measures the density fraction within the layering and bulk-like zones, i.e., $CF = \rho_{layering\ zone}/\rho_{bulk-like\ zone}$. The first-principle molecular dynamics (MD) simulation was utilized to estimate the confinement parameters. At T = 300 K, 350 K, 400 K, and 450 K, the NVT ensemble was applied to simulate slit-pore calcite with a continuous and homogeneous surface in contact with water, with pore widths ranging from 1.5 nm to 5 nm. After running each NVT ensemble for 6 ns, the energy and density of confined water were analyzed, and a deviation was discovered with different behavior from what had previously been reported. Coupling CF parameter with proposed EoS improves the absolute relative errors (ARE) at low temperatures up about 50%, leading to a good agreement between modified SAFT EoS and MD results. The methodology described here may be extended to include a mixture of associating fluids such as those found in oil composition and implemented in all SAFT versions.

1. Introduction

The prediction of phase diagrams and thermodynamic properties of fluids entrapped in confined spaces (i.e., diameters between 1 nm and 10 nm) is of wide practical interest as it appears in many applications, including heterogeneous catalysis [1], enhanced oil recovery (EOR) from shale reservoirs [2], carbon capture and storage (CCS) [3], hydrogen storage [4], geochemistry [5] and geophysics [6]. Confined fluids have distinct dynamical and structural characteristics so that their physical properties and phase behavior noticeably deviates from corresponding bulk phase. In fact, as the size of the confinement decreases and approaches the molecular dimensions of the trapped fluid (i.e., sizes comparable to the mean free path), the free thermal motion of fluid molecules is disrupted, which in turn creates different and unique thermodynamic properties. Experimental and numerical studies have shown that, depending on the intermolecular forces, confined fluids can exhibit specific interface-induced structures (i.e., molecular-scale arrangement, layering and orientation) which consequently results in interfacial regions of reduced density, saturation pressure and critical pressure. Anyhow, laboratory measurements of the confined fluids phase behavior are time-consuming and expensive and limited to a narrow temperature and pressure window.

Generally speaking, the size, shape and type of the intermolecular forces define the state and thermophysical properties of fluids. Standard engineering EoSs of the Van der Waals type (cubic type EoSs) are common choices for phase equilibria calculations of simple fluids in the bulk phase. The most important intermolecular forces incorporated in such EoSs are van der Waals attractions along with weak electrostatic forces due to dipoles, quadrupoles, etc. For more complex fluid-wall interactions with strong molecular forces, the simple repulsive reference term in engineering EoSs is not sufficient, and the predictability of fluid properties and phase equilibria (especially the subcooled liquid phase) is poor. To this end, Zarragoicoechea and Kuz [7,8] modified van der Waals EoS [9] to show the shift in critical pressure and temperature. The resulting EoS, however, failed to predict the critical density of the confined fluid accurately. Derouane [10] modified the van der

* Corresponding author.
E-mail address: sajjadah@uio.no (S. Ahmadi Goltapeh).

https://doi.org/10.1016/j.molliq.2021.118045
0167-7322/

Nomenclature

A	Helmholtz free energy [kcal]
a	Intensive Helmholtz free energy [kcal/mol]
CF	fraction of confined molecules
E_{conf}	Configurational energy [kcal]
g(r, ρ)	Radial distribution function
k	Boltzmann constant
K_E	Kinetic Energy [kcal/mol]
L	Length of the water mounted above calcite [A]
m	Particle mass [kg]
N	Total number of particles
N_C	Coordination number
p	Momentum [kg.m/s]
u	Potential energy [kcal/mol]
u^0	Segment energy for the dispersive interaction, u/k in [K]
Q	Canonical partition function
q_{int}	Contribution of the partition function for internal energy
r	Position [m]
T	Temperature [K]
U	Internal Energy [kcal]
v^{00}	Segment volume [ml/mol]
V	Volume [A^3]

Greek Letters

σ	Average molecular diameter [Å]
λ	de Broglie wave length [Å]
Λ	Segment diameter [Å]
ε	Potential of fluid-wall interaction [kcal/mol]
κ	Association volume
ρ	Density [kg/m^3]
δ	Square well potential width [Å]
ϕ	Association energy, ϕ/k in [K]
μ	Chemical potential [kcal/mol]

Subscripts and Superscripts

ass	Association
conf	Configurational
conf-ff	Configurational due to fluid-fluid interaction
conf-fw	Configurational due to fluid-wall interaction
chain	Chain
dis	Dispersion
f	free
ff	Fluid-Fluid
fw	Fluid-Wall
hs	Hard sphere
i,j	counter
int	Internal
max	maximum
z	z-axis

Waals equation with a correction parameter accounting for internal pressure caused by fluid-wall interactions to describe the behavior of confined fluid in a zeolite micropores. Although this model shows good ability in predicting reduced critical temperature and reduced critical specific volume, it still shows a significant difference in predicting increased critical pressure compared to laboratory data.

As previously stated, the cubic EoSs are far less precise to predict physical properties of the associating molecules such as water existing in porous formations in nature. The molecular associations originate from strong intermolecular forces, e.g., permanent dipoles and hydrogen bonding. The associating molecules not only have strong interaction with pore walls, but they also interact strongly with each other [11]. Thus, the framework of cubic EoS is obscured by an impediment, which is the nature of intermolecular interactions of confined fluid. On the other hand, statistical associating fluid theory (SAFT) EoSs, are built on a reference term that, unlike cubic EoSs, can account for chain length (molecular shape) and molecular association. In this regard, Pan and Piri [12] coupled the Young-Laplace Equation with PC-SAFT to investigate the phase equilibrium for pure fluids and binary mixtures confined in nanopores. The derived EoS accurately depicts the capillary-condensation phenomenon, but it overestimates the fluid–fluid molecular interaction as the pore size decreases, which is inconsistent with the original PC-SAFT EoS.

Since all other thermodynamic properties can be estimated through Helmholtz free energy, it is common to formulate the SAFT EoS in terms of dimensionless residual Helmholtz energy. To determine the residual Helmholtz energy for a confined fluid and modify SAFT-type EoS accordingly, one needs to calculate the confinement parameters and local properties in advance. Nevertheless, the underlying mechanism of fluid-wall interactions is inaccessible to current experimental techniques. Therefore, a reliable approach for confined property estimation is required. The alternative method of estimating the local properties of the fluid inside a nanopore is semi-empirical models such as Langmuir [13], Freundlich [14], and Brunauer-Emmett-Teller (BET) [15]. However, these techniques cannot capture phase transition between confined fluid and bulk fluid [16]. The next alternative is the application of molecular simulation to investigate the properties of fluid confined in pores. For example, density functional theory (DFT) [17–20] with a robust theoretical basis determines the local properties of confined fluid. DFT provides a density profile at the most stable energy state by minimizing the grand potential energy. Although DFT is a precise method, simulation of complex systems (fluid confined in a pore) with DFT is complicated and includes high computational impact.

Molecular Dynamic simulations (MD) have become a routine tool to capture the local properties of fluid confined in pores [21,22]. MD simulations not only allow simulating a molecular structure with known chemistry but also provide for comprehensive studies into the underlying mechanism of fluid-wall interaction and its impact on fluid properties. MD simulation is a reliable tool to study the effect of fluid-wall interaction on interfacial properties [23,24] and thermodynamic behavior [25] of fluid confining in the nanopores. Giovambattista et al. [26] used MD to study the behavior of water confined between hydrophobic and hydrophilic nano-plates at isobaric conditions. They reported that a drop in temperature reduces the effective hydrophobicity of nanoscale domains. Sedghi and Piri [27] investigated the pressure of methane confined in graphite pores with MD simulations. For small size pores, they reported no occurrence of capillary condensation under the critical size. In contrast, they noticed the capillary condensation within the larger pores.

Few research studies, however, have sparked interest in using MD technique to investigate the associating fluid contained in a specific mineral. For instance, Zhao et al. [28], applied MD to investigate the contact angle of n-decane dissolved in water inside a calcite nanopore at various salt concentrations. They have reported that the contact angle of n-decane decreases with increasing the

salinity implying improvement in calcite surface hydrophilicity. S. Ahmadi G. et al. [29], used MD simulation to study the water-calcite interface. They developed an EoS inspired by Perturbation-Chain SAFT (PC-SAFT) to predict the water properties near the calcite-wall, and the results were promising. There are even fewer who have developed a well-defined match parameter that is consistent with the confined fluid characteristics [30]. In the current study, first, we used statistical thermodynamics to build a model that represented the Helmholtz free energy of confined fluid as a function of nanopore characteristics. The necessary parameters for the developed Helmholtz are then calculated using MD simulation. In MD simulation, the surface $(10\bar{1}4)$ of calcite was chosen as the mineral surface to interact with pure water as the associated fluid. Finally, we presented a physical coefficient that very closely matches predictions of the modified SAFT with MD results. The rest of this paper will be structured as follows: The theoretical background is given in Section 2. Sections 2.1 and 2.1.1 discuss the EoS and SAFT key characteristics. Section 2.2 contains details on the MD simulation. Finally, in Sections 3 and 4, the study's findings are reviewed and summarized.

2. Theoretical background

In this section, the Helmholtz energy term related to fluid–solid interaction inside a slit shape calcite nanopore is derived based on statistical mechanics. Then, the theoretical aspects of MD simulation are discussed in detail.

2.1. Equation of state (EoS)

Equation of state has a crucial role in describing phase behavior and chemical equilibria in geochemical processes. Recent developments in statistical mechanics have introduced a molecular-based EoS, which models associating fluids and complex interactions accurately. The molecular-based EoS inspired by statistical association fluid theory (SAFT) [31,32] formulates all types of molecular interactions with a sum of corresponding Helmholtz energy. Unlike PVT EoS, which utilizes complex mixing rules and unphysical binary coefficients, one can model a fluid–solid interaction with a definition of Helmholtz energy for fluid–solid interaction. The following section describes the details of the Helmholtz free energy derivation.

2.1.1. Basic formulation of the Helmholtz free energy for confined fluids

This section presents an overview of a model formulation based on the generalized van der Waals partition function [33]. The supplemental information includes an in-depth explanation that may be referred to. Fig. 1 illustrates the conceptual framework used to model water confined in a calcite nanopore. As shown, the confinement is divided into three regions depending on the type of molecular interaction.

Region I (bulk-like) is the closest Region to the pore center and furthest from pore-walls, such that the interactions between pore-wall and water molecules are minimal and can be neglected. In other words, within Region I, water-water interactions provide the main contribution to the configurational energy of the system. Region II (layering zone), which surrounds Region I and lies between a bulk-like and a forbidden region, is dominated by water-calcite interactions. The thickness of Region II is shown with δ_{fw}. The nearest Region to the pore-wall is Region III, the intermediate zone between Region II and calcite slabs. The forbidden zone with a thickness of $\sigma_i/2$ displays an empty margin adjacent to the pore-walls with no water molecule inside. The mean diameter of water molecules is represented by σ_i. Thus, the thickness of Region III is sufficiently thin that no water molecule center of mass dwells there ($\sigma_i/2 \leq 0.85$ [Å]). L_Z is the distance between the pore-walls representing the confinement width and thickness of water settled within calcite slabs. In fact, summing the length of bulk-like, double layering and double forbidden zones gives the total length of the L_Z. The fluid–fluid molecular interactions are assumed to interact through a square well potential:

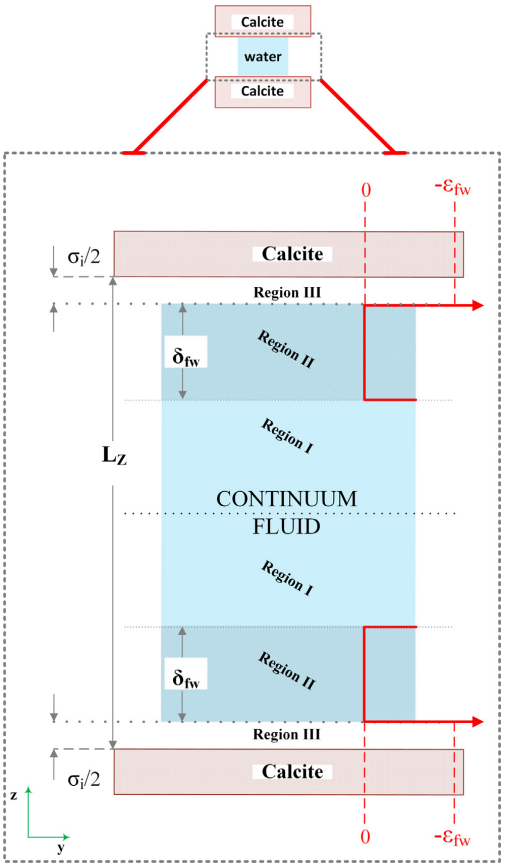

Fig. 1. Simulation geometry illustration including water molecules sandwiched within the slit shape calcite nanopore. In this sketch, L_z denotes the width of the nanopore. The pore volume has been divided into three different regions based on the interactions between different molecules. Region I is the nearest Region to the pore center and furthest from the calcite-wall. Region II is a layering zone where the dominant molecular interaction is water-calcite interaction. The thickness of Region II is shown with δ_{fw} at the top and bottom. Region III, with a thickness of $\sigma_i/2$ presents a vacant margin adjacent to the nanopore walls with no water molecule inside.

$$u_{ij}(r_{ij}) = \begin{cases} \infty & r_{ij} < \sigma_{ij} \\ -\varepsilon_{ij} & \sigma_{ij} < r_{ij} < \sigma_{ij} + \delta_{ij} \\ 0 & r_{ij} > \sigma_{ij} + \delta_{ij} \end{cases} \quad (1)$$

where, r_{ij} is molecule–molecule distance, ε_{ij} is the square well depth, δ_{ij} is the square well width, and σ_{ij} is the mean molecular diameter. The parameters of pure water utilized in SAFT2 are listed in Table 1 [34].

Table 1
SAFT2 parameters for pure water.

v^{00} [ml/mol]	u^0/k [K]	Λ	φ/k [K]	κ
9. 8307	311.959	1.5369	1481.41	0.04682

As can be seen, v^{00} segmment volume, u^0/k segment energy, Λ segment diameter, φ/k association energy and κ association volume are SAFT2 parameters for pure water. Similarly, the fluidand solid molecules interact through a square well potential of the following form:

$$u_{fw}(L) = \begin{cases} 0 & L < L_Z - 2\sigma_i - 2\delta_{fw} \\ -\varepsilon_{fw} & L_Z - 2\sigma_i - 2\delta_{fw} < L < L_Z - 2\sigma_i \\ \infty & L > L_Z - 2\sigma_i \end{cases} \quad (2)$$

As seen, L is the longitudinal position of a fluid molecule inside the pore.

The first condition in this potential function relates to Region I, which has a zero square well potential. The second depicts Region II, where water and calcite molecules interact with $-\varepsilon_{fw}$ square well potential. Region III is subjected to the last condition, in which the energy level is so high that no water molecule may settle there.

We begin by defining the partition function to develop a meaningful term for Helmholtz free energy that incorporates the pore wall effect.

$$Q_{N,V,T} = \left(\frac{q_{int}^N}{\lambda^{3N} N!}\right) V_f \exp\left(\int_\infty^T \frac{E_{conf}}{kT^2} dT\right) \quad (3)$$

For a system including N particles with mass m, the canonical partition function, Q, is defined as presented in Eq. (3) [33,35]. Where q_{int} is the internal partition function, λ is de Broglie thermal wavelength, k is Boltzmann constant and T is the absolute temperature. In Eq. (3), E_{conf} and V_f denote the configurational energy and free volume, respectively. (supplementary information, section A and B). As observed in Eq. (3), the lower limit of the integral depicts high temperature ($T \to \infty$) when fluid behavior approaches ideal gas behavior, while the upper limit of the integral represents the actual fluid situation. Once the partition function is established, we may express the Helmholtz free energy as:

$$A_{N,V,T} = -kTQ_{N,V,T} \quad (4)$$

Eqs. (3) and (4) are sufficient to model Region I dominated by water-water interactions. However, the thermodynamic description of the system is incomplete since it does not include the interaction between the water molecules and the calcite-wall. As previously stated, no water molecule resides within Region III, where no water-water and nor water-calcite interaction exists. In order to model the thermodynamics of Region II with water-calcite dominant interaction, a definition for Helmholtz free energy of water-calcite interaction must be derived. To this end, E_{conf} is split into fluid–fluid and fluid-wall species:

$$E_{conf} = E_{conf-ff} + E_{conf-fw} \quad (5)$$

replacing the recently defined E_{conf} in Eq. (5) with a similar term in Eq. (3) gives Eq. (6):

$$Q_{N,V,T} = \left(\frac{q_{int}^N}{\lambda^{3N} N!}\right) V_f \exp\left(\int_\infty^T \frac{E_{conf-ff}}{kT^2} dT\right) \exp\left(\int_\infty^T \frac{E_{conf-fw}}{kT^2} dT\right) \quad (6)$$

The first three components in Eq. (6) define Helmholtz for water-water interaction, whereas the last term defines Helmholtz for water-calcite interaction.

$$Q_{N,V,T} = \exp\left(-\frac{A^{ff}}{kT}\right) \exp\left(-\frac{A^{fw}}{kT}\right) \quad (7)$$

Eq. (7) explains the partition function with respect to the Helmholtz free energy, where the natural logarithm gives:

$$\ln Q_{N,V,T} = -\frac{1}{kT}\left(A^{ff} + A^{fw}\right) \quad (8)$$

When Eqs. (8) and (7) are compared, the independent definition of the water-calcite Helmholtz contribution may be formulated as follows:

$$\left(\frac{A^{fw}}{kT}\right) = \left(-\int_\infty^T \frac{E_{conf-fw}}{kT^2} dT\right) \quad (9)$$

Substituting A_{ff} in Eq. (8) with the appropriate contributions yields a complete description for the thermodynamics of water confined in calcite pore:

$$\ln Q_{N,V,T} = \left(\frac{-1}{NkT}\right)\left(A^{hs} + A^{dis} + A^{chain} + A^{ass} + A^{ion} + A^{fw}\right) \quad (10)$$

The superscripts of Helmholtz species in Eq. (10) refer to the hard-sphere, dispersion, chain, association, ionic and fluid-wall interactions. The closed-form expression of the partition function with respect to the residual molar Helmholtz species is stated as below:

$$\ln Q_{N,V,T} = \left(\tilde{a}^{hs} + \tilde{a}^{dis} + \tilde{a}^{chain} + \tilde{a}^{ass} + \tilde{a}^{ion} + \tilde{a}^{fw}\right) \quad (11)$$

The ion species ($\tilde{a}^{ion}$) in Eq. (11) is zero because the water is assumed pure and devoid of any ions. A bulk fluid's configurational energy is proportional to the fluid–fluid interactions occurring across the system whereas, for the confined fluid, an E_{conf} must account for the fluid-wall interactions as well. According to Eq. (2), the fluid and pore wall molecules interact through a square well. Extending the concept of E_{conf} to include fluid-wall interactions while assuming the pairwise potential for intermolecular interactions results in (supplementary information, section C):

$$E_{conf} = -\frac{N}{2} N_c \varepsilon_{ff} - N_P \varepsilon_{fw} \quad (13)$$

In Eq. (13), N_c represents coordination number and N_P is defined as:

$$N_P = N \times CF \quad (14)$$

and the following formula should be used to calculate the CF parameter:

$$CF = \frac{\rho_{RegionII}}{\rho_{RegionI}} \quad (15)$$

According to Eq. (15), the ratio density at different regions designates the CF parameter. The proposed CF carries a physical notion and depends on the properties of the fluid confined in the mineral pore. In addition to a conceptual basis, the newly defined parameter in Eq. (15) establishes a relationship between E_{conf} and the density ratio of confined fluid at various regions. From the above analysis, one can write the expression of the chemical potential of Region II as the derivative product of the partition function (supplementary information, section D):

$$\mu = kT\left(\ln(\lambda^3) - \ln\left(\frac{1}{\rho} - \frac{1}{\rho_{\max}}\right) - \left(\frac{\varepsilon_{ff}}{kT} - 1\right) - \left(\frac{\varepsilon_{fw}}{kT}\right)\right) \quad (16)$$

2.2. Molecular Dynamic (MD) simulations

Molecular dynamic simulation [36] was performed to investigate the structural configuration of confined water and calculate ρ, ρ_{max}, ε_{fw} and *CF* factor. A comprehensive approach for MD simulation is described in the next section.

2.2.1. Nanopore geometry

Fig. 2 illustrates the initial configuration of the water-calcite system inside the simulation box. The simulation box includes the mobile phase (water molecules) and immobile phase (calcite nanopore). The immobile phase is composed of two parallel calcite slabs, which enclose the water molecules with a rectangular segment normal to the z-axis. To study the effect of the pore size, we used several nanopores with fixed lengths and different widths. The pore walls were extended along the x and y axes with a length of 4 nm and 20 nm, respectively. Along the z-axis, the width of the nanopore remains fixed for each pore and varies between 1.5 nm, 2 nm, 3 nm, 4 nm, and 5 nm for various realizations. The distance between the opposing wall edge atoms identifies the pore width. The parallel calcite slabs are, composed of 6 layers of $(10\bar{1}4)$ cleaved calcite surface with rhombohedral structure, $R\bar{3}c$ space group, and unit cell parameters of a = b = 4.988 Å, c = 17.061 Å; α = β = 90°, γ = 120° [37]. The calcite was cleaved along the $(10\bar{1}4)$ surface because this plane is the most stable surface of calcite [38]. The water molecules were sandwiched within the nanopore with the PACKMOL [39] software.

2.2.2. Simulation details

The Large-scale Atomic/Molecular Massively Parallel Simulator (LAMMPS) [40] was used to run all molecular dynamic simulations. For calcite, the force field was obtained from the model developed by Raiteri et al. [41]. The SPC/Fw [42] water model, consistent with Raiteri's model, was employed to model water molecules. The long-range electrostatic interactions were calculated by the particle–particle–particle-mesh method (PPPM) [43] with a relative tolerance of 10^{-5}. The periodic boundary conditions were specified for all directions, namely x, y and z-axes. According to Raiteri's model, the cut-off 9Å was used for all short-range potentials with a taper function applied over the last 3Å. The simulation begins with the minimize function, which reduces energy by maintaining the molecules at a reasonable distance. Then, the simulation run continues with the canonical ensemble (NVT), at T = 300 K, 350 K, 400 K and 450 K. The Nose-Hoover [44] thermostat was used to regulate the temperature. Each simulation took 6 ns to complete (1 ns for equilibrium and 5 ns for data production).

2.2.3. Model parameter extraction

To determine the Helmholtz free energy at a specific pore size and a certain temperature, primarily the confinement parameters,

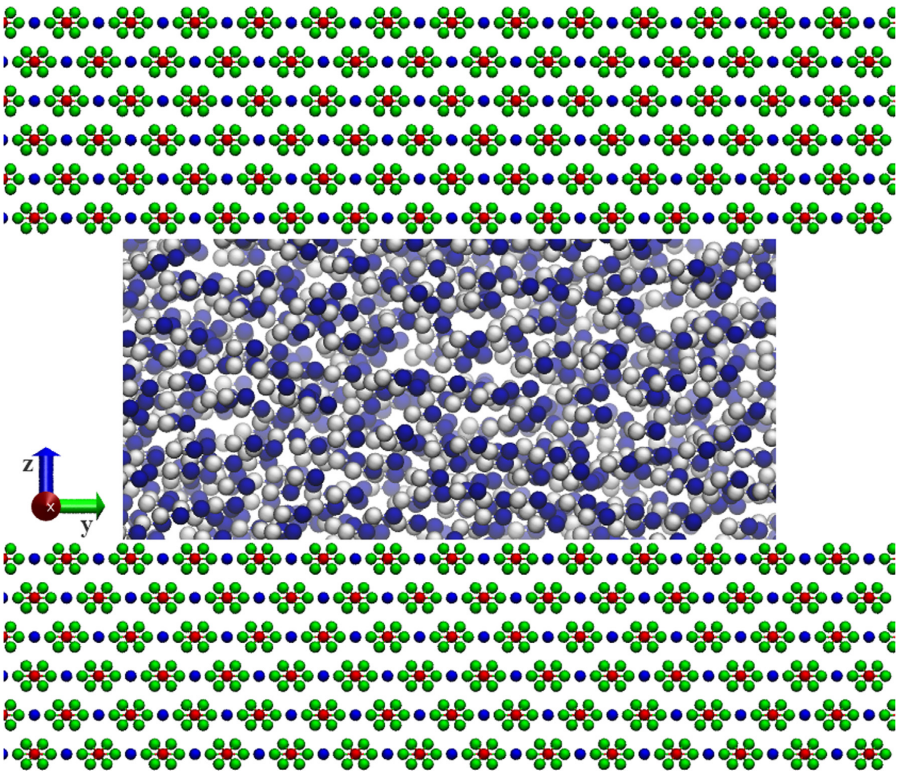

Fig. 2. Illustration of water molecules entrapped within the slit-shaped calcite nanopore, along y and z-axes. The calcite layers were cleaved along the surface $(10\bar{1}4)$ with a fixed length of 20 nm. Along the z-axis, the pore width varies between 1.5 nm, 2 nm, 3 nm, 4 m and 5 nm to make different pore sizes.

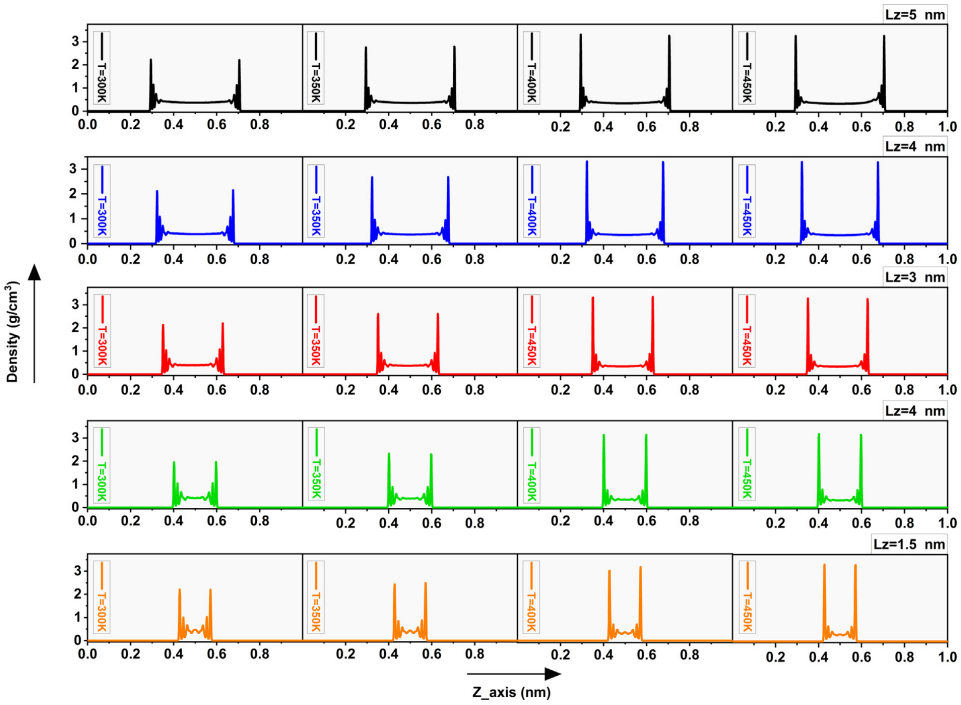

Fig. 3. Illustration of density profile inside Region I and Region II at several pore sizes and different temperatures. The plotted figures in each row and column represent the density profile at constant L_z and temperature, respectively. From left to right, the simulation temperature increases from 300 K to 450 K, while from top to bottom, the L_z increases from 1.5 nm to 5 nm.

i.e., ρ, ρ_{max}, ε_{fw} and CF factor, should be determined. In Fig. 1, δ_{fw} represents the thickness of the layering zone inside the calcite nanopore. In order to compute $\delta_{fw,}$ the margins of Region II must be specified. The terminus of Region III, where $z = \sigma_i$, is the bottom band for Region II. The top band coincides with the commencement point of Region I, where the density trend stabilizes after significant fluctuations. According to the general sketch of density profile in Figs. 3 and 4, after prominent peaks at Region II, the position in which the density experience 110% of the minimum density at the bulk-like zone is assumed the endpoint of Region II. Based on this assumption, which clarifies the thickness of δ_{fw}, the integral product of density and energy over δ_{fw} gives the average density and average energy within the layering zone. It implies that the integral swipes the area under the curve from $z = \sigma_i$ to the point where Region I and II intersect.

3. Results and discussion

In order to calculate the confinement parameters, MD simulations were conducted. The predictions of SAFT2 were then validated against MD results.

3.1. Density profile at constant L_z

Table 2 lists the water density determined using experiment, MD and SAFT2. The reported water densities in Table 2 correspond to the water molecules, which lacks a slit calcite nanopore. Indeed, Table 2 compares the MD, and SAFT2 results to experimental data obtained at T = 300 K, 350 K, 400 K and 450 K. As seen, without the presence of calcite pore, MD, and SAFT2 predict the water density with a reliable absolute relative error.

Fig. 3 illustrates the density profile of water along the z-axis, which is confined inside the calcite nanopore at different L_z and temperatures. The plots at each row include the density profile at constant $L_{z,}$ while the parallel columns show the density profile at a constant temperature. The L_z at the first row is 5 nm, decreasing to 4 nm, 3 nm, 2 nm, and 1.5 nm from top to bottom. From left to right, the temperature increases from 300 K to 350 K, 400 K and 450 K. The observed peaks and troughs coincide with the attractive potential of the parallel calcite-walls, providing two distinct layering zones within the nanopore. The layering zones correspond to the lower and upper walls in Fig. 2, showing the density profile within Region II. In other words, the large density oscillations at the left and right sides of the plots in Fig. 3 detect the boundary of Region II adjacent to the lower and upper walls in Fig. 2. In Fig. 3, the side density oscillations of each pore are considerably higher amplitude than the center ones, leading to a lower density than near the wall. The density trends from both sides then overlap at the middle, forming boundaries of Region I with lower density.

Fig. 4 compares the density profile along the z-axis at fixed confinement and different temperatures. For L_z = 5 nm, 4 nm, 3 nm, 2 nm and 1.5 nm, the density decreases within the bulk-like zone and increases at the layering zone with raising the temperature. To be specific, at each confinement, the color sequence of curves within the bulk-like zone starts from blue at the bottom and reaches red at the top, indicating that low temperature leads to higher density. This observation is similar to the thermodynamic

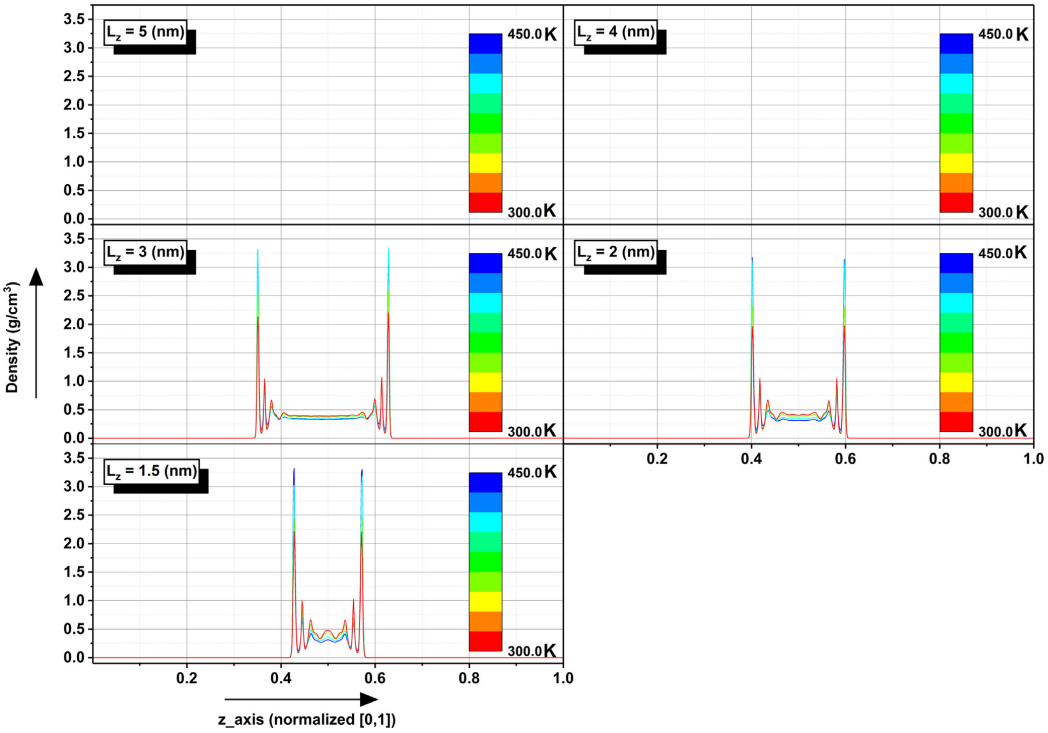

Fig. 4. Comparison of density profile inside Region I and Region II at fixed L_z and different temperatures. The cool-warm colors show the temperature variation. Within Region I, the density decreases by increasing the temperature. Inside Region II, higher temperature provides higher density values.

Table 2
List of the water density at different temperatures without the presence of calcite-wall. This table compares the laboratory data with the outcomes of MD, and SAFT2. The columns RE-1 and RE-2 display the relative error for MD and SAFT2, respectively.

	Liquid water density				
T [K]	Laboratory [kg/m^3] [45]	MD [kg/m^3]	SAFT2 [kg/m^3]	ARE-1 %	ARE-2 %
300	996.499	1000.003	996.779	0.351	0.028
350	973.693	970.383	973.567	0.339	0.013
400	937.465	923.463	936.508	1.494	0.102
450	890.319	861.221	890.234	3.268	0.954

behavior of water without the presence of a calcite pore, showing that the density inside Region I is controlled by the water-water molecule distance. In contrast, in the bottom-top view, the colors are sorted from red to blue within the layering zone as the temperature rises from low to high. The reason refers to detaching the water molecules from resided water molecules in Region I and joining the layering zone due to thermal expansion because the water molecules inside Region I have more freedom than those in Region II. Therefore, as the temperature rises, the distance between the water molecules in the bulk-like zone increases, resulting in a reduction in density.

On the other hand, a rise in temperature traps the water molecules in the layering zone, leading to an increase in density. For L_z = 1.5 nm, the density behavior at the middle of pore space differs from the observed density trend for L_z = 5 nm, 4 nm, 3 nm and 2 nm. In other words, for the confinements larger than L_z = 1.5 nm, the density trend experience a minimum at the middle of slit-pore calcite. However, for L_z = 1.5 nm, the density trends overlap at the middle of the pore after some oscillations. For L_z = 1.5 nm, although the density has not experienced a minimum, the density value at the center of the pore still remains less than the density peaks within the layering zone.

The distinct behavior of density trends within Regions I and II highlights diverse interactions within regions located inside the calcite nanopore. This categorical pattern actually supports our assumptions for Eqs. (1) and (2), which state that the dominant interactions in Regions I and II are is water-water and water-calcite interactions, respectively.

In order to calculate the average density within Region II, the integral product of the density curve within the layering zone was estimated according to the mentioned approach in Section 2.2.3. Table 3 shows the results of the integral product at various temperatures within the layering zone. According to MD predictions in Table 3, with fixed temperature, the density

Table 3
The average density within Region II, calculated with MD simulation.

	MD [kg/m^3]			
Lz [nm]	T = 300 K	T = 350 K	T = 400 K	T = 450 K
15	538.611	540.534	554.982	588.772
20	535.330	538.349	558.196	598.881
30	543.881	565.724	603.235	633.732
40	544.459	570.622	619.335	633.900
50	561.334	584.642	626.310	664.964

increases by increasing the pore size (L_z). Namely, larger L_z provides a higher density value within the layering zone. In addition, at constant L_z, the density increases with the rise in temperature from 300 K to 450 K.

3.2. Density profile at a constant temperature

Fig. 5 shows the density profile at constant temperature and various L_z. The plots in Fig. 5 are presented versus normalized L_z so that various trends on a given axis may be easily compared. As seen at the top left corner, with T = 300 K, pore size varies as L_z = 5 nm to 4 nm, 3 nm, 2 nm, and 1.5 nm. Following the same L_z trend, the temperature increases to T = 350 K, T = 400 K, and T = 450 K in the other plots. As can be observed, the area under the curve in Region I and Region II develops as L_z increases from 1.5 nm to 2 nm, 3 nm, 4 nm, and 5 nm at a fixed temperature. In other words, as the pore size rises and the temperature remains constant, the average density within the layering zone and central zone increases. This is owing to the integral product results, which show that the average density of the layering zone and central zone grow with L_z size. Beyond the mathematical reason, it is expected that the average density within the layering zone approaches ρ_{max} because when the pore size extends along the z-axis ($L_z \rightarrow \infty$), the confined water behavior approaches bulk behavior.

As the pore sizes become narrower, the oscillations become less pronounced until L_z = 1.5 nm, exhibiting a unique behavior, as seen in Figs. 4 and 5. Because the threshold of short-range potentials (i.e., cut-off) is set to 9 Å in MD simulations, causing the attractive potentials from both walls to overlap. In other words, for L_z = 1.5 nm, all water molecules inside the pore space are affected by pore-wall attraction which leads to the disappearance of the bulk-like zone. To sum up, when an associating fluid such as water is confined within a calcite nanopore, different zones in the density profile arise due to the contest between water-water and water-calcite interactions. Because the water-calcite interaction is prominent inside the layering zone, the tiny pore sizes with tighter confined water are more influenced. It means that as the pore size

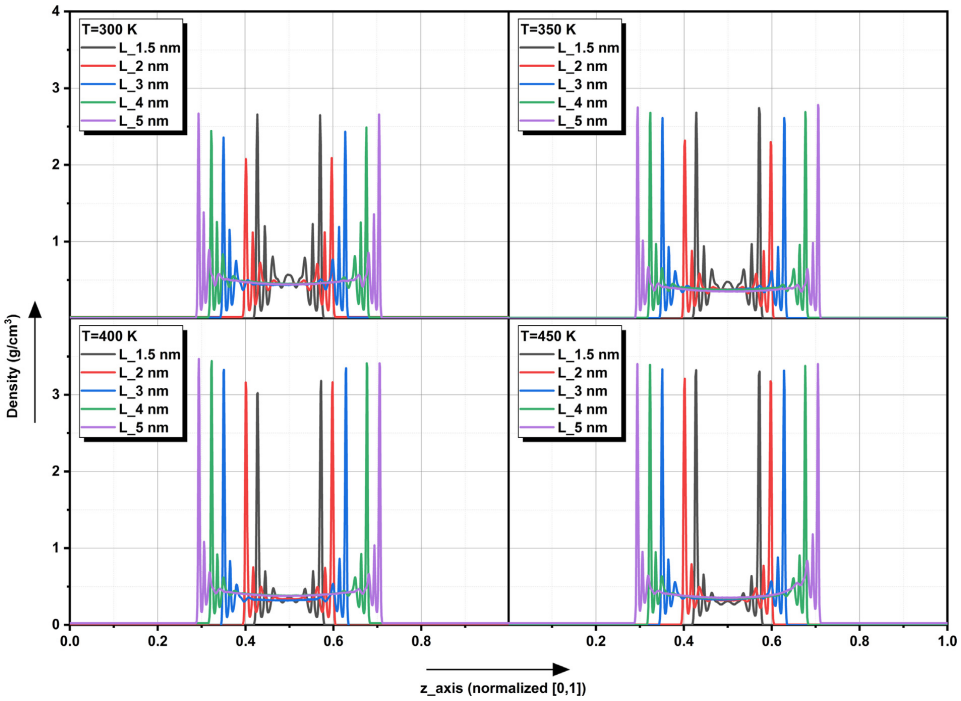

Fig. 5. Comparison of density profile at fixed temperature and different L_z. By increasing the L_z from 1.5 nm to 2 nm, 3 nm, 4 nm, and 5 nm, the area under the curve extends, which means the integral product results in a larger average density within Region II.

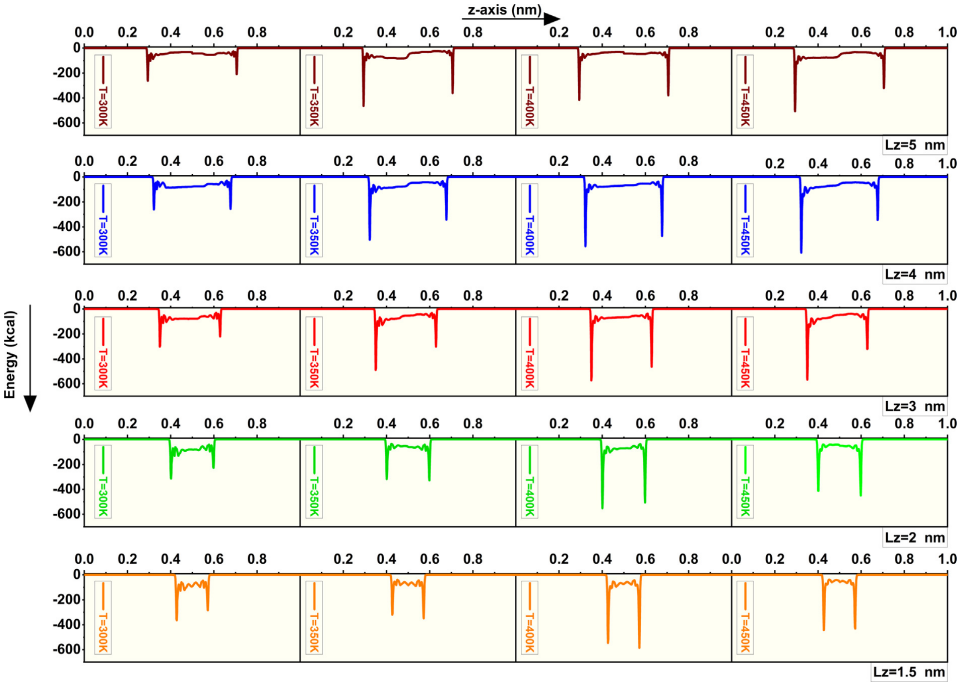

Fig. 6. Illustration of energy profile inside Region I and Region II at several L_z and different temperatures. The plotted figures in each row and column represent the energy trend at constant L_z and temperature, respectively. From left to right, the simulation temperature increases from 300 K to 350 K, 400 K and 450 K, while from top to bottom, the L_z decreases from 5 nm to 4 nm, 3 nm, 2 nm and 1.5 nm.

increases, the calcite-wall attraction over confined water diminishes and the average density within the layering zone approaches the bulk density. Therefore, the rise in pore size results in a larger average density within the layering zone.

3.3. Energy behavior

Fig. 6 displays the trend of the total energy at different L_z and temperatures. The parallel columns display the energy trend at constant temperature and L_z = 5 nm, 4 nm, 3 nm, 2 nm, and 1.5 nm. The horizontal rows depict the energy variation along the z-axis at constant pore size and T = 300 K, 350 K, 400 K and 450 K.

Within each row, the length of the energy peaks inside Region II increases by increasing the temperature. At the same time, the average energy is diminished within Region I. The average energies within Region II have been reported in Table 4 at different L_z and temperatures. To calculate the average energy amount, we utilized the same approach as the average density mentioned in Section 2.2.3. The general trend of energy follows the general profile in Fig. 3 and Fig. 4, although there are some deviations. The deviation refers to the fact that the average energy depends not only on intermolecular distance but also on the polarity of the surrounded molecules. Hence, reduction of intermolecular distances will not necessarily increase the average energy. As seen, inside Region I, far from the calcite-walls attractions, the water-water molecule

Table 4
Estimated confinement parameters with MD simulations. The ε_{fw}, ρ_{max} and CF respectively present the potential of water-calcite interaction, bulk-like density and fraction of confined molecules.

	T = 300 [K]		
L_z [nm]	ρ_{max} [kg/m^3]	ε_{fw} [kcal/mol]	CF
1.5	1000.003	−104.812	1.265
2	1000.003	−97.054	1.274
3	1000.003	−80.955	1.352
4	1000.003	−68.595	1.358
5	1000.003	−66.359	1.418
	T = 350 [K]		
1.5	970.383	−87.265	1.356
2	970.383	−82.545	1.355
3	970.383	−100.997	1.467
4	970.383	−99.374	1.479
5	970.383	−72.459	1.520
	T = 400 [K]		
1.5	923.463	−118.846	1.621
2	923.463	−107.626	1.582
3	923.463	−104.772	1.694
4	923.463	−103.333	1.693
5	923.463	−80.896	1.684
	T = 450 [K]		
1.5	861.221	−94.175	1.962
2	861.221	−96.512	1.821
3	861.221	−113.021	1.803
4	861.221	−119.647	1.737
5	861.221	−97.356	1.804

distance controls the density and energy. Whereas, within Region II, which is close to calcite-wall, water-calcite interaction and polarity of the molecules in the neighborhood control the total energy.

Raising the L_z causes a rise in the average energy within Region I. This is because when L_z increases, the confined water approaches the bulk behavior and water-water molecule distance decreases due to the growth in density. Namely, the calcite-wall shows a

Table 5
Comparison of MD and modified SAFT2 at different L_z and temperatures within Region II.

	MD [kg/m^3]			
Lz [nm]	T = 300 K	T = 350 K	T = 400 K	T = 450 K
15	538.611	540.534	554.982	588.772
20	535.330	538.349	558.196	598.881
30	543.881	565.724	603.235	633.732
40	544.459	570.622	619.335	633.900
50	561.334	584.642	626.310	664.964
L_z [nm]	Modified SAFT2 [kg/m^3]			
	T = 300 K	T = 350 K	T = 400 K	T = 450 K
15	622.658	692.575	567.507	665.047
20	653.560	711.284	611.498	655.722
30	717.403	637.836	622.817	590.227
40	765.694	644.305	628.537	564.407
50	774.111	750.790	717.793	652.355
L_z [nm]	Modified SAFT2-include CF coefficient [kg/m^3]			
	T = 300 K	T = 350 K	T = 400 K	T = 450 K
15	466.654	572.643	459.406	603.770
20	507.362	597.384	504.684	581.898
30	605.191	520.258	531.130	505.224
40	672.326	529.900	537.765	469.555
50	691.367	670.805	644.483	576.480

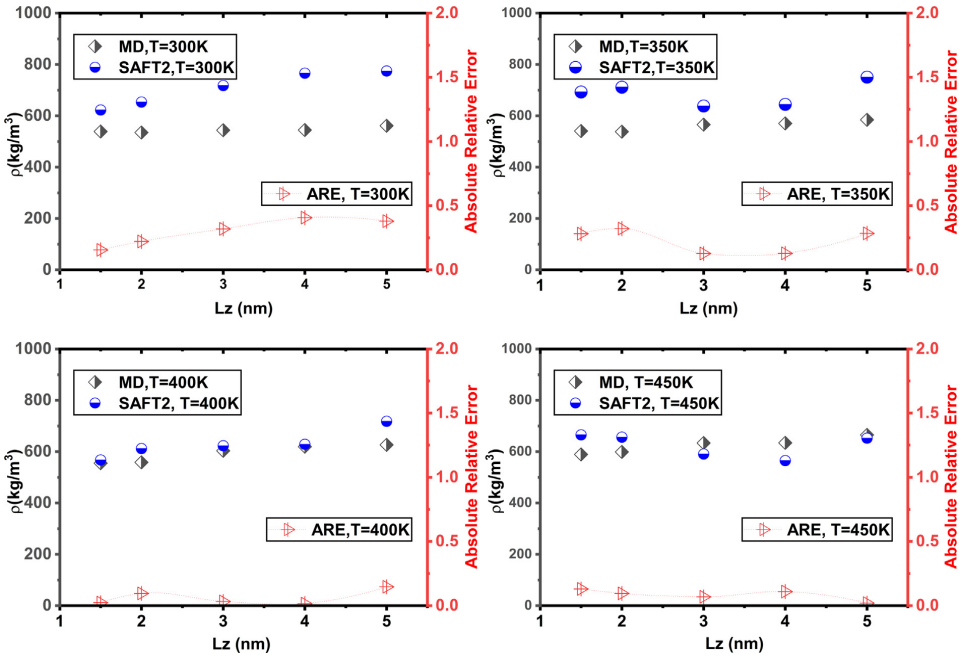

Fig. 7. The graph compares MD and modified SAFT2 predictions for T = 300 K, 350 K, 400 K, and 450 K. The diamond reflects MD findings, whereas the circles indicate modified SAFT2 results without taking the CF factor into account. The profile of absolute relative error at the bottom of each plot box depicts the divergence of modified SAFT2 from MD results. The Absolute Relative Error is higher with T = 300 K and T = 350 K, as can be observed.

stronger attraction to the thin water than the thick one. However, no consistent trend is detected within Region II. As can be seen, the average energy responds differently as the pore size rises at a constant temperature. This is because, inside Region II, the distance between water molecules does not determine the energy value, and other parameters, such as the polarity of the closed neighbors, come into play. Therefore, a larger pore size at a constant temperature necessarily does not give larger average energy.

The estimated confinement parameters with MD simulation are shown in Table 4. The ε_{fw}, ρ_{max} and CF respectively present the potential of water-calcite interaction, bulk-like density and fraction of confined molecules. The given values for ρ_{max} are identical to those calculated in Table 2 with MD.

3.4. Comparison of SAFT2 and MD simulation

Table 5 presents calculated confinement parameters under different confinement sizes and temperatures. Water was simulated using MD without the presence of the slit-pore calcite in order to calculate the bulk density. The integral of the energy distribution throughout the layering zone was utilized to calculate the potential of water-calcite interaction. The CF factor, or the fraction of confined molecules, was determined by $\rho_{RegionII}/\rho_{RegionI}$.

As indicated in Table 5, the calculated confinement parameters were entered into the modified SAFT2 to estimate the water density inside Region II. Table 5 shows the MD and modified SAFT2 projections for Region II. The graphs in Figs. 7 and 8 provide a comparison between the outcomes of MD and modified SAFT2. The vertical axis shows the Absolute Relative Error (ARE) on the right hand side of the graphs. It reflects the divergence of modified SAFT2 from the MD findings. The density values predicted by MD and modified SAFT2 are shown on the vertical axis at the left hand side. It is important to note that the CF factor is applied to Fig. 8, while it is not applied at either temperature in Fig. 7. To be specific, the circles represent modified SAFT2 findings that were obtained without taking the CF factor into consideration, while the squares represent modified SAFT2 results that were obtained with the CF factor taken into account. The diamond represents MD results, while the triangles represent the ARE.

Fig. 7 shows that when T = 400 K and T = 450 K, the predictions of modified SAFT2 match well with MD. However, when T = 300 K and T = 350 K, the reported ARE is relatively high. The increase of ARE refers to the overestimation of modified SAFT2 at low temperatures. It means, at low temperatures, the coupled ε_{fw} to Helmholtz term was not able to reduce the gap between modified SAFT2 and MD. Because, water molecules confined at low temperatures are in order and under the effect of additional confinement constraints such as layering patterns, confinement geometry and the mutual interaction of distinct regions, amongst others. Hence, the high temperature may reduce the impact of the confinement restrictions described above by raising the kinetic energy of the water molecules inside the pore and allowing them to move more freely within the pore. Thus, high temperature is able to diminish the constraint imposed on confined water. On the other hand, the error attributed to the water model owing to high temperature is negligible because in this simulation the maximum temperature does not exceed than 450 K.

Therefore, the SPC/Fw model fairly accurately predicts the thermodynamic properties of water in MD simulations. In order to compensate for the confinement effect at low temperatures, the contribution of ε_{fw} could be improved by multiplying by a coefficient inspired by the thermodynamic property of the confined

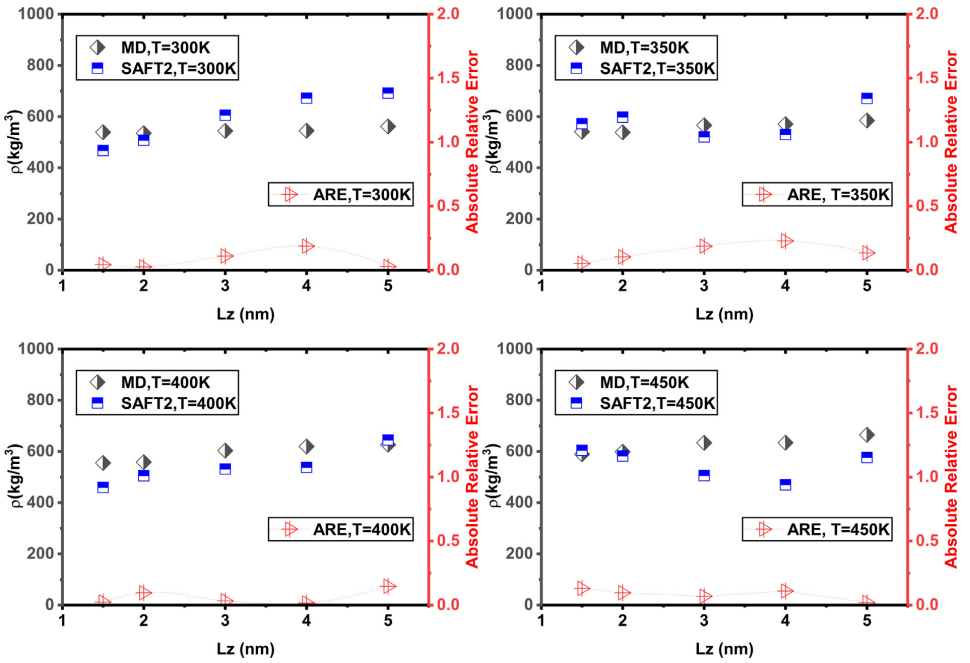

Fig. 8. The graph compares MD and modified SAFT2 predictions for T = 300 K, 350 K, 400 K, and 450 K. The diamonds indicate the MD outcomes. The squares illustrate the results of the modified SAFT2 when the CF factor is taken into account. The profile of absolute relative error at the bottom of each plot box depicts the divergence of modified SAFT2 from MD results.

water. To be specific, the newly introduced coefficient CF in Eq. (15) was applied to improve the predictions of modified SAFT2 at low temperatures.

The application of the CF factor at T = 300 K and T = 350 K decreased the divergence between MD and SAFT2, as seen in Fig. 8. While at T = 400 K and T = 450 K, approximately the same results are repeated as Fig. 7. This behavior supports our argument that high temperature diminishes the additional confinement effects that arise at low temperatures.

Our results in Fig. 8 indicate the predictions of modified SAFT2 correspond very well with MD, by taking into account ε_{fw} at T = 400 K and T = 450 K. According to the ARE trend in Fig. 8, the CF factor at T = 300 K, T = 350 K, T = 400 K and T = 450 K has narrowed the gap between MD and modified SAFT2.

4. Summary and conclusions

We have applied MD simulations to capture the interactions between confined fluid and mineral-wall inside the nanopores. In this approach, several slit-pores of calcite with fixed length and variable width, i.e., 1.5 nm, 2 nm, 3 nm, 4 nm and 5 nm, were simulated. The water molecules were sandwiched in between the calcite slabs to interact with the rigid walls of the slit nanopore. To incorporate the calcite-walls (mineral) effect into the confined water (fluid) thermodynamic properties, we used first principles to derive a term for Helmholtz energy contribution extended from SAFT2. To calculate the Helmholtz term for water-calcite interaction, the confinement parameters of slit nanopore, namely ε_{fw} and ρ_{max}, needed to be calculated in advance. The confinement parameters were then calculated by MD simulation. The predictions of modified SAF2 were validated versus MD results. A newly defined physical parameter CF is incorporated with modified SAFT2 deriving from MD results. Coupling CF with proposed EoS reduced the ARE by roughly 50% at low temperatures, resulting in satisfactory agreement with MD at all temperatures.

In conclusion, inside the layering zone, the density and energy deviate from the bulk value owing to the attraction of the rigid pore walls. Temperature causes density in Region II to rise, whereas it causes density in Region I to drop. Because in the bulk-like zone, fluid–fluid interaction is predominant, while in the layering zone, the fluid-mineral interaction is dominant. The newly introduced physical parameter, the CF factor, demonstrates that the thermodynamic of the confined fluid in the nanoscale pore depends not only on the fluid-mineral interaction potential but also on the geometry, layering pattern, the mutual interaction of different regions, which is the consequence of the rise in the surface-to-volume ratio at the nanoscale. This finding paves the way for further study into how additional constraints influence the characteristics of associating confined fluids.

CRediT authorship contribution statement

S. Ahmadi G.: Conceptualization, Methodology, Software, Validation, Writing – original draft, Visualization, Formal analysis, Investigation, Writing – review & editing. **R. Miri:** Software, Supervision, Writing – review & editing. **P. Aagaard:** Supervision, Writing – review & editing. **H. Hellevang:** Supervision, Writing – review & editing.

Declaration of Competing Interest

The authors declare that they have no known competing financial interests or personal relationships that could have appeared to influence the work reported in this paper.

Appendix A. Supplementary data

Supplementary data to this article can be found online at https://doi.org/10.1016/j.molliq.2021.118045.

References

[1] E.S. Gutterød, S. Øien-Ødegaard, K. Bossers, A.-E. Nieuwelink, M. Manzoli, L. Braglia, A. Lazzarini, E. Borfecchia, S. Ahmadigoltapeh, B. Bouchevreau, B.T. Lønstad-Bleken, R. Henry, C. Lamberti, S. Bordiga, B.M. Weckhuysen, K.P. Lillerud, U. Olsbye, CO2 hydrogenation over Pt-containing UiO-67 Zr-MOFs The base case, Ind. Eng. Chem. Res. 56 (45) (2017) 13206–13218.
[2] Q. Ma, Z. Zheng, J. Fan, J. Jia, J. Bi, P. Hu, Q. Wang, M. Li, W. Wei, D. Wang, Pore-scale simulations of CO2/oil flow behavior in heterogeneous porous media under various conditions, Energies 14 (2021) 533.
[3] T. Gu, Y. Zheng, H. Yue, Y. Zheng, Characterization of the pore structure of well cement under carbon capture and storage conditions by an image-based method with a combination of metal intrusion, ACS Omega 6 (3) (2021) 2110–2120.
[4] H. Wang, Y. Yin, B. Li, J.Q. Bai, M. Wang, High-throughput screening of metal-organic frameworks for the impure hydrogen storage supplying to a fuel cell vehicle, Transp. Porous Media. 1–16 (2021).
[5] D.R. Cole, S. Ok, A. Striolo, A. Phan, Hydrocarbon behavior at nanoscale interfaces, Rev. Mineral. Geochemistry. 75 (1) (2013) 495–545.
[6] L.D. Gelb, K.E. Gubbins, R. Radhakrishnan, M. Sliwinska-Bartkowiak, Phase separation in confined systems, Reports Prog. Phys. 62 (1999) 1573.
[7] G.J. Zarragoicoechea, V.A. Kuz, van der Waals equation of state for a fluid in a nanopore, Phys. Rev. E. 65 (2002) 21110.
[8] G.J. Zarragoicoechea, V.A. Kuz, Critical shift of a confined fluid in a nanopore, Fluid Phase Equilib. 220 (1) (2004) 7–9.
[9] J.S. Rowlinson, J.D. van der Waals, On the Continuity of the Gaseous and Liquid States, North-Holland, 1988.
[10] E.G. Derouane, On the physical state of molecules in microporous solids, Microporous Mesoporous Mater. 104 (1-3) (2007) 46–51.
[11] S.P. Tan, M. Piri, Equation-of-state modeling of associating-fluids phase equilibria in nanopores, Fluid Phase Equilib. 405 (2015) 157–166.
[12] S.P. Tan, M. Piri, Equation-of-state modeling of confined-fluid phase equilibria in nanopores, Fluid Phase Equilib. 393 (2015) 48–63.
[13] I. Langmuir, The constitution and fundamental properties of solids and liquids. Part I. Solids, J. Am. Chem. Soc. 38 (11) (1916) 2221–2295.
[14] H. Freundlich, Über die adsorption in lösungen, Zeitschrift Für Phys. Chemie. 57 (1907) 385–470.
[15] S. Brunauer, P.H. Emmett, E. Teller, Adsorption of gases in multimolecular layers, J. Am. Chem. Soc. 60 (1938) 309–319.
[16] H. Cárdenas, E.A. Müller, Extension of the SAFT-VR-Mie equation of state for adsorption, J. Mol. Liq. 294 (2019) 111639.
[17] E. Kierlik, M.L. Rosinberg, Free-energy density functional for the inhomogeneous hard-sphere fluid: Application to interfacial adsorption, Phys. Rev. A. 42 (1990) 3382.
[18] E. Kierlik, M.L. Rosinberg, Density-functional theory for inhomogeneous fluids: adsorption of binary mixtures, Phys. Rev. A. 44 (1991) 5025.
[19] R.R. Kotdawala, N. Kazantzis, R.W. Thompson, Analysis of binary adsorption of polar and nonpolar molecules in narrow slit-pores by mean-field perturbation theory, J. Chem. Phys. 123 (2005) 244709.
[20] G. Wang, J. Jiang, K. Sun, J. Wu, An improved theoretical procedure for the pore-size analysis of activated carbon by gas adsorption, Chin. J. Chem. Eng. 26 (3) (2018) 551–559.
[21] M. Zarghami Dehaghani, B. Bagheri, F. Yousefi, A. Nasiriasayesh, A. Hamed Mashhadzadeh, P. Zarrintaj, N. Rabiee, M. Bagherzadeh, V. Fierro, A. Celzard, M. R. Saeb, E. Mostafavi, Boron nitride nanotube as an antimicrobial peptide carrier: A theoretical insight, Int. J. Nanomed. 16 (2021) 1837–1847.
[22] F. Yousefi, F. Khoeini, A. Rajabpour, Thermal conductivity and thermal rectification of nanoporous graphene: A molecular dynamics simulation, Int. J. Heat Mass Transf. 146 (2020) 118884, https://doi.org/10.1016/j.ijheatmasstransfer.2019.118884.
[23] M. Sedghi, M. Piri, L. Goual, Atomistic molecular dynamics simulations of crude oil/brine displacement in calcite mesopores, Langmuir 32 (14) (2016) 3375–3384.
[24] R. Wang, F. Peng, K. Song, G. Feng, Z. Guo, Molecular dynamics study of interfacial properties in CO2 enhanced oil recovery, Fluid Phase Equilib. 467 (2018) 25–32.
[25] M. Zarringhalam, H. Ahmadi-Danesh-Ashtiani, D. Toghraie, R. Fazaeli, Molecular dynamic simulation to study the effects of roughness elements with cone geometry on the boiling flow inside a microchannel, Int. J. Heat Mass Transf. 141 (2019) 1–8.
[26] N. Giovambattista, P.J. Rossky, P.G. Debenedetti, Effect of temperature on the structure and phase behavior of water confined by hydrophobic, hydrophilic, and heterogeneous surfaces, J. Phys. Chem. B. 113 (42) (2009) 13723–13734.
[27] M. Sedghi, M. Piri, Capillary condensation and capillary pressure of methane in carbon nanopores: Molecular dynamics simulations of nanoconfinement effects, Fluid Phase Equilib. 459 (2018) 196–207.
[28] J. Zhao, G. Yao, D. Wen, Salinity-dependent alterations of static and dynamic contact angles in oil/brine/calcite systems: a molecular dynamics simulation study, Fuel 272 (2020) 117615.

[29] S.A. Goltapeh, S. Abdolahi, R. Miri, H. Hellevang, Extension of PC-SAFT equation of state to include mineral surface effect in fluid properties using molecular dynamic simulation, Sustain. Energy Technol. Assessments. 48 (2021) 101624.
[30] L. Travalloni, M. Castier, F.W. Tavares, S.I. Sandler, Thermodynamic modeling of confined fluids using an extension of the generalized van der Waals theory, Chem. Eng. Sci. 65 (10) (2010) 3088–3099.
[31] M.S. Wertheim, Fluids with highly directional attractive forces. IV. Equilibrium polymerization, J. Stat. Phys. 42 (3-4) (1986) 477–492.
[32] J.A. Barker, D. Henderson, Perturbation theory and equation of state for fluids. II. A successful theory of liquids, J. Chem. Phys. 47 (11) (1967) 4714–4721.
[33] S.I. Sandler, The generalized van der Waals partition function. I. Basic theory, Fluid Phase Equilib. 19 (3) (1985) 238–257.
[34] X. Ji, S.P. Tan, H. Adidharma, M. Radosz, Statistical associating fluid theory coupled with restrictive primitive model extended to bivalent ions. SAFT2: 2. Brine/seawater properties predicted, J. Phys. Chem. B. 110 (2006) 16700–16706.
[35] T.L. Hill, An introduction to statistical thermodynamics, Courier Corporation (1986).
[36] D. Frenkel, B. Smit, Understanding molecular simulation: from algorithms to applications, Elsevier, 2001.
[37] S.A. Markgraf, R.J. Reeder, High-temperature structure refinements of calcite and magnesite, Am. Mineral. 70 (1985) 590–600.
[38] N.H. de Leeuw, S.C. Parker, Atomistic simulation of the effect of molecular adsorption of water on the surface structure and energies of calcite surfaces, J. Chem. Soc. Faraday Trans. 93 (3) (1997) 467–475.
[39] L. Martínez, R. Andrade, E.G. Birgin, J.M. Martínez, PACKMOL: a package for building initial configurations for molecular dynamics simulations, J. Comput. Chem. 30 (2009) 2157–2164.
[40] S. Plimpton, Fast parallel algorithms for short-range molecular dynamics, J. Comput. Phys. 117 (1) (1995) 1–19.
[41] P. Raiteri, R. Demichelis, J.D. Gale, Thermodynamically consistent force field for molecular dynamics simulations of alkaline-earth carbonates and their aqueous speciation, J. Phys. Chem. C. 119 (43) (2015) 24447–24458.
[42] Z. Li, D. Cao, J. Wu, Layering, condensation, and evaporation of short chains in narrow slit pores, J. Chem. Phys. 122 (2005) 224701.
[43] W. Hockney, J.W. Eastwood, Computer Simulation Using Particles IOP Publishing Ltd, (1988)
[44] S. Nosé, A unified formulation of the constant temperature molecular dynamics methods, J. Chem. Phys. 81 (1) (1984) 511–519.
[45] M. Doble, Perry's chemical engineers' handbook, McGraw-Hill, New York, USA, 2007.

Journal of Molecular Liquids 367 (2022) 120440

Contents lists available at ScienceDirect

Journal of Molecular Liquids

journal homepage: www.elsevier.com/locate/molliq

Corrigendum

Corrigendum to "Extension of SAFT equation of state for fluids confined in nano-pores of sedimentary rocks using molecular dynamic simulation" [J. Mol. Liquids (348) (2022) 118045]

Sajjad Ahmadi Goltapeh [a,*], Rohaldin Miri [b], Per Aagaard [a], Helge Hellevang [a]

[a] Department of Geosciences, University of Oslo, PO Box 1047 Blindern, 0316 Oslo, Norway
[b] School of Chemical Engineering, Iran University of Science and Technology (IUST), PO Box 16765-163, Tehran, Iran

The authors regret to notify the Journal of Molecular Liquids that Fig. 4 from above-mentioned article was not entirely printed out. In other words, Fig. 4 should have five boxes, each containing the density profiles relevant to a specific Lz. However, as shown in the published article, the curves for Lz = 5 nm and Lz = 4 nm are missing.

It is worth to note that Fig. 4 addresses a key aspect of the research work and the present published Fig. is considered as a critical error. The authors would appreciated if the editorial team could replace the previous version of Fig. 4 with a newly attached one and publish a Corrigendum in a forthcoming issue.

DOI of original article: https://doi.org/10.1016/j.molliq.2021.118045
* Corresponding author.
E-mail address: sajjadah@uio.no (S.A. Goltapeh).

https://doi.org/10.1016/j.molliq.2022.120440
0167-7322/

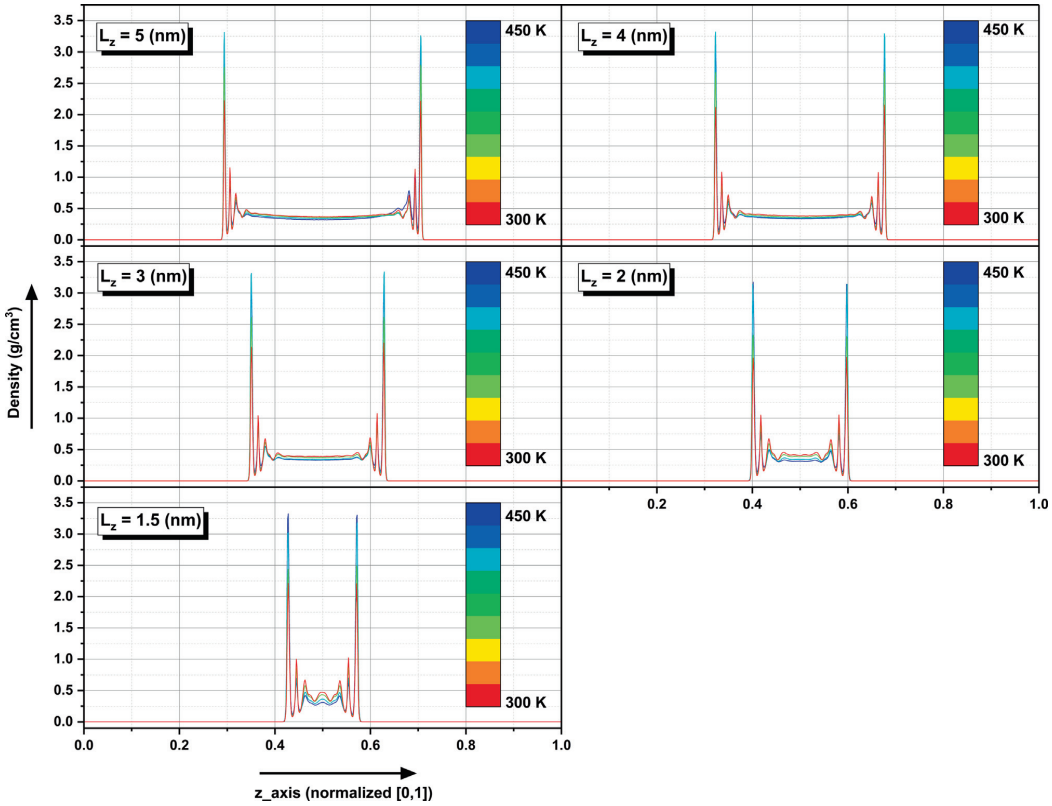

The authors would like to apologise for any inconvenience caused.

Supplementary Information

Extension of SAFT Equation of State for Fluids Confined in Nano-pores of Sedimentary Rocks Using Molecular Dynamic Simulation

S. Ahmadi G.[a*], R. Miri[b], P. Aagaard[a], H. Hellevang[a]

[a] *Department of Geosciences, University of Oslo, P.O. Box 1047 Blindern, 0316 Oslo, Norway*

[b]*School of Chemical Engineering, Iran University of Science and Technology (IUST), P.O. Box 16765-163, Tehran, Iran*

Section A: Partition Function

The canonical partition function, Q, is defined as follows for a system of N identical particles of mass m.

$$Q_{N,V,T} = \frac{q_{\text{int}}}{N!}\frac{1}{h^{3N}}\int\int dp^N dr^N \exp\left(-\frac{H\left(p^N, r^N\right)}{kT}\right) \tag{A.1}$$

Where h represents Planck's constant, T denotes the temperature and k is the Boltzmann constant. The factor $N!$ vanishes when the particles are distinguishable. In Equation (A.1), q_{int} is the internal partition function. The Hamiltonian $H(p^N,r^N)$ represents the total energy of the system. The Hamiltonian is defined as the sum of the system's kinetic and potential energies, as shown below.

$$H\left(p^N, r^N\right) = \sum_{i=1}^{N}\frac{|\,p_i\,|^2}{2m} + u\left(r^N\right) \tag{A.2}$$

Thus we have

$$Q_{N,V,T} = \frac{q_{\text{int}}}{N!}\frac{1}{h^{3N}}\int dp^N \exp\left(-\frac{|\,p_i\,|^2}{2mkT}\right)\int_V\int dr^N \exp\left(-\frac{u\left(r^N\right)}{kT}\right) \tag{A.3}$$

The analytical solution of the momenta integral product is as follows:

$$\int dp^N \exp\left(-\frac{|\,p_i\,|^2}{2mkT}\right) = \left(2\pi mkT\right)^{\frac{3N}{2}} \tag{A.4}$$

In Equation (A.7), m is the mass of the particle and π=3.14 is the result of the Gaussian integral. Thus we have

$$Q_{N,V,T} = \frac{q_{\text{int}}}{N!}\frac{1}{h^{3N}}\left(2\pi mkT\right)^{\frac{3N}{2}}\int_V\int dr^N \exp\left(-\frac{u\left(r^N\right)}{kT}\right) \tag{A.5}$$

The configuration integral Z is defined as the integral product of all positions:

$$Z_{N,V,T} = \int_V\int dr^N \exp\left(-\frac{u\left(r^N\right)}{kT}\right) \tag{A.6}$$

the de Broglie thermal wavelength λ is defined as:

$$\lambda = \sqrt{\left(\frac{h^2}{2\pi mkT}\right)} \tag{A.7}$$

Thus we have:

$$Q_{N,V,T} = \frac{q_{\text{int}}}{N!}\frac{1}{\lambda^{3N}} Z_{N,V,T} \tag{A.8}$$

Section B: Configurational Energy

Once the partition function is determined, to calculate various thermodynamic properties from canonical partition function, the easiest starting point is the Helmholtz free energy:

$$A = -k_b T \ln(Q) \tag{B.1}$$

To calculate the entropy *S*, one can write the Helmholtz free energy in differential form:

$$dA = \left(\frac{\partial A}{\partial T}\right)_{V,N} dT + \left(\frac{\partial A}{\partial V}\right)_{T,N} dV \tag{B.2}$$

By Comparison of Equation (B.2) with characteristics function of *A* in Equation (B.3)

$$dA = -SdT - PdV \tag{B.3}$$

The entropy *S* therefore can be written as:

$$S = -\left(\frac{\partial A}{\partial T}\right)_{V,N} = k\left[\ln Q + T\left(\frac{\partial \ln Q}{\partial T}\right)_{V,N}\right] \tag{B.4}$$

The internal energy *U* then can be written with respect to the *A*, *T* and *S*:

$$A = U - TS \Rightarrow U = A + TS \tag{B.5}$$

Substitution of *S* from Equation (B.4) into Equation (B.5) then gives:

$$U = -kT\ln Q + kT\ln Q + kT^2\left(\frac{\partial \ln Q}{\partial T}\right)_{V,N} = kT^2\left(\frac{\partial \ln Q}{\partial T}\right)_{V,N} \tag{B.6}$$

Equation (B.7) can be used to determine the configurational energy, which is the difference between the internal energy of a real fluid and the internal energy of an ideal gas [29]:

$$E_{conf} = U_{N,V,T} - U^{ig}_{N,V,T} = kT^2 \left(\frac{\partial \ln Z}{\partial T} \right)_{V,N} \quad \text{(B.7)}$$

When Equation (B.7) is substituted into Equation (A.8), the result is:

$$Q_{N,V,T} = \left(\frac{q^N_{\text{int}}}{\lambda^{3N} N!} \right) V_f^N \exp\left(\int_{\infty}^{T} \frac{E_{conf}}{kT^2} dT \right) \quad \text{(B.8)}$$

In Equation (B.7), V_f represents the free volume, namely the volume which is excluded by the fluid molecule and defined as follows:

$$V_f = V - \frac{N}{\rho_{\max}} \quad \text{(B.9)}$$

In Equation (B.9), The closed packed density is shown with $\rho_{\max}$. Considering the calcite-wall effect let to split the into fluid-fluid and fluid-wall species

$$Q_{N,V,T} = \left(\frac{q^N_{\text{int}}}{\lambda^{3N} N!} \right) V_f^N \exp\left(\int_{\infty}^{T} \frac{E_{conf-ff}}{kT^2} dT \right) \exp\left(\int_{\infty}^{T} \frac{E_{conf-fw}}{kT^2} dT \right) \quad \text{(B.10)}$$

$E_{\text{conf-ff}}$ and $E_{\text{conf-fw}}$ represent the configurational energy for fluid-fluid and fluid-wall, respectively.

89 **Section C: Configurational energy of fluid-wall interaction: pure fluid**

90 A bulk fluid's configurational energy is proportional to the fluid-fluid interactions occurring
91 across the system. On the other hand, for the confined fluid, an E_{conf} model must account for the
92 fluid-wall interactions. According to Equation (1), the fluid and pore wall molecules interact
93 through a square well. For a system with *N* molecules in volume *V* and temperature *T*, the E_{conf},
94 or average total interaction energy, is defined as

$$E_{conf} = \frac{N^2}{2V}\int u(r)g(r,\rho)\,dr \tag{C.1}$$

95

96 Where the intermolecular interaction energy *u* is assumed pairwise additive. By this hypothesis,
97 the interaction energy equals the sum of every single pair interaction as following:

$$u(r_1, r_2, ..., r_N) = \sum_i \sum_j u(r_{ij}) \tag{C.2}$$

98

99 In Equation (C.1), $g(\rho,r)$ is radial distribution function [32] which is defined as:

$$g(r) = \begin{cases} 0 & r_{ij} < \sigma_{ij} \\ \exp\left(\dfrac{\varepsilon_{ij}}{kT}\right) & \sigma_{ij} < r_{ij} < \sigma_{ij} + \delta_{ij} \\ 1 & r_{ij} > \sigma_{ij} + \delta_{ij} \end{cases} \tag{C.3}$$

100

101 In Equation (C.3), *r* is the distance between two molecules, σ is the average molecule diameter,
102 and δ is the width of the square well. To implement the integral product, we must substitute $g(\rho,r)$
103 and $u(r)$ in Equation (C.1). Assuming that $g(\rho,r)$ inside the bulk and forbidden zone equal 1 and 0,
104 respectively, we get

$$\begin{aligned} E_{conf} &= \frac{N^2}{2V}\int u(r)g(r,\rho)\,dr \\ &= \frac{N^2}{2V}\int \big(u(r)\times g(r,\rho)\big)dr + \frac{N^2}{2V}\int \big(u(r)\times g(r,\rho)\big)dr + 0 \end{aligned} \tag{C.4}$$

105

Substituting the potentials from Equation (1) and (2) in the manuscript gives:

$$E_{conf} = \frac{N^2}{2V}\int\left(-\varepsilon_{ff} \times g\left(r,\rho\right)\right)dr + \frac{N^2}{2V}\int\left(-\varepsilon_{fw} \times g\left(r,\rho\right)\right)dr \quad \text{(C.5)}$$

Due to the water-calcite interaction, the 2 in the second component of Equation (C.5) decreases to 1. Thus, we have the following:

$$\begin{aligned} E_{conf} &= -\frac{N}{2}\varepsilon_{ff}\frac{N}{V}\int g\left(r,\rho\right)dr + \frac{N}{V}\varepsilon_{fw}\int g\left(r,\rho\right)dr \\ &= -\frac{N}{2}\varepsilon_{ff}\left(\frac{N}{V}C\right) + \left(N\frac{C'}{V}\right)\varepsilon_{fw} \\ &= -\frac{N}{2}N_C\varepsilon_{ff} + N_P\varepsilon_{fw} \end{aligned}$$

$$E_{conf} = -\frac{N}{2}N_C\varepsilon_{ff} + N_P\varepsilon_{fw} \quad \text{(C.6)}$$

Section D: Chemical Potential

Chemical potential is defined as the amount of energy that may be absorbed or released when the number of particles in a given species varies. Taking into account that the water in this simulation is supposed to be pure, we have:

$$\mu = \left(\frac{\partial A}{\partial N}\right)_{T,V} \quad \text{(D.1)}$$

Equation (D.1) means the chemical potential equals the partial derivative of Helmholtz free energy with respect to the number of moles. According to Equation (D.1), the chemical potential remains constant as long as the corresponding natural variables, temperature and volume, are held constant. To recall from Equation (B.1), once the partition function is determined, it is possible to calculate the Helmholtz free energy as below:

$$A = -k_b T \ln\left(Q\right) \quad \text{(D.2)}$$

123 The chemical potential also is defined as:

$$\mu = -k_b T \left(\frac{\partial \ln Q}{\partial N} \right)_{T,V} \tag{D.3}$$

124

125 When Equations (D.1) and (D.2) are compared, it becomes clear that Equation (D.3) provides a
126 straightforward method for estimating the chemical potential from the partition function. Equation
127 (D.3) means the chemical potential equals the partial derivative of the natural logarithm of the
128 partition function with respect to the number of moles.

129 To derive a proper definition for *A*, we have:

$$A = -kT \ln\left(\left(\frac{V_f^N}{\lambda^{3N} N!} \right) \exp\left(\int_{\infty}^{T} \frac{E_{conf-ff}}{kT^2} dT \right) \exp\left(\int_{\infty}^{T} \frac{E_{conf-fw}}{kT^2} dT \right) \right) \tag{D.4}$$

130

131 Replacing the $E_{conf\text{-}ff}$ and $E_{conf\text{-}fw}$ with the energy per particle i.e. $\varepsilon_{conf\text{-}ff}$ and $\varepsilon_{conf-fw}$ gives:

$$\begin{aligned} A &= -kT \left(\ln\left(\frac{V_f^N}{\lambda^{3N} N!} \right) + \left(N \int_{\infty}^{T} \frac{\varepsilon_{conf-ff}}{kT^2} dT \right) + \left(N \int_{\infty}^{T} \frac{\varepsilon_{conf-fw}}{kT^2} dT \right) \right) \\ &= -kT \left(-3N \ln(\lambda) + \ln\left(V_f^N\right) - \ln(N!) + \left(N \frac{\varepsilon_{conf-ff}}{kT} \right) + \left(N \frac{\varepsilon_{conf-fw}}{kT} \right) \right) \end{aligned} \tag{D.5}$$

132

133 Using the Stirling approximation to expand the factorial gives:

$$\begin{aligned} A &= -kT \left(-3N \ln(\lambda) + N \ln\left(V_f\right) - N \ln N - N + \left(N \frac{\varepsilon_{conf-ff}}{kT} \right) + \left(N \frac{\varepsilon_{conf-fw}}{kT} \right) \right) \\ &= -NkT \left(-3 \ln(\lambda) + \ln V_f - \ln N - 1 + \left(\frac{\varepsilon_{conf-ff}}{kT} \right) + \left(\frac{\varepsilon_{conf-fw}}{kT} \right) \right) \\ &= NkT \left(\ln\left(\lambda^3\right) - \ln V_f + \ln N + 1 - \left(\frac{\varepsilon_{conf-ff}}{kT} \right) - \left(\frac{\varepsilon_{conf-fw}}{kT} \right) \right) \\ &= NkT \left(\ln\left(\lambda^3\right) + \ln\left(\frac{N}{V_f} \right) - \left(\frac{\varepsilon_{conf-ff}}{kT} - 1 \right) - \left(\frac{\varepsilon_{conf-fw}}{kT} \right) \right) \\ &= NkT \left(\ln\left(\lambda^3\right) + \ln\left(\frac{N}{V_f} \right) - \left(\frac{\varepsilon_{conf-ff}}{kT} - 1 \right) - \left(\frac{\varepsilon_{conf-fw}}{kT} \right) \right) \end{aligned}$$

$$A = NkT\left(\ln\left(\lambda^3\right)+\ln\left(\frac{N}{V_f}\right)-\left(\frac{\varepsilon_{conf-ff}}{kT}-1\right)-\left(\frac{\varepsilon_{conf-fw}}{kT}\right)\right) \quad \text{(D.6)}$$

134

135 By plugging the definition of V_f from Equation (B.9) into Equation (D.6), we have:

$$\begin{aligned} A &= NkT\left(\ln\left(\lambda^3\right)+\ln\left(\frac{N}{V-\frac{N}{\rho_{\max}}}\right)-\left(\frac{\varepsilon_{conf-ff}}{kT}-1\right)-\left(\frac{\varepsilon_{conf-fw}}{kT}\right)\right) \\ &= NkT\left(\ln\left(\lambda^3\right)+\ln\left(\frac{N}{\frac{N}{\rho}-\frac{N}{\rho_{\max}}}\right)-\left(\frac{\varepsilon_{conf-ff}}{kT}-1\right)-\left(\frac{\varepsilon_{conf-fw}}{kT}\right)\right) \\ &= NkT\left(\ln\left(\lambda^3\right)-\ln\left(\frac{1}{\rho}-\frac{1}{\rho_{\max}}\right)-\left(\frac{\varepsilon_{conf-ff}}{kT}-1\right)-\left(\frac{\varepsilon_{conf-fw}}{kT}\right)\right) \\ A &= NkT\left(\ln\left(\lambda^3\right)-\ln\left(\frac{1}{\rho}-\frac{1}{\rho_{\max}}\right)-\left(\frac{\varepsilon_{conf-ff}}{kT}-1\right)-\left(\frac{\varepsilon_{conf-fw}}{kT}\right)\right) \quad \text{(D.7)} \end{aligned}$$

136

137 To derive a proper definition for μ one can use the definition of chemical potential in Equation
138 (D.1):

$$\mu = kT\left(\ln\left(\lambda^3\right)-\ln\left(\frac{1}{\rho}-\frac{1}{\rho_{\max}}\right)-\left(\frac{\varepsilon_{conf-ff}}{kT}-1\right)-\left(\frac{\varepsilon_{conf-fw}}{kT}\right)\right) \quad \text{(D.8)}$$

139

Paper III

Drivers of Low Salinity Effect in Carbonate Reservoirs Using Molecular Dynamics Simulation

Sajjad Ahmadi Goltapeh, Saeed Abdolahi, Jens Sigurd Jahren, Rohaldin Miri and Helge Hellevang

Published in *Journal of Molecular Liquids*, 2022, volume 360, pp. 119490. DOI: https://doi.org/10.1016/j.molliq.2022.119490.

III

Journal of Molecular Liquids 360 (2022) 119490

Contents lists available at ScienceDirect

Journal of Molecular Liquids

journal homepage: www.elsevier.com/locate/molliq

Drivers of Low Salinity Effect in Carbonate Reservoirs Using Molecular Dynamic Simulation

Sajjad Ahmadi Goltapeh [a,*], Saeed Abdolahi [b], Jens Jahren [a], Rohaldin Miri [a,c], Helge Hellevang [a]

[a] Department of Geosciences, University of Oslo, PO Box 1047 Blindern, 0316 Oslo, Norway
[b] Department of Chemical Engineering, Amirkabir University of Technology, 424 Hafez Avenue, Tehran, Iran
[c] School of Chemical Engineering, Iran University of Science and Technology (IUST), PO Box 16765-163, Tehran, Iran

ARTICLE INFO

Article history:
Received 4 February 2022
Revised 21 April 2022
Accepted 26 May 2022
Available online 30 May 2022

Keywords:
Molecular dynamic simulation
Smart water flooding
Water-based EOR
Low salinity water
Enhanced oil recovery
Wettability alteration
Calcite mineral

ABSTRACT

Low salinity water (LSW) flooding has yielded promising results in improving the enhanced oil recovery (EOR) techniques in sandstone and carbonate reservoirs. Despite various studies and advances, the main mechanism behind the oil displacement in the rock-brine-oil system is unclear. To get a better understanding of the governing mechanisms, we used the molecular dynamic (MD) method to simulate a system including calcite-brine-oil under two different scenarios. At T=300 K and T=360 K each scenario is completed during 40 ns using a canonical ensemble. The results show that all mono/divalent ions are hydrated initially. Furthermore, Na^+, Cl^- and H_2O molecules reside close to the calcite surface and their positions show little change at different time steps. However, the position of divalent ions is dynamic depending on the simulation time steps. Ca^{2+}, which is initially detected at 2.35 Å above the solid surface at T=300 K and T=360 K, migrates away by time. On the other hand, Mg^{2+} and SO_4^{2-} which are invisible up to t = 16 ns even at the radius of 10 Å, move gradually toward the surface with time and consolidate their position after oil displacement. Namely, prior to oil displacement, a shift in Na^+, Cl^- and Ca^{2+} locations is noticed, and the trend of double electric layer (EDL) is extended, which might be the cause of oil displacement. The findings of this study are applicable in the improvement of EOR technology, water resource treatment and contaminant transfer from geological systems, dealing with solid solutions such as ocean-soil systems.

1. Introduction

Calcite, the most stable polymorph of calcium carbonate ($CaCO_3$), is the mineral found in most geological systems. The behavior of calcite in the natural systems in contact with saline water is significantly dependent on the calcite surface chemistry. That is why extensive research studies have focused on the surface specifications of the calcite slab in an aqueous environment [1–4]. For instance, Fenter et al. [5] demonstrated that one or two monolayers of protonated hydroxyl groups are adsorbed onto the calcite surface depending on the pH value. They afterward measured the distance of the adsorbed monolayers from the calcite surface, which were 2.14 Å and 3.44 Å [6]. The saline water in contact with calcite may enforce new characteristics on the mineral surface. Due to this fact, some enhanced oil recovery (EOR) techniques are concerned with the properties of the calcite-saline water interface because water acts as a carrier to transport chemical agents to the surface, and through this, it is possible to change the wettability and release oil.

Among the numerous EOR techniques, the low salinity water flooding (LSW) approach is inexpensive and additionally is suggested to be promising for both sandstones and carbonates reservoirs [7,8]. The LSW technique was first introduced by Bernard et al. [9] in 1967, who observed an increase in oil recovery when the concentration of NaCl brine remained within 0% to 1%. To this end, in the 1990s, a series of extensive experiments were carried out to assess Bernard's observations [10–12]. Lately, various mechanisms have been proposed to interpret the impact of the LSW, such as multi-component ion exchange (MIE) [13,14], osmotic pressure [15], fines migration [16], the extension of the electrical double layer [17], wettability alteration [18], etc.

Zhang et al. [19] investigated the wettability alteration in carbonate surface in contact with Ca^{2+}, Mg^{2+} and SO_4^{2-}. They reported that divalent anions show a more substantial effect on wettability alteration than their monovalent counterparts. On the other hand, Fathi et al. [20] reported a crucial role of Ca^{2+}, Mg^{2+}, and SO_4^{2-} in the

* Corresponding author.
E-mail address: sajjadah@uio.no (S. Ahmadi Goltapeh).

https://doi.org/10.1016/j.molliq.2022.119490
0167-7322/

wettability change of carbonates and represented about 10% improvement in oil recovery by eliminating the Na^+ and Cl^- ions from seawater. Using experiment and modeling, Song et al. [21] pinpoint monovalent ions of LSW as the key factors of improved oil recovery in limestone reservoirs. In contrast, Zeng et al. [22] found that the absence of Ca^{2+} and Mg^{2+} had no influence on the adsorption of benzoic acid on the calcite surface. Moreover, Zhang et al. [23], within a series of long-term tests, declared that the oil recovery was greatly improved by fixing the Ca^{2+} and raising SO_4^{2-}. On the contrary, Karousi et al., by measuring the disjoining pressure for different systems, shows that the presence of Mg^{2+} ions in water containing SO_4^{2-} allows a more stable water film on the calcite surface. Yousef et al. [24] have studied the effect of water ions on the surface chemistry of carbonate reservoirs. Although they acknowledge that the driving mechanism of using LSW is dictated by wetting properties of the carbonate surface, they have declared that a comprehensive study is required to tune the ionic composition [25].

It seems the most complex element of the postulated EOR mechanisms is the link between macroscopic observations and molecular-scale mechanisms because the molecular features of the calcite-oil-brine interfaces remain a mystery. Although the role of the reactive ions such as Na^+, Ca^{2+}, Mg^{2+}, Cl^- and SO_4^{2-} on calcite surface property change is inescapable [26,27], a deeper investigation of the calcite-oil-brine interactions is necessary to resolve the molecular scale ambiguities. In this regard, molecular dynamics (MD) simulations have emerged as a popular method to capture the underlying processes at the calcite-fluid interface at the nanoscale [28,29].

For instance, Kerisit and Parker used molecular dynamic simulation to represent the adsorbed water layer losing the hydrogen bond, causing density oscillation within the calcite-water interface [30]. Ahmadi G. et al. [31] studied the thermodynamic properties of the transition zone in the vicinity of the calcite-water interface with MD. According to this study, two fully ordered monolayers of water adsorb to the calcite surface, causing the density of the transition zone and bulk-like region to drop as the temperature rises. Using the MD results, they developed an equation of state inspired by Perturbation-Chain SAFT [32] to predict the thermodynamic properties of the confined interface at the calcite-water system. Zhao et al. [33] measured the contact angle between an n-decane nanodroplet and the surface of a calcite nanopore with classical MD simulation. Using numerous salinity concentrations, they demonstrated that the solid surface wettability is diminished after a certain concentration threshold. Koleini et al. [34] used MD to investigate the behavior of the brine water at the calcite-brine interface. They introduced two different brine water to the calcite surface, with total salinity of 46000 ppm and 189000 ppm. They believed that the divalent cation's contribution to EDL formation is reduced due to the high energy impact of the hydration shells encapsulating them. Although several studies investigated the role of the reactive ions such as Na^+, Ca^{2+}, Mg^{2+}, Cl^- and SO_4^{2-} on oil displacement [26,27], there is still a lack of studies investigating the time dependency of ion distribution and charge density profile at the molecular scale.

There is growing evidence showing chemical interactions between crude oil and water in contact with the rock surface can considerably change the microscopic efficiency of the water flooding technique. In this study, we performed MD simulation to gain a better understanding of the molecular interactions between LSW and calcite solid surface within the thin brine film. A nanoscale version of calcite-oil-brine system is simulated with a calcite slab with neutral surface, high salinity brine (formation water), oil and LSW. The main objective is to track the changes in ion distribution and charge density over time.

2. Methodology

Two distinct simulation scenarios were defined, with each scenario executing the simulation at a specific temperature. In other words, the same composition as in scenario 1 with T=300 K was examined at scenario 2 with T=360 K. The following subsections summarize the utilized chemical components, physical geometry and detail of MD simulation.

2.1. Material

The rock surface is modeled by calcium carbonate in the form of a calcite slab. Formation water (FW), oil and LSW are inorganic and organic fluids interacting with the solid surface. Fig. 1 represents the initial configuration of the simulated system in the MD simulation box. As delineated, the calcite slab is regarded as a solid phase on the bottom side, while molecules of FW, oil and LSW on top of the calcite slab interact with each other and the solid surface. In this simulation approach, two different types of brine, namely FW (i.e., H_2O, Na^+, Cl^- and Ca^{2+}) and LSW (i.e., H_2O, Na^+, Cl^-, Mg^{2+} and SO_4^{2-}) represent the high salinity and low salinity brine water adopted from Zhang and Sarma experimental study [35]. It is necessary to note that, FW and LSW, both are far from supersaturated conditions. The composition of oil was adjusted based on the SARA test including toluene (37%), decane (44.7 %) and benzoic acid (18.3%). To be specific, the results of SARA test contains a mixture of saturated hydrocarbons, resins and aromatic compounds. Thus, toluene was chosen as an aromatic compound while decane and benzoic acid were selected as saturated hydrocarbon and resin, to mimic the oil model [36,37].

Table 1 summarizes the chemical composition of distinct components. It is worth noting that the number of elements in each scenario is calculated based on their density at a temperature of 300 K and pressure of 1 atm.

Table 2 shows the number of molecules utilized in MD simulation. To put it differently, Table 2 lists the number of molecules required to make the chemical compositions indicated in Table 1.

2.2. Geometry description

In this simulation, calcite with rhombohedral structure and cell parameters of a = b = 4.988 Å, c = 17.061 Å, $\alpha = \beta = 90°$, $\gamma = 120°$ [38] is representative of the mineral surface interacting with brine and

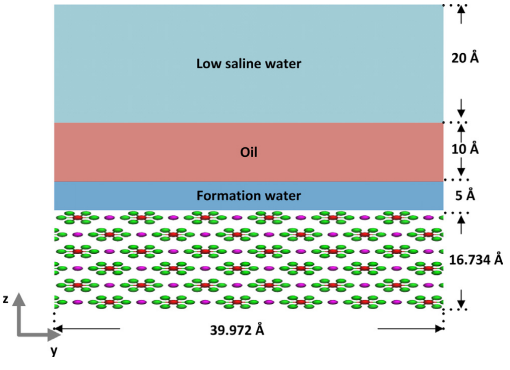

Fig. 1. The sketched geometry represents the schematic configuration of the system simulated with MD, which includes FW (H_2O, Na^+, Cl^-,and Ca^{2+}), oil (toluene, decane, and benzoic acid) and LSW (H_2O, Na^+, Cl^-, Mg^{2+}, and SO_4^{2-}) interacting with a calcite slab.

Table 1
Composition for the brines [35] (FW and LSW) and oil phase, which are used in MD simulation.

Fluid									
Formation water[2]			Oil phase[3]			Low saline water[1]			
[ppm]			[weight%]			[ppm]			
Na^+	Cl^-	Ca^{2+}	Toluene	Decane	Benzoic acid	Na^+	Cl^-	Mg^{2+}	SO_4^{2-}
56,200	124,100	770	37	44.7	18.3	13,700	24,468	1620	3310

Notes: The density of low saline water, formation water and oil phase are as following:
(1)-Total density of Low saline water = 1.196 gr/cm^3.
(2)-Total density of Formation water = 1.462 gr/cm^3.
(3)-Total density of Oil phase = 0.938 gr/cm^3.

Table 2
The number of molecules associated with each component at different, which are used in MD simulation.

Fluid												
Calcite slab	Formation water				Oil phase			Saline water				
[no. of molecules]	[no. of molecules]				[no. of molecules]			[no. of molecules]				
$CaCO_3$	H_2O	Na^+	Cl^-	Ca^{2+}	Toluene	Decane	Benzoic acid	H_2O	Na^+	Cl^-	Mg^{2+}	SO_4^{2-}
12,000	276	18	26	4	38	29	14	1101	14	16	2	1

oil species. To this end, six atomic calcite layers were cleaved parallel along the plane $(10\bar{1}4)$[39,40] to provide the 16.734 Å thickness along the z-axis, while the slab foundation with 41.183 Å×39.972 Å lays on the xy-plane. A layer of FW including the 276 water molecules combined with mono/divalent inorganic ions mounted over the calcite slab using PACKMOL [41] to provide a thickness of 5 Å along the z-axis, as shown in Fig. 1. The next fluid phase is oil with a particular composition of organic compounds that adds 10 Å thickness to the top of FW. The LSW is placed on top of FW and oil, wherein 1101 water molecules are coupled with mono/divalent inorganic ions to create a 20 Å thickness above oil along the z-axis.

2.3. Details of MD simulation

All MD simulations in this work were conducted by Large Atomic/Molecular Massively Parallel Simulator [42] (LAMMPS). LAMMPS is an open-source MD code, which applies efficient parallel algorithms to simulate the thermodynamic ensembles in 2D and 3D, wherein the particles interact with various force fields. For two reasons, the calcite slab was treated as a rigid solid in this simulation. i) calcite slabs have a dynamic nature in reality that constantly reconfigure in response to their environment. ii)dissolution and chemical precipitation over calcite surfacewill alter the rock's morphology and thermodynamic equilibrium. For example,

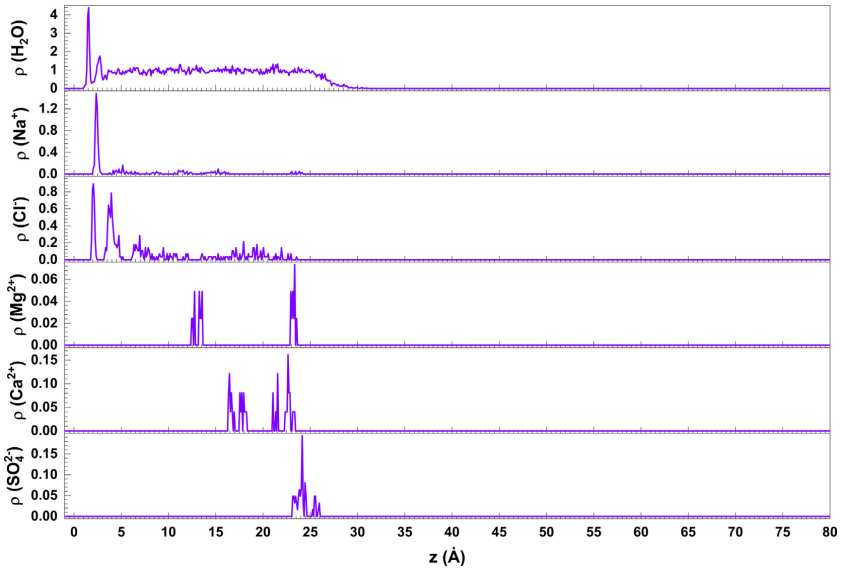

Fig. 2. The graph represents the mass density profile of H_2O, Na^+, Cl^-, Mg^{2+}, Ca^{2+} and SO_4^{2-} at T=300 K. The arrangement of Na^+ and Cl^- layers above the calcite mineral is an appropriate testimony to the monovalent ion's tendency for binding to the calcite surface.

as brine salinity decreases, trapped organic molecules in the calcite crystal are expelled into the solution, which alters the history of the rocks. Therefore, by simulating a calcite slab as a rigid solid, we excluded the dynamics of the calcite surface restructuring in our study in order to avoid overly complicated simulation [43]. Here, the proposed force field by Xiao et al. [44] defines the interatomic potential between calcite particles. Parameters describing the force field are listed in supplementary material. The three-sites rigid water model TIP3P [45] was employed to represent the force field between the water molecules. In order to model the interatomic potential of ions present in LSW and FW, two different protocols were utilized. Namely, the interatomic potential of Na^+, Cl^-, Mg^{2+}, and Ca^{2+} were modeled using OPLS-AA [46] (Optimized Potentials for Liquid Simulations-All-Atom). Whereas the force field for SO_4^{2-} anion is determined by the potential developed by Williams et al. [47]. The geometric mixing rules were considered to calculate the cross-term interatomic potentials of different atoms. Additionally, OPLS-AA [46] force field controls the interatomic potential of oil components including decane, toluene and benzoic acid. The long-range electrostatic interactions were calculated by the particle–particle–particle-mesh method [48] (PPPM) with a relative tolerance of 10^{-6}. For determining all short-range potentials, on the other hand, a cut-off of 10 Å was applied. To prevent the molecule run away from the top of the simulation box, a repulsive wall was embedded in the uppermost of the simulation box. The periodic boundary conditions were applied along the x and y-axes, while the boundary condition along the z-axis was considered fixed. The simulations were executed with the canonical ensemble (NVT) at T=300 K and T=360 K. In each simulation, the temperature was controlled using the Nose-Hoover [49] thermostat, which is one of the most accurate algorithms for modeling the NVT ensemble with classical MD simulations. The simulation run time for all scenarios are 45 ns, 5 ns for equilibration and 40 ns for production, with time step of 0.5 fs to achieve high resolution.

3. Results and discussion

The results of two defined scenarios, including low temperature (T=300 K) and high temperature (T=360 K), are analyzed and discussed in the following subsections. To begin, Section 3.1 illustrates the formation of structured water layers on the uppermost layer of the calcite. Then, in Sections 3.2, 3.3 and 3.4, we will explore the hydration of monovalent and divalent ions, as well as mass density and charge density profile. Finally, the evolution of ion distribution over time will be investigated and explained in Section 3.5.

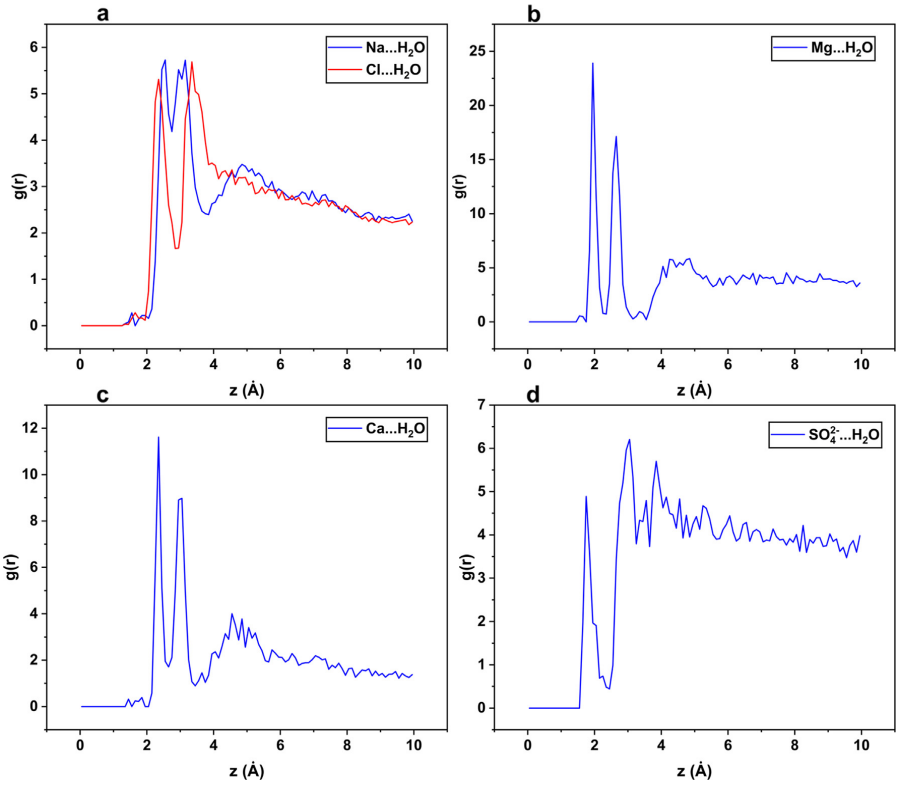

Fig. 3. At the last timestep of the simulation, the radial distribution function g(r) of mono/divalent ions with respect to the H_2O molecule at T=300 K is plotted. The closest distances between Na^+, Cl^-, Mg^{2+}, Ca^{2+} and SO_4^{2-} and the first H_2O molecule are 2.45 Å, 2.35 Å, 1.95 Å, 2.35 Å and 1.75 Å, indicating that all of the existing mono/divalent ions are hydrated.

3.1. Calcite surface hydration

Fig. 2 depicts the density profile of different ions and water along the z-axis, the axis normal to the calcite surface. The density profile plotted in Fig. 2 helps evaluate the proclivity of various species to accumulate on a thin calcite-brine film. The depicted density profile explicitly demonstrates the adsorption of two water monolayers onto the calcite surface. In other words, the uppermost layer of calcite mineral is hydrated by a couple of highly structured water monolayers. Various ions density profiles immediately follow the structured water monolayers covering the calcite surface, with much lower densities. The adsorption of water monolayers at the calcite mineral surface is consistent with de Leeuw and Parker's [50] observations. Fenter et al. [5] also reported hydration of the calcite surface when they used high-resolution X-ray to probe the calcite-water interface. Two structured layers of Na^+ and Cl^- also are visible above the calcite mineral. As seen, the structured layer of Na^+ is located within the fully ordered layers of adsorbed water. While the tight peak of Cl^- appeared after the fully ordered layers of adsorbed water. The arrangement of Na^+ and Cl^- layers above the calcite mineral as a result of the energy penalty imposed by the ion solvation shell [51] is an appropriate testimony to the

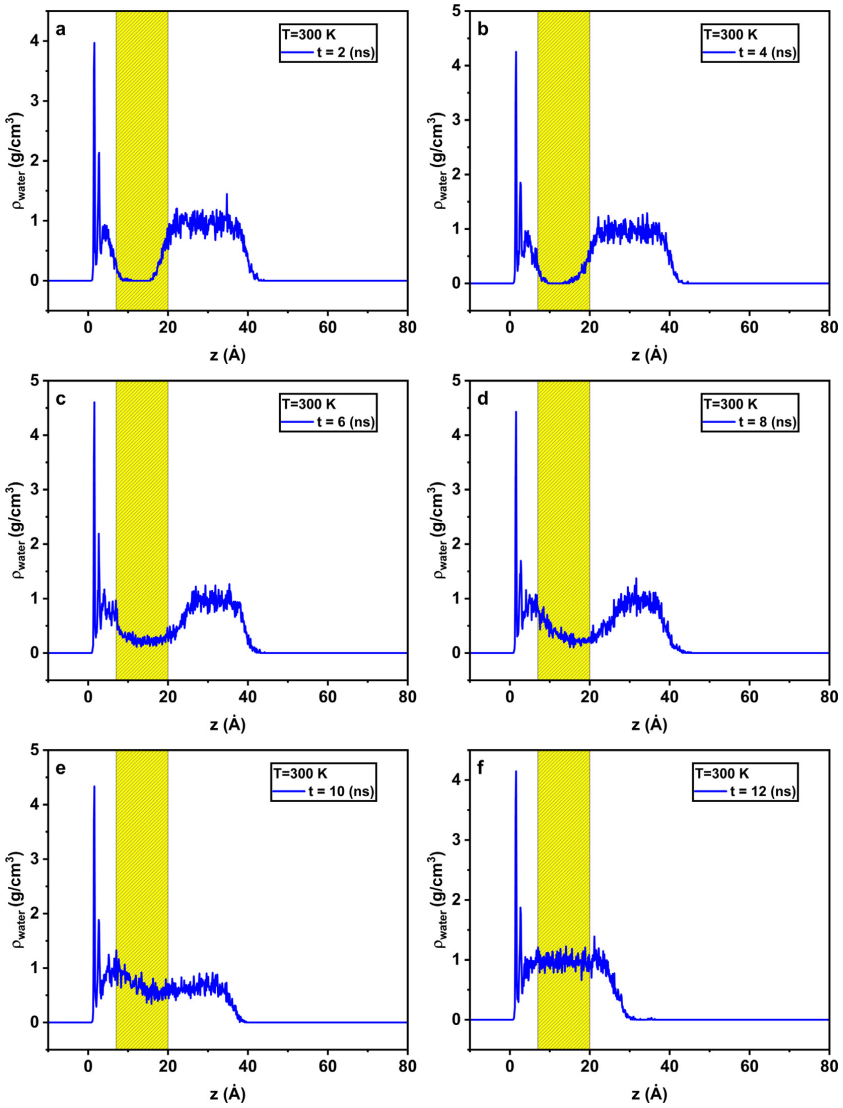

Fig. 4. Illustration of water density profile along the z-axis at T=300 K at initial (t = 2 ns and 4 ns), transition (t = 6 ns, 8 ns and 10 ns) and completion stages (t = 12 ns). The yellow shadow has highlighted the transition in the density profile.

ion's tendency for binding to the calcite surface. Furthermore, the appearance of the first monolayer of water at about 2 Å above the calcite surface indicates that neither Na^+ nor Cl^- are directly adsorbed on the calcite surface. In other words, the first monolayer of water bridges between monovalent ions (herein, Na^+ and Cl^-) and calcite surface, as Koleini et al. [52] previously reported on this issue.

On the other hand, the divalent cations, i.e., Mg^{2+} and Ca^{2+}, remain far from the calcite surface, presumably due to the higher energy penalty as reported by Chen et al. [53]. In addition, SO_4^{2-} stays far from calcite as divalent cations do. Section 3.5 will scrutinize the distribution of the divalent ions over time.

3.2. Hydration of ions

In the first and second scenarios, the hydration of the ions was initially explored. Specifically, the radial distribution function (rdf), also known as g(r), was employed to calculate the distance between mono/divalent ions and molecules of water settled at a certain radius around the ions. Fig. 3 shows the radial distribution function for different ions at the last timestep and T=300 K. As displayed, the adjacent H_2O molecules encircle Na^+, Cl^-, Mg^{2+}, Ca^{2+} and SO_4^{2-} at the radius of 2.45 Å, 2.35 Å, 1.95 Å, 2.35 Å and 1.75 Å, indicating that all of the existing mono/divalent ions are hydrated.

3.3. Evolution of water density profile over time

Figs. 4 and 5 show the water density profile at certain timesteps when T=300 K and T=360 K, respectively. The chosen snapshots in Figs. 4 and 5 demonstrate different stages in which the water density profile develops, including the initial, transition, and completion stages. In each plot box from left to right, a couple of structured water layers are observed near the solid surface, depicting the layering zone formed within the FW phase as reported in previous studies [54]. Following fully ordered water layers, a pit pattern in the water density profile represents the oil phase mounting above the FW. In fact, at the initial stage, the water density curve declines and experiences zero after some oscillation within FW. More precisely, within Fig. 4a-b and 5a-b, the position of the oil phase is distinguishable, where the curve touches zero and forms a pit-like appearance in the profile. On the right side of the plot box, the density profile rises again and LSW curve emerges on the tail of the water density profile.

As seen in Figs. 4c-d and 5c, a shift in water density profile commences, which is called transition hereafter. To be specific, when T=300 K, the transition occurs in two steps (t = 8 ns and t = 10 ns) before reaching a complete density profile (completion stage) without a pit-like pattern, signifying the exit of the oil phase that was sandwiched between FW and LSW. Whereas, with T=360 K, the transition of density profile is a one-step process, indi-

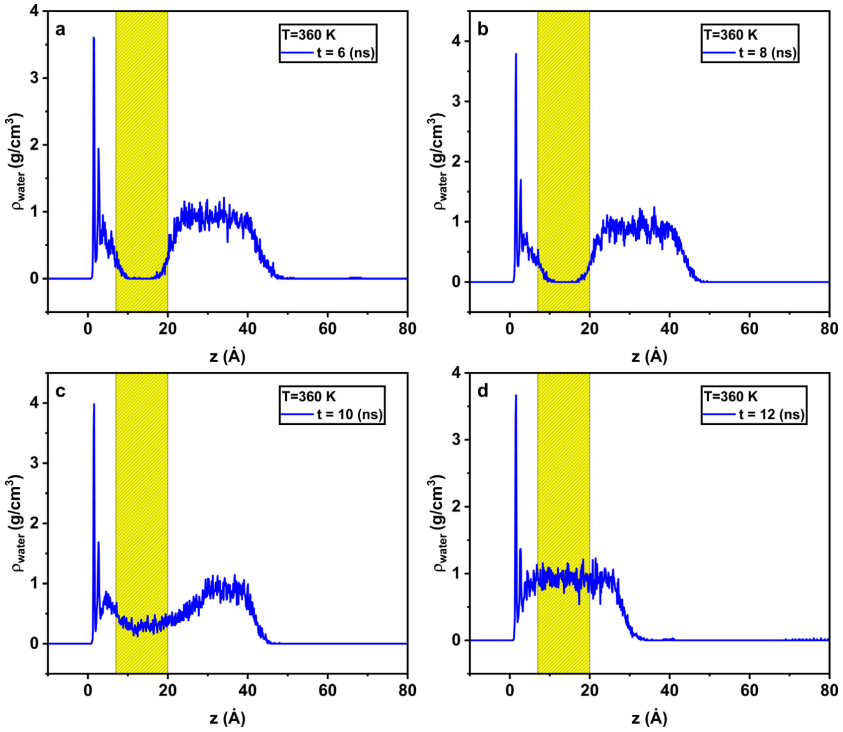

Fig. 5. Illustration of water density profile along the z-axis at T=360 K at initial (t = 6 ns and 8 ns), transition (t = 10 ns) and completion stages (t = 12 ns). The yellow shadow has highlighted the transition in the density profile.

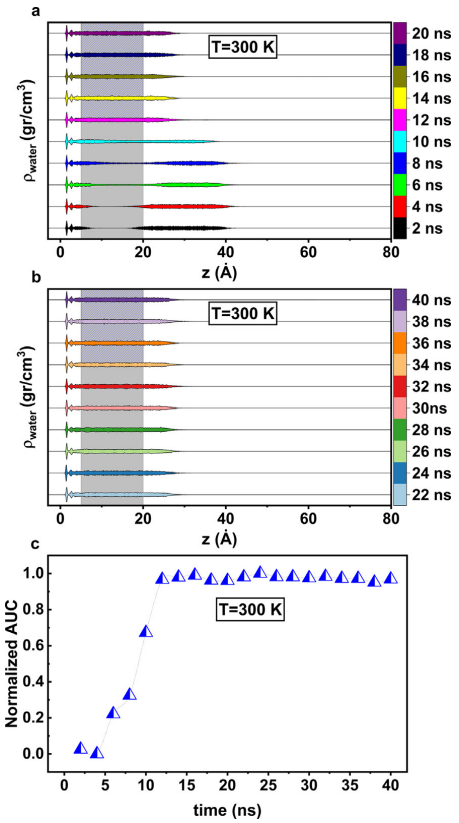

Fig. 6. Plots a-b show the evolution of the density profiles at T=300 K across different time steps. Plot c, depicts the behavior of the normalized area under the density curve (AUC), which is determined using the temporal evolution of the water density curve at T=300 K.

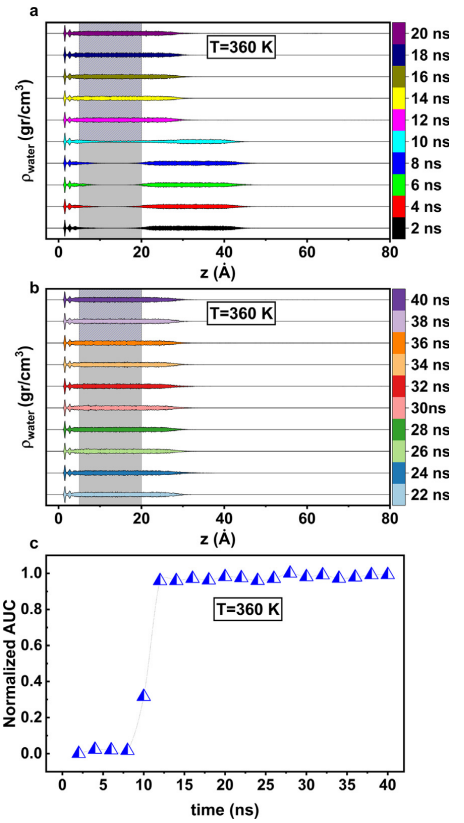

Fig. 7. Plots a-b show the evolution of the density profiles at T=360 K across different time steps. Plot c, depicts the behavior of the normalized area under the density curve (AUC), which is determined using the temporal evolution of the water density curve at T=360 K.

cating that the trapped oil phase has departed at t = 10 ns. Finally, in Figs. 4f and 5d, where t = 12 ns, the density profile of water is developed and no pit-like pattern is visible.

The evolution of the water density profile throughout all simulation time steps is demonstrated in Figs. 6 and 7. These figures provide a comprehensive view of the time evolution of the water density profile.

In Figs. 6 and 7, each density profile is merged with its vertical mirrored trend to indicate the intersection with the z-axis and take off from zero, marking the initial, transition and completion stages. The distinct colors assigned to each curve serve as a reference point to indicate the state of evolution at a certain time step.

As seen in Fig. 6a, before t = 8 ns, the coexistence of FW, oil and LSW is apparent, addressing the initial stage. From t = 6 ns to t = 12 ns, the oil phase is displaced gradually within the transition stage, which results in the extension of the colored region. Beyond the t = 12 ns, the colored regions in Fig. 6a-b remain almost unchanged, representing the completion stage. To precisely capture the boundaries of the different stages, the normalized area under the density curve (AUC) is calculated using a numerical integral product. Its evolution is then plotted over time in Fig. 6c. Using AUC, one can easily trace the transition steps at T=300 K, which are t = 6 ns, t = 8 ns and t = 10 ns.

On the other hand, when T=360 K, a distinction between FW, oil and LSW is traceable till t = 10 ns in Fig. 7a. After the initial state, the oil phase translates within t = 8–12 ns and since then, the colored regions become stable in Fig. 7a-b, implying the completion stage. By following the profile of the AUC in Fig. 7c, one realizes that at T=360 K, the transition occurs at one step, i.e., t = 10 ns. A comparison of Fig. 6c and Fig. 7c reveals that at T=300 K, the breakthrough in normalized AUC occurs in three steps (t = 6 ns, 8 ns, and 10 ns), whereas at T=360 K, the breakthrough appears at t = 10 ns. Although both density profiles at T=300 K and T=360 K possess a stable profile after t = 12 ns, the transition state at T=300 K occurs earlier than at T=360 K. Furthermore, at T=360 K, the transition stage, which coincides with oil displacement, is performed within one step.

To sum up, a one-stage transition at T=360 K implies a quick shift when compared to a three-stage transition at T=300 K. Namely, the transition at T=360 K begins with a delay and lasts for a shorter time. The observed breakthrough in Fig. 6c and Fig. 7c reveals microscopic changes in the organic and inorganic fluids interacting with the calcite surface.

3.4. Evolution of charge density profile over time

The local charge density is defined as a difference between the number of positive and negative charges. Thus, the charge density trend can indicate which charge is present and how it is distributed throughout the calcite surface.

To better understand the ionic environment in the vicinity of calcite substrate the contribution of all types of ions based on the charge density are plotted in Figs. 8 and 9, displaying the charge density development with time at T=300 K and T=360 K.

It was mentioned that monovalent ions (Na^+ and Cl^- in Fig. 2) have a higher affinity for calcite surface than divalent ones. Because, the monovalent ions diffuse into the structured water layers and divalent ones stay far from the calcite surface [55]. Figs. 8-9 demonstrate how the presence of structured ion layers in vicinity of calcite substrate leads to the formation of EDL which is compatible with the double layer theory of Gouy-Chapman [56]. The EDL is made of stern layer with positive charge (Na^+) and diffuse layer with negative charge (Cl^-). This arrangement is in agreement with Koleini et al. [43] observation. As they reported in a different study used a neutral substrate of calcite and found that the protrude oxygen atoms of neutral calcite surface interact with Na^+ and develop the EDL [36].

In Fig. 8a-b and Fig. 9a-b, the charge density curve oscillates initially, then experiences zero along with the oil phase, and finally oscillates again where the LSW exists. According to Fig. 8, which presents charge density at T=300 K, a discontinuity is noticed between the oscillations at left and right at t = 2 ns and 4 ns, indicating no charge has been distributed. The observed gap began to build up at t = 6 ns, continued at t = 8 ns, 10 ns, then completed at t = 12 ns so that no gap is noticed in charge density within t = 14--20 ns.

On the other hand, the charge density behaves differently in terms of extension with time at T=360 K. As seen, in Fig. 9a-b, a discontinuity similar to what is presented at T=300 K sepa-

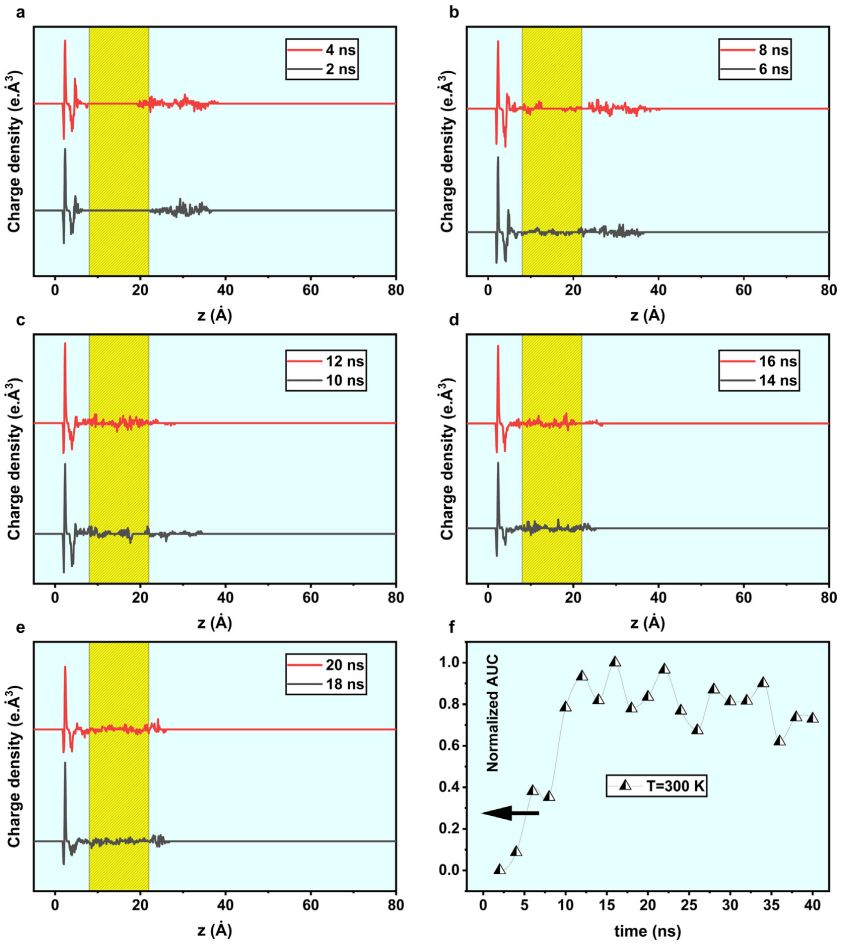

Fig. 8. At T=300 K and several time steps, the charge density profile above the calcite surface is depicted within plots a-f. The oscillations near the solid surface show the double electrical layer (EDL) curve, which experiences zero across the oil phase until t = 8 ns. The observed gap in charge density oscillations starts bridging at t = 10 ns, which is accompanied by escaping the oil phase and merging FW with LSW.

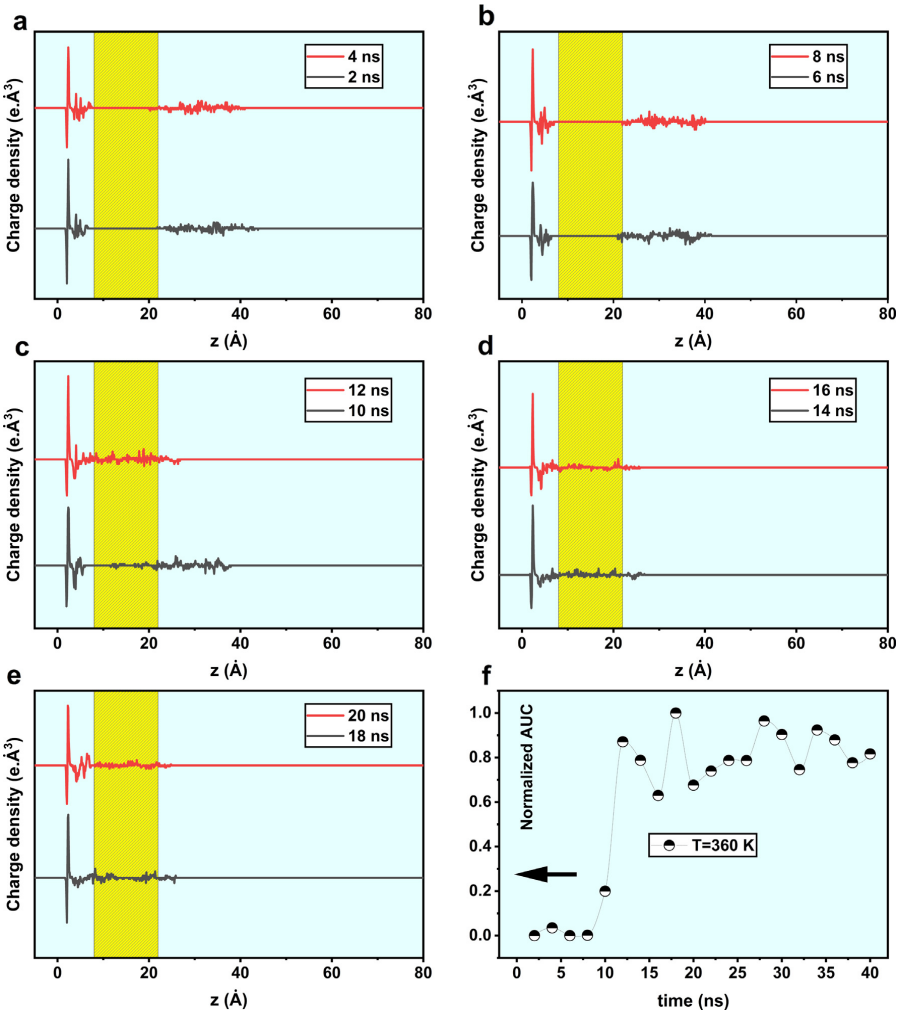

Fig. 9. At T=360 K and several time steps, the charge density profile above the calcite surface is depicted within plots a-f. The oscillations near the solid surface show the double electrical layer (EDL) curve, which experiences zero across the oil phase until t = 8 ns. The observed gap in charge density oscillations starts bridging at t = 10 ns, which is accompanied by escaping the oil phase and merging FW with LSW.

rates the charge density profile into two parts until t = 8 ns, meaning that the oil phase resided between the FW and LSW phase.

When the simulation time step reaches 10 ns at T=360 K, the gap in the charge density profile starts filling up. By integrating the area under the charge density curve (AUC) and normalizing, one may follow the change of the charge density evolution at each time step such as what is presented in Figs. 8f and 9f. The patterns represented in Fig. 8f and Fig. 9f track the charge density evolution with respect to the simulation time step at T=300 K and T=360 K, respectively. As seen, at T=300 K, the charge density development starts earlier than T=360 K. In contrast, the transition state at T=360 K occurs quicker than the transition state at T=300 K. There are several similarities between Figs. 6–7 and Figs. 8–9. In other words, the charge density and water density not only evolve in the same timestep but also behave similarly over time. Therefore, oil detachment from calcite-brine interface occurs concurrently with bridging the observed gap in charge density which is consistent with Alotaibi [57] and Mahani [58] findings.

3.5. Distribution of the mono/divalent ions

The charge density trend is the result of the local distribution of various anions and cations. Each anion and cation depends on the inherent charge and hydration energy has a unique interaction with the calcite surface. In this section, the distribution of the mono/divalent ions will be investigated as a function of the simulation time step to study the repositioning of the ions before and

after oil detachment from calcite-rock interface. The mass density and charge density profile in previous sections showed that the transition stage at T=300 K and T=360 K happens at different time-steps i.e., t = 4 ns and t = 8 ns, respectively. Hence, any displacement of mono/divalent ions before t = 4 ns and t = 8 ns could be related to a potential cause for oil displacement. To this end, Figs. 10 and 11 were plotted to track the position of various ions along the z-axis. The blue vertical axis at the left side of each plot box displays z-axis. While the red vertical axis at the right side presents normalized AUC. As shown in Figs. 10a-b and 11a-b, the position of Na^+ and Cl^- stabilizes at around 2.35 Å and 2.85 Å and temperature have no severe effect on the repositioning of Na^+ and Cl^-. Regarding time dependency of ions position, Na^+ settles at a fixed position before t = 4 ns and have no intention to translate by temperature.

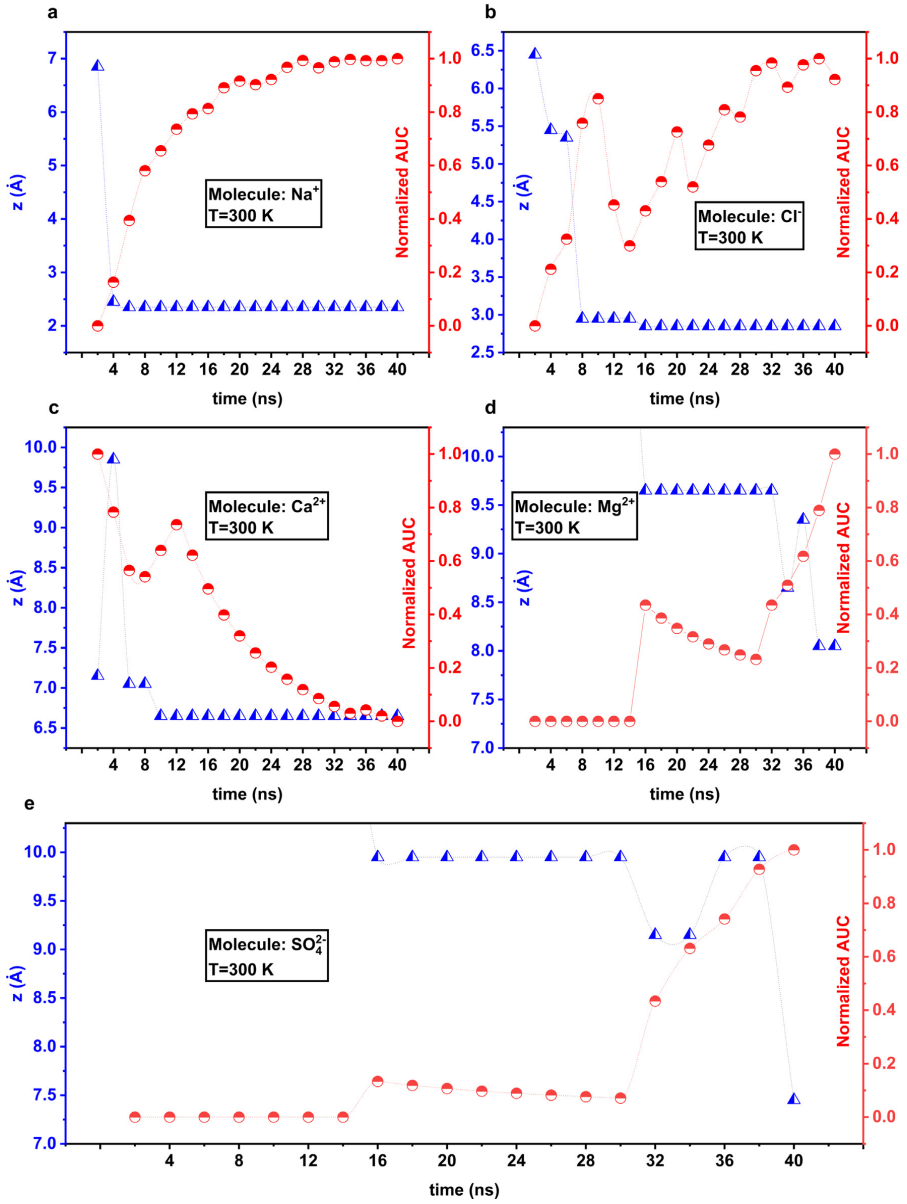

Fig. 10. The graphs illustrate the normalized AUC of g(r) at the right vertical axis and distance from the solid surface at the left vertical axis with respect to the time at T=300 K.

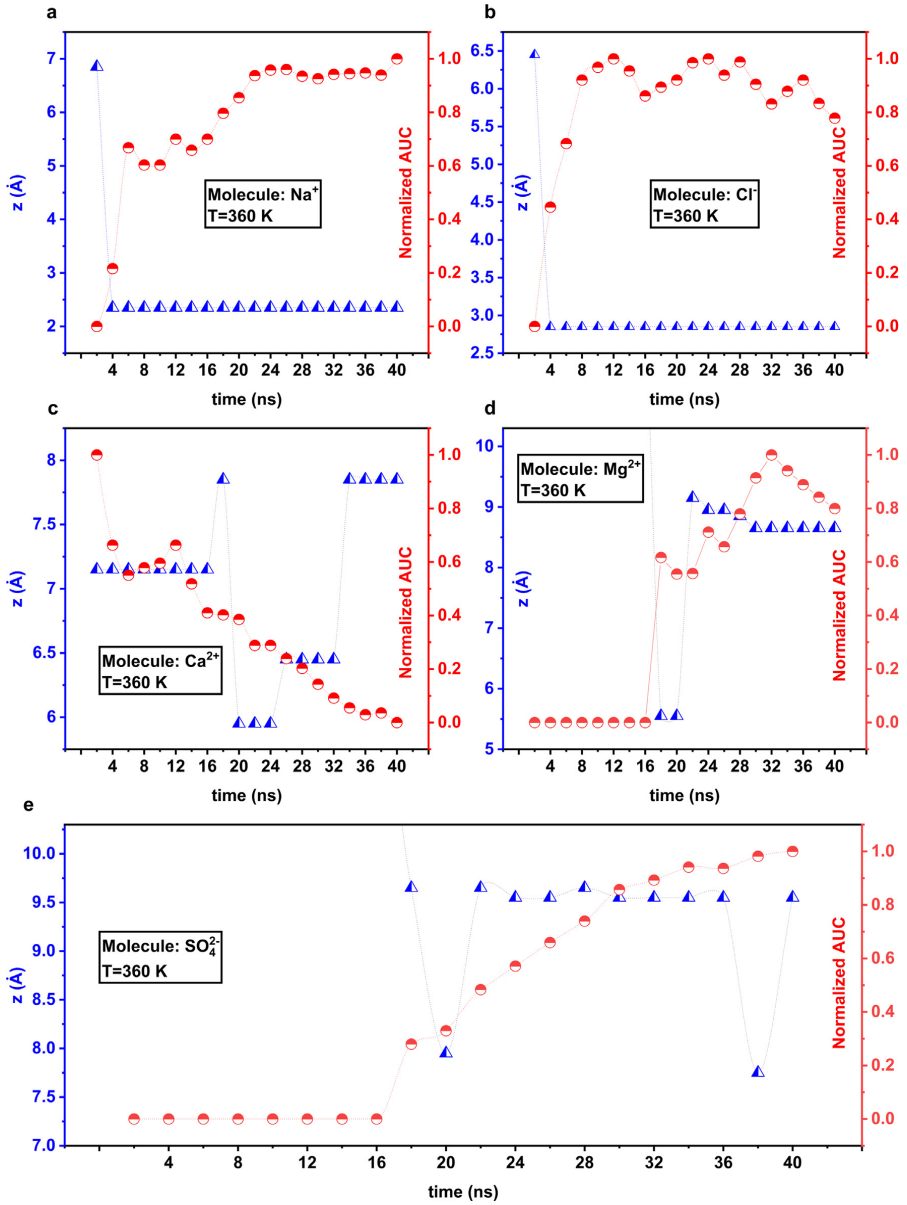

Fig. 11. The graphs illustrate the normalized AUC of g(r) at the right vertical axis and distance from the solid surface at the left vertical axis with respect to the time at T=360 K.

At the same time, Cl^- behaves similarly to Na^+ at T=360 K. Nevertheless, when T=300 K the position of Cl^- stabilizes a bit later at t = 8 ns. A previous study by Liu et al. [59] found that the monovalent ions (Na^+ and Cl^-) settle on the calcite surface, disturbing the structured water layers. In terms of monovalent ions, our observation is consistent with them.

Figs. 10c and 11c have recorded the position and distribution probability of divalent cation Ca^{2+}. Although, at T=300 K, the blue curve lands on a fixed position after t = 8 ns and it oscillates between different positions at T=360 K. Nevertheless, the distribution probability of Ca^{2+} at high and low temperature decreases with time, as depicted with the red curve.

On the other hand, no severe change in the distribution probability of SO_4^{2-} and Mg^{2+} is noticed before t = 16 ns, as displayed in Figs. 10d-e and 11d-e. In other words, because the red curve intersects zero, the blue curve ascends (beyond the axis scale) prior to t = 16 ns, meaning that no SO_4^{2-} and Mg^{2+} ions were detected at a radius of 10 Å. By 10 Å, we mean the cut-off radius for g(r) function. Thus, any value greater than 10 Å will go to infinity, as shown in Figs. 10d-e and 11d-e. Although, the divalent ions i.e., SO_4^{2-} and Mg^{2+} move toward the solid surface after t = 16 ns and the relevant distribution probability increases simultaneously. However, in Sections 3.2 and 3.3, it was denoted that the oil detachment takes place much earlier than t = 16 ns. This finding verifies the results reported by Alotaibi [57], Mahani [58] and Mehana [60] who found that divalent ions (i.e., Ca^{2+}, Mg^{2+} and SO_4^{2-}) had a minor impact compared to the critical role of EDL in oil detachment from calcite-brine interface.

4. Conclusion

We utilized LAMMPS to conduct molecular dynamics simulations to explore the interaction of low salinity brine with a calcite mineral in a molecular scale. To mimic the rock-brine-oil system, the neutral surface of calcite is chosen as a rock surface, the oil is modeled with decane (hydrocarbon), toluene (aromatic) and benzoic acid (polar) and the low/high saline brines were simulated with different mixtures of Na^+, Cl^-, Ca^{2+}, Mg^{2+}, and SO_4^{2-}. For this simulation, two different scenarios were established so that each simulation scenario was completed within the 45 ns at a specific temperature, i.e., T=300 K and T=360 K. The results show that:

- All of the mono/divalent ions were hydrated by H_2O molecules.
- The H_2O molecules are adsorbed onto the calcite surface as structured layers.
- Following the H_2O molecules, the monovalent ions $Na^+$and Cl^--settle adjacent to the calcite surface until the last timestep of simulation.
- The ordered layering of monovalent ions $Na^+$and Cl^- form an EDL at calcite-brine interface.
- The detachment of oil from calcite-brine interface occurs concurrently with extension in charge density.
- The position of Ca^{2+} ions at T=300 K is morre stable than at T=360 K.
- Up to 16 ns the divalent ions Mg^{2+} and SO_4^{2-} were not traceable within the 10 Å above the surface along the z-axis. Mg^{2+} and SO_4^{2-} ions travel toward the calcite mineral surface after 16 ns and remain within 10 Å distance from surface.
- According to the results, the temperature change approximately didn't affect the position of Na^+, Cl^- and H_2O molecules. Whereas, the location of the Ca^{2+}, Mg^{2+} and SO_4^{2-} ions varies as a function of temperature, indicating a dynamic behavior with the temperature change.

CRediT authorship contribution statement

S. Ahmadi G.: Conceptualization, Methodology, Software, Validation, Writing – original draft, Visualization, Formal analysis, Investigation, Writing – review & editing. **S. Abdolahi:** Software, Validation, Investigation. **J. Jahren:** Supervision. **R. Miri:** Supervision, Writing – review & editing. **H. Hellevang:** Supervision, Writing – review & editing.

Declaration of Competing Interest

The authors declare that they have no known competing financial interests or personal relationships that could have appeared to influence the work reported in this paper.

Appendix A. Supplementary material

Supplementary data to this article can be found online at https://doi.org/10.1016/j.molliq.2022.119490.

References

[1] M. Mohapatra, S. Anand, B.K. Mishra, D.E. Giles, P. Singh, Review of fluoride removal from drinking water, J. Environ. Manage. 91 (1) (2009) 67–77.
[2] H. Ono, Y. Deng, Flocculation and retention of precipitated calcium carbonate by cationic polymeric microparticle flocculants, J. Colloid Interface Sci. 188 (1) (1997) 183–192.
[3] D.N. Rao, S.C. Ayirala, A.A. Abe, W. Xu, Impact of low-cost dilute surfactants on wettability and relative permeability, SPE/DOE Symposium on Improved Oil Recovery, OnePetro, 2006.
[4] P. Fenter, S. Kerisit, P. Raiteri, J.D. Gale, Is the calcite–water interface understood? Direct comparisons of molecular dynamics simulations with specular X-ray reflectivity data, J. Phys. Chem. C. 117 (10) (2013) 5028–5042.
[5] P. Fenter, P. Geissbühler, E. DiMasi, G. Srajer, L.B. Sorensen, N.C. Sturchio, Surface speciation of calcite observed in situ by high-resolution X-ray reflectivity, Geochim. Cosmochim. Acta 64 (7) (2000) 1221–1228.
[6] P. Fenter, N.C. Sturchio, Calcite (1 0 4)–water interface structure, revisited, Geochim. Cosmochim. Acta 97 (2012) 58–69.
[7] F. Hussain, A. Zeinijahromi, P. Bedrikovetsky, A. Badalyan, T. Carageorgos, Y. Cinar, An experimental study of improved oil recovery through fines-assisted waterflooding, J. Petrol. Sci. Eng. 109 (2013) 187–197.
[8] E. Pooryousefy, Q. Xie, Y. Chen, A. Sari, A. Saeedi, Drivers of low salinity effect in sandstone reservoirs, J. Mol. Liq. 250 (2018) 396–403.
[9] G.G. Bernard, Effect of floodwater salinity on recovery of oil from cores containing clays, SPE California Regional Meeting, OnePetro, 1967.
[10] P.P. Jadhunandan, N.R. Morrow, Effect of wettability on waterflood recovery for crude-oil/brine/rock systems, SPE Reservoir Eng. 10 (1995) 40–46.
[11] H.O. Yildiz, M. Valat, N.R. Morrow, Effect of brine composition on wettability and oil recovery of a Prudhoe Bay crude oil, J. Can. Pet. Technol. 38 (1999).
[12] G.-Q. Tang, N.R. Morrow, Influence of brine composition and fines migration on crude oil/brine/rock interactions and oil recovery, J. Petrol. Sci. Eng. 24 (2-4) (1999) 99–111.
[13] S.Y. Lee, K.J. Webb, I.R. Collins, A. Lager, S.M. Clarke, M. O'Sullivan, A.F. Routh, X. Wang, Low salinity oil recovery–Increasing understanding of the underlying mechanisms, SPE Improved Oil Recovery Symposium, OnePetro, 2010.
[14] J.C. Seccombe, A. Lager, K.J. Webb, G. Jerauld, E. Fueg, Improving waterflood recovery: LoSalTM EOR field evaluation, SPE Symposium on Improved Oil Recovery, OnePetro, 2008.
[15] K. Sandengen, O.J. Arntzen, Osmosis during low salinity water flooding, IOR 2013-17th European Symposium on Improved Oil Recovery, European Association of Geoscientists & Engineers, 2013, p. cp-342.
[16] M. Yu, A. Zeinijahromi, P. Bedrikovetsky, L. Genolet, A. Behr, P. Kowollik, F. Hussain, Effects of fines migration on oil displacement by low-salinity water, J. Petrol. Sci. Eng. 175 (2019) 665–680.
[17] R.A. Nasralla, H.A. Nasr-El-Din, Double-layer expansion: is it a primary mechanism of improved oil recovery by low-salinity waterflooding?, SPE Reservoir Eval Eng. 17 (2014) 49–59.
[18] H. Ding, S. Rahman, Experimental and theoretical study of wettability alteration during low salinity water flooding-an state of the art review, Colloids Surf., A 520 (2017) 622–639.
[19] P. Zhang, M.T. Tweheyo, T. Austad, Wettability alteration and improved oil recovery by spontaneous imbibition of seawater into chalk: Impact of the potential determining ions Ca2+, Mg2+, and SO42−, Colloids Surf., A 301 (2007) 199–208.
[20] S.J. Fathi, T. Austad, S. Strand, Water-based enhanced oil recovery (EOR) by "smart water": Optimal ionic composition for EOR in carbonates, Energy Fuels 25 (2011) 5173–5179.
[21] J. Song, Q. Wang, I. Shaik, M. Puerto, P. Bikkina, C. Aichele, S.L. Biswal, G.J. Hirasaki, Effect of salinity, Mg2+ and SO42− on "smart water"-induced carbonate wettability alteration in a model oil system, J. Colloid Interface Sci. 563 (2020) 145–155.
[22] H. Zeng, F. Zou, G. Horvath-Szabo, S. Andersen, Effects of brine composition on the adsorption of benzoic acid on calcium carbonate, Energy Fuels 26 (7) (2012) 4321–4327.
[23] P. Zhang, T. Austad, Wettability and oil recovery from carbonates: Effects of temperature and potential determining ions, Colloids Surf., A 279 (2006) 179–187.
[24] A.A. Yousef, S. Al-Saleh, M. Al-Jawfi, Smart waterFlooding for carbonate reservoirs: Salinity and role of ions, SPE Middle East Oil and Gas Show and Conference, OnePetro, 2011.
[25] A.A. Yousef, S. Al-Saleh, M. Al-Jawfi, Improved/enhanced oil recovery from carbonate reservoirs by tuning injection water salinity and ionic content, SPE Improved Oil Recovery Symposium, OnePetro,, 2012.
[26] S.F. Shariatpanahi, S. Strand, T. Austad, Initial wetting properties of carbonate oil reservoirs: effect of the temperature and presence of sulfate in formation water, Energy Fuels 25 (2011) 3021–3028.
[27] T. Austad, Water-based EOR in carbonates and sandstones: New chemical understanding of the EOR potential using "smart water", in: Enhanced Oil Recovery Field Case Studies, Elsevier, 2013, pp. 301–335.

[28] F. Rezaee, F. Yousefi, F. Khoeini, Heat transfer in strained twin graphene: A non-equilibrium molecular dynamics simulation, Physica A 564 (2021) 125542.
[29] F. Yousefi, M. Shavikloo, M. Mohammadi, Non-equilibrium molecular dynamics study on radial thermal conductivity and thermal rectification of graphene, Mol. Simul. 45 (8) (2019) 646–651.
[30] S. Kerisit, S.C. Parker, J.H. Harding, Atomistic simulation of the dissociative adsorption of water on calcite surfaces, J. Phys. Chem. B 107 (31) (2003) 7676–7682.
[31] S.A. Goltapeh, S. Abdolahi, R. Miri, H. Hellevang, Extension of PC-SAFT equation of state to include mineral surface effect in fluid properties using molecular dynamic simulation, Sustainable Energy Technol. Assess. 48 (2021) 101624.
[32] J. Gross, G. Sadowski, Perturbed-chain SAFT: An equation of state based on a perturbation theory for chain molecules, Ind. Eng. Chem. Res. 40 (2001) 1244–1260.
[33] J. Zhao, G. Yao, D. Wen, Salinity-dependent alterations of static and dynamic contact angles in oil/brine/calcite systems: a molecular dynamics simulation study, Fuel 272 (2020) 117615.
[34] M.H. Ghatee, M.M. Koleini, S. Ayatollahi, Molecular dynamics simulation investigation of hexanoic acid adsorption onto calcite (101 4) surface, Fluid Phase Equilib. 387 (2015) 24–31.
[35] Y. Zhang, H. Sarma, Improving waterflood recovery efficiency in carbonate reservoirs through salinity variations and ionic exchanges: A promising low-cost Smart-Waterflood approach, Abu Dhabi International Petroleum Conference and Exhibition, OnePetro, 2012.
[36] M.M. Koleini, M.H. Badizad, H. Mahani, A.M. Dastjerdi, S. Ayatollahi, M.H. Ghazanfari, Atomistic insight into salinity dependent preferential binding of polar aromatics to calcite/brine interface: implications to low salinity waterflooding, Sci. Rep. 11 (2021) 1–17.
[37] M.M. Thomas, J.A. Clouse, J.M. Longo, Adsorption of organic compounds on carbonate minerals: 1. Model compounds and their influence on mineral wettability, Chem. Geol. 109 (1993) 201–213.
[38] S.A. Markgraf, R.J. Reeder, High-temperature structure refinements of calcite and magnesite, Am. Mineral. 70 (1985) 590–600.
[39] S.C. Parker, P.M. Oliver, N.H. De Leeuw, J.O. Titiloye, G.W. Watson, Atomistic simulation of mineral surfaces: studies of surface stability and growth, Phase Transitions 61 (1997) 83–107.
[40] B.R. Heywood, S. Mann, Molecular construction of oriented inorganic materials: controlled nucleation of calcite and aragonite under compressed Langmuir monolayers, Chem. Mater. 6 (1994) 311–318.
[41] L. Martínez, R. Andrade, E.G. Birgin, J.M. Martínez, PACKMOL: a package for building initial configurations for molecular dynamics simulations, J. Comput. Chem. 30 (2009) 2157–2164.
[42] S. Plimpton, Fast parallel algorithms for short-range molecular dynamics, J. Comput. Phys. 117 (1) (1995) 1–19.
[43] M.M. Koleini, M.H. Badizad, Z. Kargozarfard, S. Ayatollahi, The impact of salinity on ionic characteristics of thin brine film wetting carbonate minerals: An atomistic insight, Colloids Surf., A 571 (2019) 27–35.
[44] S. Xiao, S.A. Edwards, F. Gräter, A new transferable forcefield for simulating the mechanics of CaCO3 crystals, J. Phys. Chem. C. 115 (41) (2011) 20067–20075.
[45] W.L. Jorgensen, J. Chandrasekhar, J.D. Madura, R.W. Impey, M.L. Klein, Comparison of simple potential functions for simulating liquid water, J. Chem. Phys. 79 (2) (1983) 926–935.
[46] W.L. Jorgensen, D.S. Maxwell, J. Tirado-Rives, Development and testing of the OPLS all-atom force field on conformational energetics and properties of organic liquids, J. Am. Chem. Soc. 118 (45) (1996) 11225–11236.
[47] C.D. Williams, N.A. Burton, K.P. Travis, J.H. Harding, The Development of a Classical Force Field to Determine the Selectivity of an Aqueous Fe3+–Eda Complex for Tco4– and So42–, J. Chem. Theory Comput. 10 (8) (2014) 3345–3353.
[48] W. Hockney, J.W. Eastwood, Computer Simulation Using Particles, IOP Publishing Ltd, 1988.
[49] S. Nosé, A unified formulation of the constant temperature molecular dynamics methods, J. Chem. Phys. 81 (1) (1984) 511–519.
[50] N.H. de Leeuw, S.C. Parker, Atomistic simulation of the effect of molecular adsorption of water on the surface structure and energies of calcite surfaces, J. Chem. Soc., Faraday Trans. 93 (3) (1997) 467–475.
[51] M. Ricci, P. Spijker, F. Stellacci, J.-F. Molinari, K. Voïtchovsky, Direct visualization of single ions in the Stern layer of calcite, Langmuir 29 (7) (2013) 2207–2216.
[52] M.M. Koleini, M.F. Mehraban, S. Ayatollahi, Effects of low salinity water on calcite/brine interface: A molecular dynamics simulation study, Colloids Surf., A 537 (2018) 61–68.
[53] H. Chen, A.Z. Panagiotopoulos, E.P. Giannelis, Atomistic molecular dynamics simulations of carbohydrate–calcite interactions in concentrated brine, Langmuir 31 (8) (2015) 2407–2413.
[54] S. Ahmadi Goltapeh, R. Miri, P. Aagaard, H. Hellevang, Extension of SAFT equation of state for fluids confined in nano-pores of sedimentary rocks using molecular dynamic simulation, J. Mol. Liq. 348 (2022) 118045, https://doi.org/10.1016/j.molliq.2021.118045.
[55] M.L. Schlegel, K.L. Nagy, P. Fenter, L. Cheng, N.C. Sturchio, S.D. Jacobsen, Cation sorption on the muscovite (0 0 1) surface in chloride solutions using high-resolution X-ray reflectivity, Geochim. Cosmochim. Acta 70 (14) (2006) 3549–3565.
[56] E.J.W. Verwey, J.T.G. Overbeek, Theory of the stability of lyophobic colloids, J. Colloid Sci. 10 (2) (1955) 224–225.
[57] M.B. Alotaibi, H.A. Nasr-El-Din, J.J. Fletcher, Electrokinetics of limestone and dolomite rock particles, SPE Reservoir Eval. Eng. 14 (2011) 594–603.
[58] H. Mahani, A.L. Keya, S. Berg, W.-B. Bartels, R. Nasralla, W.R. Rossen, Insights into the mechanism of wettability alteration by low-salinity flooding (LSF) in carbonates, Energy Fuels 29 (3) (2015) 1352–1367.
[59] J. Liu, O.B. Wani, S.M. Alhassan, S.T. Pantelides, Wettability alteration and enhanced oil recovery induced by proximal adsorption of Na+, Cl−, Ca 2+, Mg 2+, and SO 4 2− ions on calcite, Phys. Rev. Appl 10 (2018) 34064.
[60] M. Mehana, M. Fahes, Q. Kang, H. Viswanathan, Molecular simulation of double layer expansion mechanism during low-salinity waterflooding, J. Mol. Liq. 318 (2020) 114079.

Supplementary material for

Drivers of Low Salinity Effect in Carbonate Reservoirs Using Molecular Dynamic Simulation

Sajjad Ahmadi Goltapeh[a*], Saeed Abdolahi[b] , Jens Jahren[a], Rohldin Miri[a,c], Helge Hellevang[a]

[a] *Department of Geosciences, University of Oslo, PO Box 1047 Blindern, 0316 Oslo, Norway*

[b]*Department of Chemical Engineering, Amirkabir University of Technology, 424 Hafez Avenue, Tehran, Iran*

[c]*School of Chemical Engineering, Iran University of Science and Technology (IUST), PO Box 16765-163, Tehran, Iran*

The nonbonding interaction between atoms is described by a Lennard-Jones 12−6 expression plus columbic term:

$$U(r_{ij}) = 4\varepsilon_{ij}\left[\left(\frac{\sigma_{ij}}{r_{ij}}\right)^{12} - \left(\frac{\sigma_{ij}}{r_{ij}}\right)^{6}\right] + \frac{1}{4\pi\varepsilon_0}\left(\frac{q_i q_j}{r_{ij}}\right)$$

The bond stretching, angle bending, dihedral torsion and improper are represented, respectively, by:

$$U_b = k_b(r - r_0)^2$$

$$U_\theta = k_\theta(\theta - \theta_0)^2$$

$$U_{dihedral} = \frac{1}{2}k_1(1 + \cos(\varphi)) + \frac{1}{2}k_2(1 + \cos(2\varphi)) + \frac{1}{2}k_3(1 + \cos(3\varphi)) + \frac{1}{2}k_4(1 + \cos(4\varphi))$$

$$U_{improper} = K(\chi - \chi_0)$$

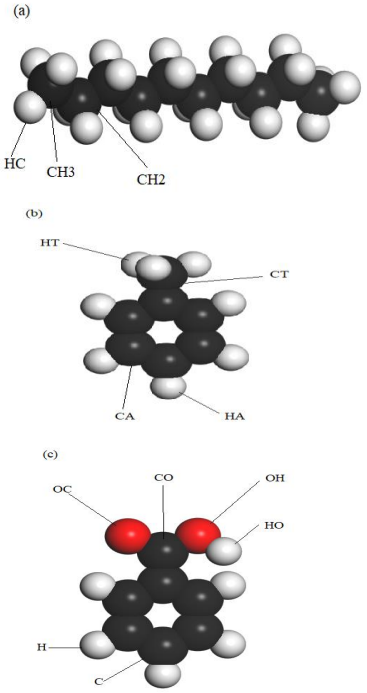

Figure S1. Molecular structure of (a) Decane, (b) Toluene, (c) Benzoic acid and definition of atom types

Table S1. Mass, charge, and Lennard-Jones parameters for water, Decane , Toluene, Benzoic acid, ions, and calcite

Symbols	Mass [g/mol]	Charge [e]	ε_{ii} [kcal/mol]	σ_{ii} [Å]
Water (TIP3P[1])				
Ow	15.9994	-0.83	0.102	3.188
Hw	1.008	+0.415	0.0	0.0
Decane (OPLS-AA[2])				
CH3	12.0107	-0.18	0.066	3.55
CH2	12.0107	-0.12	0.066	3.55
HC	1.00784	+0.06	0.03	2.5
Toluene (OPLS-AA[2])				
HT	1.00784	+0.06	0.03	2.5
CT	12.0107	-0.065	0.066	3.5
CA	12.0107	-0.115	0.07	3.55
HA	1.00784	+0.115	0.03	2.42
Benzoic Acid (OPLS-AA[2])				
C	12.0107	-0.115	0.07	3.55
H	1.00784	+0.115	0.03	2.42
OC	15.999	-0.44	0.21	2.96
CO	12.0107	+0.635	0.105	3.75
OH	15.999	-0.53	0.17	3
HO	1.00784	+0.45	0.0	0.0
Ions (OPLS-AA[2] and Williams et al.[3])				

Na	23.0	+1.0	0.0005	4.07
Cl	35.453	-1.0	0.71	4.02
Mg	24.305	+2.0	0.875044	1.6444471
S	32.065	+2.3	0.1999	3.55
Os	15.999	-1.075	0.15525	3.25
Ca	40.0780	+2.0	0.449657	2.412031
Calcite (Xiao et al.[4])				
$C_{calcite}$	12.0107	+0.999	0.088131	3.8233
$Ca_{calcite}$	40.0780	+1.668	0.477866	2.3705
$O_{calcite}$	15.9994	-0.889	0.13902	3.09086

The interatomic LJ parameters for calcite and water is represented in table S.2, while the geometric mixing rules were considered to calculate the cross-term interatomic potentials of other atoms.

$$\varepsilon_{ij} = \sqrt{\varepsilon_i \varepsilon_j}$$

$$\sigma_{ij} = \sqrt{\sigma_i \sigma_j}$$

Table S2. Interatomic LJ parameters for Calcite and water

Atom Type	Atom Type	ε_{ii} [kcal/mol]	σ_{ii} [Å]
Calcite-Calcite			
$C_{calcite}$	$O_{calcite}$	6.27	1.197
$O_{calcite}$	$O_{calcite}$	0.000273	4.744
Calcite-Water			
Ca	Ow	0.269896	2.76

C	Ow	0.116079	3.46
O	Ow	0.14603	3.118
O	Hw	0.000006968	4.497

Table S3. Bonded stretch, angle bend and dihedral parameters for water, calcite and sulfate ion

Bond stretch	Bond type	k_b [kcal/(mol·Å^2)]	r_0 [Å]
	$C_{calcite}$-$O_{calcite}$	314.5	1.294
	Hw-Ow	450.0	0.9572
	S-Os	525.15	1.487
Angle bend	Angle type	k_θ [kcal/(mol·deg^2)]	θ_0 [deg]
	Hw-Ow-Hw	55.0	104.52
	$O_{calcite}$-$C_{calcite}$-$O_{calcite}$	221.3	120.0
	Os-S-Os	139.906	109.47

Table S4. Bonded stretch, angle bend and dihedral parameters for Decane

Bond stretch	Bond type	k_b [kcal/(mol·Å^2)]	r_0 [Å]
	CH3-CH2	268	1.529
	CH2-CH2	268	1.529

	CH3-HC	340		1.09	
	CH2-HC	340		1.09	
Angle bend	Angle type	k_θ [kcal/(mol·deg^2)]		θ_0 [deg]	
	CH3-CH2-CH2	58.35		112.7	
	CH2-CH2-CH3	58.35		112.7	
	CH2-CH2-CH2	58.35		112.7	
	HC-CH3-HC	33		107.8	
	HC-CH2-HC	33		107.8	
Dihedrals	Dihedral type	k_1 [kcal/mol]	k_2 [kcal/mol]	k_3 [kcal/mol]	k_4 [kcal/mol]
	CH3-CH2-CH2-CH2	1.3	-0.05	0.2	0.0
	CH2-CH2-CH2-CH3	1.3	-0.05	0.2	0.0
	CH2-CH2-CH2-CH2	1.3	-0.05	0.2	0.0
	CH3-CH2-CH2-HC	0.0	0.0	0.3	0.0
	CH2-CH2-CH3-HC	0.0	0.0	0.3	0.0
	CH2-CH2-CH2-HC	0.0	0.0	0.3	0.0
	HC-CH3-CH2-HC	0.0	0.0	0.3	0.0
	HC-CH2-CH3-HC	0.0	0.0	0.3	0.0
	HC-CH2-CH2-HC	0.0	0.0	0.3	0.0

Table S5. Bonded stretch, angle bend, dihedral and improper parameters for Toluene

Bond stretch	Bond type	k_b [kcal/(mol·Å^2)]		r_0 [Å]	
	CT-HT	340.0		1.09	
	CA-CT	317.0		1.51	
	CA-CA	469.0		1.4	
	CA-HA	367.0		1.08	
Angle bend	Angle type	k_θ [kcal/(mol·deg^2)]		θ_0 [deg]	
	HT-CT-HT	33.0		107.8	
	CA-CT-HT	35.0		109.5	
	CA-CA-CA	63.0		120.0	
	CA-CA-CT	70.0		120.0	
	CA-CA-HA	35.0		120.0	
Dihedrals	Dihedral type	k_1 [kcal/mol]	k_2 [kcal/mol]	k_3 [kcal/mol]	k_4 [kcal/mol]
	CA-CA-CT-HT	0.0	0.0	0.0	0.0
	CA-CA-CA-CT	0.0	7.25	0.0	0.0
	CT-CA-CA-HA	0.0	7.25	0.0	0.0
	CA-CA-CA-CA	0.0	7.25	0.0	0.0
	CA-CA-CA-HA	0.0	7.25	0.0	0.0
	HA-CA-CA-HA	0.0	7.25	0.0	0.0
Impropers	Improper type	K [kcal/mol]		χ_0 [deg]	
	CA-CA-CA-HA	2.5		180.0	

	CA-HA-CA-CA	2.5	180.0
	CA-CA-CA-CT	2.5	180.0
	CA-CT-CA-CA	2.5	180.0

Table S6. Bonded stretch, angle bend, dihedral and improper parameters for Benzoic acid

Bond stretch	Bond type	k_b [kcal/(mol·Å^2)]		r_0 [Å]	
	OC-CO	570.0		1.229	
	CO-OH	450.0		1.364	
	C-CO	400.0		1.49	
	OH-HO	553.0		0.945	
	C-C	469.0		1.4	
	C-H	367.0		1.08	
Angle bend	Angle type	k_θ [kcal/(mol·deg^2)]		θ_0 [deg]	
	OH-CO-OC	80.0		121.0	
	OH-CO-C	70.0		120.0	
	OC-CO-C	80.0		120.4	
	CO-OH-HO	35.0		113	
	C-C-C	63.0		120.0	
	CO-C-C	85.0		120.0	
	C-C-H	35.0		120.0	
Dihedrals	Dihedral type	k_1 [kcal/mol]	k_2 [kcal/mol]	k_3 [kcal/mol]	k_4 [kcal/mol]

	OC-CO-OH-HO	0.0	5.0	0.0	0.0
	C-CO-OH-HO	4.0	5.0	0.0	0.0
	OC-CO-C-C	0.0	2.1	0.0	0.0
	OH-CO-C-C	0.0	2.1	0.0	0.0
	CO-C-C-C	0.0	7.25	0.0	0.0
	CO-C-C-H	0.0	7.25	0.0	0.0
	C-C-C-C	0.0	7.25	0.0	0.0
	C-C-C-H	0.0	7.25	0.0	0.0
	H-C-C-H	0.0	7.25	0.0	0.0
Impropers	Improper type	K [kcal/mol]		χ_0 [deg]	
	OH-C-CO-OC	10.5		180.0	
	OC-OH-CO-C	10.5		180.0	
	CO-C-C-C	2.5		180.0	
	C-C-C-H	2.5		180.0	
	C-H-C-C	2.5		180.0	
	C-CO-C-C	2.5		180.0	

References

[1] W.L. Jorgensen, J. Chandrasekhar, J.D. Madura, R.W. Impey, M.L. Klein, Comparison of simple potential functions for simulating liquid water, The Journal of Chemical Physics. 79 (1983) 926–935.

[2] W.L. Jorgensen, D.S. Maxwell, J. Tirado-Rives, Development and testing of the OPLS all-atom force field on conformational energetics and properties of organic liquids, Journal of the American Chemical Society. 118 (1996) 11225–11236.

[3] C.D. Williams, N.A. Burton, K.P. Travis, J.H. Harding, The Development of a Classical Force Field to Determine the Selectivity of an Aqueous Fe3+–Eda Complex for Tco4–and So42–, Journal of Chemical Theory and Computation. 10 (2014) 3345–3353.

[4] S. Xiao, S.A. Edwards, F. Gräter, A new transferable forcefield for simulating the mechanics of CaCO3 crystals, The Journal of Physical Chemistry C. 115 (2011) 20067–20075.

Appendices

Appendix A

InterPore 13th Annual Meeting, 31May - 4June 2021

Author:
Sajjad Ahmadigoltapeh
Co-authors:
Saeed Abdollahi , Helge Hellevang, Miri Rohaldin

On the fluid-rock interface, the order of the molecular structure and dynamical properties of fluid deviates from that of the bulk phase and the fluid exhibits a different thermodynamic behavior. To develop an understanding of the fluid-rock interface molecular dynamic (MD) simulation is conducted for water-calcite system. In this study, the results of MD simulations explicitly exhibit the layering transition of water on water-calcite interface. To predict the water properties near calcite wall, we have defined a contribution for Helmholtz energy extended from SAFT equation of state (EOS). In this approach, the confined water molecules interact with calcite surface through a square well energy ε estimated by MD simulation at a certain temperature (T). The outcomes of MD simulations confirm the fluctuation of energy, within the confinement, corresponds to the the calcite electrostatic field on the bulk water. The modified SAFT shows a good agreement with MD observations and the introduced model can predict the thermodynamic properties of water at systems with low water content.

Appendix B

83rd EAGE Annual Conference & Exhibition

Mineral-Fluid Interface Properties: A Molecular Dynamic Study

Introduction

Along with the mineral-fluid interfaces, a transition zone exists wherein the fluid exhibits different thermodynamic properties from the bulk phase. The interfacial properties of mineral-fluid interfaces are the consequences of mineral and fluid mutual interaction. Evaluating the properties of the fluid confined within the mineral-fluid interface is of interest to a variety of research fields such are bio (Walsh and Knecht, 2017), energy (Zhu et al., 2018), surface chemistry (Wang et al., 2018) and geology (Mishra et al., 2014). In order to accurately estimate the confined fluid properties, it is essential to develop our understanding of underlying mechanisms of interaction between a solid mineral and fluid.

There is a scarcity of experimental data on interfacial properties, thus modeling approaches can play an essential role in capturing the thermodynamic properties at the interface. The Monte Carlo (MC) algorithm is one option for gaining insights into confined fluid properties (Jin et al., 2017). In this regard, Li et al. (Li et al., 2005) have investigated capillary condensation and evaporation of the confined phase in slit-like pores with MC simulations. They reported that the phase transfer under pore confinement occurs at a pressure lower than bulk pressure. Zhang et al. (Zhang and Wang, 2006) investigated the fluid-solid interaction on the critical point change by applying the discrete wall potential model. They found the critical point increases for weak fluid-solid interactions and decreases for strong interface interactions. Barbosa et al. (Barbosa et al., 2016) modified the Travalloni (Travalloni et al., 2014) model by evaluating the effect of different confinement degrees on the fluid structure. However, the samples in MC method do not need to follow a physical process because of the ergodic generation process. Hence, additional alternatives, such as molecular dynamic (MD), come into consideration. Using MD, one can simulate the mineral-fluid interfaces using a known molecular interaction so-called force field. Unlike MC, MD simulation does not lose information about the actual physical process. In other words, not only can one gain information about the equilibrium state in MD, but one can also pursue the physical path reaching equilibrium. This simulation approach has demonstrated its potential as a viable tool for exploring the interfacial effects in systems with solid-fluid interactions (Sedghi and Piri, 2018). The use of MD simulation to study the mineral-fluid interface has received considerable attention in the literature (Adapa et al., 2018). For instance, Zhang et al. (Zhang et al., 2021) have studied the transport of two phase flow inside a calcite nanopore with MD. They observed the formation of the water bridge in the center of the nanopore when the water/oil proportion was high. Kirch et al.(Kirch et al., 2018) investigated the interface of calcite and brin water (including Na^+, Cl^- and Ca^{2+} ions) with MD simulation. The observed epitaxial ordering of water molecules on the surface of calcite precludes the direct adsorption of various chemical species.

Theory

In this study, calcite is chosen as the mineral which is one of the most abundant minerals in nature with rhombohedral structure, $R\bar{3}c$ space group, and unit cell parameters of a=b= 4.988 Å, c= 17.061 Å; α=β= 90°, γ= 120° (Markgraf and Reeder, 1985). The calcite layers were cleaved along the $(10\bar{1}4)$ surface. Then, water molecules were mounted above the calcite slab with PACKMOL (Martínez et al., 2009) software. Figure 1 shows the configuration of calcite-water in the simulation box. Water was provided in three different lengths, i.e., L_z = 2.5 nm, 4 nm and 7 nm. The boundary condition along x and y-axes is periodic, while along the z-axis, the boundary condition is fixed. The open source LAMMPS (Plimpton, 1995) software is used to conduct the MD simulations. The Nose-Hoover (Nosé, 1984) thermostat is applied to implement a canonical ensemble at T=300 K, 400 K and 500 K. Zhao (Zhao et al., 2019) and SPC/E (Berendsen et al., 1987) are two different force fields that were applied in this simulation. The former describes the interaction of calcite species, whereas the latter models the interactions of water molecules. Each simulation run took 2 ns to complete, including 1 ns for equilibration and 3 ns for production.

Results and discussion

Figure 2 displays the water density profile along the z-axis. Figure 2a depicts the density profile for L_z=2.5 nm, whereas 2b and 2c exhibit the density trends for L_z=4 nm and L_z=7 nm, respectively. Based

on the density profile behavior, three distinct zones (depicted in Figure 1) could be identified. The layering zone dominated by the interaction of calcite and water molecules is depicted by the first two large oscillations (peaks). The threshold of oscillations then drops, and the curve continues with a horizontal-like trend demonstrating the density behavior in the bulk-like region. About 0.5 Å above the calcite slab and before the largest peak is named the free zone, which is narrower than a radius of a water molecule and therefore, no water exists there. As shown, for the local density within the layering and bulk-like zones, one can write $\rho_{300\ K} > \rho_{400\ K} > \rho_{500\ K}$. Since local density cannot reflect a density inside the classified zones, the average density should be calculated instead. To this end, the integral product over the marked zones should be calculated. δ and σ in Figure 1 represent the thickness of the layering and free zones, respectively. The free zone starts from the surface of the calcite slab and ends at $z = \sigma$. Here, $\sigma = 0.5$ Å, which is around half of the radius of a water molecule and also equals the lower band of layering zone. The top band of the layering zone is the position in which the density experience 110% of the minimum density at the bulk-like zone. On the other hand, the end of the bulk-like zone is considered a position wherein the density reaches 90% of the minimum density at the bulk-like zone.

Figure 3 shows the calculated densities based on the results of MD simulations at different temperatures and various water lengths. The density at T=300 K, 400 K, and 500 K is displayed by black squares, red circles, and green triangles. The placement of the black squares in the top row demonstrates that low temperatures induce larger density values at a constant L_z. The green triangles at the bottom, on the other hand, illustrate that low densities correspond to high temperatures for a given L_z. In other words, T=300 K offers the highest density for all simulated lengths of water. It is worth mentioning that without calcite presence, the water density at T=300 K, 400 K, and 500 K is 996 kg/m^3, 937 kg/m^3, and 831 kg/m^3, respectively (Green and Southard, 2019). However, with T = 300 K at the calcite-water interface, the projected density based on the MD results becomes 890 kg/m^3, 899 kg/m^3 and 916 kg/m^3 for L_z =2.5, 4 and 7 nm, respectively. When the results mentioned above are compared, one can see that the density within the confinement at the calcite-water interface has diminished. Furthermore, comparing the black squares, red circles, and green triangles at a given temperature reveals that the higher L_z causes a higher density value. To understand this behavior, the intermolecular interactions inside the simulation box might be agued. It is known that at the calcite-water interface and very close to the calcite surface, the interaction between solid calcite and water prevails over the interaction between water molecules. This explains explicitly why two water layers (two huge peaks in Figure 2) are adsorbed to the calcite surface. According to Figure 3, raising L_z corresponds to the rise in density, meaning the calcite effect diminishes by increasing the average energy in the waterside. In other words, the confinement approaches the properties of the water without the presence of calcite.

Conclusion

The calcite-water interface is simulated using MD technique and the density trends were plotted at different T and L_z. In the density profiles, three distinct zones can be recognized. In order to calculate the average density inside each region, the numerical integral product was applied and it is assumed that 110% of the minimum density at the bulk-like is the end of the layering zone. Although due to the effect of the calcite slab, the large oscillations are observed within the layering zone, the average density at a given temperature is smaller than the density at the same temperature without the presence of calcite. The explanation is the peaks coincide with troughs which mitigates the average value. The bolt findings of this study are:

- The maximum local density (peak) within the layering zone at T=300 K reaches 2140, 2020 and 1760 kg/m^3 for L_z=2.5 nm, 4 nm and 7 nm, respectively.
- The minimum local density (tough) within the layering zone at T=300 K reaches 488, 501 and 504 kg/m^3 for L_z=2.5 nm, 4 nm and 7 nm, respectively.
- The average density at T=300 K becomes 890 kg/m^3, 899 kg/m^3 and 916 kg/m^3 for L_z =2.5, 4 and 7 nm, respectively.
- The average densities in the layering zone lay on lower values because the integral product sums the peaks and troughs.
- At a fixed L_z, the high density values correspond to the low temperature.

- At a fixed T, the high density values correspond to high L_z.

References

Adapa, S., Swamy, D.R., Kancharla, S., Pradhan, S., Malani, A., 2018. Role of mono-and divalent surface cations on the structure and adsorption behavior of water on mica surface. Langmuir 34, 14472–14488.

Barbosa, G.D., Travalloni, L., Castier, M., Tavares, F.W., 2016. Extending an equation of state to confined fluids with basis on molecular simulations. Chem. Eng. Sci. 153, 212–220.

Berendsen, H.J.C., Grigera, J.R., Straatsma, T.P., 1987. The missing term in effective pair potentials. J. Phys. Chem. 91, 6269–6271.

Green, D.W., Southard, M.Z., 2019. Perry's chemical engineers' handbook. McGraw-Hill Education.

Jin, B., Bi, R., Nasrabadi, H., 2017. Molecular simulation of the pore size distribution effect on phase behavior of methane confined in nanopores. Fluid Phase Equilib. 452, 94–102.

Kirch, A., Mutisya, S.M., Sánchez, V.M., de Almeida, J.M., Miranda, C.R., 2018. Fresh molecular look at calcite–brine nanoconfined interfaces. J. Phys. Chem. C 122, 6117–6127.

Li, Z., Cao, D., Wu, J., 2005. Layering, condensation, and evaporation of short chains in narrow slit pores. J. Chem. Phys. 122, 224701.

Markgraf, S.A., Reeder, R.J., 1985. High-temperature structure refinements of calcite and magnesite. Am. Mineral. 70, 590–600.

Martínez, L., Andrade, R., Birgin, E.G., Martínez, J.M., 2009. PACKMOL: a package for building initial configurations for molecular dynamics simulations. J. Comput. Chem. 30, 2157–2164.

Mishra, R.K., Fernández-Carrasco, L., Flatt, R.J., Heinz, H., 2014. A force field for tricalcium aluminate to characterize surface properties, initial hydration, and organically modified interfaces in atomic resolution. Dalt. Trans. 43, 10602–10616.

Nosé, S., 1984. A unified formulation of the constant temperature molecular dynamics methods. J. Chem. Phys. 81, 511–519.

Plimpton, S., 1995. Fast parallel algorithms for short-range molecular dynamics. J. Comput. Phys. 117, 1–19.

Sedghi, M., Piri, M., 2018. Capillary condensation and capillary pressure of methane in carbon nanopores: Molecular Dynamics simulations of nanoconfinement effects. Fluid Phase Equilib. 459, 196–207.

Travalloni, L., Castier, M., Tavares, F.W., 2014. Phase equilibrium of fluids confined in porous media from an extended Peng–Robinson equation of state. Fluid Phase Equilib. 362, 335–341.

Walsh, T.R., Knecht, M.R., 2017. Biointerface structural effects on the properties and applications of bioinspired peptide-based nanomaterials. Chem. Rev. 117, 12641–12704.

Wang, R., Peng, F., Song, K., Feng, G., Guo, Z., 2018. Molecular dynamics study of interfacial properties in CO2 enhanced oil recovery. Fluid Phase Equilib. 467, 25–32.

Zhang, W., Feng, Q., Jin, Z., Xing, X., Wang, S., 2021. Molecular simulation study of oil-water two-phase fluid transport in shale inorganic nanopores. Chem. Eng. Sci. 245, 116948.

Zhang, X., Wang, W., 2006. Square-well fluids in confined space with discretely attractive wall-fluid potentials: Critical point shift. Phys. Rev. E 74, 62601.

Zhao, J., Yao, G., Ramisetti, S.B., Hammond, R.B., Wen, D., 2019. Molecular dynamics investigation of substrate wettability alteration and oil transport in a calcite nanopore. Fuel 239, 1149–1161.

Zhu, Y., Zhan, K., Hou, X., 2018. Interface design of nanochannels for energy utilization. ACS Nano 12, 908–911.

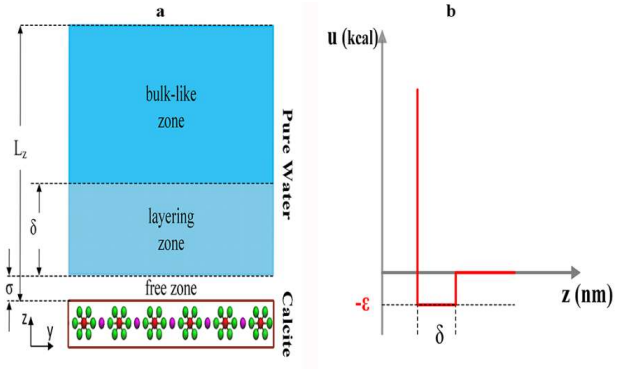

Figure 1. *The diagram illustrates the calcite-water configuration in MD simulation box.Three different zones are observed which are free zone, layering zone and bulk-like zone.*

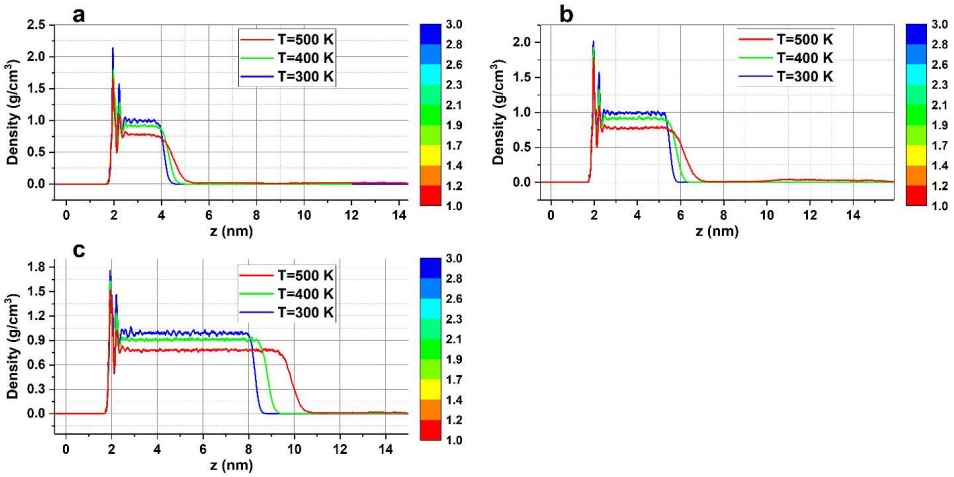

Figure 2. *The profile of density of water along the z-axis for different lengths of water. As observed, the highest local density value belongs to the lowest temperature (blue curve), which is T=300 K*

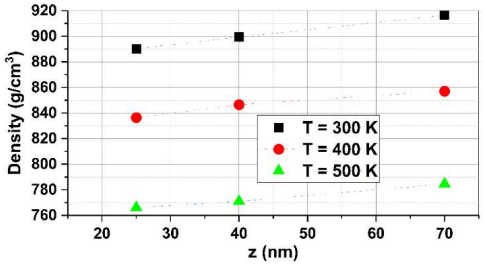

Figure 3. *The density value at calcite-water interface at different temperatures and various water lengths. The density within the layering zone is maximum and minimum when T=300 K and 500 K, respectively. The increase in L_z at a given temperature corresponds to the rise in density value.*

Appendix C

InterPore 14th Annual Meeting, 30May - 2June 2022

Author:
Sajjad Ahmadigoltapeh
Co-authors:
Miri Rohaldin, Per Aagaard, Helge Hellevang

The thermodynamic characteristics of water confined inside a nano-mineral pore differs from the bulk properties because of the competition between water-water and wall-water attractions near the solid walls. We used molecular dynamic (MD) simulation, to capture the influence of the solid walls of a slit shape calcite nanopore on the confined water provided in different widths namely 2 nm, 3 nm, 4 nm and 5 nm. The simulations are conducted with NVT ensemble at T = 300 K, 350 K, 400 K, and 450 K while each simulation run is completed within 6 ns. The results shows the density and total energy near the pore wall increases with temperature. To determine the new properties imposed by the nano-calcite pore, an equation of state (EoS) was developed based on the statistical association fluid theory (SAFT) by introducing a new term for Helmholtz free energy. Within a reliable absolute relative error (ARE), the results of the modified SAFT overlap with the outcomes of MD simulation. This approach can be applied in predicting the fluid properties near wall, which is the concern of several fields such as CO_2 storage, hydrogen storage and enhanced oil recovery (EOR) and etc.

Appendix D

Geoconvension 2022

geoconvention
Calgary • Canada • June 20-22 2022

Low Salinity Water Impact on the Calcite-Water Interface: A Molecular Dynamic Study

Sajjad Ahmadigoltapeh[1], Saeed Abdolahi[2], Rohaldin Miri[3], Helge Hellevang[1]

[1]University of Oslo (UiO), [2]Amirkabir University of Technology, [3]Iran University of Science and Technology (IUST)

Summary

In recent years, low salinity water (LSW) injection into carbonates and sandstone reservoirs, known as water flooding, has been adopted as a promising technique for enhanced oil recovery (EOR). This technology which is appealing to industry because of its low cost, can maintain pressure after initial depletion and displace oil by exploiting the effect of the viscous forces. Despite the rising industrial interest in LSW method, a coherent mechanism explanation for the technology has yet to be developed. Unknown molecular interactions in a rock-brine system are the primary cause for the lack of a cohesive mechanism driving LSW. In order to study molecular aspects of the interaction between a rock slab (solid phase) and brine (fluid phase), we used the molecular dynamic (MD) technique to simulate a system including calcite and brine solution. The results show that all mono/divalent ions are hydrated initially and a layer of water molecules located at 1.85 Å above the calcite surface. The Na^+, Cl^-, Mg^{2+} and SO_4^{2-} ions scatter at a radius of 2.45 Å, 4.15 Å, 4.45 Å, and 4.15 Å from the calcite slab, establishing the electrical double layer (EDL) along the z-axis and parallel to the calcite surface.

Introduction

Over millions of years, the cohabitation of brine water and oil within an oil reservoir has resulted in a thermodynamic equilibrium between reservoir rock, brine and oil. Water flooding with a known composition can disrupt the current equilibrium by altering the rock's wettability. Rock wettability within the oil reservoirs plays an essential role in subsurface multiphase flow behavior. Thus, advancements in EOR techniques are directly or indirectly related to changes in the wetting properties of the reservoir. Recently, water flooding has been utilized widely to displace oil, thereby improving the EOR technology. Injection of water with low salinity includes injection of diluted brine in either carbonates or sandstone reservoirs through secondary recovery/tertiary mode to enhance the oil recovery[1]. The industry as well showed immense interest in this technology. Because LSW injection, on the one hand, is cheap and straightforward to apply. On the other hand, it can maintain pressure after initial depletion and displace oil by exploiting the effect of the viscous forces.

Many research studies have focused on the capability of LSW injection until now. It is known that the presence of mono/divalent ions (i.e., Na^+, Cl^-, Mg^{2+} and SO_4^{2-}) control the wettability transition of the reservoir from thoroughly oil-wet to water-wet [2]. For example, Austad [3] et al. have reported that $CaSO_4$ is a key chemical for observing the LSW injection effect. They raised the sulfate content within an experiment while decreasing the NaCl concentration, and they found 88 percent

improvement in recovery. They also declared that the EOR low salinity impact is feasible in both carbonate and sandstone reservoirs. Mehraban[4] et al. have observed that not only concentrations of sulfate ions but also higher Ca^{2+} and Mg^{2+} concentrations resulted in considerable improvements in wettability alteration and recovery.

Improved oil recovery using the LSW approach is ascribed to several mechanisms, such as interfacial tension reduction[5], multicomponent ion exchange (MIE)[6], and electrical double layer (EDL) expansion[7]. Despite numerous attempts to realize the driving processes of wettability change, the interaction mechanism between LSW ions and the rock surface remains unknown at the molecular scale. To investigate the molecular interactions between a rock slab and brine, we employed molecular dynamic (MD) simulation. In this simulation, calcite plays role of the solid mineral interacting with a brine solution, including H_2O molecules, Na^+, Cl^-, Mg^{2+} and SO_4^{2-} ions.

Theory

Calcite ($CaCO_3$) is a mineral found in abundance in natural geological systems. Since calcite is a key ingredient of limestone, dolomite, and chalk, it is also among the most prevalent mineral observed in oil reservoirs. Hence, investigation of the calcite mineral interacting with the brine on a molecular scale can shed light on the complexity of the molecular mechanism leading to the oil displacement due to the injection of LSW. As a result, several studies have focused on the surface characteristics of calcite.

To study molecular interactions between a calcite slab and brine solution, we employed LAMMPS[8] (Large Atomic/Molecular Massively Parallel Simulator) for molecular dynamic (MD) simulations. In this study, calcite ($CaCO_3$) was chosen as the rock mineral because it is among the most prevalent mineral found in oil reservoirs. The most stable cleavage of calcite, 1014 plane, was utilized to construct a rock surface and the established force field by Xiao[9] was chosen to control the interaction among different species of calcite (i.e., Ca, C and O) in the solid phase. Then, the water molecules are wrapped and mounted above the constructed calcite slab with PACKMOL[10] software. TIP3P[11] defines the force field between the water molecules.

Table 1. Chemical composition of the different components in low saline water (LSW).

Low saline water ions			
Na^+ [ppm]	Cl^- [ppm]	Mg^{2+} [ppm]	SO_4^{2-} [ppm]
13700	24468	1620	3310
**Note:Total density of Low saline water = 1.196 gr/cm^3*			

The utilized elements and associated concentrations have been tabulated in Table 1. The number of elements is based on the density at T=300 K and pressure of 1 atm.

Table 2. calculated number of LSW molecules for MD simulation.

Low saline water ions				
H_2O	Na^+	Cl^-	Mg^{2+}	SO_4^{2-}
1101	14	16	2	1

Table 2 includes the number of required molecules to make the chemical concentrations which are mentioned in Table 1.

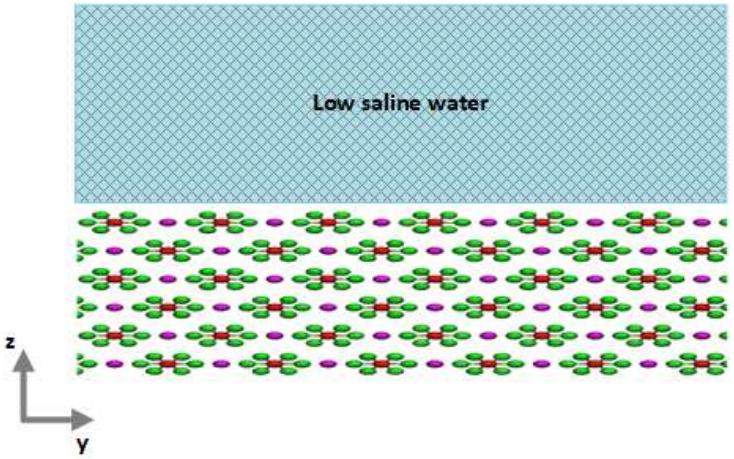

Figure 1. The sketched geometry represents the schematic configuration of the second system simulated with MD, which includes LSW (H_2O, Na^+, Cl^-, SO_4^{2-} and Mg^{2+}) interacting with a calcite slab.

To make a brine solution, it is required to mix the pure water molecules with mono/divalent ions. To this end, water molecules are combined with Na^+, Cl^-, Mg^{2+} and SO_4^{2-} representing the brine solution. Different protocols define the governing force field between mentioned cations and anions. To put it differently, the OPLS-AA[12] force field models the interaction of Na^+, Cl^- and Mg^{2+}, whereas the interaction of divalent anion SO_4^{2-} is modeled by Williams[13] force field. A canonical ensemble (NVT) implemented by the Nose-Hoover[14] thermostat ensures that the simulation is conducted at T=300 K. Taking a timestep of 1 ns, the simulation run is completed within 20 ns, 5 ns for equilibration and 15 ns for production.

Results and discussions

The trend of the radial distribution function of different ions and water molecules are plotted in Figure 2. According to Figure 2e, a layer of water is adsorbed on the rock surface with a local density that is 2-3 times that of the bulk density. This observation and relevant consequences have been reported in previous studies[15,16]. The water molecules connect to the oxygen of the calcite from the hydrogen side and locate at a radius of 1.85 Å along the z-axis. After water molecules, Na^+ ions stay at the closest distance to the calcite surface, which is 2.45 Å, as shown in Figure 2a.

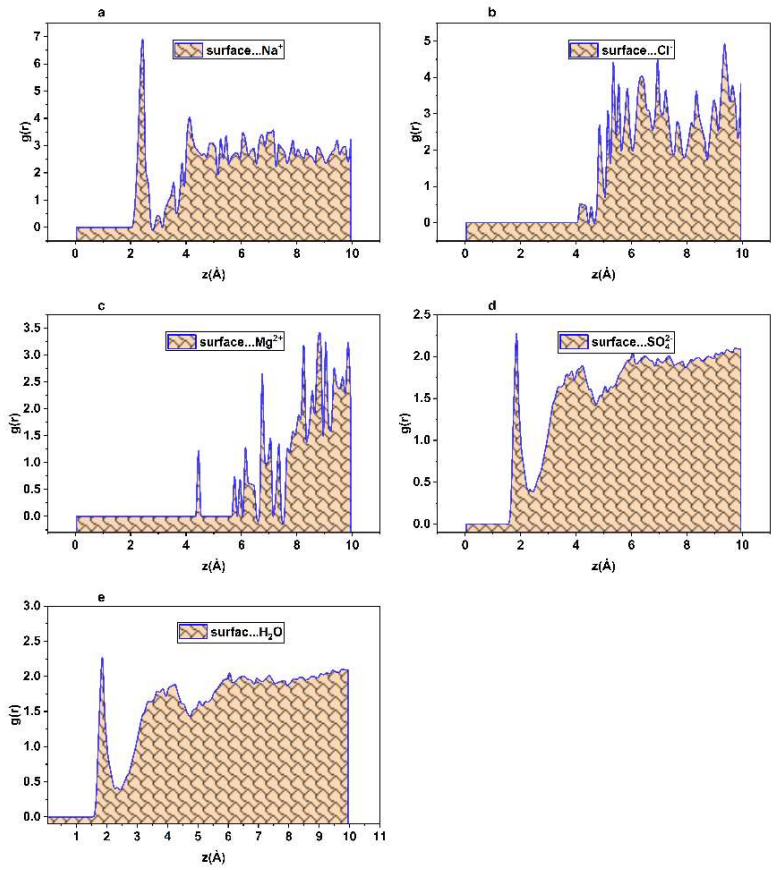

Figure 2. Illustration of the radial distribution function for different ions and water molecules with respect to the solid surface at T=300 K. The distance between Na^+, Cl^-, Mg^{2+}, SO_4^{2-} and H_2O from solid surface is 2.45 Å, 4.15 Å, 4.45 Å, 4.15 Å and 1.85 Å, respectively.

Rest of the mono and divalent ions are Cl^-, Mg^{2+} and SO_4^{2-} which are scatter at a radius of 4.15 Å, 4.45 Å, and 4.15 Å from the calcite slab, respectively.
The trend of radial distribution function g(r) in Figure 3 presents the distance between each anion and cation and the water molecules which surrounded them at T=300K. As seen, all of the mono/divalent ions are hydrated because the water molecules scatter at a distance of 2.5 Å, 2.2 Å, 1.85 Å, and 2.4 Å, from Na^+, Cl^-, Mg^{2+} and SO_4^{2-}, respectively. The shorter hydration radius is due to the higher hydration energy impact.

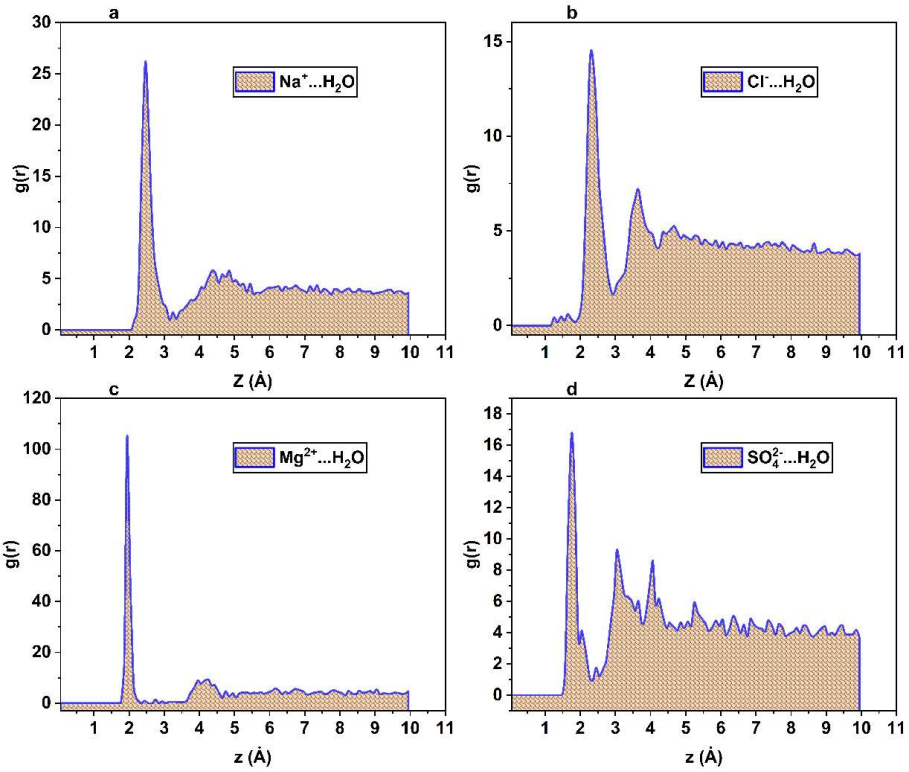

Figure 3. The prfile of the radial distribution function shows the distance between the water molecules and different ions at T=300 K. All of the mono/divalent ions are hydrated and the water molecules scatter at a distance of 2.5 Å, 2.2 Å, 1.85 Å, and 2.4 Å, from Na^+, Cl^-, SO_4^{2-} and Mg^{2+}, respectively.

Figure 4 shows the charge density profile. As seen, the development of a positive stern layer and negative diffuse layer is indicated by a positive and negative peak next to the calcite surface. The charge density profile above the calcite slab demonstrates the establishment of an electrical

double layer (EDL) parallel to the calcite slab, which includes monovalent cations in the starn layer and anions within the diffuse layer. Calculation of the mathematical area under the curve for charge density (Figure 4a) shows that the charge summation is negative.

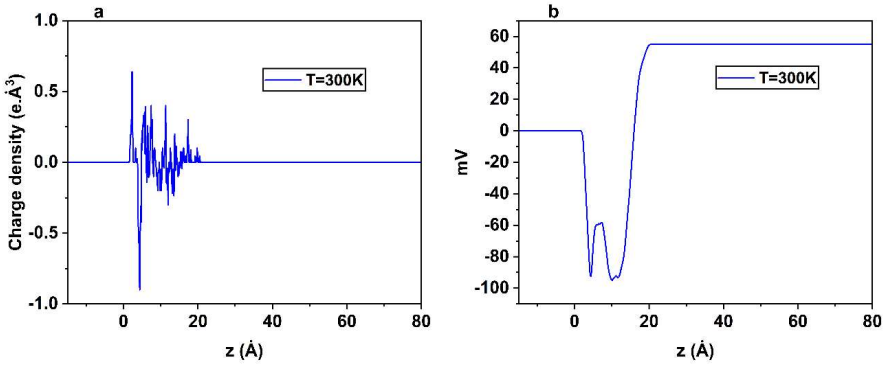

Figure 4. The charge density and zeta potential are shown with plots a and b, repectively.

Conclusions

Calcite is one of the most common minerals identified in oil reservoirs because it is the main component of limestone, dolomite, and chalk. Thus, investigation of the underlying mechanism of calcite-LSW interaction in a molecular scale can result in new understandings which can improve the efficicency of the EOR technology. Since, the influence of the LSW on EOR improvement has rarely been addressed at the molecular level, we used LAMMPS to explore the surface interaction of calcite with brine solution. Study of the different ions interaction with the calcite surface shows that the mono/divalent ions initially are hydrated. Water molecules from the first adsorbed layer on the calcite surface, dwelling at the closest distance, 1.85 Å above the calcite surface. Following that, hydrated Na^+, Cl^-, Mg^{2+} and SO_4^{2-} remain at 2.45 Å, 4.15 Å, 4.45 Å, and 4.15 Å with respect to the solid surface, respectively. The charge density profile also exhibits the formation of the EDL parallel to the calcite surface, including the positive stern layer and the negative diffuse layer. Therefore, it can be said that the positive stern layer is formed by Na^+ and Cl^- stablished the negative diffuse layer. The observed oscillation of charge density curve after the diffuse layer reflects the presence of Mg^{2+} and SO_4^{2-}. The presence of SO_4^{2-} in the outer layer of EDL and negative charge summation of EDL might be a good cause for repulsion of the oil molecules and turning the calcite surface water wet.

References

(1) Fredriksen, S. B.; Rognmo, A. U.; Sandengen, K.; Fernø, M. A. Wettability Effects on Osmosis as an Oil-Mobilization Mechanism during Low-Salinity Waterflooding. *Petrophysics-The SPWLA J. Form. Eval. Reserv. Descr.* **2017**, *58* (01), 28–35.

(2) Austad, T.; Shariatpanahi, S. F.; Strand, S.; Black, C. J. J.; Webb, K. J. Conditions for a Low-Salinity Enhanced Oil Recovery (EOR) Effect in Carbonate Oil Reservoirs. *Energy & fuels* **2012**, *26* (1), 569–575.

(3) Austad, T.; Shariatpanahi, S. F.; Strand, S.; Aksulu, H.; Puntervold, T. Low Salinity EOR Effects in Limestone Reservoir Cores Containing Anhydrite: A Discussion of the Chemical Mechanism. *Energy & Fuels* **2015**, *29* (11), 6903–6911.

(4) Mehraban, M. F.; Afzali, S.; Ahmadi, Z.; Mokhtari, R.; Ayatollahi, S.; Sharifi, M.; Kazemi, A.; Nasiri, M.; Fathollahi, S. SmartWater Flooding in a Carbonate Asphaltenic Fractured Oil Reservoir-Comprehensive Fluid-Fluid-Rock Mechanistic Study. In *IOR 2017-19th European Symposium on Improved Oil Recovery*; European Association of Geoscientists & Engineers, 2017; Vol. 2017, pp 1–15.

(5) McGuire, P. L.; Chatham, J. R.; Paskvan, F. K.; Sommer, D. M.; Carini, F. H. Low Salinity Oil Recovery: An Exciting New EOR Opportunity for Alaska's North Slope. In *SPE western regional meeting*; OnePetro, 2005.

(6) Lee, S. Y.; Webb, K. J.; Collins, I. R.; Lager, A.; Clarke, S. M.; O'Sullivan, M.; Routh, A. F.; Wang, X. Low Salinity Oil Recovery–Increasing Understanding of the Underlying Mechanisms. In *SPE Improved Oil Recovery Symposium*; OnePetro, 2010.

(7) Nasralla, R. A.; Nasr-El-Din, H. A. Double-Layer Expansion: Is It a Primary Mechanism of Improved Oil Recovery by Low-Salinity Waterflooding? *SPE Reserv. Eval. Eng.* **2014**, *17* (01), 49–59.

(8) Plimpton, S. Fast Parallel Algorithms for Short-Range Molecular Dynamics. *J. Comput. Phys.* **1995**, *117* (1), 1–19.

(9) Xiao, S.; Edwards, S. A.; Gräter, F. A New Transferable Forcefield for Simulating the Mechanics of CaCO3 Crystals. *J. Phys. Chem. C* **2011**, *115* (41), 20067–20075.

(10) Martínez, L.; Andrade, R.; Birgin, E. G.; Martínez, J. M. PACKMOL: A Package for Building Initial Configurations for Molecular Dynamics Simulations. *J. Comput. Chem.* **2009**, *30* (13), 2157–2164.

(11) Jorgensen, W. L.; Chandrasekhar, J.; Madura, J. D.; Impey, R. W.; Klein, M. L. Comparison of Simple Potential Functions for Simulating Liquid Water. *J. Chem. Phys.* **1983**, *79* (2), 926–935.

(12) Jorgensen, W. L.; Maxwell, D. S.; Tirado-Rives, J. Development and Testing of the OPLS All-Atom Force Field on Conformational Energetics and Properties of Organic Liquids. *J. Am. Chem. Soc.* **1996**, *118* (45), 11225–11236.

(13) Williams, C. D.; Burton, N. A.; Travis, K. P.; Harding, J. H. The Development of a Classical Force Field to Determine the Selectivity of an Aqueous Fe3+–Eda Complex for Tco4–and So42–. *J. Chem. Theory Comput.* **2014**, *10* (8), 3345–3353.

(14) Nosé, S. A Unified Formulation of the Constant Temperature Molecular Dynamics Methods. *J. Chem. Phys.* **1984**, *81* (1), 511–519.

(15) Goltapeh, S. A.; Abdolahi, S.; Miri, R.; Hellevang, H. Extension of PC-SAFT Equation of State to Include Mineral Surface Effect in Fluid Properties Using Molecular Dynamic Simulation. *Sustain. Energy Technol. Assessments* **2021**, *48*, 101624.

(16) Goltapeh, S. A.; Miri, R.; Aagaard, P.; Hellevang, H. Extension of SAFT Equation of State for Fluids Confined in Nano-Pores of Sedimentary Rocks Using Molecular Dynamic Simulation. *J. Mol. Liq.* **2021**, 118045.